



**UNIVERSITA' DEGLI STUDI DI PADOVA**  
**Centro Interdipartimentale di Studi e Attività Spaziali (CISAS)**

**DOTTORATO DI RICERCA IN SCIENZE TECNOLOGIE E MISURE  
SPAZIALI CICLO XX**

Sede amministrativa: Università degli Studi di Padova

**INDIRIZZO: MISURE MECCANICHE PER L'INGEGNERIA**

**TITOLO TESI:**

**GENERATION AND PROPAGATION OF VIBRATIONS ON SATELLITE  
STRUCTURES AND PLANETARY BODIES AFTER HYPERVELOCITY  
IMPACTS**

(Generazione e propagazione di vibrazioni su strutture satellitari e corpi planetari in conseguenza di impatti iperveloci)

**Direttore:** Prof. Pierluigi Bernacca  
**Coordinatore:** Prof. Francesco Angrilli  
**Supervisore:** Prof. Pavarin Daniele  
**Supervisore:** Prof. Alessandro Francesconi

**Dottorando:** Alberto Bettella

31 Gennaio 2008

<b>1</b>	<b>RIASSUNTO</b> .....	<b>I</b>
<b>2</b>	<b>ABSTRACT</b> .....	<b>IV</b>
<b>3</b>	<b>INTRODUCTION</b> .....	<b>1</b>
<b>4</b>	<b>THE HVI PHENOMENOLOGY</b> .....	<b>4</b>
4.1	PROBLEMS CONNECTED WITH THREAT OF SPACE DEBRIS AND MICROMETEORIDS.....	4
4.1.1	<i>Micrometeoroids and space debris population</i> .....	4
4.1.2	<i>Potential damage</i> .....	5
4.2	HVI DISTURBANCE ENVIRONMENT .....	5
4.2.1	<i>Application of Pyro standard to HVI-induced vibration environment</i> .....	6
4.2.2	<i>HVI-induced vibration environment</i> .....	7
4.2.3	<i>Physical parameters used to define HVI-induced environment</i> .....	7
4.3	THESIS LOGIC AND OBJECTIVES .....	9
4.3.1	<i>Spacecraft structures</i> .....	9
4.3.2	<i>Planetary objects</i> .....	11
4.3.3	<i>Thesis structure</i> .....	12
<b>5</b>	<b>EXPERIMENTAL METHODS</b> .....	<b>13</b>
5.1	MEASUREMENT CHAIN.....	13
5.1.1	<i>Acceleration sensors</i> .....	13
5.1.1.1	List of the accelerometers used for experiments .....	16
5.1.1.2	Accelerometer resonance .....	16
5.1.1.3	Accelerometer mounting .....	16
5.1.2	<i>Signal conditioner</i> .....	18
5.1.3	<i>Anti-aliasing filters</i> .....	19
5.1.4	<i>Sampling modules</i> .....	19
5.1.5	<i>System set-up and measurement chain</i> .....	20
5.2	ANALYSIS TOOLS .....	20
5.2.1	<i>Signal quality assessment</i> .....	23
5.3	PREPARATORY TEST ON SATELLITE STRUCTURES .....	25
5.3.1	<i>Uncertainty analysis</i> .....	26
5.3.2	<i>Noise source due to LGG operations and HVI physic</i> .....	27
5.3.3	<i>Acceleration levels on simple targets (near field)</i> .....	32
5.3.3.1	Acceleration levels for simple thin Al plates .....	33
5.3.3.2	Acceleration levels for simple Al HC plates .....	36
5.3.4	<i>Acceleration levels in complex targets (mid and far field)</i> .....	37
5.3.4.1	GOCE satellite .....	38
5.3.4.2	Test on complex targets .....	41
5.3.4.3	GOCE type "E" .....	41
5.3.4.4	GOCE type "C" .....	43
5.3.4.5	GOCE type "D" .....	45
<b>6</b>	<b>VIBRATION ENVIRONMENT OF SPACECRAFT STRUCTURES</b> .....	<b>48</b>
6.1	SRS OF THE DISTURBANCE GENERATED BY HVI ON SIMPLE TARGETS.....	48
6.1.1	<i>Tests on Al honeycomb sandwich panels (near field environment)</i> .....	49
6.1.2	<i>Test logic for Al HC SP</i> .....	51
6.1.2.1	Data scattering and noise evaluation (TS225) .....	52
6.1.2.2	Influence of existing damage (TS228).....	55
6.1.2.3	Scaling effects (TS224) .....	59
6.1.2.4	Load effects (TS227) .....	66

6.1.2.5	Type of waves.....	69
6.1.2.6	Effects of projectile mass (TS221 and TS223) .....	76
6.1.2.7	Effects of impact velocity (TS221 and TS222) .....	85
6.1.2.8	Oblique impacts (TS226).....	89
6.1.2.9	Relevant results for AI HC SP .....	99
6.2	PROPAGATION OF HVI-INDUCED DISTURBANCES IN COMPLEX TARGETS .....	101
6.2.1	<i>Method of analysis.....</i>	101
6.2.2	<i>Target configuration and test logic.....</i>	104
6.2.3	<i>Estimation of uncertainty.....</i>	106
6.2.3.1	Data scattering .....	106
6.2.3.2	Load effects.....	108
6.2.4	<i>Transmission functions (calibration vs mass and velocity).....</i>	110
6.2.5	<i>Influence of impact velocity (TS313).....</i>	113
6.2.6	<i>Influence of projectile mass (TS314).....</i>	115
6.2.7	<i>Summary of results .....</i>	118
6.2.8	<i>Joints and propagation attenuation functions due to HVI .....</i>	118
6.2.9	<i>Relevant results for TS31 (GOCE E target).....</i>	122
6.2.10	<i>Relevant result for other test .....</i>	123
6.2.11	<i>Relevant results for TS32 .....</i>	123
6.2.12	<i>Relevant results for TS33 .....</i>	124
6.2.13	<i>Relevant results for TS34 .....</i>	125
6.3	MOMENTUM TRANSFER EVALUATION (TS4).....	127
6.3.1	<i>Test logic for TS4 .....</i>	129
6.3.2	<i>Measurement method .....</i>	129
6.3.3	<i>Experimental set-up .....</i>	131
6.3.4	<i>Calibration.....</i>	132
6.3.5	<i>Uncertainty analysis.....</i>	135
6.3.6	<i>Back ground environment (TS40).....</i>	136
6.3.7	<i>Relevant results for TS4 .....</i>	138
6.4	WAVELET ANALYSIS .....	139
6.4.1	<i>Mathematical model of elastic waves inside plates .....</i>	139
6.4.2	<i>Validation of the WT method.....</i>	142
6.4.3	<i>Experimental signals: low velocity impacts on simple plates.....</i>	144
6.4.4	<i>HVI on simple aluminium plates .....</i>	147
6.4.5	<i>HVI on honeycomb aluminium panels .....</i>	149
<b>7</b>	<b>SHOCK WAVE PROPAGATION INTO MINOR BODIES OF THE SOLAR SYSTEM.....</b>	<b>152</b>
7.1	INTRODUCTION .....	152
7.1.1	<i>Constitutive models .....</i>	152
7.1.2	<i>Target material: Concrete.....</i>	153
7.1.3	<i>Porosity.....</i>	153
7.2	SIGNAL ANALYSIS STRATEGY.....	153
7.3	WAVES IN SPHERES MADE OF POROUS CONCRETE .....	154
7.3.1	<i>Wave speed and frequency.....</i>	156
7.3.2	<i>Wave reflection .....</i>	158
7.3.3	<i>Load effect .....</i>	160
<b>8</b>	<b>CONCLUSIONS .....</b>	<b>164</b>
8.1	PREPARATORY TESTS .....	164
8.2	HVI ON SATELLITE STRUCTURES .....	164
8.2.1	<i>Simple targets (near-field environment ()).....</i>	165

8.2.2	<i>Complex targets (mid- and far-field environment)</i> .....	166
8.3	MOMENTUM TRANSFERRED TO TARGETS BY HVI .....	168
8.4	WAVELET ANALYSIS ON SATELLITE COMPONENTS .....	169
8.5	SHOCK WAVE PROPAGATION INTO MINOR BODIES OF THE SOLAR SYSTEM.....	169
<b>9</b>	<b>REFERENCES .....</b>	<b>171</b>
<b>10</b>	<b>LIST OF ABBREVIATIONS AND ACRONYMS.....</b>	<b>174</b>

# 1 Riassunto

Gli impatti iperveloci (HVI: Hyper-Velocity-Impacts) sono un problema comune nell'ambiente spaziale. Essi interessano, in particolare, le missioni spaziali, in termini di:

- Potenziale danneggiamento delle sonde spaziali e dei satelliti
- Sviluppo collisionale di piccoli e grandi corpi del Sistema Solare.

Questa tesi si concentra sull'effetto di tali impatti, attraverso l'analisi del campo di vibrazione generato da HVI in entrambe le tematiche appena introdotte.

Riguardo al disturbo indotto da HVI su elementi interni di satelliti, è stata condotta un'estesa campagna sperimentale su bersagli rappresentativi di tali parti. Lo scopo di quest'attività è acquistare dati su onde e vibrazioni generate dopo un HVI e che propagano dal punto d'impatto. Il campo di vibrazione indotto è stato valutato sotto forma di accelerazione.

Tale attività ha permesso di raccogliere dati insostituibili, poiché un HVI può sollecitare una struttura fino a frequenze che non sono esplorate nella comune pratica delle prove dinamiche e tali carichi possono danneggiare componenti elettronici e sensori montati su satelliti. Per questo motivo, tale campagna sperimentale rappresenta un'occasione unica per la raccolta di dati del comportamento transitorio di strutture sottoposte alla minaccia di HVI. Questo studio abbraccia sia target semplici (e.g. piastre semplici e pannelli sandwich di alluminio e materiali compositi) e target complessi (e.g. assemblati strutturali, inclusi giunti), colpiti da proiettili con diametri variabili tra 0.6 a 2.3 mm e con velocità comprese tra 2 a 5 km/s.

Il test-case selezionato per questa attività sperimentale è il satellite GOCE. Il suo obiettivo principale è di misurare il campo gravitazionale terrestre, modellando il geode con estrema accuratezza e risoluzione spaziale. Per fare questo, incorpora un gradiometro sensibile a campi di disturbo simili a quelli generati da un HVI. E' fondamentale per questo motivo, la verifica del campo vibratorio generato dopo un tale evento.

Il risultato principale di questa attività è stata la creazione di un esteso database dei disturbi generati e propagati da un HVI su target semplici e assemblati complessi, sottolineando inoltre la dipendenza della risposta strutturale alla velocità e massa del detrito impattante. Il disturbo è stato quantificato computando lo spettro SRS dei segnali di accelerazione misurati.

Questa attività ha inoltre reso possibile la valutazione del momento trasferito dal proiettile al bersaglio impattato. Questa misura si è resa necessaria per validare le tecniche numeriche usate nell'estrapolazione dei risultati sperimentali su strutture e condizioni di impatto differenti da quelli raggiungibili in laboratorio con le facility di ipervelocità attualmente esistenti [28].

Inoltre, per investigare nel dettaglio le caratteristiche tipiche del disturbo transitorio, è stato intrapreso uno studio dedicato sull'applicazione della Trasformata Wavelet (WT) su segnali di accelerazione acquisiti su piastre di alluminio semplici e su pannelli sandwich. La WT è stata usata per caratterizzare i comportamenti propagatori delle onde in questi bersagli, grazie alla sua abilità nell'identificare le seguenti caratteristiche delle: velocità di propagazione, proprietà di dispersione e contenuto in frequenza. Questo lavoro ha condotto ad una migliore comprensione delle origini del campo di disturbo dovuto ad HVI, dimostrando che la tecnica wavelet può essere usata per analizzare i componenti elementari di segnali transitori di vibrazione.

Per quanto riguarda il secondo punto, cioè lo studio dell'evoluzione collisionale dei corpi minori del sistema solare, alcune simulazioni sono state completate per analizzare la propagazione delle onde su tali corpi.

Gli impatti iperveloci caratterizzano la storia evolutiva dei piccoli e grandi corpi del Sistema Solare. Per questo motivo, lo scopo delle simulazioni su corpi porosi (il cemento è stato utilizzato come test-case in questa tesi) è di ottenere una miglior comprensione dei processi di impatto e di fornire uno strumento per valicare i risultati dei modelli numerici, attraverso l'analisi della propagazione e generazione di onde su materiali differenti.

I risultati di questa attività mirano a contribuire all'interpretazione dei dati di osservazioni da terra e spazio, in particolare riguardo a missioni come *Smart1*, *MarsExpress*, *VenusExpress*, *BepiColombo*, *Cassini-Huygens*, *Rosetta*, *Dawn*.

Gli esperimenti di impatto, utili a investigare la dinamica di craterizzazione e distruzione catastrofica su oggetti planetari, sono limitati per colpa di effetti scala (e.g. dimensione dei bersagli, ambiente gravitazionale terrestre, e prestazione delle moderne facility di impatto). Perciò un metodo possibile per lo studio dei processi di impatto è quello di condurre simulazioni numeriche con idrocodici. Le problematiche principali di questi strumenti è la sconosciuta risposta dei materiali agli impatti ad alta velocità, a pressioni di svariati Mpa e alla propagazione di onde di shock. La loro validazione obbliga a testare con le facility di impatto disponibili, bersagli di scala ridotta, pur sempre rappresentativi di veri asteroidi, e di riprodurre gli esperimenti con le simulazioni numeriche. Le onde che si propagano all'interno dei bersagli impattati possono essere usate per validare questi modelli, attraverso il confronto delle caratteristiche delle onde come: velocità, frequenza e riflessioni.

In questa tesi è stata esplorata la possibilità di usare un accelerometro per misurare la propagazione di tali onde in sfere di cemento (che rappresentano bersagli porosi), e di identificare le loro caratteristiche con la WT.

A tale fine, sono state condotte simulazioni SPH, per meglio capire le dinamiche di propagazione e per quantificare possibili effetti di carico imputabili alla massa dell'accelerometro sulla sfera di cemento. I risultati dell'analisi mostrano che la misura è possibile, anche se è necessaria una strumentazione molto dedicata.

I capitoli della tesi trattano i seguenti argomenti:

Capitolo 4: fenomenologia dell'impatto ad ipervelocità: descrizione dell'ambiente meteorico e detritico e del loro potenziale di danneggiamento su satelliti, descrizione delle procedura standard nell'analisi di shock e presentazione della logica e degli obiettivi della tesi.

Capitolo 5: metodi sperimentali. Definizione di una catena di misura adatta all'acquisizione di segnali di shock. Presentazione dei metodi comunemente usati (standard) nell'analisi di segnali di accelerazione. Test preparatori su componenti di satelliti (target semplici e complessi), volti ad identificare l'involuppo del disturbo e l'effetto di carico dovuto alla facility di impatto.

Capitolo 6: misura e analisi dell'ambiente vibrazionale su strutture semplici, quali pannelli sandwich in alluminio e su strutture complesse, quali assemblati di pannelli sandwich (in composito ed in alluminio) connessi con giunti. Il campo vibratorio è stato caratterizzando variando massa e velocità del proiettile e variando le condizioni di impatto. Sono stati misurati i livelli di accelerazione transitori ed è stato computato l'SRS per ognuno di essi. E' stata definita per ogni tipologia di test l'incertezza

connessa con la misura. Nel caso dei bersagli complessi sono state definite anche le funzioni di trasferimento dei giunti. Inoltre, è stato misurato il momento trasferito dai proiettili ai bersagli (sia su piastre semplici che su pannelli sandwich in alluminio e composito). Tale attività ha permesso di validare le simulazioni numeriche utilizzate per estrapolare il disturbo (valutato mediante SRS) a condizioni di impatto ed a componenti non testabili in laboratorio. Infine è stata condotta un'analisi del disturbo transitorio a livello di "propagazione di onde" utilizzando la trasformata Wavelet. Tale analisi ha permesso di identificare le caratteristiche principali delle onde indotte su pannelli semplici e sandwich di alluminio.

Capitolo 7 analisi della propagazione delle onde di shock in simulacri di corpi minori del sistema solare (simulati mediante sfere di cemento). Tale analisi è stata condotta mediante la trasformata Wavelet, con lo scopo di identificare le caratteristiche propagative del disturbo, e di stimare il possibile effetto di carico connesso all'utilizzo di un accelerometro. L'obiettivo è la misura del campo vibratorio indotto da HVI con lo scopo di impostare la validazione tra esperimenti e simulazioni sull'equivalenza delle caratteristiche delle onde generate.

## 2 Abstract

Hyper-Velocity-Impacts (HVI) are a common problem in the space environment. They especially concern space missions, in terms of:

- Potential damage to spacecrafts and satellites
- Collisional evolution of small and large bodies of the Solar System

This thesis focuses on the effect of such impacts, through the analysis of the vibration field generated by HVI on both of the aforementioned cases.

Referring to the first point, i.e. the HVI-induced disturbances on spacecraft internal components, a wide experimental campaign has been performed on targets representative of S/C structures, making it possible to measuring and reproducing the HVI-induced vibration field on the selected targets. The aim of this activity was to acquire data on transient waves generated after an HVI and propagating from the impact point. Such disturbances have been evaluated in from of acceleration signals.

The invaluable information achievable from such an activity is related to the HVI ability of loading structures up to frequencies that are normally not explored in the standard practice for mechanical dynamic testing. These loads can damage electronic components and sensors mounted on S/C.

An experimental campaign on structural components represents a unique mean of collecting data about the transient behaviour of spacecraft components subjected to HVI threat. The Study is relevant to both "simplified" (i.e. simple plates and sandwich panels made by Aluminium alloy and composite materials) and "complex" (i.e. structural assemblies including joints) targets, hit by projectiles in the range 0.6 – 2.3 mm at velocity from 2 to 5 km/s.

The test-case selected for the experimental activity is the GOCE satellite, whose mission main objective is to measure the Earth's gravity field modelling the geoid with extremely high accuracy and spatial resolution. To do this, it will carry a gradiometer that is sensitive to disturbances, like the one generated by HVI. For this reason, the assessment of the vibration field that propagates after an HVI is fundamental.

As a conclusion, the activity on spacecraft structures resulted in the creation of an extensive database of the disturbance field generated and propagated by HVI on simple and complex assemblies, even highlighting the dependence of the structural response from the mass and velocity of the impacting debris. The disturbance was quantified computing SRS spectra of the measured acceleration signals.

This activity made also possible to evaluate the momentum transferred by the projectiles to the impacted targets. This measurement was necessary to validate the numerical technique used to extrapolate the experimental results to structures and impact conditions different from those achievable at laboratory scale with the existing hypervelocity facilities [28].

Moreover, to investigate in detail the typical features of transient disturbances, a dedicated study was implemented on the application of Wavelet Transform (WT) to the sampled acceleration signal on aluminium simple plates and honeycomb sandwich panels. WT was used to explore the complex wave generation and propagation behaviour inside these targets, thanks to its ability of identifying the following wave features: speed of propagation, type, dispersion properties and frequency content. This work led to a better understanding of the origin of disturbance field due to HVI, demonstrating that WT technique may be used to analyse the elementary constituents of transitory signals.



Referring to the second point, i.e. the study of the collisional evolution of minor bodies of the Solar System, several numerical simulations were carried out to study the wave propagation on planetary-like objects.

HVI characterize the evolutionary story of all the small and large bodies of the Solar System. For this reason, the goal of simulations on porous materials (concrete was used as test-case in this thesis) was to obtain a better comprehension of the impact processes and to provide a tool to validate the results of numerical models, through the analysis of wave generation and propagation on different materials. The results of this activity aimed also to contribute to the data interpretation of the ground and space based observations, in particular in view of space missions such as Smart1, MarsExpress, VenusExpress, BepiColombo, Cassini-Huygens, Rosetta, Dawn.

Impact experiments to investigate craterization and catastrophic disruption on planetary objects are limited due to scale effect (i.e. size of the targets, Earth gravity environment, actual performance of the modern hypervelocity facilities). Therefore, a possible method used to study the impact processes is to perform numerical simulations with hydrocodes. The main issue with these tools is the unknown response of materials to high velocity impacts, pressures of several MPa and shock wave propagation. The validation of such models implies to test with the available impact facilities small-scale targets representative of real asteroids and to match experiments and numerical simulations. Waves propagating within the impacted target can be used in the assessment of such numerical models, through the comparison of waves features like: speed, frequency and reflections.

In this thesis the possibility to use an accelerometer to measure waves propagation in concrete spheres (representative of porous targets) and to identify wave features with WT is explored. For this reason, SPH (smooth particles hydrocode) simulations have been carried out on a small-scale concrete sphere to better understand the propagation of shock waves and to evaluate the load effects due to the accelerometer mass. Results show that this measurement is possible, even if it is necessary to perform it with a highly sensitive measurement chain.

### 3 Introduction

Hyper-Velocity-Impacts (HVI) are a common problem in the space environment. They concern especially space missions, in terms of potential damage to spacecrafts and satellites and concern small and big bodies of the Solar System that show a deep collisional evolution.

In the case of spacecraft structures, most part of the past studies focuses on the primary effects of impact, like perforation, craterization and fragmentation. However, some studies evidence that secondary effect, like the vibration field generated near the impact point, can cause severe damage to the equipment installed on the impacted object.

This thesis focuses on the experimental study of generation and propagation of disturbance and in particular, waves, after a hypervelocity impact in these two fields:

- Impacts on spacecraft structures for human and automatic space missions
- Impacts on bodies of solar system (i.e. cratering)

GOCE satellite (Fig. 3-1) is the object of the first field of study (space missions). The Gravity Field and Steady-State Ocean Circulation Explorer (GOCE) is dedicated to measuring the Earth's gravity field and modelling the geoid with extremely high accuracy and spatial resolution. It is the first Earth Explorer Core mission to be developed as part of ESA's Living Planet Programme and is scheduled for launch in 2007.



**Fig. 3-1 Artist's impression of GOCE.**

From ESA Web site ([http://www.esa.int/esaLP/ESAYEK1VMOC\\_LPgoce\\_0.html](http://www.esa.int/esaLP/ESAYEK1VMOC_LPgoce_0.html)):

*"The geoid, which is defined by the Earth's gravity field, is a surface of equal gravitational potential. It follows a hypothetical ocean surface at rest (in the absence of tides and currents). A precise model of the Earth's geoid is crucial for deriving accurate measurements of ocean circulation, sea-level change and terrestrial ice dynamics – all of which are affected by climate change. The geoid is also used as a reference surface from which to map all topographical features on the planet. An improved knowledge of gravity anomalies will contribute to a better understanding of the Earth's interior, such as the physics and dynamics associated with volcanism and earthquakes and also further our knowledge of land uplift due to post-glacial rebound".*

To achieve these objectives GOCE has been equipped with a Gradiometer (3 pairs of 3-axis, servo-controlled, capacitive accelerometers, each pair separated by a distance of 0.5 m). The gradiometer is very sensible to disturbances, like the acceleration field induced by HVI. Vibrations can propagate from the impact point through the joints to the gradiometer base, disturbing the measure, saturating the channel and thus forcing the recalibration of the sensor. Thus, the first objective of this study is to assess the vibration environment levels (both as acceleration intensity e frequency) generated and propagated through spacecraft structural components by HVI.

This thesis has been done in the frame of ESA contract [9]. The specific work done by the author is detailed in this document and the work connected to it, but accomplished by other colleagues, is briefly summarized for completeness.

The second part of the thesis focuses on impacts on planetary objects, like asteroids, usually made by porous materials. The goal of this field of research is to obtain a better comprehension of the impact processes. The aim is to analyse the evolution of the surface of the solid bodies and the collisional evolution of the minor bodies of the Solar System. A deeper understanding of impact processes is needed to increase our knowledge of the surface evolution of the solid bodies in the Solar System and to allow remote sensing data from forthcoming missions as Smart1, MarsExpress, VenusExpress, Cassini/Huygens, Rosetta to be correctly interpreted. Furthermore, impact fragmentation and collisional break-up processes have to be better understood in order to investigate the evolution of the asteroids, comets, Trans Neptunian Objects (TNO) and the small natural satellites and for developing more complete and accurate theoretical models.

New data from ground-based observations and spacecraft encounters are giving us evidence of the low density and significant porosity of the asteroids (see Fig. 3-2, on the left) as well as for the icy satellites of Saturn. Porosity is an important physical characteristic of the minor bodies, affecting their behaviour during cratering and catastrophic disruption. High velocity impacts in porous materials of ice and silicates haven't been performed in sufficient details and the available experimental data sets are limited.

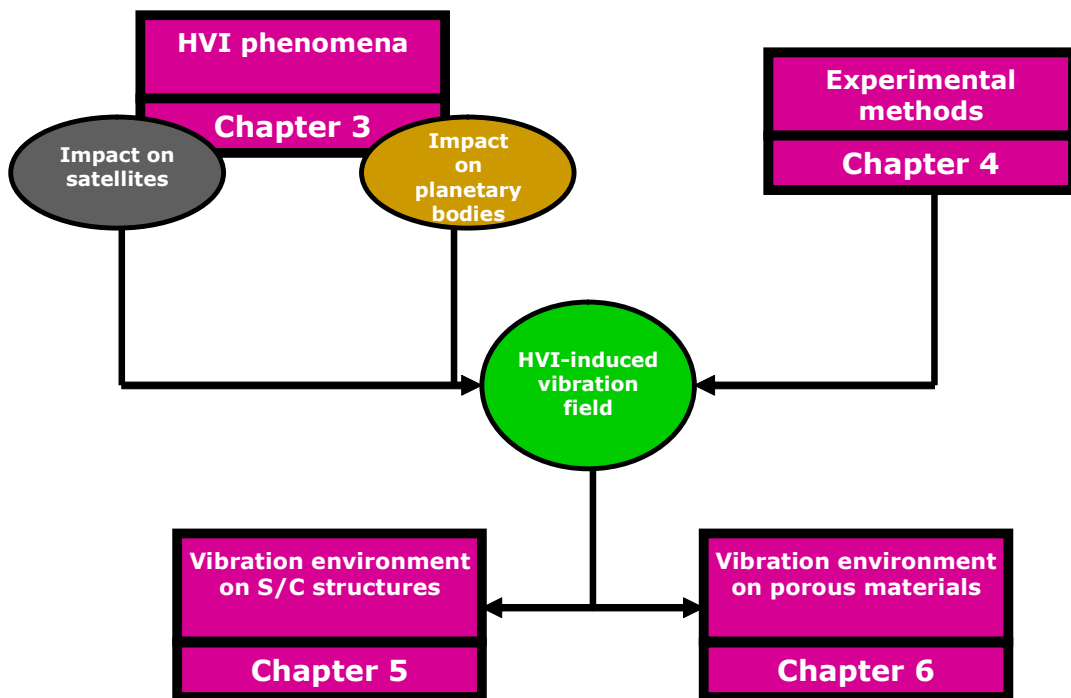
Therefore, we focus on the study of impact processes on porous targets in order to complement and extend the available data to ranges of velocity and physical conditions not yet explored [19].

The results of this research are also aimed to contribute to the data interpretation of the ground and space based observations, in particular in view of space missions such as Smart1, MarsExpress, VenusExpress, BepiColombo, Cassini-Huygens, Rosetta, Dawn.



**Fig. 3-2** The image of a 20 km diameter crater of the asteroid Mathilda (on left): the dimension of the crater suggest that the shock wave have been attenuated by its high porosity. An artist impression of an impact on Earth (on the right)

The following figure shows the work flow chart.



**Fig. 3-3** Scheme of the work of this thesis

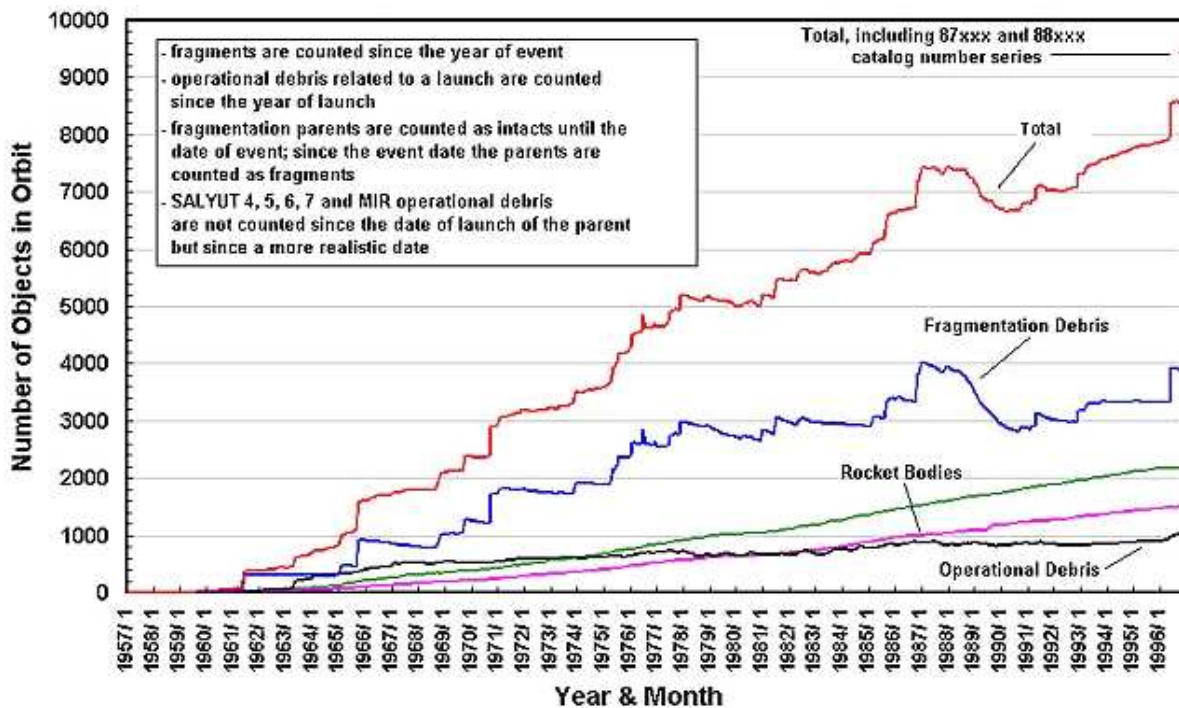
## 4 The HVI phenomenology

### 4.1 Problems connected with threat of space debris and micrometeoroids.

Particles and bodies of different shape, outside the earth atmosphere, expose structures in orbit to collision risk. We call "space debris" all the particles that derive from human activity in space (mostly made of aluminium) and "micrometeoroids" the natural particles in orbit around the Earth and Sun (they have the medium density of silicates).

#### 4.1.1 Micrometeoroids and space debris population

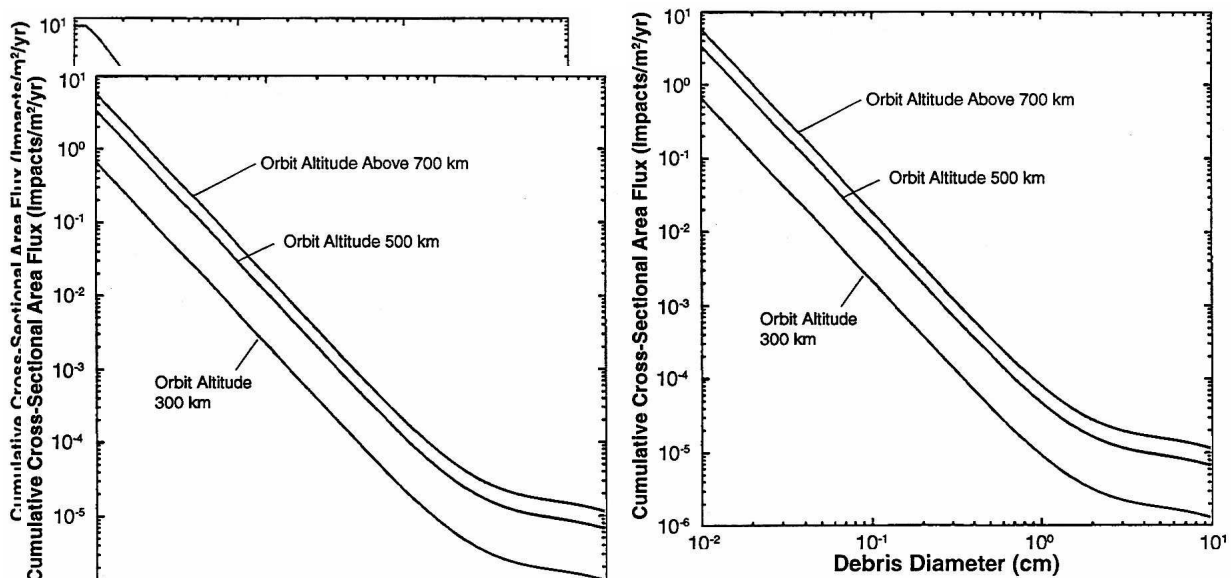
Actually, we know that over 9.000 objects larger than 10 cm exist (Fig. 4-1), while the estimated population of particles between 1 and 10 cm in diameter is greater than 100.000 and the number of particles smaller than 1 cm probably exceeds tens of millions.



**Fig. 4-1 Number of tracked objects in orbit based on the Satellite Catalogue, 1997 [JSC OD Off., V2 I3 1997].**

Measurements conducted during the 1960s, revealed that the threat of colliding with a meteoroid capable of inflicting significant damage to a spacecraft, is remote (the probability that a square meter of exposed surface in LEO will be struck by a 1 cm diameter meteoroid during a year in space, is about one in a million. Simple design features are capable of protecting spacecrafts against small and light natural particles (average meteoroid density is about 500 kg/m<sup>3</sup>). Hence, the natural meteoroid environment does not pose a serious hazard to most satellites in Earth orbit and shielding measures must be tuned to protect spacecrafts against debris impacts,

which are more probable (Fig. 4-2) and more hazardous (average debris density is about  $2700 \text{ kg/m}^3$ ).



**Fig. 4-2 Cross-sectional area flux for meteoroids and debris as a function of particle diameter [NASA SS 1740.14].**

#### 4.1.2 Potential damage

Micrometeoroids and space debris travel at high velocity and in this case, the impact of even small particles, can cause a serious threat to space missions. The range of velocities is up to 16 km/s for space debris, up to 80 km/s for micrometeoroids.

We can divide potential damage depending on dimensions and velocity of particles:

- Primary damage, like direct impact and perforation of the structure in orbit
- Secondary damage, like impacts of debris cloud on internal components, electromagnetic emissions and plasma, electric bows, disturbances or failure of components sensitive to vibrations

Up to now, all data on hypervelocity impacts refers to quantitative and qualitative analysis of the first of the above aspects.

This approach is good to design defence systems against impacts, but it does not consider the aspect of propagation of vibrations, from the shields to the equipment installed on satellites. Those impacts, due to their high energy, generate a very intense vibration field, characterized by high frequency and acceleration content (up to 100 kHz and 80.000 g) near the impact point (about 200 mm).

#### 4.2 HVI disturbance environment

Hypervelocity impacts (HVI) are difficult to characterize, due to the high acceleration and high frequency vibration field they generate. In the field of shock measurement, pyroshock are phenomena that better approximate a hypervelocity impact.

The following paragraphs summarize the main findings of literature survey on high-energy-shocks generation and propagation on structures.

The subject is shock generated by pyrotechnic devices actuation, because of two main reasons:

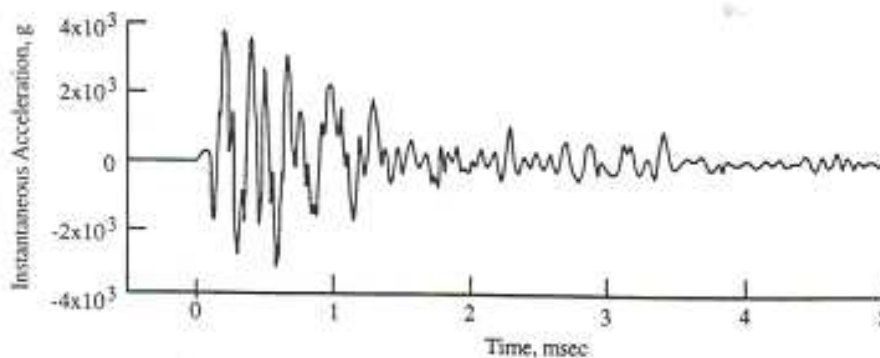
- To date, the state of the art of shock analysis on spacecraft refers mainly to pyroshocks and only limited literature is available on hypervelocity-induced shocks
- From preliminary investigations, we suppose that HVI-induced shocks have similar characteristics to those originated by pyros. Therefore, procedures used to analyze the shock environment produced by pyros would provide very useful guidelines even for studying HVI-induced shocks

#### 4.2.1 Application of Pyro standard to HVI-induced vibration environment

The term pyroshock (or pyrotechnic shock) generally refers to the severe mechanical transients caused by detonation of an ordnance device on a structure. Such devices, including flexible linear shaped charges, explosive nuts, pin pullers and cable cutters, are widely used to accomplish the in-flight separation of structural elements on aerospace vehicles, and are a significant cause of flight failures.

Pyroshock generates on space vehicles a vibration environment potentially very dangerous for different components. International standards defines general rules to deal with this specific problem, through the definition of the general morphology of the shock induced vibration environment, and what must be considered as maximum predicted pyro-shock environment for test qualification.

Pyroshocks are commonly measured using accelerometers because of their small size and weight, and wide frequency range capabilities. Fig. 4-3 shows a typical time history signal measured with an accelerometer.



**Fig. 4-3 Typical pyroshock acceleration signal measured with a 20 kHz bandwidth**

HVI produces even higher vibration environment than pyro, both in frequency and acceleration content. The assessment of the induced HVI disturbance follows the same procedures of pyros: accelerometers are positioned on structural components and the induced vibration is quantified using the same analysis tools.

Up to now, HVI have not been studied in terms of "disturbance environment", but only in ballistic terms, (i.e. a projectile with mass  $x$  and velocity  $y$  does perforate a certain structural component?). There are nearly no information about the intensity of shock waves and vibration environment that are generated after impact and that propagate through structures.

#### 4.2.2 HVI-induced vibration environment

NASA standards [3] present a general description of the shock-environment's morphology. They broadly divide the induced vibration environment into three categories: near-field, mid-field and far-field. The magnitude (acceleration) and spectral content of the induced disturbance is the parameter that set the area of influence of these categories.

The magnitude of shock depends on the type and strength of the pyroshock device, the source/hardware distance, and the configuration details of the intervening structure (especially discontinuities like joints, corners, lumped masses, and resilient elements, which can significantly attenuate the high frequency content of the pyroshock environment).

In the case of HVI, the magnitude depends on the energy of the projectile.

- **The near-field environment** is ruled by direct wave propagation from the source, causing peak accelerations in excess of 5000 g and substantial spectral content above 100 kHz. For very intense sources, such as most line sources, the near-field usually includes structural locations within approximately 15 cm of the source (unless there are intervening structural discontinuities). For less intense sources, such as most point sources, the near-field usually includes locations within approximately 3 cm of the source. For HVI, near field includes zones that sustain severe plastic deformation and vaporization of the material. In these zones, the plastic wave behaviour rules with the highest acceleration/frequency environment.
- The **mid-field environment** is characterized by a combination of elastic wave propagation and structural resonance, causing peak accelerations between 1000 and 5000 g and substantial spectral content above 10 kHz. For very intense sources, the mid-field usually includes structural locations between approximately 15 cm and 60 cm of the source (unless there are intervening structural discontinuities). The mid-field may extend between 3 cm and 15 cm from less intense sources.
- Structural resonance dominates the **far-field environment**, with peak accelerations below 1000 g and most of the spectral content below 10 kHz. The far-field distances occur outside the mid-field.

#### 4.2.3 Physical parameters used to define HVI-induced environment

NASA standards [3] provide some general indications on the parameters to use when we analyse the shock environment. Although force, strain or velocity may characterize a pyro, it is usually described in terms of an **acceleration time history** and its computed **spectrum**.

High intensity, high frequency, and acceleration time histories of very short duration characterize a pyrotechnic shock environment (and HVI). It resembles a summation of decaying sinusoids with very rapid rise times. Most realistically, it is as a travelling wave rather than a classical standing wave response of vibration modes (at least, near the impact zone). Typically, at or very near the source, the acceleration time history can have levels in the thousands of g's, have primary frequency content from 10 kHz to 100 kHz, and decay within 3-15 milliseconds.

We can represent the time history or waveform in terms of its **absolute acceleration** and duration. Vibration and/or electrical noise can occur simultaneously with



pyroshock, which may make it difficult to ascertain the total duration. In this case, the pyro ends the instant that the waveform has decayed to 10 percent of the absolute peak value. It should be noted that velocity, rather than acceleration, has been proposed by some organizations dealing with transients as the preferred response parameter, since resonant stresses have been shown to be theoretically proportional to velocity.

**Spectra** may be computed to characterize the frequency content of a transient: the most used are the Fourier (FFT), and the Shock Response Spectra (SRS).

## 4.3 Thesis logic and objectives

This thesis focuses on characterizing the vibration field generated on spacecraft structures and on planetary objects by HVI. Such disturbance has been reproduced in laboratory using the CISAS LGG, impacting satellite components and simulating the HVI-induced shock environment on planetary objects using hydrocodes. The resulting vibration field has been measured (with accelerometers) and analysed, as detailed in the following paragraphs.

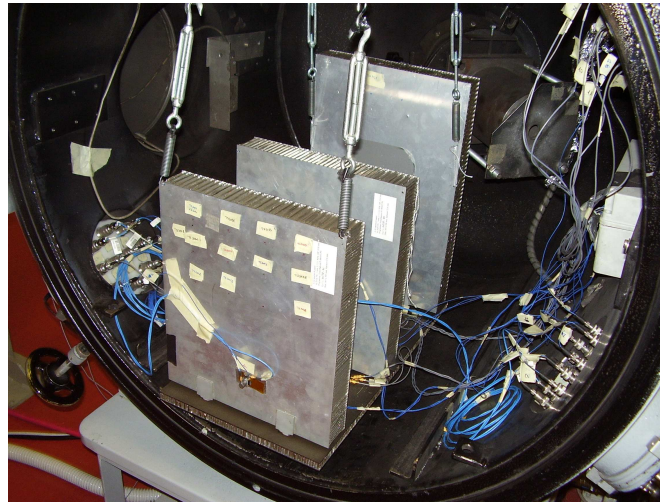
### 4.3.1 Spacecraft structures

The aim of the work regarding spacecraft structures is to provide a characterization of the vibration field generated after HVI and propagated on different types of satellite components (protective panels or instrumentation floors). The objective of this activity is dual: assessing the vibration field on GOCE satellite and build up a method to test a generic satellite against HVI without having to do experiments (expensive) on it.

The results the experiments on GOCE have been extrapolated (coupling numerical simulation and experimental SRS) to predict the vibration field generated on generic satellite. In fact, the analysis performed on GOCE is an expensive procedure and in general is often unreliable due to the dimension of the spacecraft components; instead, this method can be used to design and size new spacecrafts without having to test them. The activity presented in this thesis is limited to the evaluation of the disturbance levels, while details on extrapolation procedures can be found in [24].

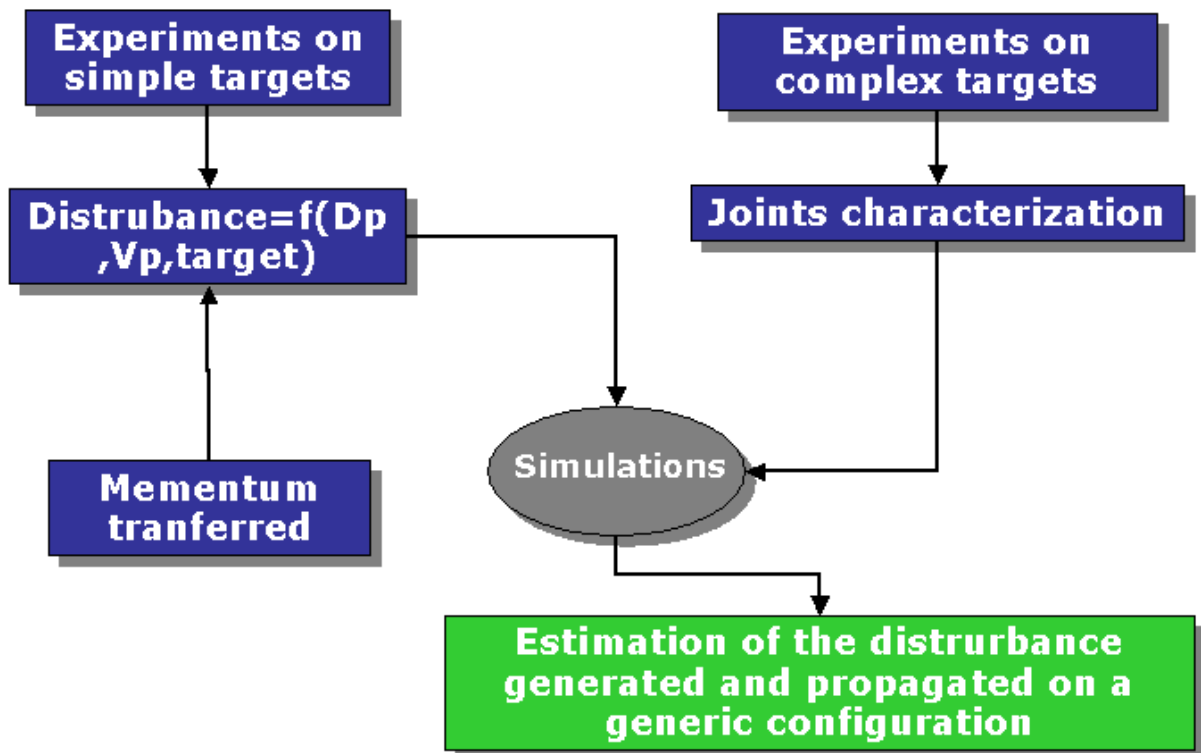
Experiments have been carried on simulacra of GOCE structure and following the main steps of this method, they can be used to asses the vibration field induced by HVI on a generic satellite, made of the same components tested.

1. Collection of vibration data on a single impacted target with different projectile conditions (i.e. velocity and mass) and on different targets (i.e. plate or honeycomb). The vibration (or disturbance) field is a function of these parameters and is characterized using an SRS
2. Extrapolation of the vibration data (SRS resulting from point 1) for projectile's parameters not testable in laboratory (i.e. velocities or masses) using a method involving SPH simulation and the evaluation of the momentum transferred from the projectile to the target
3. Propagation of the vibration using numerical codes (FEA and SEA) and definition of transfer functions for HVI on complex target assemblies (i.e. plates jointed together). These functions shall provide the SRS on a target not directly impacted by the projectile, but connected to it with joints, starting from the SRS computed on the impacted plate. Fig. 4-4 shows a complex target.



**Fig. 4-4 Test target for HVI impact, the sensors (accelerometers) are attached on different plates.**

This procedure is summarised in the following figure



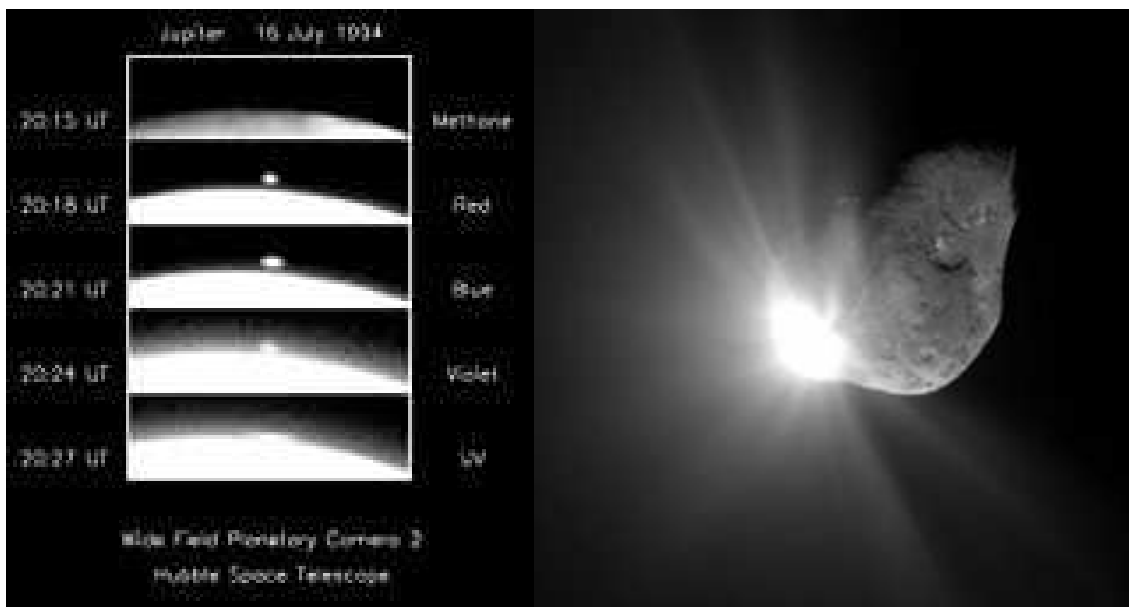
**Fig. 4-5 Scheme followed to provide and estimation of the HVI-induced vibration field on a generic satellite structure**

Moreover, a detailed analysis of the vibration field has been done using wavelets (see paragraph 6.4) to better understand how waves behave after an HVI, even on complex targets (honeycombs panels).

All tests were performed on different types of target and under different types of impact parameters and all the experimental work was made at the CISAS LGG (Light Gas Gun) facility.

#### 4.3.2 Planetary objects

The damage of an HVI on planetary bodies, from the simple cratering to the total disruption, is due to waves propagating, interfering and reflecting inside them. Experiments in this field are difficult and so tests are usually possible only on scale models. One way to perform an analysis of HVI on real asteroids or on a planet is to impact it with a satellite (i.e. Deep Impact mission) or observing natural phenomena (i.e. the Comet Shoemaker-Levy 9).



**Fig. 4-6** On the left an image of the Comet Shoemaker-Levy 9 on Jupiter, on the right the flash resulting from the impact of a part of Deep Impact probe with the comet 9P/Tempel

Another way is to make accurate numerical simulations. These simulations (usually made with SPH codes) must be validated, especially due to the uncertainty on the materials constitutive models. The aim of this work on planetology is to provide a method to accomplish this task. The validation can be made comparing experimental results of HVI on scale models to the results of simulations: the characteristics of waves (i.e. type, velocity, frequency) predicted by simulations and experimentally measured (with accelerometers) can be extracted using the wavelet transform from a simple acceleration signal and compared.

Regarding simulations, the work focus on assessing the wave field generated after impact and on simulating the load effect of an accelerometer mounted on a scale mode of planetary object. This was done because shock accelerometers (used to measure acceleration field generated by the waves inside the simulacra) have finite dimensions, and scale models cannot be too wide (due to the maximum size of targets

that can be tested at the CISAS HVI facility). For this reasons the load-effect can be excessively high and have been assessed with simulations before performing expensive experimental test.

### 4.3.3 Thesis structure

The thesis will follow this logic:

<b>Chapter 5</b>	<b>Experimental methods</b>
<b>Objective</b>	To introduce the tools used to measure and analyse acceleration signals representative of the HVI induced disturbance. Since the HVI vibration environment is unknown, preparatory tests have been made to set-up the facility, measurement chain and sensors type and position on test targets.

<b>Chapter 6</b>	<b>Vibration environment of spacecraft structures</b>
<b>Objective</b>	The analysis of generation and propagation of shock waves on structural components of satellites (GOCE), from data acquired after a wide experimental campaign. These data were used to predict the vibration field on satellite components not tested experimentally.

<b>Chapter 7</b>	<b>Shock wave propagation into minor bodies of the Solar System</b>
<b>Objective</b>	The analysis of generation and propagation of shock waves on porous bodies, like asteroids, comets and icy satellites, from simulations with SPH on concrete spheres

## 5 Experimental methods

The chapter focus on the specific problems connected with HVI measure and analysis. Here are covered the following aspects:

- Instrumentation used for recording the acceleration field generated by HVI
- Signal quality assessment and data analysis tools
- Preparatory test made to assess the HVI-induced vibration environment and to reach a good set-up of the measurement chain

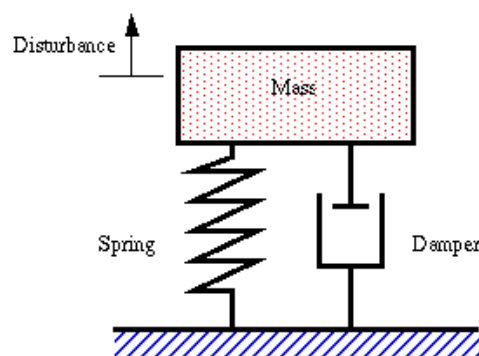
### 5.1 Measurement chain

The aim of the following description is to provide a general insight of the instrumentation used for HVI measurement. As stated before, high intensity and frequency characterize the HVI acceleration signal. The ranges of these two parameters depends heavily on the projectile energy, impacted structure and distance of the sensor from the impact point (also, joints have a fundamental role in attenuating the signal).

The measurement chain is composed by the following elements: accelerometers, amplifiers, anti-aliasing filters, ADC (analog-digital-converters), and data recorders/storage. Every component must be carefully set-up, in accordance with the expected/know environment. Now it follows a brief description of each element of the measurement chain and of its problematic.

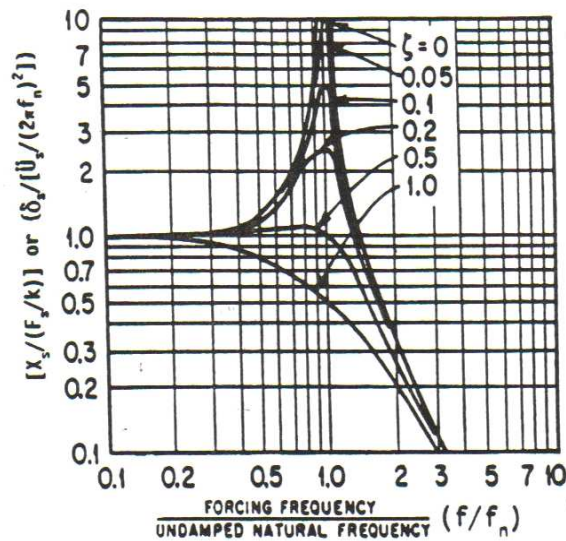
#### 5.1.1 Acceleration sensors

We can idealize the accelerometer as simple mass-spring-damper SDF (Single Degree of Freedom) system. The sensing element converts the acceleration at its base in electrical signal; it is the core of the sensor. Fig. 5-1 shows the simple SDF model.



**Fig. 5-1 Idealization of an accelerometer as mass-spring-damper SDF system.**

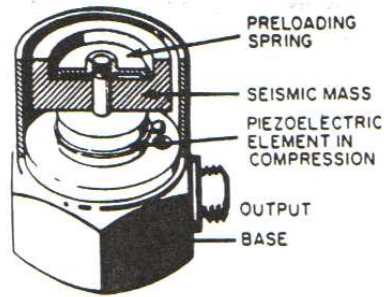
The typical accelerometer transfer function is shown in Fig. 5-2.



**Fig. 5-2 Accelerometer transfer function for different damping values ( $\xi$ ). The working range should be under 20% of resonant frequency.**

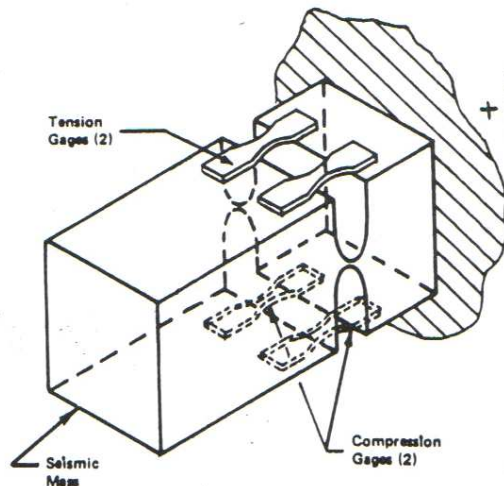
The sensing element differentiates the accelerometer type. HVI measurements are made with piezoresistive and piezoelectric sensors. This, thanks to their high resonant frequency, has a simple mounting and small size and weight. State of art commercial sensors have sensing elements with resonance over one MHz and can sustain acceleration levels up to 200.000 g. The main characteristics of the two types are the following [2]:

- **Piezoelectric** sensors use a PE (piezoelectric) crystal as spring between the base and mass, to sense the dynamic acceleration applied to it. When a force is applied to the crystal, a proportional electrical charge is generated. The amplifier converts it in a voltage value. The main advantage of this sensor is its high frequency resonance (due to the lightweight of the crystal), while the main fault is the small damping factor ( $\xi < 0.005$ ). In addition, the inherent sensibility of the charge signal to noise, force to use short and shielded cables. Fig. 5-3 shows a PE accelerometer. Some PE sensors use an integrated charge-voltage converter (ICP sensor), this solve the cable-shielding problem, but limits the sensitivity and the lightweight too.



**Fig. 5-3 Typical single-ended compression PE accelerometer**

- Piezoresistive** sensors or PR (semiconductor strain gage) accelerometers use strain sensitive materials (SS). A SS material changes its electrical resistance in proportion to the instantaneous spatial-average strain applied over the surface area of the material. Fig. 5-4 shows a sensor with four active gages for all the four arms of the Wheatstone bridge, this quadruples the transducer sensitivity and provides temperature compensation as long as the four gages are exposed to the same temperature. The PR sensor is not capable of high sensitivity but is smaller and lighter than the PE one (provide a higher resonant frequency). Due to this, it is used for high frequency and high acceleration measurements.



**Fig. 5-4 PR accelerometer using four semiconductor strain gages**



### 5.1.1.1 List of the accelerometers used for experiments

Accelerometer	Range [ms <sup>-2</sup> ]	Bandwidth ± 1 dB [KHz]	Resonant frequency [KHz]
Endevco 7270 – 200k	1e3 – 2e6	200	1200
Bruel & Kjaer 4374	1e-5 – 2e5	26	85
PCB 352B01	500 – 5e4	10 (±5%) 20 (±10%)	65

**Tab. 5-1 List of the accelerometer used for the experiments.**

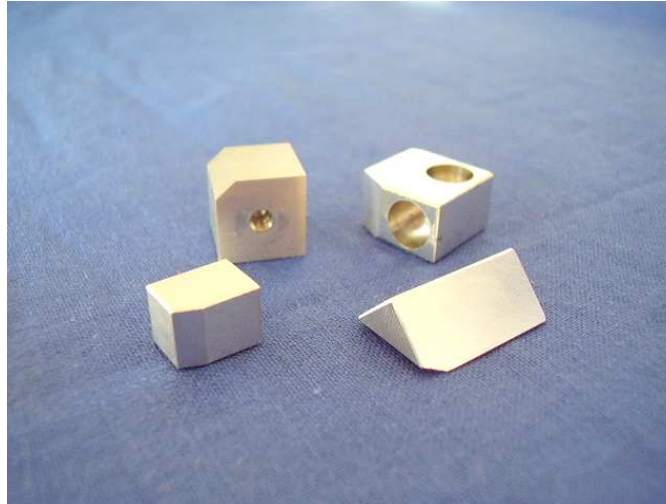
### 5.1.1.2 Accelerometer resonance

We must use much care with PR and PE accelerometers. The sensing element low damping ratio brings high resonance values; to restrict the accelerometer output to no more than 5% of the sensitivity (see Fig. 5-2), the maximum frequency value should be 20% of the resonant frequency of the sensing element. If the sensor is excited to its resonance, the sensor output could be very high, but still linear. Adequate filtering can easily correct this problem, but the output of the accelerometer may be too high for the signal conditioner (which comes before filters). If the output is too high, it may bring to amplifier overload; this brings to internal capacitors discharge, giving invalid data. The same problem may occur if the input frequencies are outside the bandwidth of the signal conditioner (saturation): in this case, the high frequency components of the signals are shifted as low frequency slope, like aliasing.

### 5.1.1.3 Accelerometer mounting

Accelerometers are seldom fixed directly to the test target. In fact, this can be difficult to achieve (i.e. if there is no space for the sensor, or if the target surface is too small for sensor base), moreover the target defromation can warp the accelerometer base, causing noise and spurious, non-physical outputs (in this case, the sensing element defromation does not depend on the base acceleration).

While is always desirable attach the sensor directly to the structure, for this reason mounting block are usually used (see Fig. 5-5).

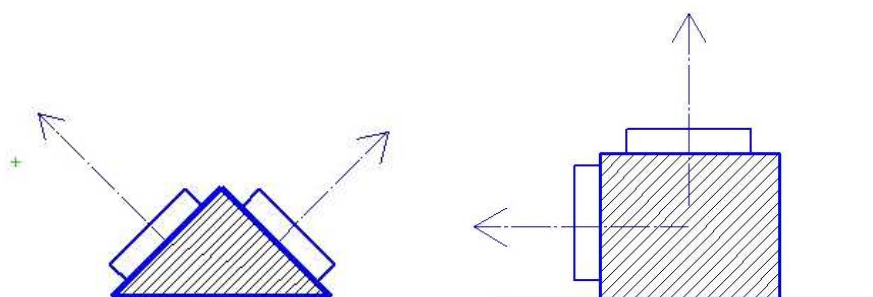


**Fig. 5-5 Different types of accelerometer aluminium mounting blocks.**

Moreover, in all tests, three types of waves (or vibration direction) are considered:

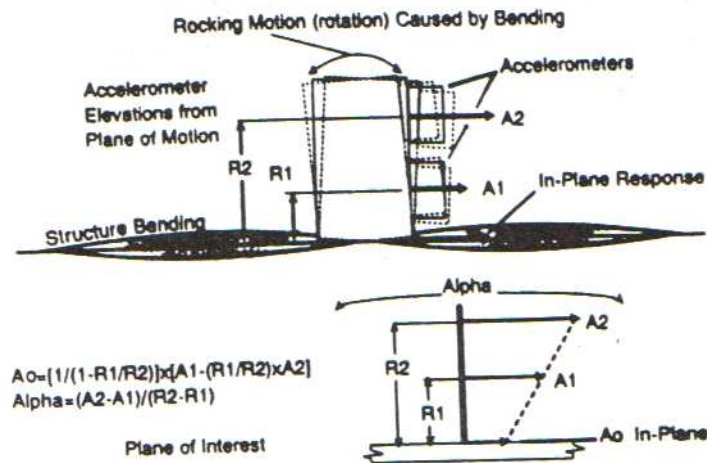
- In plane: the vibration (displacement, velocity and acceleration) of the material particles is mainly in the direction of the wave propagation, from impact point. These waves are called longitudinal or compressive
- Out plane: the vibration (displacement, velocity and acceleration) of the material particles is mainly perpendicular to the direction of wave propagation; the direction of motion is also perpendicular to the surface. These waves are also called flexural
- In plane shear: the shear term refers to the direction of the particles motion, orthogonal respect to the wave propagation direction, but parallel to the material surface.

Two type of mounting block have been applied, a  $90^\circ$  configuration on which the accelerometer axis are aligned with in-plane or out plane direction and a  $45^\circ$  on which accelerometers axis are  $45^\circ$  respect to target in-plane or out-plane directions (Fig. 5-6).



**Fig. 5-6 Two types of accelerometers mounting blocks,  $45^\circ$  triangular prism and  $90^\circ$  prism.**

The  $45^\circ$  configuration minimizes the influence of rotational motion on in-plane measurements (Fig. 5-7), however, to be effective, the sensitivity and phase of the two accelerometers channels must be very accurately matched.



**Fig. 5-7 Effect of rotational inertia on sensor mounted on different types of blocks.**

We used a Hopkinson Bar to calibrate sensors mounted on each type of Al block, to assess their transfer function. In this test, we compare a mounted accelerometer (for both 45° and 90° solutions) to an accelerometer of the same type, but directly attached to the Hopkinson Bar.

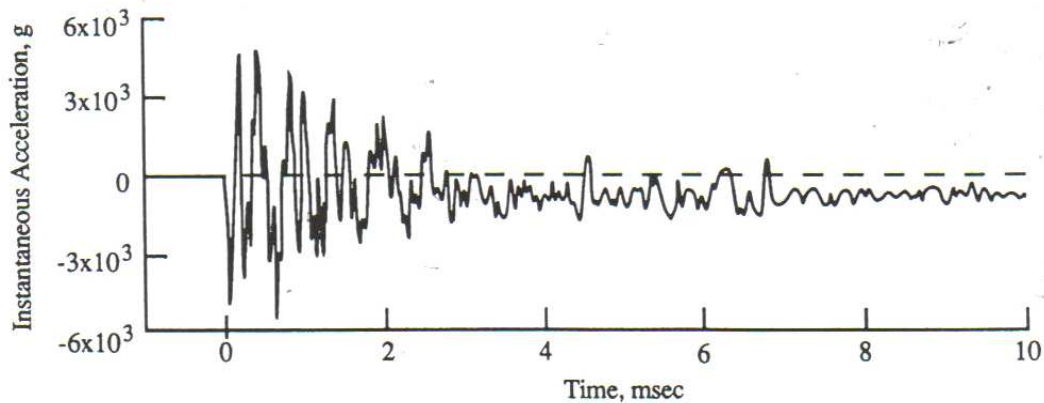
**The result is that the transfer function, for frequencies up to 50 kHz, is equal to one** (i.e. the mounting does not interfere, in any way, with the measure, for frequencies up to 50 kHz).

### 5.1.2 Signal conditioner

Signal conditioners are the power supply and amplifiers for PR and PE-ICP accelerometers; in the case of PE sensors, in their first stadium they also convert the charge signal in a voltage signal. Sometimes conditioners have built-in low-pass filters.

As previously stated, care must be taken when using signal conditioners: If the input signal has **high acceleration components with frequency outside the conditioner bandwidth**, the system could be overloaded and the measure may be altered (i.e. this is the case of an accelerometer that hits its resonance). We can proceed in two ways:

- If the input do not overcome the instrument range, unexpected signal clipping (due to too high gain set on the amplifier), may still occur. If the vibration environment is not well known, the amplifier gain should be kept low.
- If the input is outside the instrument range, the conditioners internal capacitors may discharge. In this case, the only solution is to apply a mechanical filter to the sensor. The result of the saturation is a low-frequency asymmetric term added to the sampled time history, as shown in Fig. 5-8.



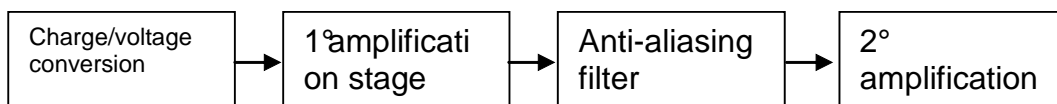
**Fig. 5-8 Effect on a sampled signal of the amplifier saturation**

### 5.1.3 Anti-aliasing filters

We must use anti-aliasing filters to avoid aliasing due to not proper sampling rate. In fact, aliasing appears when we sample a signal with a frequency content that is higher than 5/10 of the sampling frequency of the ADC. Aliasing converts high frequency portion of the signal, above the 5/10 limit, in low frequency content. Aliasing makes the signal useless; to avoid this problem we have used two types of filter, with cut-off frequencies of 20 kHz and 200 kHz, depending on the type of sampling module. Filter characteristics are as follow:

- Input signal attenuation of 3 dB a 10 kHz, 2% at 40 kHz and 0.5% at 80 kHz
- Filter order = 5 (no overshoot with a square wave as input)

These filters have been used only for PR and PE-ICP sensors. PE sensors have an integrated band-pass filter in their signal conditioner, as shown in Fig. 5-9.



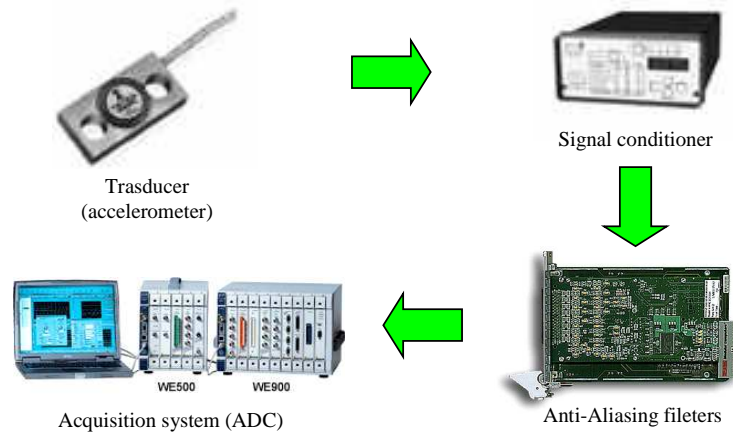
**Fig. 5-9 Scheme of the signal conditioner used for PE accelerometers. The low-pass, anti-aliasing filter is integrated.**

### 5.1.4 Sampling modules

The last element of the measurement chain is the sampling module. Its role is to turn the analog signal in a digital one. Digital signals are easy to analyse with common PC systems. The ADC (Analog to Digital Converter) is characterized by its sampling frequency and by its word size (bit). The ADC sampling frequency must be adequate to the input signal high frequency content. Moreover, the word size is crucial for the correct acquisition of the entire signal dynamic range. Two systems have been used for all the experiments: one with 32 channels with maximum sampling frequency of 100 kHz and one with 8 channels with 1 MHz maximum sampling frequency; both have output range of 12 bit.

### 5.1.5 System set-up and measurement chain

Fig. 5-10 shows the typical measurement chain. The output of the accelerometer (charge or voltage) enters the signal conditioner. Here, it can be converted in voltage or simply amplified and then enters the filter module. The last stage is the ADC and sampling.



**Fig. 5-10 Elements of the measurement chain.**

Each element must be set accordingly to the measure dynamic range. To achieve a good set-up of the measurement chain we should know the acceleration range that we are going to measure. For this reason, the first experiments have this objective. Here there are few steps for a correct set-up:

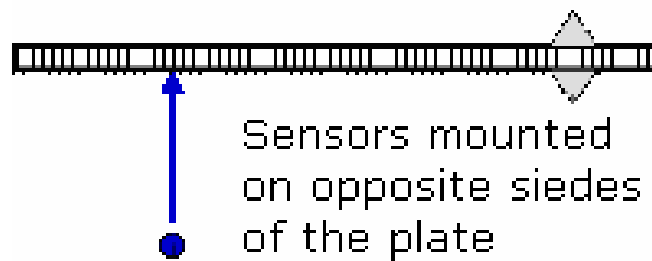
- We should place accelerometers accordingly to their dynamic range and to the expected intensity of the vibration filed. If the environment level is too high, sensors ringing or failure may occur.
- We must not overload the signal conditioner. If the signal has too high frequency, we should use a conditioner with a broader cut-off frequency or adopt a mechanical filter for the accelerometers (i.e. the adhesive tape used for the experiments). The amplifier gain must be set correctly.
- Filters must be set to avoid aliasing problems on the sampled signal.
- Initially, the intensities of inputs are not known, so it is necessary to perform a pre-experimental campaign to assess the acceleration levels, for all the different test parameters. After completing these tests, the amplifiers can be set accordingly to the expected environment, thus avoiding saturation or overloads of the measuring chain.

Moreover, care must be taken for the cable length and position. Charge sensors (PE) are very sensible to EM noise and to other disturbances, like cables twisting and displacement during the measure.

## 5.2 Analysis tools

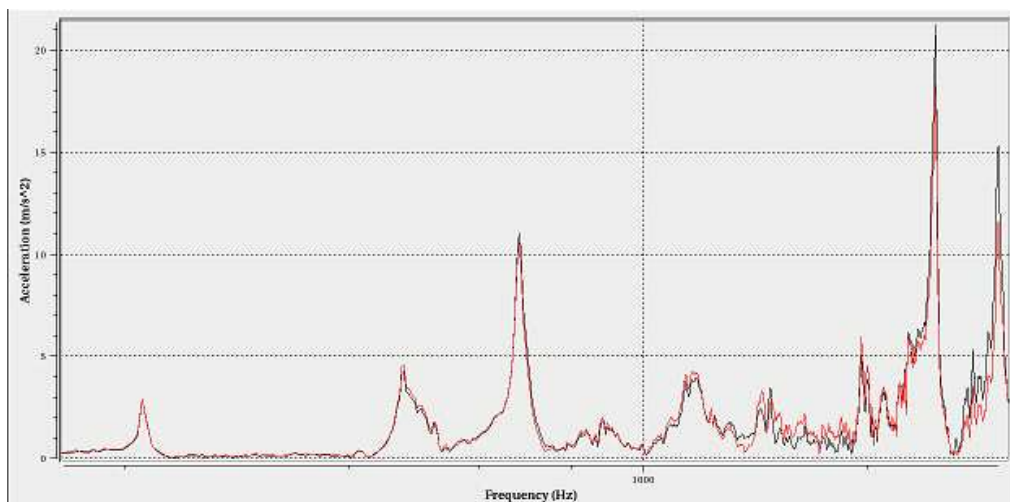
Scope of this section is to provide a general insight on the most used data analysis tools. The role of analysis tools is to extrapolate information that are not noticeable simply looking at the signal time history

**FFT** is the common way of analysing a signal: it shows the dominant frequencies of an acceleration time history, that can be related to waves propagation or to modal resonances of the impacted structure. This tool is also very useful for quality assessment; a visual inspection of the FFT of HVI signals is advised, because the signal spectrum could hold frequency component unexpected, generated by errors or noise in the measurement chain. In many experiments, the common procedure to verify the signal consistence (see chapter 0) is to compare the FFT of sensors mounted at the same distance from the impact point, but on opposite faces (Fig. 5-11). Obviously, the two spectrums should be very similar.



**Fig. 5-11 A common check of signal quality is to compute the FFT of two sensors attached at the same position, but on the opposite faces of the plate.**

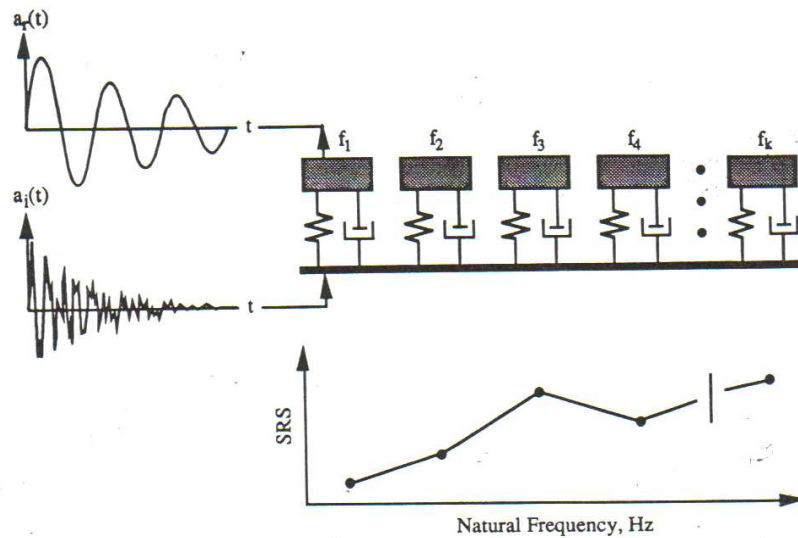
This easy procedure permits to assess possible problems in the measurement chain. Fig. 5-12 shows the FFT comparison of two HVI signals recorded by opposite OP sensors.



**Fig. 5-12 FFT comparison of two signal recorded from accelerometer mounted on target opposite faces.**

**SRS** is the most used tool to describe pyroshock environment and test specification criteria. It asses the threat level of a shock (HVI or Pyro), computing the peak acceleration of the mass of a SDF mass-spring-damper system, subjected to the shock acceleration history at his base. It results in a spectrum with natural frequency

on x-axis (i.e. the resonant frequency of the SDF) and the corresponding acceleration peak on y-axis (Fig. 5-13).



**Fig. 5-13 Mechanical analog for Shock Response Spectrum calculation.**

The parameters of the SDF systems are the damping value  $z$  and the resonant frequency  $f_n$ . In [2] it is advised to compute SRS for natural frequencies  $f_n$  that correspond to 1/6 octave band centre frequencies over the frequency range of interest, while the constant quality factor is selected as  $Q=10$ , corresponding to a critical damping of  $z = 0.05$ . In addition, there are several different categories of SRS magnitude other than max positive peak: negative, primary, residual and maximax SRS. The latter SRS envelops the previous four and is the one most commonly used for pyros testing.

The theory behind the SRS analysis is as follows. We want to assess the response to the transient (shock) of a SDF component mounted on the target surface. We know its natural frequency  $f_n$  and damping value  $z$ , so this hardware will be subjected to the corresponding acceleration value reported on the SRS (for its natural frequency). In many cases, it is not even necessary to know the exact natural frequency, since the SRS is computed for all the frequency range of interest.

Most frequently, the hardware has multiple resonant frequencies; in this case, we can extrapolate the maximum system response from the responses of the corresponding SDF systems (see [3]). The specifications for structural design can be provided in terms of maximum SRS levels.

Another use of SRS is also as descriptor (for tests) of the source of HVI shock environment. Unlike the FFT, the SRS spectrum does not have a unique relationship with its source signal (because it misses the phase relationship), so it is possible for different transients to have the same SRS.

We can use the SRS computed from experiments data as descriptor for laboratory generated force shock pulses (i.e. try to generate simpler force histories with the same SRS generated by the pyro/HVI). This can be useful also for numerical simulations: it is difficult for standard codes, like FEM, to reproduce the physics of an HVI. A clever approach to the problem is to generate an equivalent force pulse, with

the same SRS of the real shock signal, and use it as forcing impulse in numerical analysis.

**Wavelet Transform** (WT) is a particular method of signal analysis, very similar to FFT under many facets.

The classical Fourier theory shows that a signal can be described as a sum of sine and cosine functions at different frequencies; in this way we obtain information about the frequency content of a signal but we do not know the time at which each frequency component appears in the signal.

To study wave propagation, we need a tool that gives both these information, since the phenomenon is strictly bound to the relation between time and frequency: this is exactly what WT do.

**Velocity and Displacement** signals are sometimes computed from acceleration. This is mainly a quality assessment tool; for example, if the velocity or displacement of an acceleration signal presents a mean different from zero, without a net variation of the target velocity or displacement, probably there is a fault in the signal acquisition, and the data should be rejected.

### 5.2.1 Signal quality assessment

Data validation is a fundamental step in transient-shock analysis, especially on case of signal with wide frequency content. Quality assessment procedures are necessary to ensure data have been reliably acquired. Following are presented some possible problems related to signal acquisition and their identification methods; this is only a brief description, not intended as an exhaustive guide on signal quality assessment (for further explanation see [1], [2] and [3]).

In the field of the HVI signal quality assessment, there is not a standard; rather there are many practical rules that should be observed, especially for SRS. All the following considerations derive from the pyros test, but they can be considered like a standard for HVI. Many data analysis tools are also used as quality tests for signals, so many quality procedures can be performed while analysing the signal to extrapolate "hidden" information.

There are several issues on shock data validation:

- Signal clipping
- Excessive instrumentation noise
- Intermittent noise
- Power line pick-up
- Spurious trend

**Signal Clipping** is the failure to provide an adequate upper limit for the dynamic range due to sensitivity (gain) setting too high. Clipping appears normally as signal peak saturation that could be easily detected by visual inspection, however if the signal is analogically filtered it may be not the case. The signal is usually checked to do not overcome 95% of the maximum instrumentation voltage.

A hard to detect clipping case happens when high frequency components enter the signal conditioner (if frequencies are higher than the amplifier band pass, see also 5.1.1.2). In this case, the signal manifests as a zero-shift (signal mean  $\neq 0$ ) followed by a slow recovery that appear as a time varying trend in the mean value of the



signal. The signal appears to be not symmetric. SRS validation and velocity validation detects time-signal unsymmetrical shape.

**Excessive instrumentation noise** is the other extreme of an improper upper limit for the dynamic range of acquisition system. It happens when the data acquisition system has too low sensitivity setting (gain) or in case the selected instrumentation (i.e. accelerometers) has a range too big respect to the signal level. The result is a signal that is too small relative to the instrumentation noise with inadequate signal-to-noise ratio. The procedure used to validate this is SRS signal to noise ratio (further explanation at the end of the paragraph, under the section of SRS checks).

**Intermittent noise** is a problem that sometimes arises during data acquisition. It is the presence of intermittent "noise spike" in a measured time history. Spikes can be detected through: (i) velocity validation procedure, (ii) visual checking of signals provided from accelerometers on different locations looking for simultaneous events. Spike has been considered affecting validity of signals, leading to data rejection, if velocity validation is not passed.

**Power pick up:** the contamination of a measured signal by power line pick-up (at 50 Hz) commonly occurs if the data acquisition system is not properly shielded and grounded. Power line pick up can be detected by visual inspection and spectral analysis (FFT). If present, the signal is notched filtered at 50 Hz.

**Spurious trend** appears in measured time history of signals; we refer to a relatively slow variation of the mean value as a function of time, often with a period that is longer than the measurement duration. It may occur due to severe saturation of the signal conditioner or the sensing element in a piezoelectric transducer, and generally renders data worthless. Spurious trend can arise also in the integration of an accelerometer output (to calculate velocity and displacement) due to noise and zero offset in the measurement system. Spurious trend are easy to identify by signal visual inspection. Acceleration time histories are always checked to identify zero-shifts prior, during and after the shock event. If a significant, residual zero-shift, is detected after the end of the signal, this must be considered not valid.

**SRS check** is common tool for HVI/pyros signal quality assessment, because it is a quantitative method to verify the consistency of a signal. The test sets checks that every acceleration signal should pass; it is performed both for the transient part of the signal and for its noise, before and after the transient. It follows the schedule of SRS checks; they are the same used for pyros:

- Experience indicates that valid HVI measurements generally produce similar positive and negative SRS values at all natural frequencies. For this reason, the signal should be considered invalid if the difference between  $SRS^+$  and  $SRS^-$  is greater than 6 dB
- The SRS results should be considered invalid at those frequencies where the difference between the SRS computed from the noise before and after the transient and the signal SRS, is greater than 6 dB
- The signal is invalid if the slope of the SRS at frequencies well below the first nominal mode of the structure is significantly less than 6 dB/Octave

### 5.3 Preparatory test on satellite structures

Accelerometers can measure disturbances up to a maximum value, that depends on the type of sensor used and on its distance from the impact point. For this reason, the position of each sensor should be chosen carefully. A series of experiments have been performed to study the **acceleration peak** for near, mid and far field disturbances. Signal intensity is characterized through the maximum (peak) acceleration levels, both for structural and porous body tests.

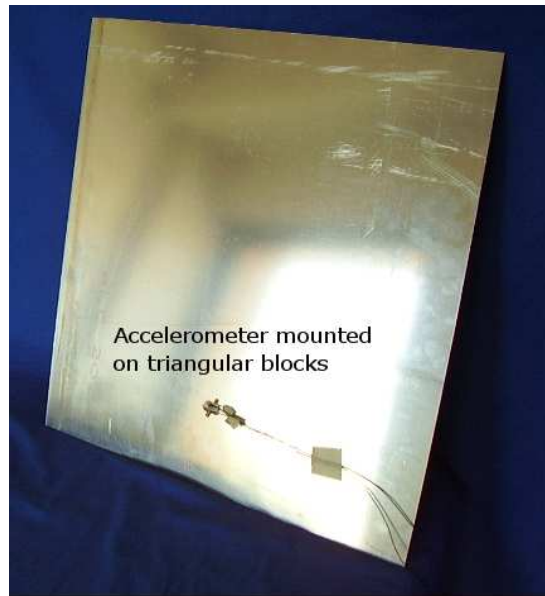
The LGG (Light-Gas-Gun) used for the tests is one of the bigger noise source, since its activation transmits vibrations through the structure to the test target. Noise levels have been assessed through a series of dedicated experiments. The noise levels and the complete uncertainty of the measured signals will be given in terms of SRS.



**Fig. 5-14 The LGG used for all HVI experiments.**

The preparatory tests can be summarised as:

- **Near field tests:** they have been performed, shooting projectile of various mass and velocity on simple targets (Al thin and HC plates, Fig. 5-15), to investigate the intensity of vibration environment produced by different HVI conditions near the impact location (near field). Thus, accelerometers have been tested, to assess their correct mounting technique and to set-up the measurement chain (as reported in paragraph 5.1).
- **Mid and far field tests:** some tests have been performed on real GOCE test experiment targets; in such way, we can also identify the acceleration levels on plates jointed to the impacted one (mid and far field behaviour).



**Fig. 5-15 Al simple thin plate target used for preparatory tests with mounted accelerometers.**

The topics covered in this chapter are:

- Uncertainty analysis for HVI signals
- Assessment of background noise source due to LGG operations
- Maximum vibration environment in simple targets (thin and HC, Al plates)
- Maximum vibration environment in complex target (GOCE test targets, CFRP and Al HC)
- Conclusions

### **5.3.1 Uncertainty analysis**

We need to evaluate uncertainty to correctly interpret and compare the measured acceleration signals. The concepts here presented will be used for the analysis of all acceleration signals in the following chapters.

More precisely, the uncertainty comes out from:

- A systematic term, which is related to the overall impact facility background noise: this represents an interfering input, which is added, in some way, to the vibration environment produced by the phenomenon under investigation (i.e. the HVI itself). To assess such noise contribution, dedicated preparatory tests (this chapter) and specific experiments on the most important target geometries, have been performed.
- A scattering term, which has been evaluated through a statistical analysis on nominally identical impact tests realised on each target configuration. The scattering is therefore expressed as a frequency-dependant standard deviation.
- A term related to the accuracy of the measurement chain, defined as the combination of single components uncertainty as indicated by the manufacturer. This term has been included into the overall facility background noise.

These components are combined according to ENV 13005 [4], considering that the HVI and the noise phenomena are correlated in an unknown way (which is the most conservative assumption):

$$U_{signal} = \sqrt{U_{noise}^2 + U_{scatter}^2} \quad \text{Eq. 5-1}$$

$$U_{noise} = \sqrt{\frac{SRS_{noise}^2}{3} + \frac{\sigma_{noise}^2}{n}} \quad \text{Eq. 5-2}$$

Where  $n$  is the number of experiments, performed to evaluate the background noise; the line-above indicates the average value.

$$U_{scatter} = \frac{\sigma_{scatter}}{SRS_{scatter}} \cdot SRS_{signal} \quad \text{Eq. 5-3}$$

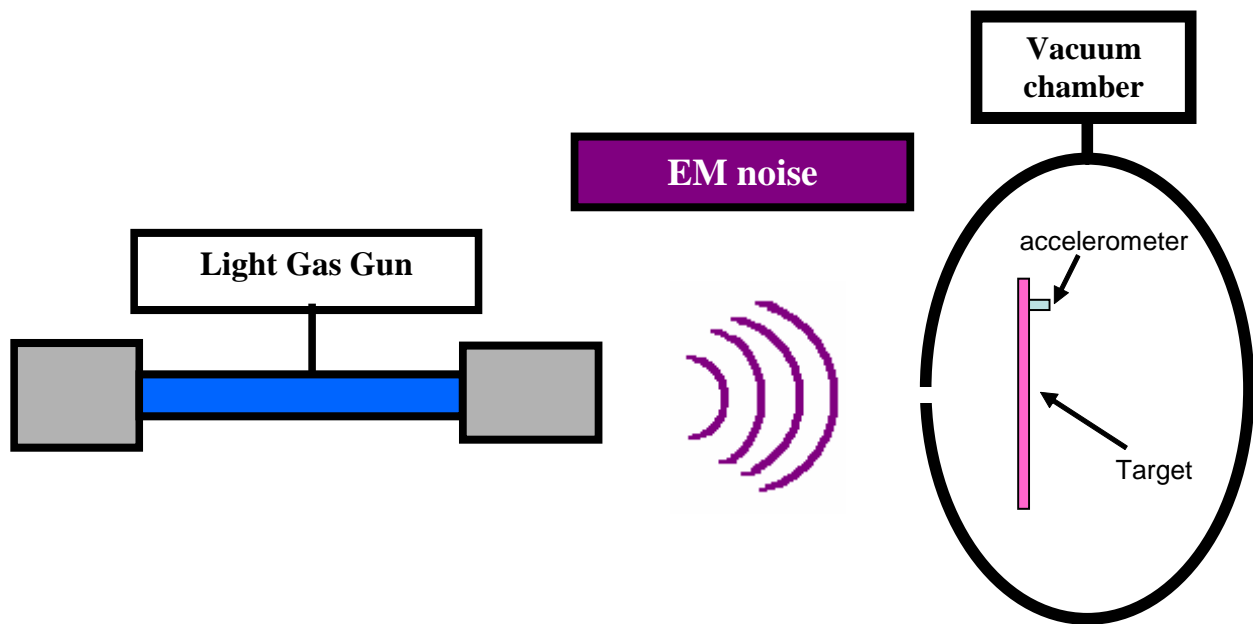
Previous relations are used to evaluate the uncertainty on calculated SRS, for each kind of target and for each kind of elementary disturbance wave (in plane longitudinal, in plane shear, out of plane).

### 5.3.2 Noise source due to LGG operations and HVI physic

Signals acquired from sensors located on targets are affected by interferences, which are not related to HVI: many effects associated to the LGG operations determine disturbances, which can propagate to the target thus affecting the measurements accuracy, especially far away from the impact point where signals are attenuated by distance and structural joints.

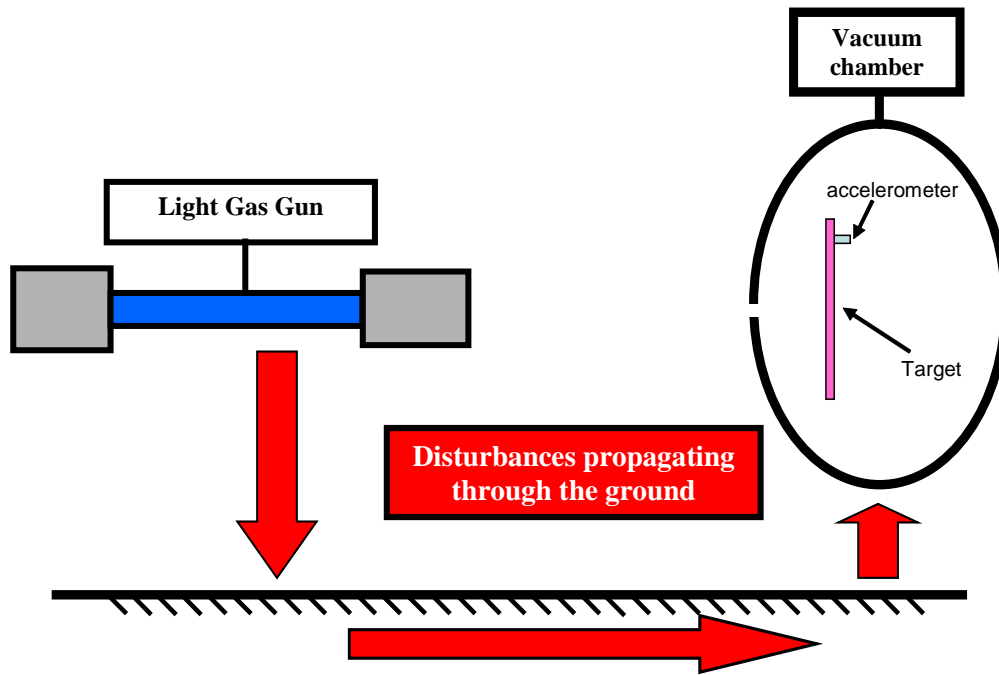
The LGG set-up is the same used during real impact tests, but operation sequences and conditions have been changed in order to isolate the contributions of the different components. LGG operations considered as noise sources are:

**EM noise:** some tests have been made operating the facility electrically/electronically, without propellant, Fig. 5-16.

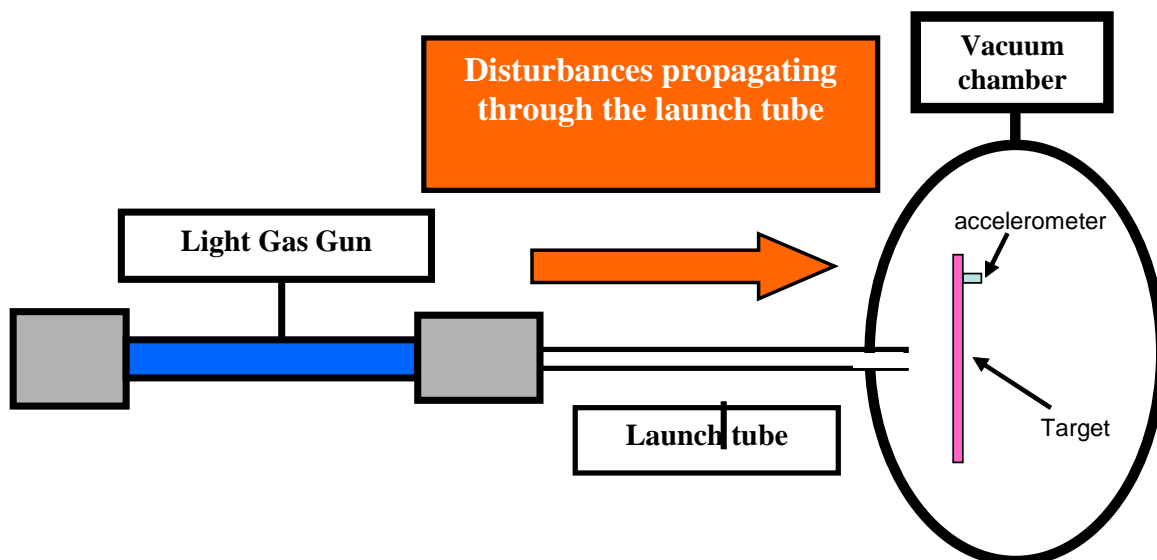


**Fig. 5-16 EM noise, generated by LGG electrical actuated components (like electro-valves) can interfere with accelerometers mounted inside the vacuum chamber.**

**Mechanical coupling noise:** first, the gun has been activated without launch tube, to assess disturbances propagating only through the ground. Then, the LGG has been activated with the launch tube mechanically sealed, in a way that no propellant has been injected into the impact chamber, Fig. 5-17. It was done to verify effect of vibrations propagating through the launch tube-flight chamber interface another test has been performed with the LGG launch tube connected to the vacuum chamber; the gas is still sealed in the LGG main structure, Fig. 5-18.

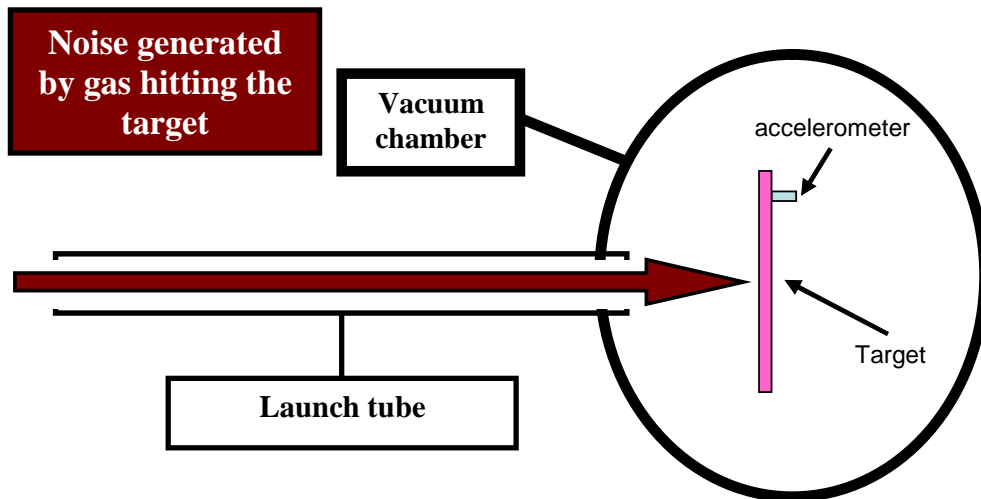


**Fig. 5-17 Mechanical disturbances can propagate from the LGG to the target mounted in the vacuum chamber, through the ground.**



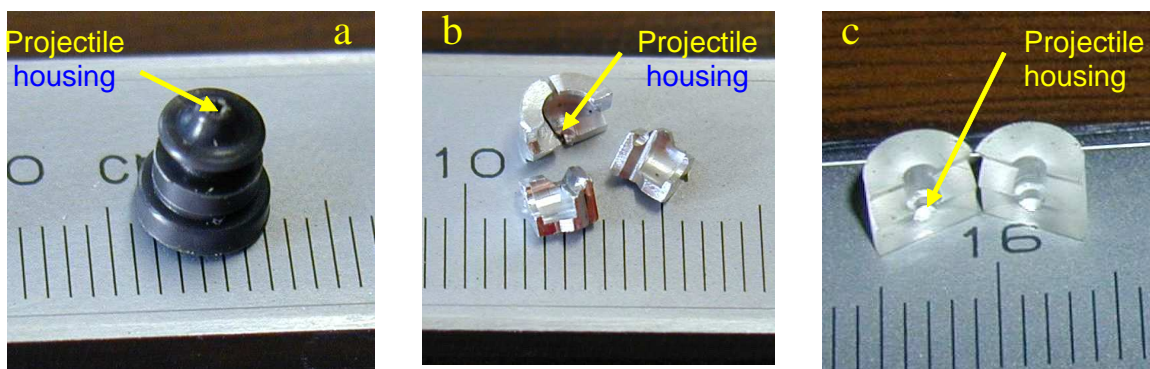
**Fig. 5-18 Mechanical disturbances can propagate from the LGG to the target mounted in the vacuum chamber, through the launch tube.**

**Acoustic noise** refers to the acceleration level induced when the gas, used to accelerate the projectile, hits the target. This disturbance includes the previous three sources, Fig. 5-19.



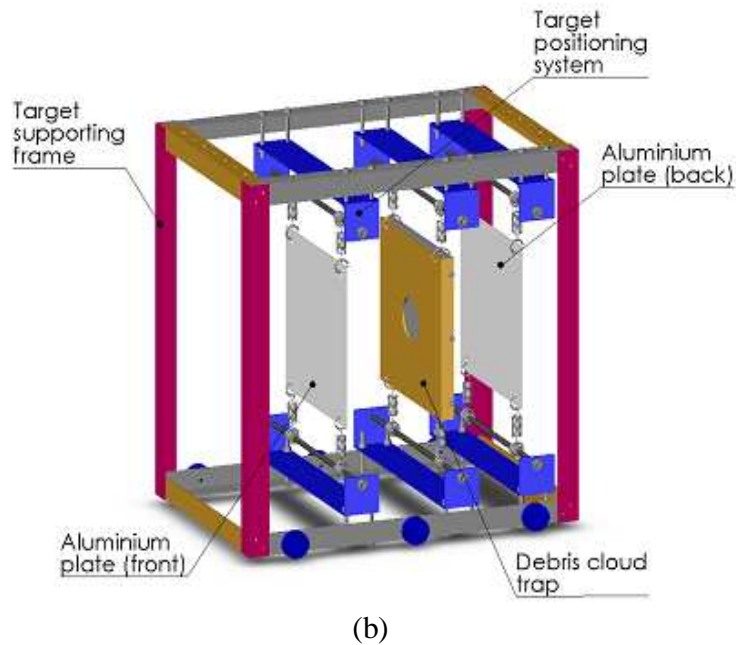
**Fig. 5-19** The gas used to accelerate the projectile generate a vibro-acoustic vibration field, the related recorded accelerations are acoustic noise.

**Sabot stopping noise:** Sabots used to fit the projectile in the launch tube. Before entering the vacuum chamber the sabot finger split and hit a sabot stopper, while the projectile pass through it. Sabot fingers (Fig. 5-20) carry a relevant amount of momentum since each of them has a weight even higher than that of the aluminium spheres used in the study (from 0.6 to 2.9 mm) and travels almost at the same speed. Therefore, a sabot hitting on the stopper plate produces a shock that can propagate through structures (impact chamber and target supports) to the target. This disturbance includes EM and mechanical coupling, but not acoustic noise.



**Fig. 5-20** Sabot are used to match the projectile diameter to the launch tube.

The **debris cloud** expansion may perturb the quasi-stationary acoustic environment inside the impact chamber (Argon) and the debris trap can transfer vibrations to the target, through its suspension arrangement (Fig. 5-21). Two types of test have been performed: without (only 5 mbar) inert gas in the vacuum chamber (acoustic noise de-coupled) and with an atmosphere of 80 mbar. The impacting projectiles (debris generators) are massive Al sphere (10 mg) and nylon cylinders (94 mg).



**Fig. 5-21 Experimental set-up for assessing the debris-cloud induced disturbance on complex targets. The target-supporting frame is placed inside the vacuum chamber.**

For each of these sources a test has been performed, assessing the acceleration levels induced on the test target.

The gun has been operated at working conditions during all tests, and the parameters of these tests were inside the experimental range for the following shots:

- Velocity of Al spherical projectiles up to 3 mm between 2 and 5 km/s
- Targets were 500x500 mm Aluminium 2024-81 plate (1 or 2 mm thick)
- Targets are mounted on a supporting frame, which reduces the transmission of spurious disturbances from surrounding structures, using elastic suspensions and soft damping materials

The instrumentation set-up is based on Endevco, B&K and PCB accelerometers (Tab. 5-1), mounted on the target plates diagonal 300 mm away from the nominal impact point (Fig. 5-15).

Tab. 5-2 shows upper-maximum acceleration limits for each source of disturbance. For each test, is has been de-coupled from the other sources, when possible (i.e. acoustic noise includes mechanical coupling influence).



Test type	In plane max acceleration [ $\text{ms}^{-2}$ ]	Out of plane max acceleration [ $\text{ms}^{-2}$ ]	comments
EM noise	<10	<10	Signal level under the measurement chain noise
Mechanical coupling	<10	<20	Disturbances comes mainly from coupling with lunch tube
Acoustic noise	<300	<300	Only gun gas propellant
Sabot stopping	<60	<60	Only sabot fingers
Debris cloud - 1	<50	<100	5 mbar inert gas
Debris cloud - 2	<300	<700	80 mbar inert gas

**Tab. 5-2 Maximum limits of acceleration levels, for each source of noise.**

**The acoustic disturbances coupled with debris cloud results to be the bigger source of noise ( $300 \text{ ms}^{-2}$  in plane and  $700 \text{ ms}^{-2}$  out of plane).** Moreover, it includes all the noise sources, whose effect is low, compared to acoustic disturbance. To limit the noise caused by gas hitting the target (acoustic noise), the internal configuration of the vacuum chamber has been modified, by covering its inside walls with soft absorbing material. Diaphragms with calibrated holes for the projectile passage have been also used to confine the expansion-induced acoustic field. After this modification, the intensity of the acoustic noise results sensibly reduced.

Obviously, debris-acoustic coupling depends on the dimension and energy of debris and on the geometry of the target. In this preparatory test, the target was a simple Al thin plate, but in complex ones, there are up to tree/four jointed HC Al-CFRP plates, so we expect different acoustic coupling with different targets configuration. In addition, the influence of debris depends heavily on the type of impact (perforating or not perforating). Moreover, the effect of debris is heavily over-estimated, because of the thin Al plate and the massive projectiles. For these reasons, the influence of this noise source has been defined without the effect of debris (they influence only out of plane accelerations), which is very variable and of the same order of magnitude of the sole acoustic noise.

Since the intensity of major noise source (gas-target acoustic coupling) depends on target type, at least two "noise assessment" tests have been made **for each target configuration**; an empty sabot (no projectile) is shoot with the target mounted in the vacuum chamber. The measured accelerations represent the systematic term of the measure uncertainty, as explained in paragraph 5.3.1.

### **5.3.3 Acceleration levels on simple targets (near field)**

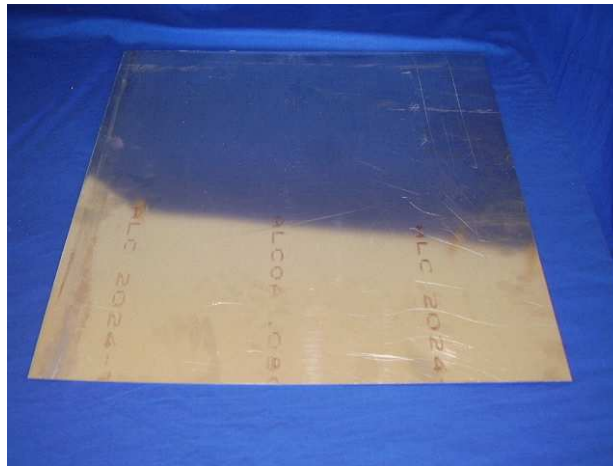
The outputs of the first series of tests are the acceleration intensities on simplified targets: Al thin plates and Al honeycombs. This has been done to define the

accelerometer type and position through the measure of the maximum acceleration peaks and to evaluate the influence of projectile mass and target thickness on maximum acceleration levels. For each target type, the test specifications are reported on the following tables.

### 5.3.3.1 Acceleration levels for simple thin Al plates

Simple targets have the following specifications:

- Targets are 500x500 mm Aluminium 2024-81 plate (1 or 2 mm thick), see Fig. 5-22.
- Targets are mounted on a supporting frame, which reduces the transmission of spurious disturbances from surrounding structures, using elastic suspensions and soft damping materials



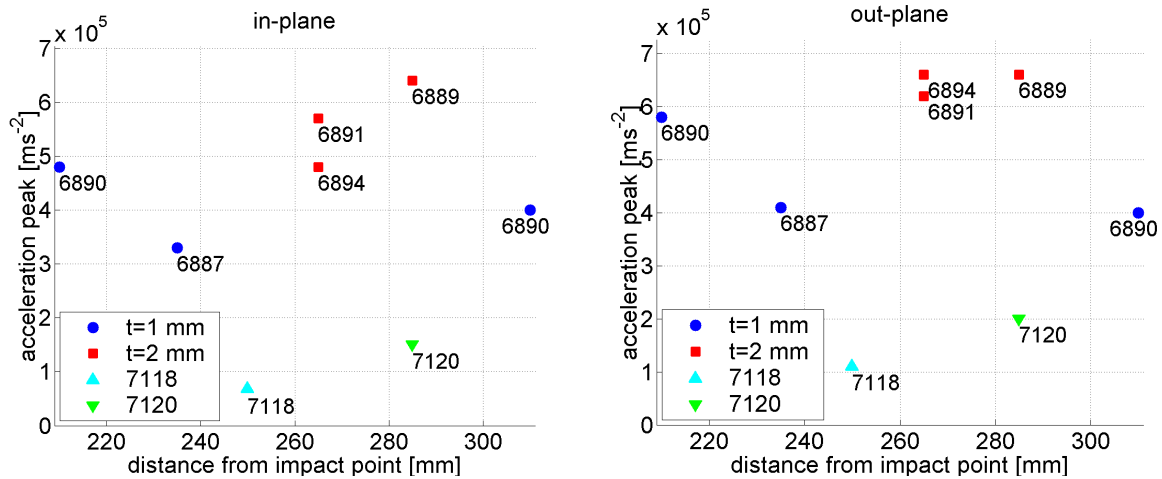
**Fig. 5-22 Al thin plate are 500x500 mm Aluminium 2024-81 plate.**

Test specifications and corresponding acceleration peaks are reported on Tab. 5-3 and Fig. 5-23 for Al thin plates.

CISAS ID	Target Type [mm]	dp [mm]	vp [km/s]	Coarse Damage	Comments
6887	Al 500x500x1	1.5	4.7	P	Sensors (Endevco) fixed on mountings by glue
6889	Al 500x500x2	1.5	4.7	P	Sensors (Endevco) fixed on mountings by glue
6890	Al 500x500x1	1.5	4.7	P	Sensors (Endevco) fixed on mountings by glue
6891	Al 500x500x2	1.5	4.6	P	Sensors (Endevco) fixed on mountings by glue
6894	Al 500x500x2	1.5	4.9	P	Sensors (Endevco) fixed on mountings by glue
7118	Al 500x500x2	1	5.1	P	Sensors (Endevco) fixed on mountings through 0.23 mm adhesive layer

7120	Al 500x500x2	1.5	5.0	P	Sensors (Endevco) fixed on mountings through 0.23 mm adhesive layer
------	--------------	-----	-----	---	---

**Tab. 5-3 Acceleration levels on simplified targets (Al thin plates).**

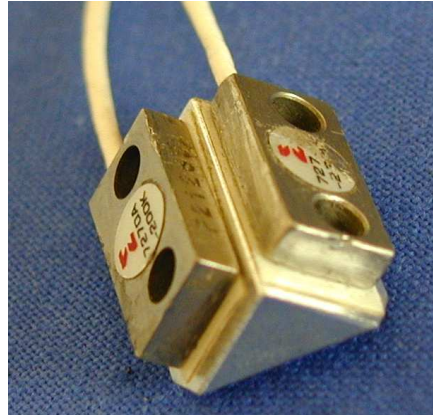


**Fig. 5-23 Acceleration peaks for test reported on Tab. 5-3.**

On t=2 mm thick targets (shots 6891, 6894 and 6889), in plane and out of plane waves rise up to  $6.4 \times 10^5 \text{ ms}^{-2}$  and  $6.6 \times 10^5 \text{ ms}^{-2}$ , respectively. This is still well below the acceptable range for near-field Endevco sensors. Possible effects of vibrations damping with the distance fall inside the scattering of data.

On t=1 mm thick targets (shots 6887 and 6890), in plane and out of plane waves rise up to  $4.8 \times 10^5 \text{ ms}^{-2}$  and  $5.8 \times 10^5 \text{ ms}^{-2}$ , respectively. These levels are reached at the minimum distance from the impact point (210 mm).

The frequencies present in both classes of test (t=1 and t=2 mm) exceeded the Endevco amplifier dynamic range. This leads to amplifier overload, as explained in paragraph 5.1.2. For this reason, tests 7120, 7118 explored a different mounting strategy for Endevco accelerometers: Loctite 454 Gel glue has been replaced by a calibrated (0.23 mm) adhesive layer (Fig. 5-24).



**Fig. 5-24 Endevco accelerometers attached on a triangular prism mounting using calibrated adhesive film**

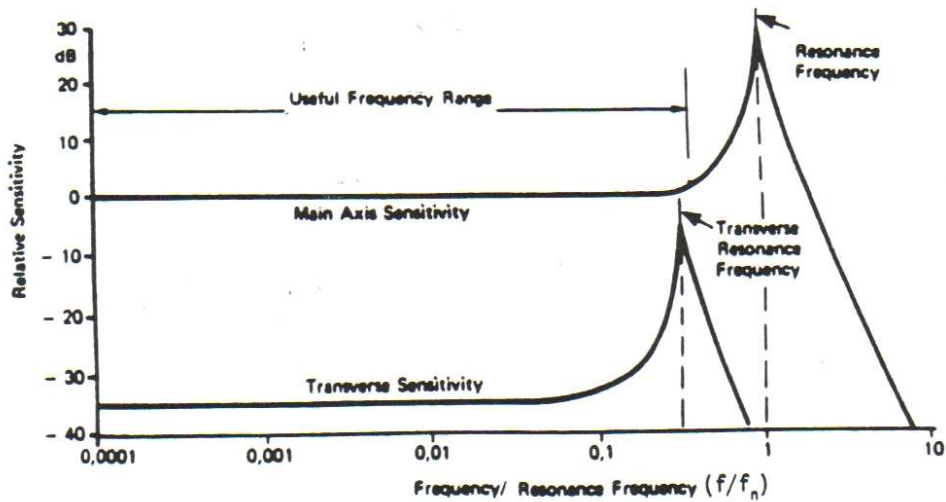
With this solution, **the acceleration peaks are sensibly lower**. This is because the adhesive layer acts as a mechanical low-pass filter, cutting-off those high-frequency acceleration components that bring to bad signal acquisition. In fact, with respect to calibrated adhesive films, the glue realizes a more rigid bond between mounting blocks and accelerometers, because of the extreme thinness of the obtainable glue layer. Therefore, glued-accelerometers can record signals with higher frequency content.

Several experiments a Hopkinson Bar have been realized to characterize and compare the high-frequency mechanical behavior of mounting assemblies with tape. No difference appeared between the two techniques (glue and tape) inside the experimental range of the available Hopkinson Bar (50 kHz).

Among the filtering behaviour of the two examined sticking solutions, the glue layer is not easily controllable in both thickness and homogeneity, leading to a scarcely repeatable mechanical behaviour for the assembly. Moreover, the glue is more difficult to remove and necessitates accurate cleaning procedures, with a consequent time penalty for the preparation of each experiment.

In summary, considering the aforementioned benefits of calibrated adhesive films and reminding that they allow for a cut-off frequency greater than 50 kHz (well above the 10 kHz limit for this study), their use was preferred for the following experiments.

This solution brings another big advantage: the adhesive layer has a low resistance to shear forces, and so behave like low-pass filter with very low cut-off frequency for transversal accelerations (see Fig. 5-25).

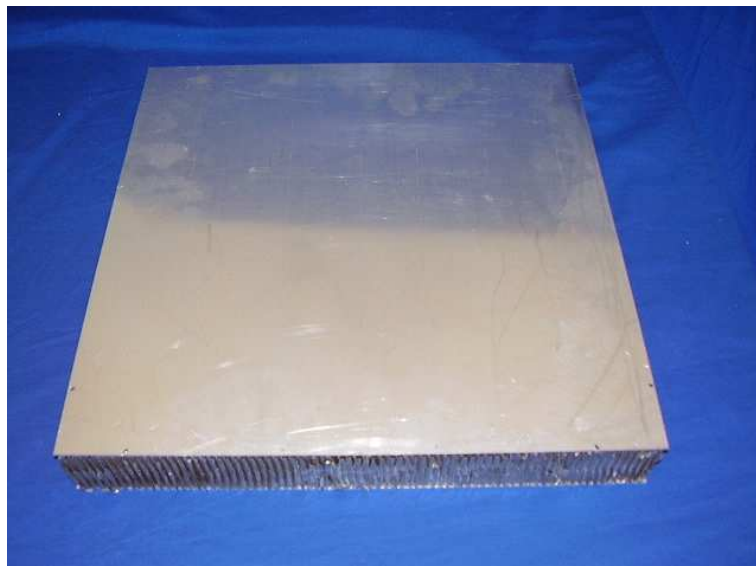


**Fig. 5-25 Transversal sensitivity and resonance of an accelerometer.**

### 5.3.3.2 Acceleration levels for simple Al HC plates

Simple HC targets have the following specifications:

- Targets are sandwich panels 400x400x52.8 mm with Al 2024-T81 face-sheets thick 1 mm and Al H/C core 3.1 3/16 5056 10P thick 50.8 mm (Fig. 5-26).
- Targets are mounted on a supporting frame, which reduces the transmission of spurious disturbances from surrounding structures, using elastic suspensions and soft damping materials



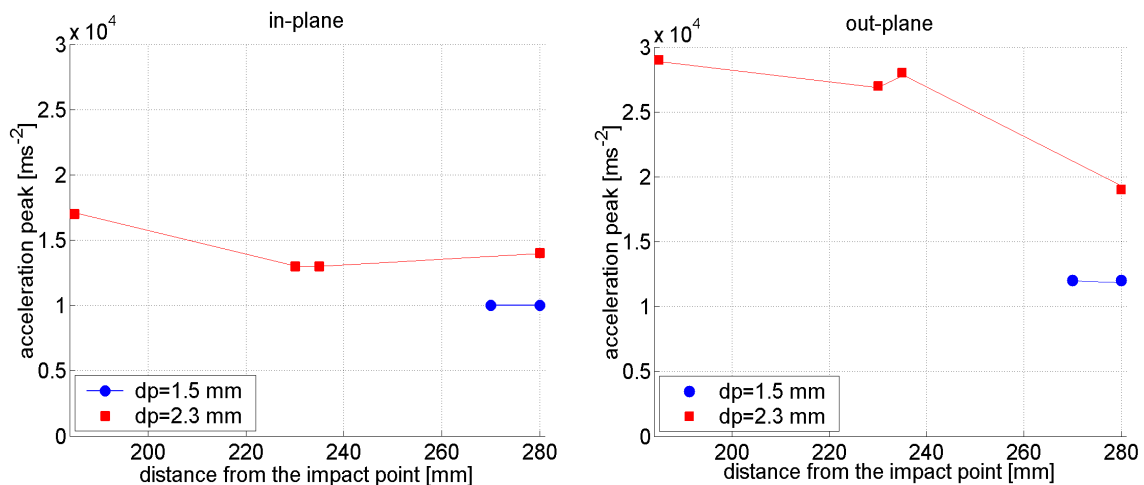
**Fig. 5-26 Al HC target 400x400x52.8 mm with Al 2024-T81 face-sheets thick 1 mm and Al H/C core 3.1 3/16 5056 10P thick 50.8 mm.**

Tab. 5-4 summarizes test specification and acceleration peaks for simple Al HC plates, and Fig. 5-27 shows the corresponding acceleration levels. To verify the influence of

the distance on acceleration levels, the sensors have been mounted at various distances from the impact point, to assess the influence of this parameter too.

CISAS ID	Target Type [mm]	dp [mm]	vp [km/s]	Coarse Damage	Comments
7303	Al HC SP 500x500x52.8	1.5	5.0	BL>=	Sensors (Endevco) fixed on mountings through 0.23 mm adhesive layer
7305	Al HC SP 500x500x52.8	1.5	5.1	BL<=	Sensors (Endevco) fixed on mountings through 0.23 mm adhesive layer
7315	Al HC SP 500x500x52.8	2.3	5.1	P	Sensors (Endevco) fixed on mountings through 0.23 mm adhesive layer
7316	Al HC SP 500x500x52.8	2.3	5.0	P	Sensors (Endevco) fixed on mountings through 0.23 mm adhesive layer

**Tab. 5-4 Acceleration levels on simplified targets (HC panels).**



**Fig. 5-27 Acceleration peaks for tests reported in Tab. 5-4, on the left side the in plane, on the right the out of plane.**

Acceleration levels on Al HC SP appear to be systematically lower than on simple Al plates, both on the impact face and on the rear face of the target.

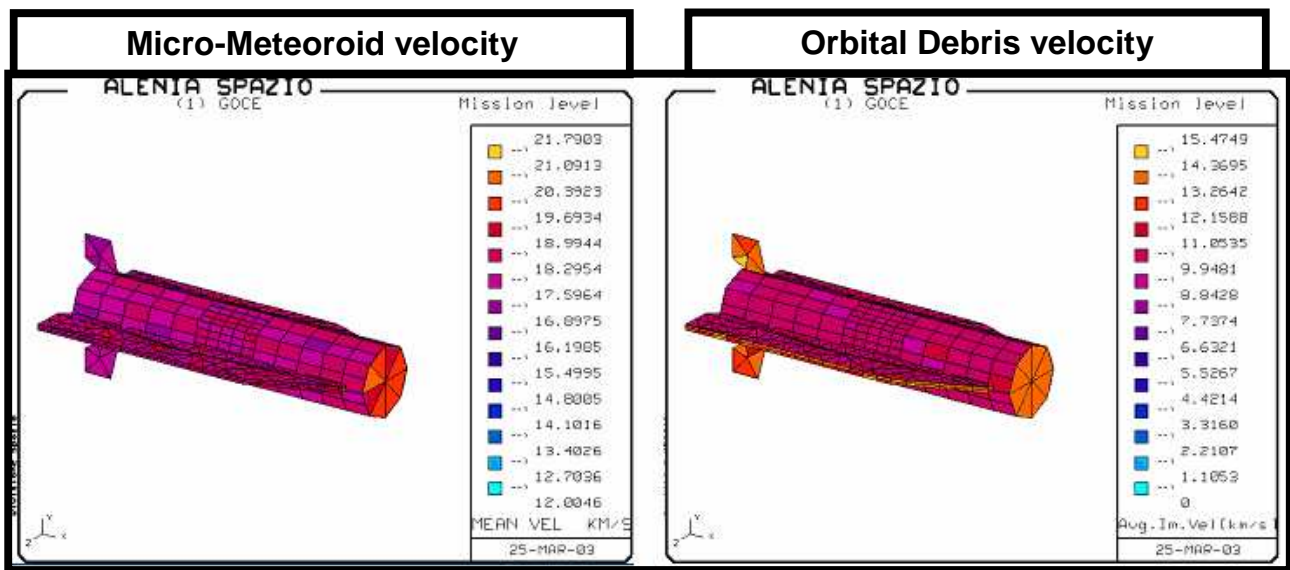
### 5.3.4 Acceleration levels in complex targets (mid and far field)

Tests for mid and far field vibration assessment have been performed on configurations that are representative of the GOCE structure (complex targets). For

this reason, a brief overview of the satellite structure is needed, to better understand the shape of these targets.

### 5.3.4.1 GOCE satellite

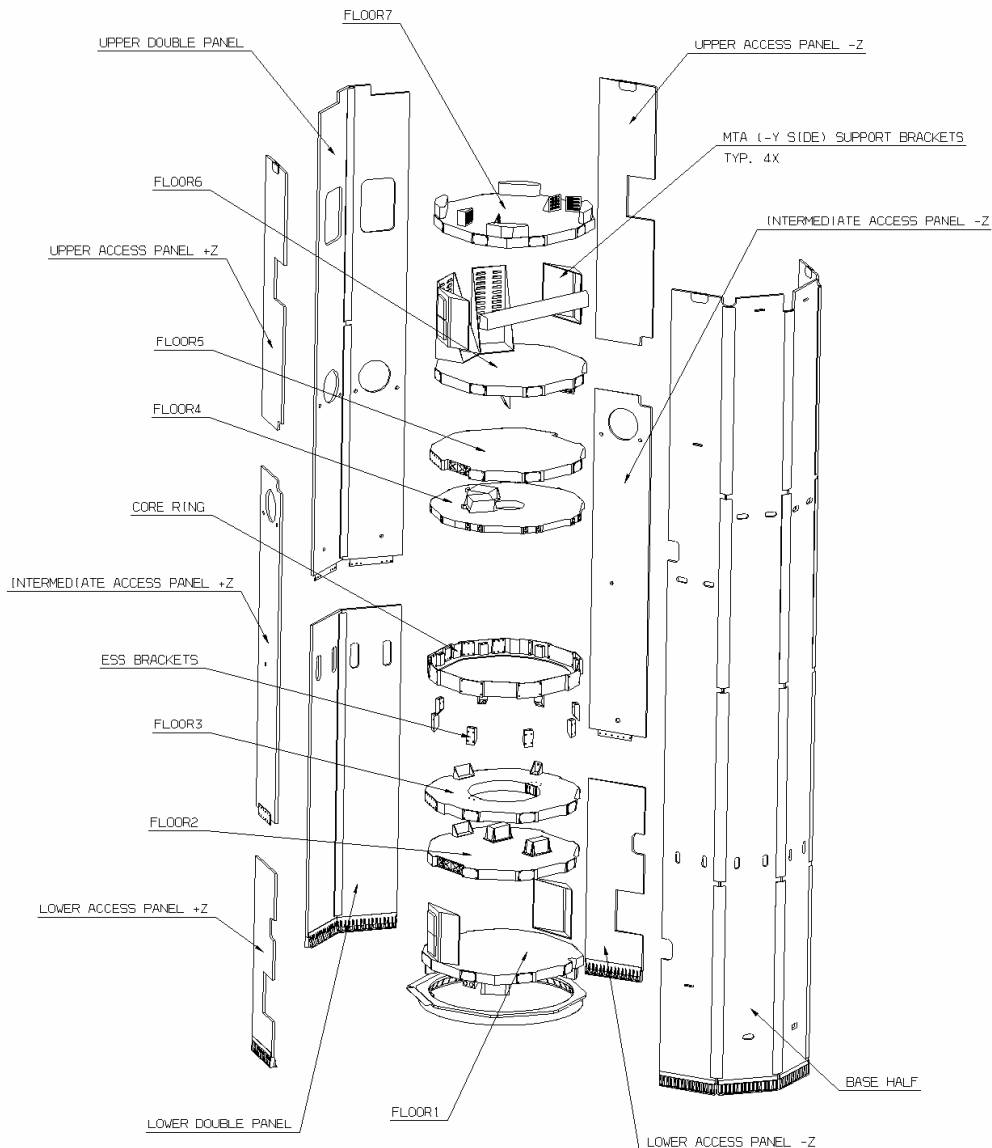
A deep study on the structural components of GOCE more subjected to impacts has been done. The output of this analysis gives the expected micro-meteoroids and space debris threat assessment. The frequency, dimension, velocity and impact angle of impacting bodies can be given as function of the position on GOCE structure, as shown for velocity in. Through this analysis, a deeper investigation of the vibration environment can be addressed to the components more subjected to HVI (see Fig. 5-28).



**Fig. 5-28 Velocity distribution of HVI on GOCE body, both for space debris and micro-meteoroids.**

GOCE satellite body is made of several Al HC floors, covered by jointed CFRP/Al HC panels, as shown in Fig. 5-29. The structure components are:

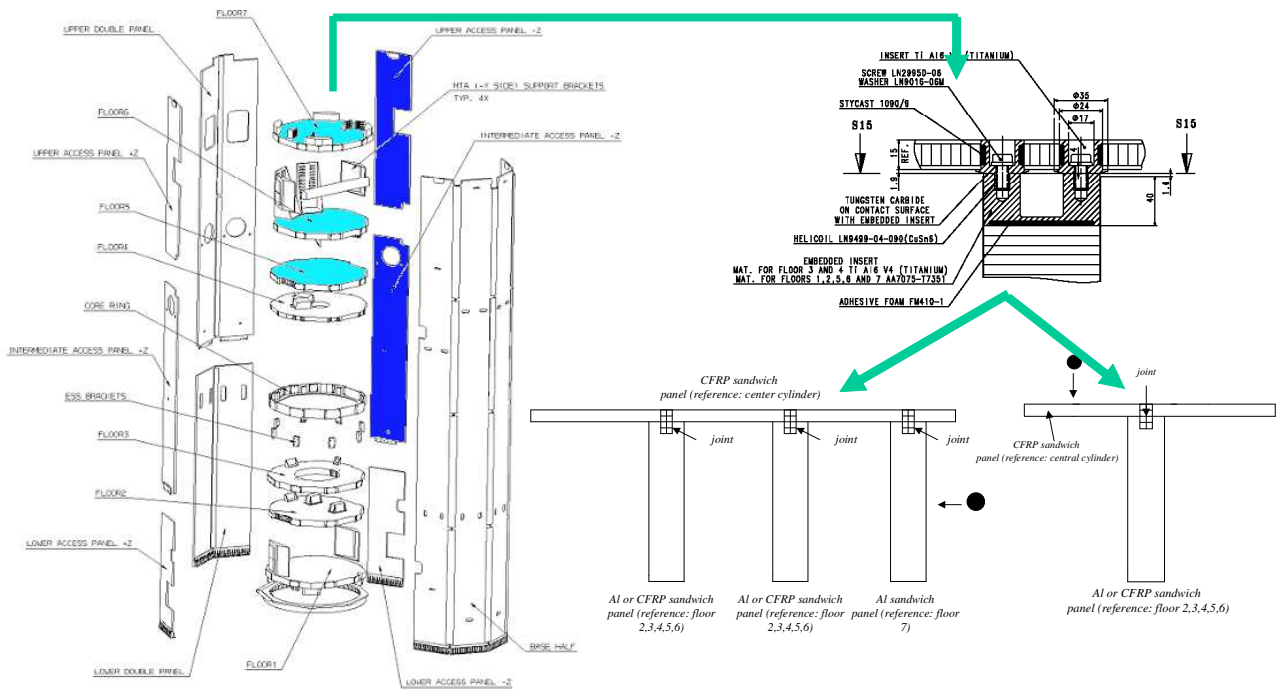
- Octagonal cylinder: CFRP face-sheets (2+2 mm), Al H/C (11 mm)
- Floors 1, 2, 5, 6, 7: Al face-sheets (1+1 mm), Al H/C (58.4 mm)
- Floors 3: CFRP face-sheets (0.75+0.75 mm), Al H/C (58.4 mm)
- Floors 4: CFRP face-sheets (0.75+0.75 mm), Al H/C (39.25 mm)
- Body-mounted solar array: CFRP face sheets (0.5+0.5 mm), Al H/C (29 mm)



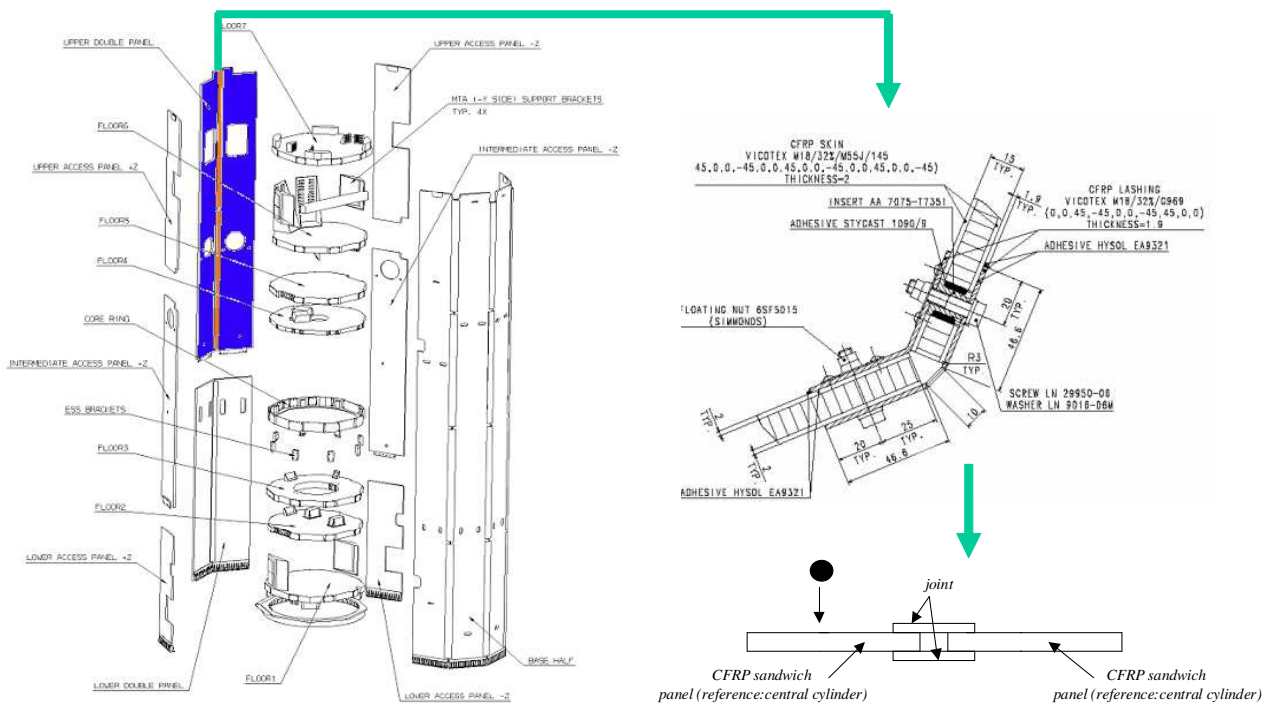
**Fig. 5-29 GOCE spacecraft exploded structure, there are several floors, covered by CFRP HC face-sheets.**

Complex target are representative of structural components of the GOCE body. Not every satellite components have been tested, but only those parts where HVI is more probable and frequent. As an example, the following images (Fig. 5-30 and Fig. 5-31) show the correspondence between complex target used for this study and the equivalent structural components of GOCE.





**Fig. 5-30** The complex target type "E" correspond to GOCE external face-sheet jointed to three Al HC floors.



**Fig. 5-31** The complex target type "C" correspond to two GOCE external face-sheets jointed together.

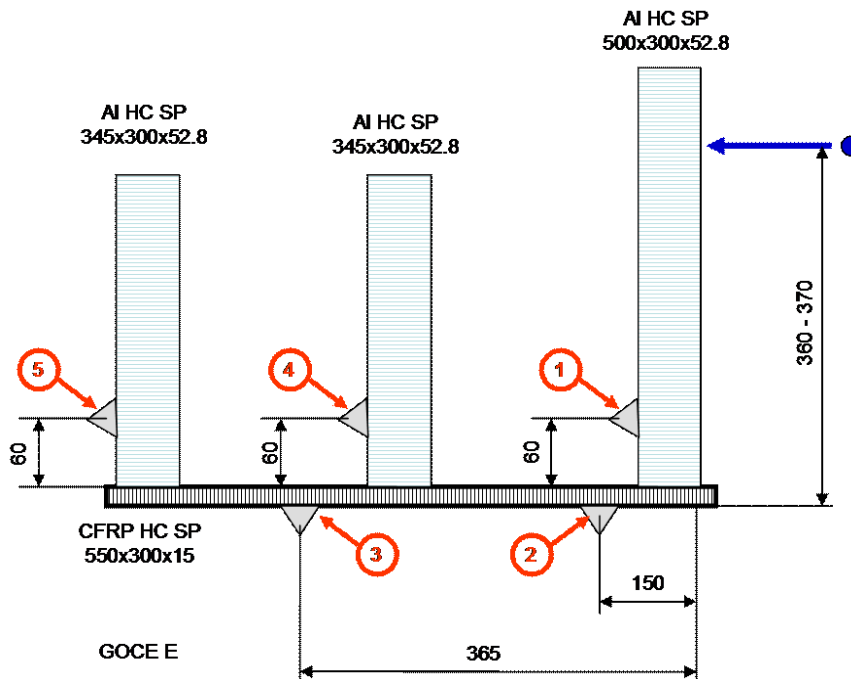
### 5.3.4.2 Test on complex targets

Accordingly, to the subdivision of the HVI environment levels presented in chapter 4.2.2, the results of experiments on simple targets have been used as starting point to verify the acceleration levels on complex targets. Three complex configuration have been tested, and for each of them the result are presented in from of a table, which reports the test condition and a figure that show the acceleration levels behaviour on target surfaces. For reference to the GOCE satellite structure, see paragraph 5.3.4.1. If not otherwise specified, materials of complex targets are representative of the real GOCE in-flight materials (i.e. CFRP-AI HC and AI HC).

**To avoid amplifiers saturation the Endevco sensors attached on the impacted plate have been mounted with the double-layer tape interface.**

### 5.3.4.3 GOCE type "E"

Fig. 5-32 shows the configuration of GOCE target type "E" and Tab. 5-5 the sensor used at each position. Five different sensors positions have been tested; for each of them we measured the acceleration peaks, to evaluate the disturbance intensity through joints and to assess the correct sensor to use for experimental measures. Different impact condition have been tested, accordingly to tests scheduled for the following experiments (see chapter 0).



**Fig. 5-32 GOCE target type "E". 3 Al HC plates + 1 CFRP plate connected with AI joints.**

Sensors		Results		CISAS ID	
Pos.	Assembly	Description	Unit	7344	7349
1	2 Endevco on triangular prism	Max Outplane	ms <sup>-2</sup>	3.50e4	2.2e4
		Max Inplane	ms <sup>-2</sup>	1.30e4	0.60e4
		Freq. content	kHz	<25	<25
2	2 B&K on triangular prism	Max Outplane	ms <sup>-2</sup>	0.55e4	0.26e4
		Max Inplane	ms <sup>-2</sup>	0.40e4	0.33e4
		Freq. content	kHz	<25	<20
3	2 B&K on triangular prism	Max Outplane	ms <sup>-2</sup>	0.20e4	0.24e4
		Max Inplane	ms <sup>-2</sup>	0.22e4	0.21e4
		Freq. content	kHz	<20*	<20*
4	2 B&K on triangular prism	Max Outplane	ms <sup>-2</sup>	0.85e4	0.44e4
		Max Inplane	ms <sup>-2</sup>	0.18e4	0.14e4
		Freq. content	kHz	<20*	<20*
5	2 PCB on triangular prism	Max Outplane	ms <sup>-2</sup>	0.80e4	0.41e4
		Max Inplane	ms <sup>-2</sup>	0.22e4	0.12e4
		Freq. content	kHz	<20*	<20*

**Tab. 5-5 Acceleration peaks and frequency content vs. sensor position (\*signals low-pass filtered at 20 kHz before acquisition) as reported in.**

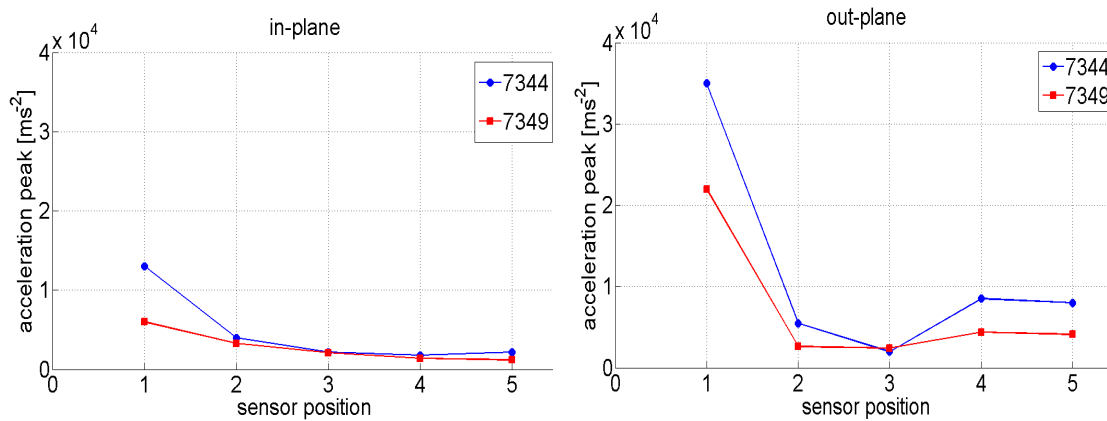
Tab. 5-6 reports the tests configuration, while Fig. 5-33 shows the behaviour of acceleration peaks as function of sensor position for the last two tests; after these experiments, we can to evaluate the correct type of sensor for measures in each position.

CISAS ID	Target Type [mm]	dp [mm]	vp [km/s]	Coarse Damage	Comments
7081	GOCE E All-AI	1.5	4.6	P	None
7084	GOCE E All-AI	1.5	4.7	P	None
7294	GOCE E All-AI	1.5	5.1	P	None

7295	GOCE E All-Al	1.5	5.4	P	None
7296	GOCE E All-Al	1.5	5.2	P	None
7344	GOCE E	2.3	4.7	P	None
7349	GOCE E	1.9	4.7	P	None

**Tab. 5-6 Experiments performed on GOCE configuration "E".**

Some tests have been performed with thin plates instead of HC, due to materials availability. Shock levels are higher for Al plates, so test made on such structures are conservative compared to the expectable acceleration levels on the corresponding HC ones.

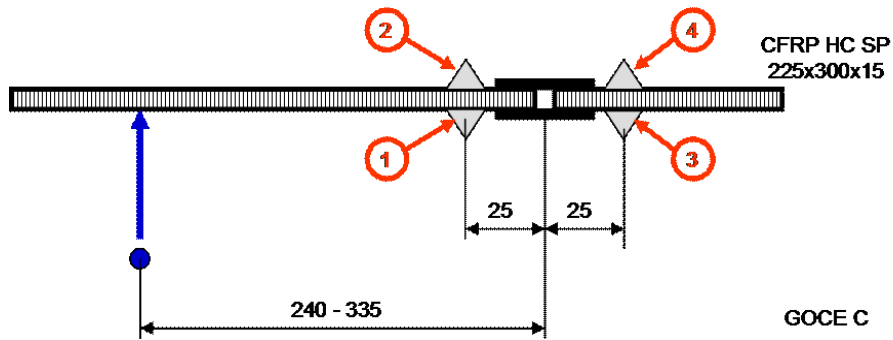


**Fig. 5-33 Maximum acceleration peaks in function of sensors position (for shots 7344 and 7349).**

We can infer that the first joint reduces drastically the acceleration level and frequency content, thus allowing using sensors with reduced acceleration range and lower resonant frequency respect to sensors placed in the front plate. The joints after position 2 do not determine further strong signal attenuation, mainly because of the already low frequency content of the acceleration field. Comparing sensor frequency content with 20 kHz low-pass filter On and Off turns out that the signal conditioners will not have problems of saturation or overload.

#### 5.3.4.4 GOCE type "C"

Fig. 5-34 shows the configuration of GOCE type "C" target and Tab. 5-7 the sensor used at each position. The same test conditions of the previous type "E" have been used. Tab. 5-8 reports the test performed, while summarizes the acceleration peaks behaviour in function of sensor position.



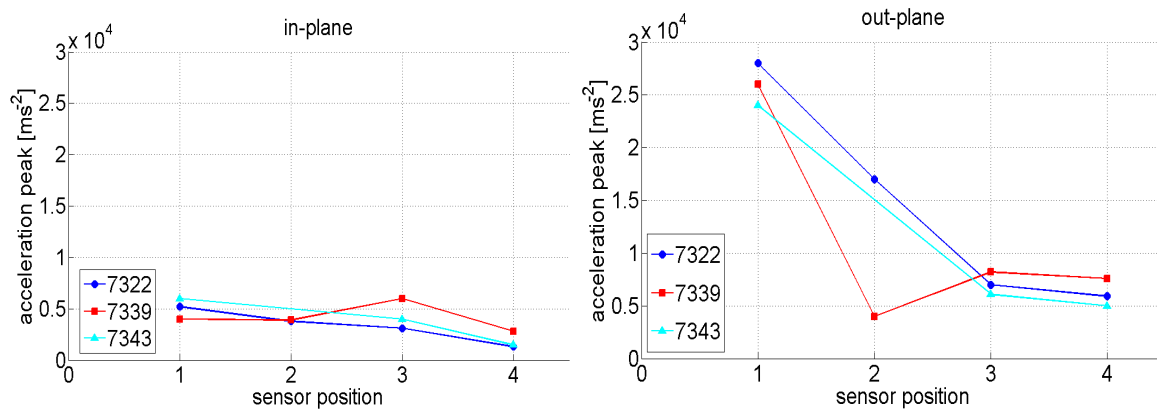
**Fig. 5-34 GOCE target type "C". 2 CFRP plates connected with CFRP plane joints.**

Sensors		Results		CISAS ID		
Pos.	Assembly	Description	Unit	7322	7339	7343
1	2 Endevco on triangular prism	Max Outplane	ms <sup>-2</sup>	2.80e4	2.60e4	2.40e4
		Max Inplane	ms <sup>-2</sup>	0.52e4	0.40e4	0.60e4
		Freq. content	kHz	100	100	100
2	2 Endevco on triangular prism	Max Outplane	ms <sup>-2</sup>	1.70e4	0.40e4	NA
		Max Inplane	ms <sup>-2</sup>	0.38e4	0.39e4	NA
		Freq. content	kHz	100	100	NA
3	2 B&K on triangular prism	Max Outplane	ms <sup>-2</sup>	0.70e4	0.82e4	0.61e4
		Max Inplane	ms <sup>-2</sup>	0.31e4	0.60e4	0.40e4
		Freq. content	kHz	100	100	100
4	2 B&K on triangular prism	Max Outplane	ms <sup>-2</sup>	0.59e4	0.76e4	0.50e4
		Max Inplane	ms <sup>-2</sup>	0.13e4	0.28e4	0.15e4
		Freq. content	kHz	<20*	<20*	<20*

**Tab. 5-7 Acceleration peaks and frequency content vs. sensor position (\*signals low-pass filtered at 20 kHz before acquisition) as reported in Fig. 5-34.**

CISAS ID	Target Type [mm]	dp [mm]	vp [km/s]	Coarse Damage	Comments
7322	GOCE C	1.5	4.5	NP	None
7339	GOCE C	2.3	4.8	P	None
7343	GOCE C	2.3	4.7	P	None

**Tab. 5-8 Experiments performed on GOCE type "C" target.**

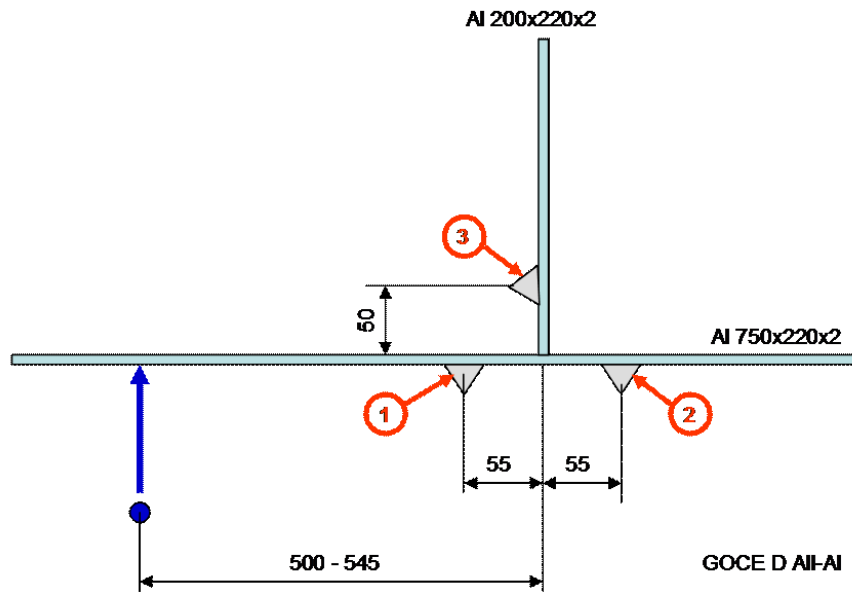


**Fig. 5-35 Maximum acceleration peaks in function of sensors position (for all shots).**

Tests show a reduction of the acceleration level through the joints (positions 3 and 4) for the out of plane signal, while there is only a small attenuation for the in plane components. The frequency content of the signal after the joints is still high, up to 100 kHz; we can argue that sensor resonant frequency has been reached. For this reason, if a sensor with a low resonant frequency is applied at position 1 and 2, it must be sized considering a resonant operative conditions (i.e. possible overload or saturation of amplifiers).

#### 5.3.4.5 GOCE type "D"

Fig. 5-36 shows the configuration of GOCE type "D" target and Tab. 5-9 the sensor used at each position. In addition, this configuration has been tested with Al thin plates instead of HC Al and CFRP panels, due to material availability. As previously stated, this is a conservative approach, since acceleration levels on thin Al plates are higher than HC corresponding targets. Tab. 5-10 reports the test performed, while summarizes the acceleration peaks behaviour in function of sensor position.



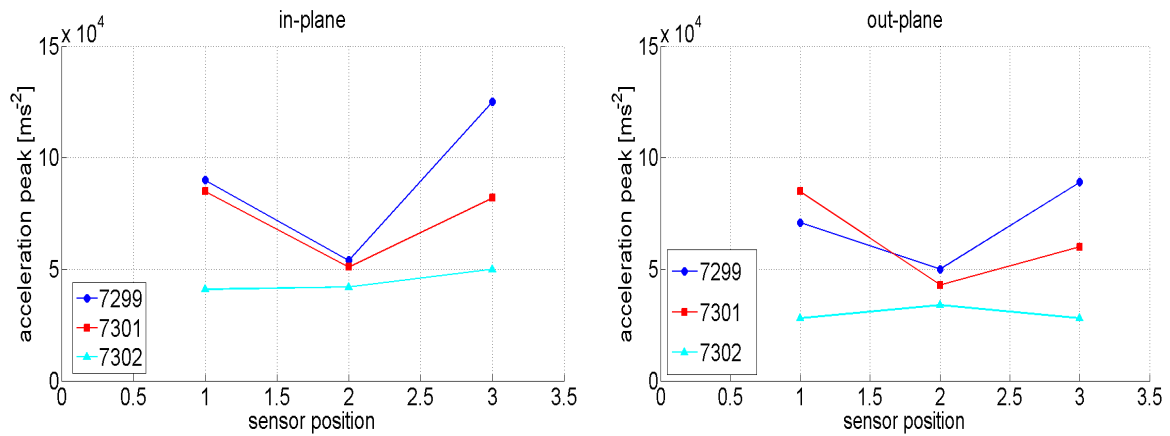
**Fig. 5-36 GOCE target type "D". 3 Al plates connected with Al joints.**

Sensors		Results		CISAS ID		
Pos.	Assembly	Description	Unit	7299	7301	7302
1	2 Endeeco on triangular prism	Max Outplane	ms <sup>-2</sup>	7.10e4	8.50e4	2.80e4
		Max Inplane	ms <sup>-2</sup>	9.00e4	8.50e4	4.10e4
		Freq. content	kHz	200	200	200
2	2 Endeeco on triangular prism	Max Outplane	ms <sup>-2</sup>	5.00e4	4.30e4	3.40e4
		Max Inplane	ms <sup>-2</sup>	5.40e4	5.10e4	4.20e4
		Freq. content	kHz	200	200	200
3	2 B&K on triangular prism	Max Outplane	ms <sup>-2</sup>	8.90e4	6.00e4	2.80e4
		Max Inplane	ms <sup>-2</sup>	1.25e5	8.20e4	5.00e4
		Freq. content	kHz	100	100	100

**Tab. 5-9 Acceleration peaks and frequency content vs. sensor position, as shown in Fig. 5-36.**

CISAS ID	Target Type [mm]	dp [mm]	vp [km/s]	Coarse Damage	Comments
7299	GOCE D All-AI	1.5	4.0	P	None
7301	GOCE D All-AI	1.5	4.9	P	None
7302	GOCE D All-AI	1	5.1	P	None

**Tab. 5-10 Experiments performed on GOCE type "D" target.**



**Fig. 5-37 Maximum acceleration peaks in function of sensors position (for all shots).**

Aluminium joints do not introduce strong attenuation on the frequency content of the signal, so resonant condition of Bruel&Kjaer sensors is reached (resonance at 85 kHz, sensor position 3). Since accelerations are so high at position 1 and 2 (respect to types E and C), the full thin plate AI configuration highly overestimate the instrumentation requirements respect to HC configuration (especially for in plane accelerations).



## 6 Vibration environment of spacecraft structures

This part of the research work aims to investigate the vibration environment induced by HVI on spacecraft structure (GOCE) through direct experimental analysis.

Two methodologies have been applied:

- The first, called experimental model, is based on the direct characterization of the vibration environment on panels and through joints, through SRS comparisons on different part of the structure. The analysis has been conducted on simple honeycomb panels (paragraph 6.1) and on complex assemblies representative of real spacecraft elementary-structure (paragraph 6.2).
- The second called numerical analysis, applies wavelet analysis to investigate into detail wave propagation (paragraph 6.4). This new advanced methodology has been applied only on simple panel structure to introduce this new tool into wave propagation analysis.

The work is summarized in the following points:

- Impact test on simple targets, under different impact conditions, with the aim of characterizing the vibration field on the impacted structure (near field)
- Impact test on complex targets (far field), under different impact conditions, with the aim of characterizing the vibration field propagated from the impacted structure to others components, through joints

### 6.1 SRS of the disturbance generated by HVI on simple targets

Experimental model are focused on two type of targets: simple aluminium honeycomb targets, tested in order to identify the near field environment (the disturbance on the impacted target) and complex CFRP and Al targets, tested to identify the mid and far-field environment (the disturbance propagated from the impacted target to others components jointed with it).

The experiments presented in this paragraph aim at characterizing the vibration field generated by HVI on simple honeycomb panels and at defining if it is function and how of different impact conditions and target configurations. The projectile mass and velocity directly influences the vibration filed, but other effects, such as impact angle, may modify the disturbance.

### 6.1.1 Tests on Al honeycomb sandwich panels (near field environment)

The content of paragraph is summarised in the following table:

Main task	Description	Page
Test logic for Al plates	Summary of the performed tests with description of their objective	51
Data scattering and noise evaluation	Estimation of uncertainty consequent to data scattering and facility background noise	52
Influence of existing damage	Evaluation of the effect of previous HVI damage on HC core	55
Scaling effects	Evaluation of the effect of different target size from 200x200 to 450x430 mm <sup>2</sup>	59
Load effects	Assessment of the influence of point mass added to targets	66
Wave types	Comparative analysis of the main properties of OP, IP-longitudinal and IP-transversal waves on both front and rear target side	69
Effects of projectile mass	Evaluation of SRS variations due to HVI with projectile having increasing mass (momentum)	72
Effects of impact velocity	Evaluation of SRS variations due to HVI with projectile having increasing velocity (momentum)	85
Impact obliquity	Evaluation of possible SRS variations due to impact angles other than 0°	89
Relevant results for Al plates	Summary of the main engineering results relevant to HVI onto Al HC SP	99

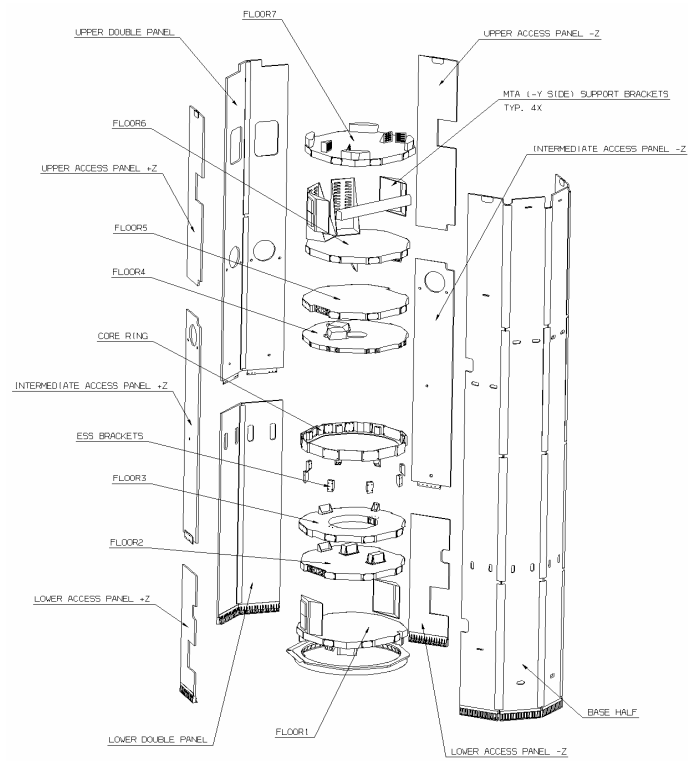
**Table 6-1 Summary of contents for paragraph 6.1.1**

All targets are Al2024-T81 1mm 3.1 3/16 5056 10P, panel height 52.8 mm. The basic size of each panel was 400x400 mm, other dimensions were considered performing scaling effects test.

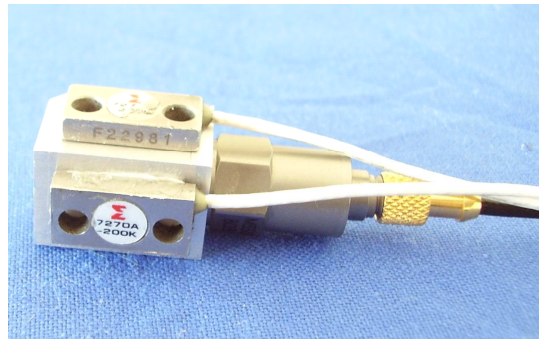
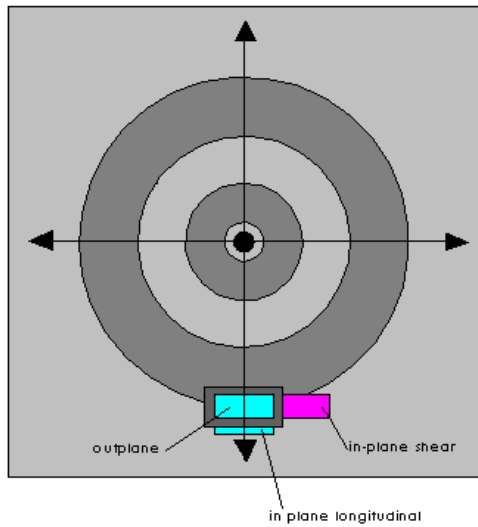
They are representative of GOCE floors 1, 2, 5, 6 and 7.

The experimental configuration is represented in Fig. 6-3: panels are connected to the supporting frame through springs and accelerometers are mounted on tri-axial assemblies, fixed at 150 from the impact point (nominal distance).

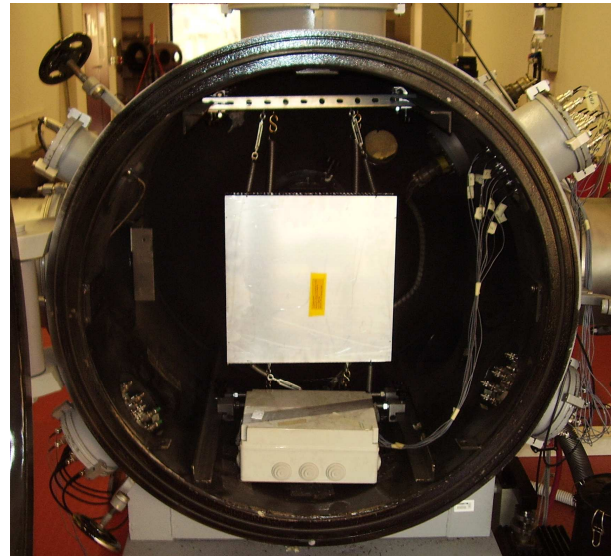
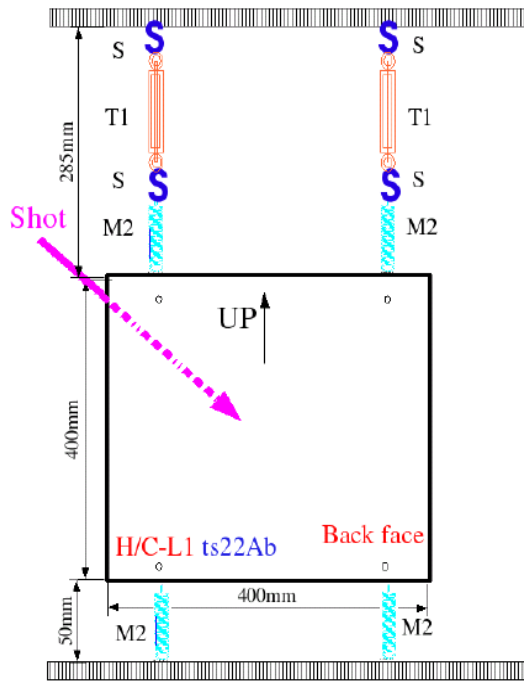
One sensor assembly was placed on each face of the target. Such assemblies are made by a parallelepiped-mounting block and three shock accelerometers (2 Endevco 7270-200k for out-plane and in-plane longitudinal waves, one PCB M350B02 mechanically limited to 10 kHz for in-plane shear waves). Fig. 6-2 shows the sensors configuration.



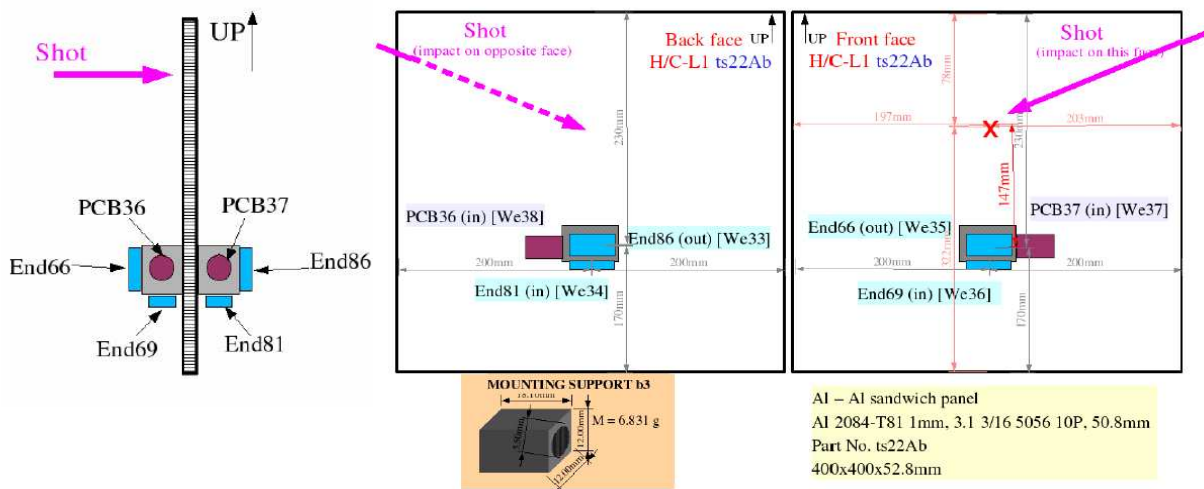
**Fig. 6-1 GOCE structure configuration**



**Fig. 6-2 Wave propagation from the impact point (left). Accelerometers mounting assembly (right)**



**Fig. 6-3 Experimental configuration for impact test on simple targets**



**Fig. 6-4 Sensors disposition for impact test on simple targets**

In summary, for each test six acceleration signals are recorded, three of them on the front (impact) side of the SP, three of them for the rear side.

Signals refer to in-plane-longitudinal, in-plane-shear and out-plane waves.

Test results are presented in the following through the SRS of recorded signals.

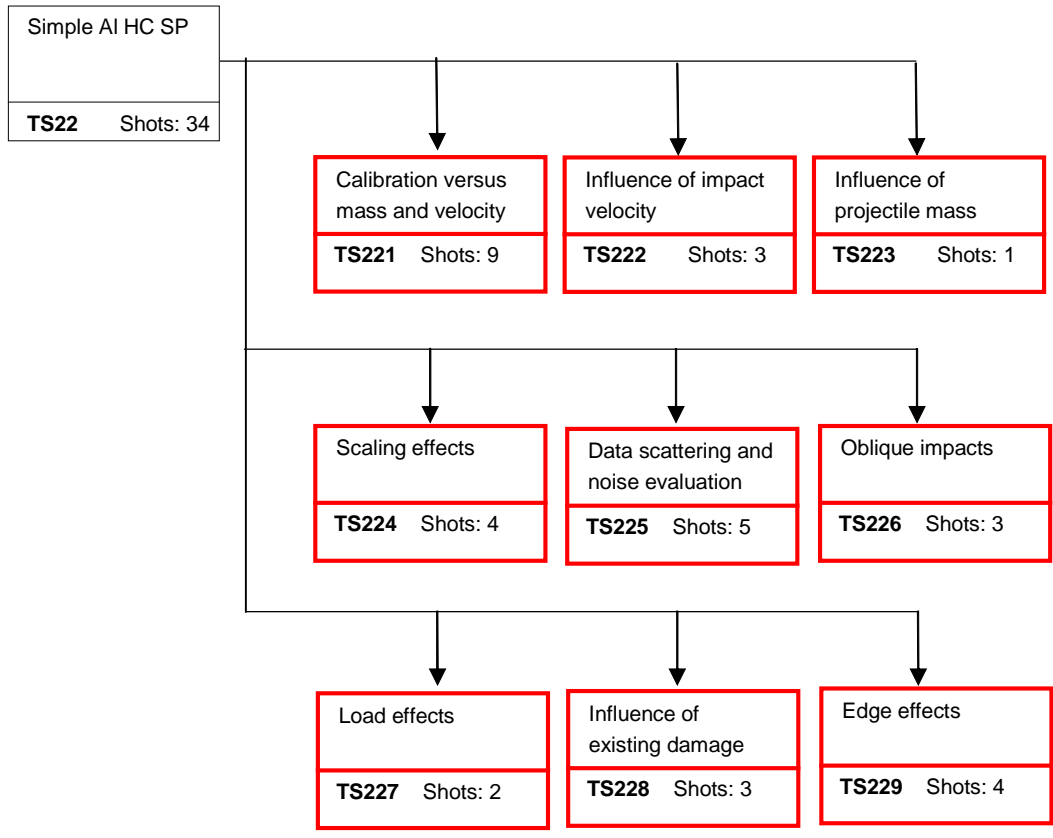
### 6.1.2 Test logic for Al HC SP

Tests on Al HC SP are summarized in Fig. 6-5.

The test grouping was conceived to assess the following points (the test code is the one used in the frame of the ESA contract):

TS221, 222, 223: wave properties and their dependence on projectile mass and velocity

TS224: influence of target size on waves properties  
 TS225: measurement uncertainty for interpreting data from TS22, including terms from data scattering and facility background noise  
 TS226: influence of impact angle on waves properties  
 TS227: load effects on measurements  
 TS228: effects of existing damage on wave properties  
 TS229: influence of distance from edges on wave properties



**Fig. 6-5. Test logic for impact test on simple targets**

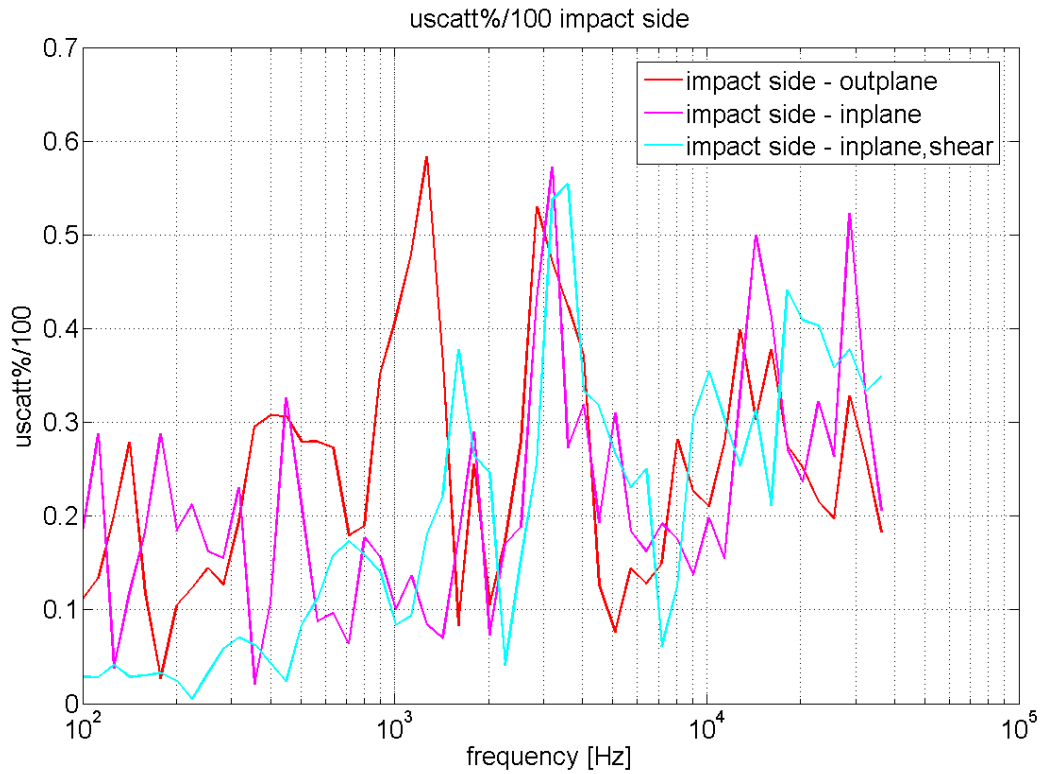
**6.1.2.1 Data scattering and noise evaluation (TS225)**

CISAS ID	ESA ID TS-	dp [mm]	vp [km/s]	Coarse damage	Comments
7549	225/1 227/1	1.5	4.9	P	Test used also for TS227
7550	225/2	1.5	4.8	P	None
7568	221/3 225/3	1.5	5.0	BL<=	Test used also for TS221
7855	225/4	-	-	-	Only propellant
7856	225/5	-	-	-	Only propellant
7857	225/6	-	-	-	Only propellant

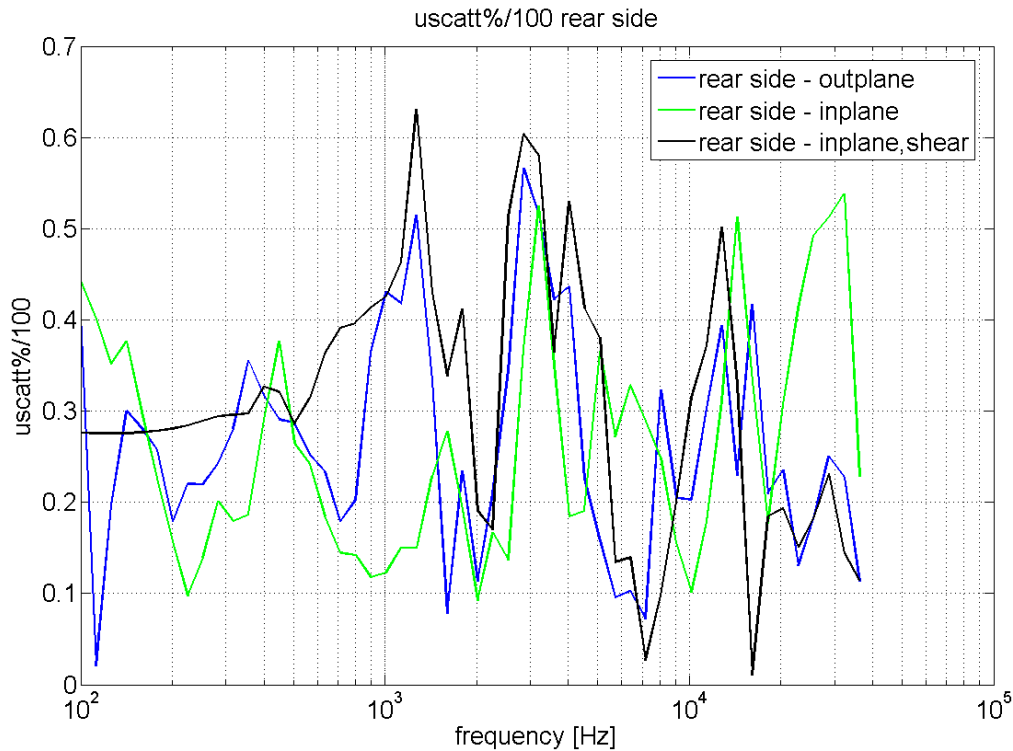
**Tab. 6-1. Summary of TS225**

Tests 7549, 7550 and 7568 were performed at nominally identical conditions, i.e. launching 1.5 mm projectiles at 5 km/s. Each experiment was realised on completely new targets, to avoid corruption of information resulting from the existing damage by previous shots.

Statistical analysis was used to estimate the scattering  $U_{scatt}$  through the percent standard deviation on each signal (Fig. 6-6 and Fig. 6-7).



**Fig. 6-6. SRS of  $U_{scatt}$  (SP front side)**

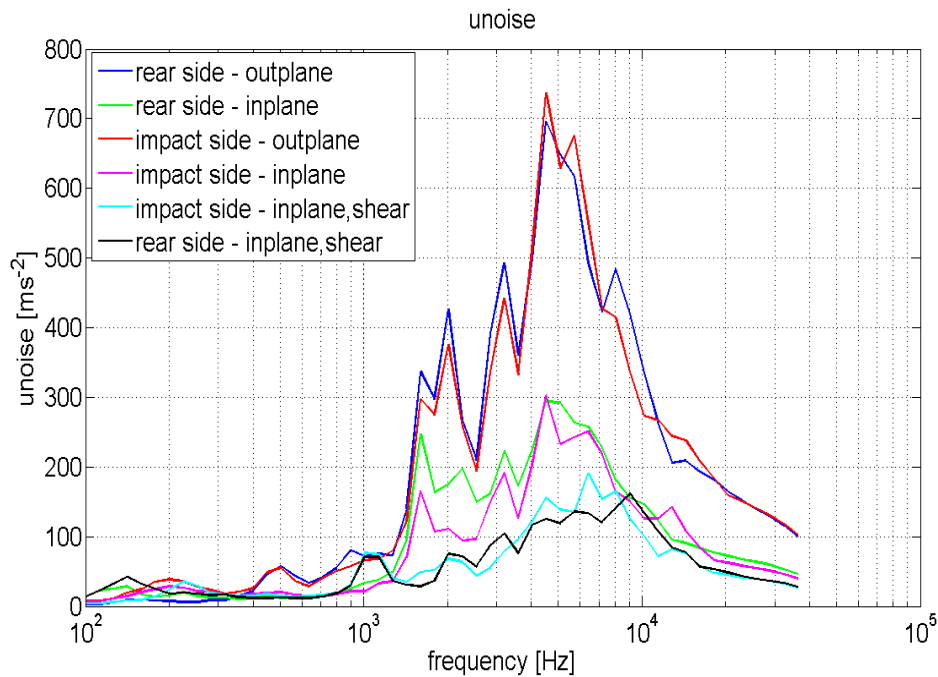


**Fig. 6-7. SRS of  $U_{scatt}$  (SP rear side)**

From previous figures, it appears that data scattering has complex dependence from frequency. Nevertheless, a growing trend may be recognised for the SRS of scattering from below to above  $10^3$  Hz, with maximum value increasing from  $\sim 2$  dB to  $\sim 4$  dB.

Tests 7855, 7856 and 7857 were performed by launching only hydrogen propellant, to evaluate the background noise contribution  $U_{noise}$  (Fig. 6-8) to the overall uncertainty  $U$ .

As for the scattering, the SRS of noise appears to be strongly frequency-dependent, with a pronounced increasing trend above  $10^3$  Hz.



**Fig. 6-8. SRS of  $U_{noise}$**

$U_{scatt}$  and  $U_{noise}$  are used for calculating the overall uncertainty to be applied to each SRS.

Specific uncertainty is estimated for each SRS, it is plotted (dash-dot line) together with the calculated SRS (solid line), to which it refers.

For TS228, realized at nominally identical conditions, only the uncertainty on the average SRS was plotted. This provides a preliminary idea on SRS compatibility without making confuse the graphical representation (but the compatibility should be searched for between uncertainty bands over the SRS under comparison, not over the average).

### 6.1.2.2 Influence of existing damage (TS228)

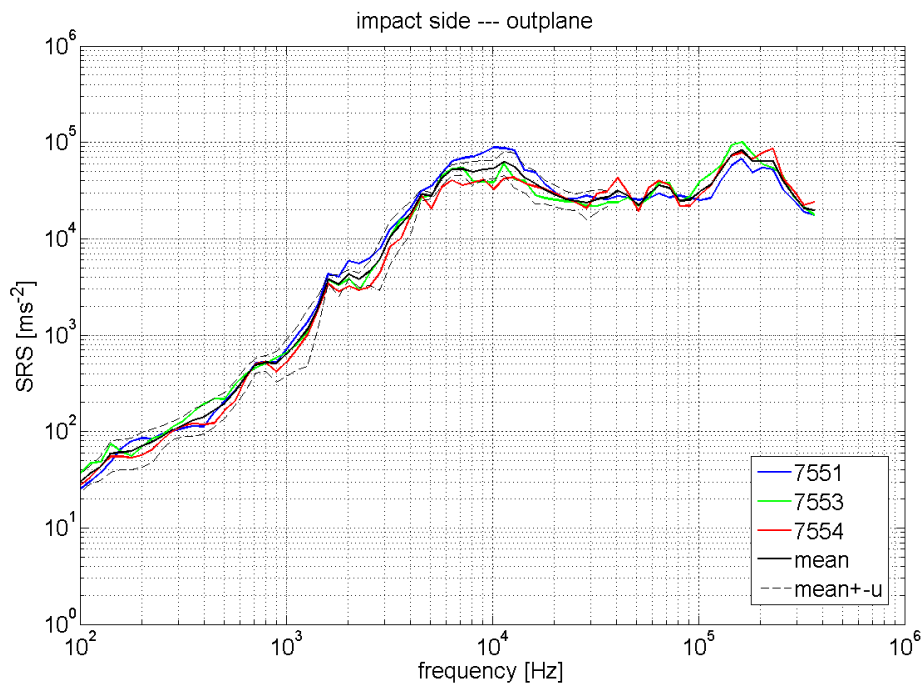
CISAS ID	ESA ID TS-	dp [mm]	vp [km/s]	Coarse damage	Comments
7551	228/1	1.9	4.9	P	None
7553	228/2	1.9	5.1	P	None
7554	228/3	1.9	5.0	P	None

**Tab. 6-2. Summary of TS228**

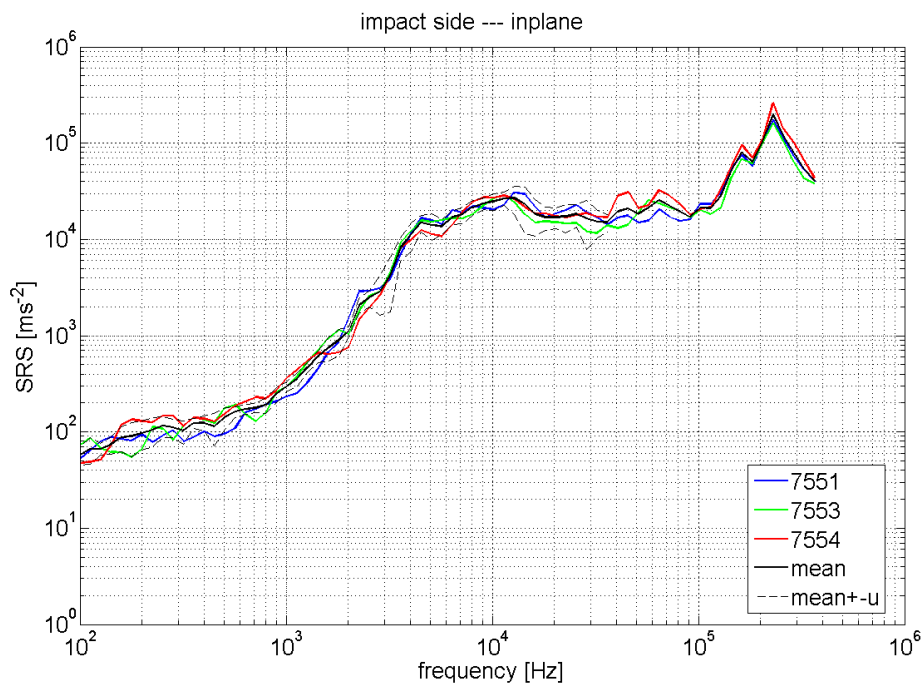
Tests 7551, 7553 and 7554 were performed at nominally identical conditions, i.e. launching 1.9 mm projectiles at 5 km/s. Each experiment was realised on targets already injured by HVI, to assess the variability of signals consequent to existing damage. Multiple shots were done at the minimum distance avoiding superimposition of the HC core internal damage.

Results are reported from Fig. 6-8 to Fig. 6-14 for both front and rear side, for all the types of waves analysed. Each plot presents the SRS obtained from each test of TS228, plus the average SRS and its uncertainty band (estimated up to ~36 kHz).

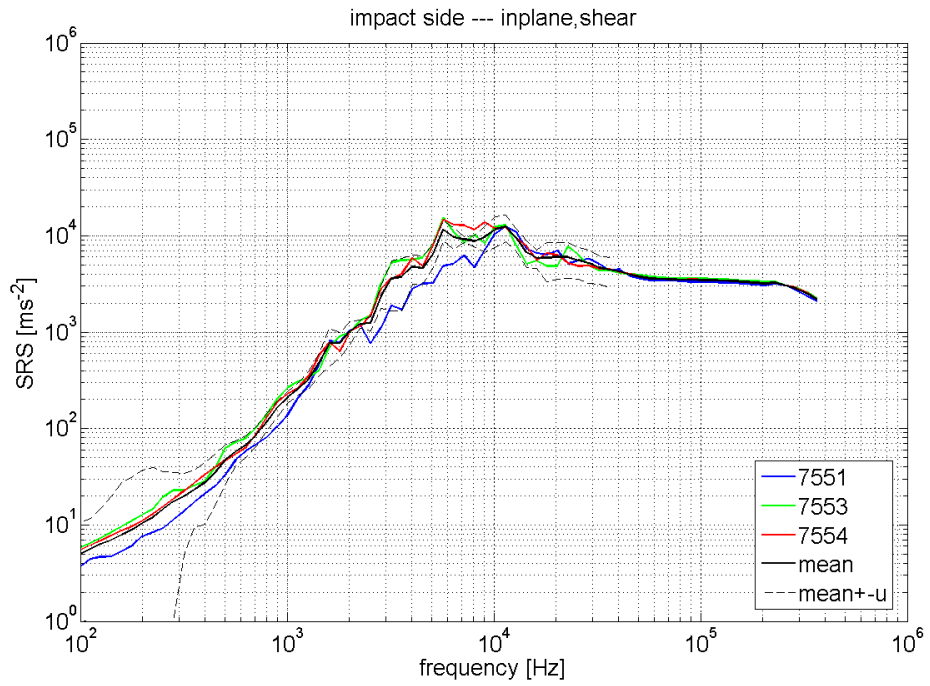




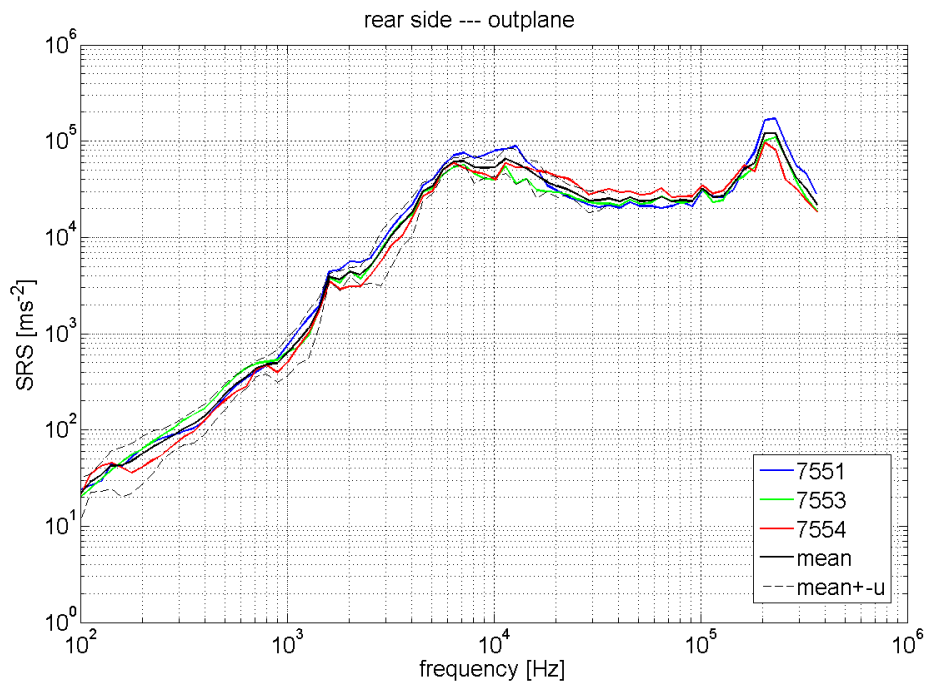
**Fig. 6-9. Influence of existing damage. Front side, out-plane**



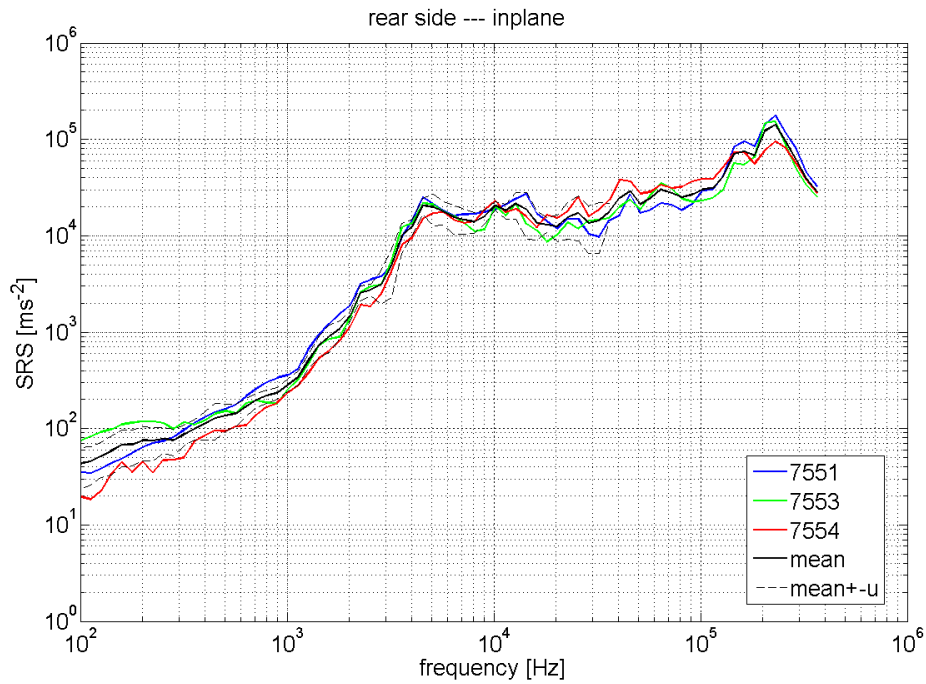
**Fig. 6-10. Influence of existing damage. Front side, in-plane-longitudinal**



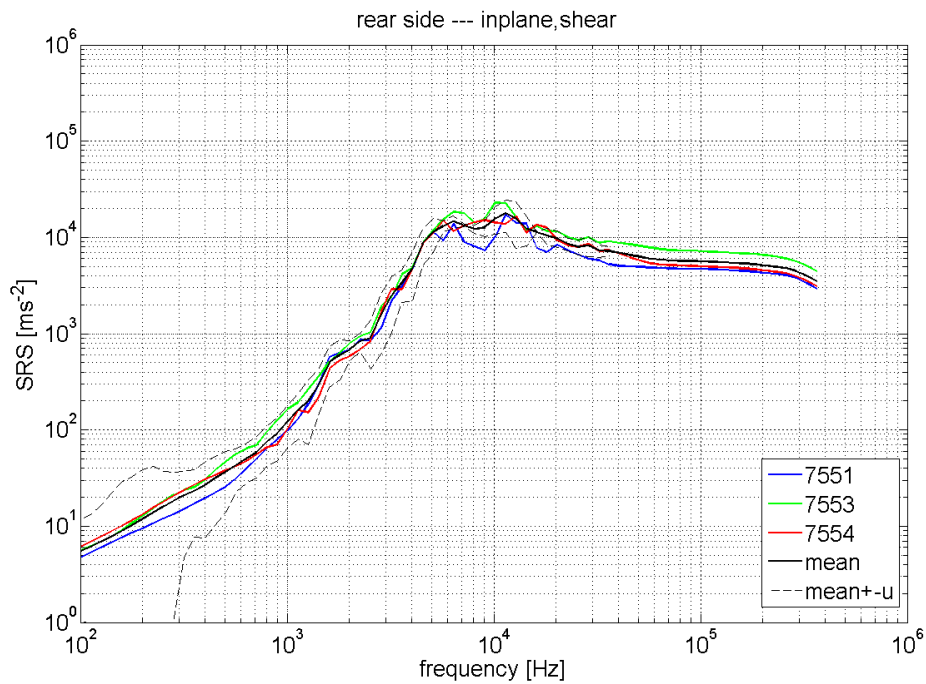
**Fig. 6-11. Influence of existing damage. Front side, in-plane-shear**



**Fig. 6-12. Influence of existing damage. Rear side, out-plane**



**Fig. 6-13. Influence of existing damage. Rear side, in-plane-longitudinal**



**Fig. 6-14. Influence of existing damage. Rear side, in-plane-shear**

Looking at the plots, it may be concluded that the influence of existing damage on SRS is below the measurement uncertainty.

Therefore it is acceptable to perform more than one test on the same target, with the only limitation of keeping a minimum distance between impact points, to avoid superimposition between HC core internal damage.

### 6.1.2.3 Scaling effects (TS224)

CISAS ID	ESA ID TS-	dp [mm]	vp [km/s]	Coarse damage	Comments
7555	224/4 221/11	1.9	5.1	P	Test used also for TS221 Target size 400x400 mm <sup>2</sup>
7563	224/3	1.0	5.0	NP	Target size 400x400 mm <sup>2</sup>
7564	224/1 221/1	1.0	4.9	NP	Test used also for TS221 Target size 450x430 mm <sup>2</sup>
7566	224/2 221/4	1.9	4.8	P	Test used also for TS221 Target size 450x430 mm <sup>2</sup>
7587	224/6	1.9	4.6	BL>=	Target size 203x249 mm <sup>2</sup>
7589	224/5	1.0	5.1	NP	Target size 203x249 mm <sup>2</sup>

**Tab. 6-3. Summary of TS224**

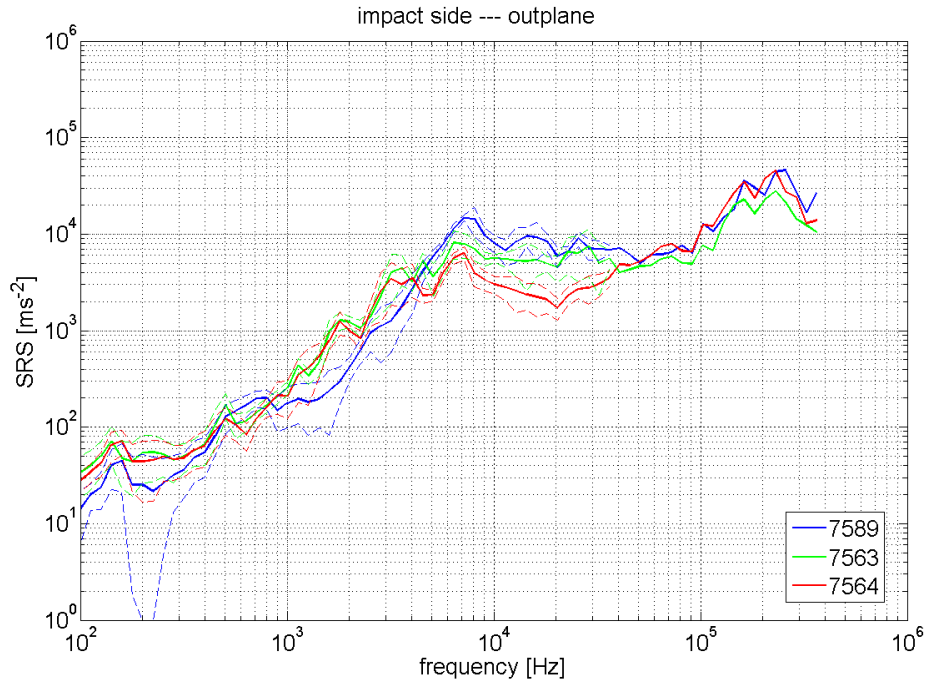
To evaluate scaling effects on wave properties, 6 experiments were performed on targets having size 204x209 mm<sup>2</sup>, 400x400 mm<sup>2</sup> and 450x430 mm<sup>2</sup>.

All the shots were done nominally at 5 km/s, with different projectile size (3 tests with dp=1mm, below BL; 3 tests with dp=1.9mm, above BL)

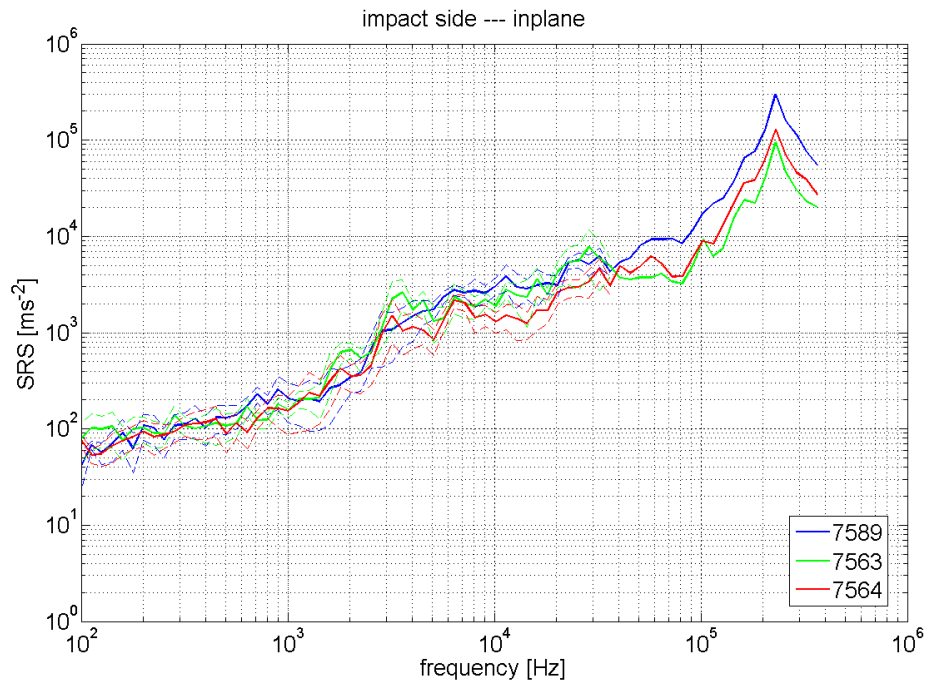
Scaling effects with dp=1mm

For dp=1mm, results are reported from Fig. 6-15 to Fig. 6-20 for both front and rear side, for all the types of waves analyzed.

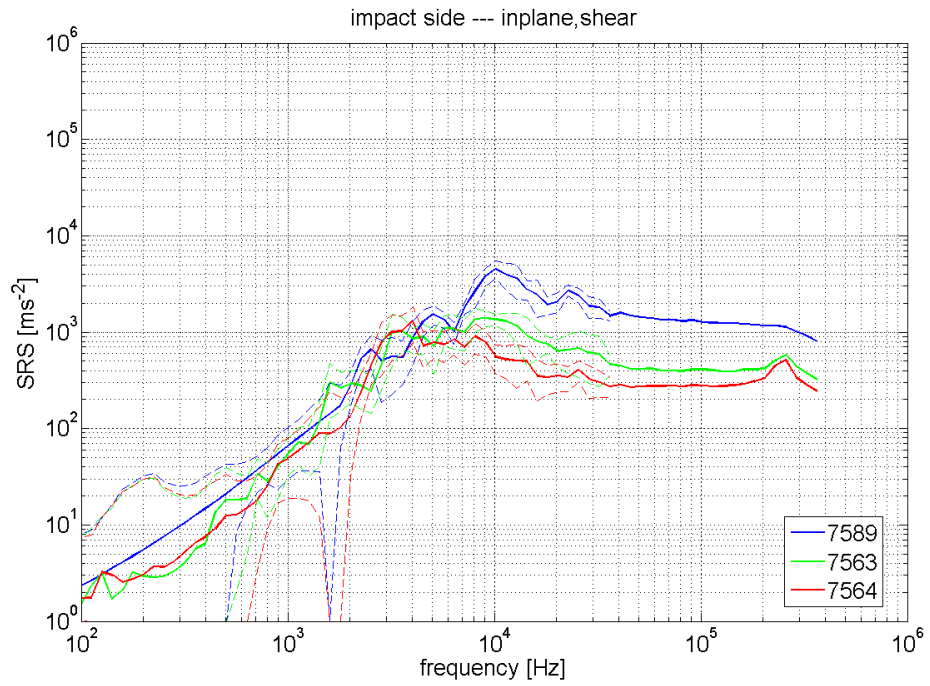
Each plot presents the SRS obtained from each test, together with its own uncertainty band (dash-dot lines, estimated up to ~36 kHz).



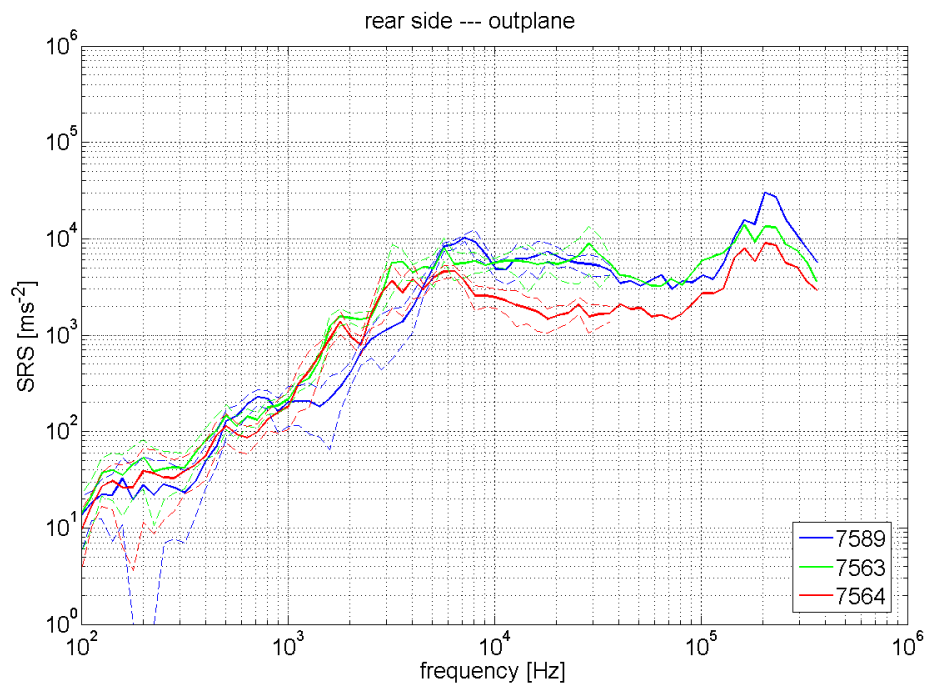
**Fig. 6-15. Scaling effects, dp=1mm. Front side, out-plane.**



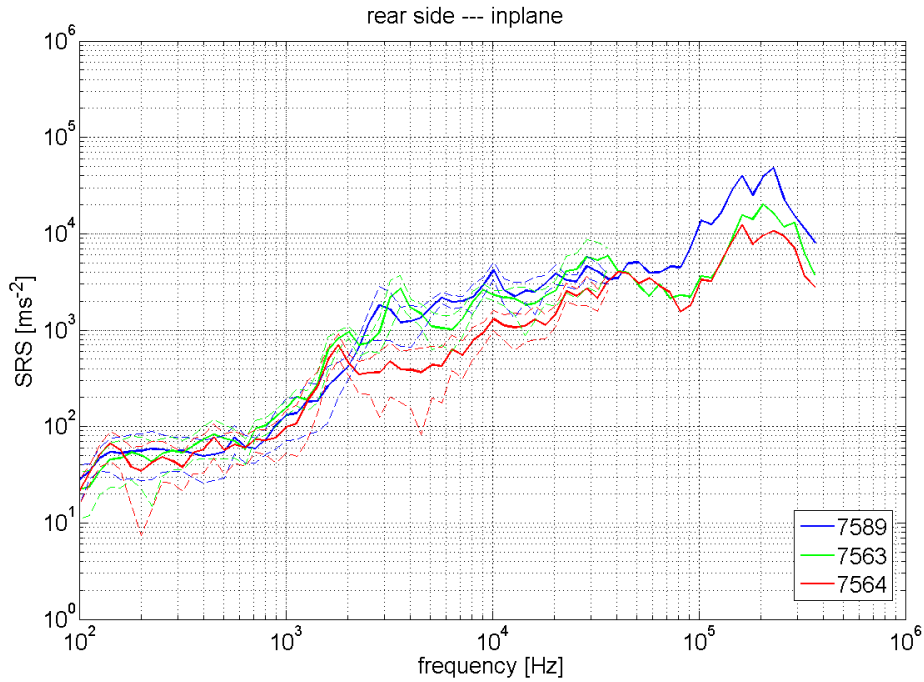
**Fig. 6-16. Scaling effects, dp=1mm. Front side, in-plane-longitudinal.**



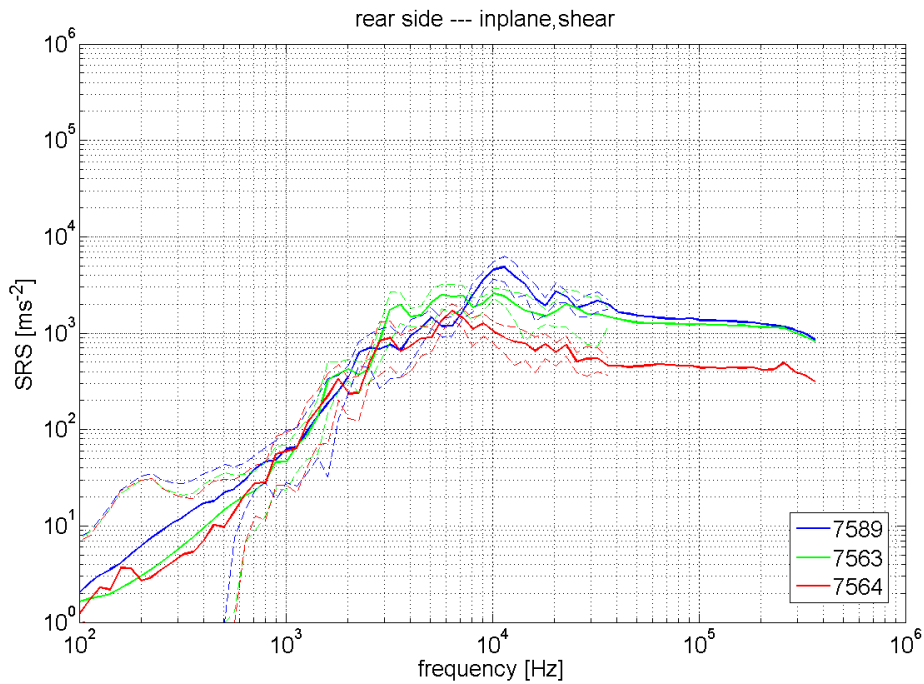
**Fig. 6-17. Scaling effects, dp=1mm. Front side, in-plane-shear.**



**Fig. 6-18. Scaling effects, dp=1mm. Rear side, out-plane.**



**Fig. 6-19. Scaling effects, dp=1mm. Rear side, in-plane-longitudinal.**



**Fig. 6-20. Scaling effects, dp=1mm. Rear side, in-plane-shear**

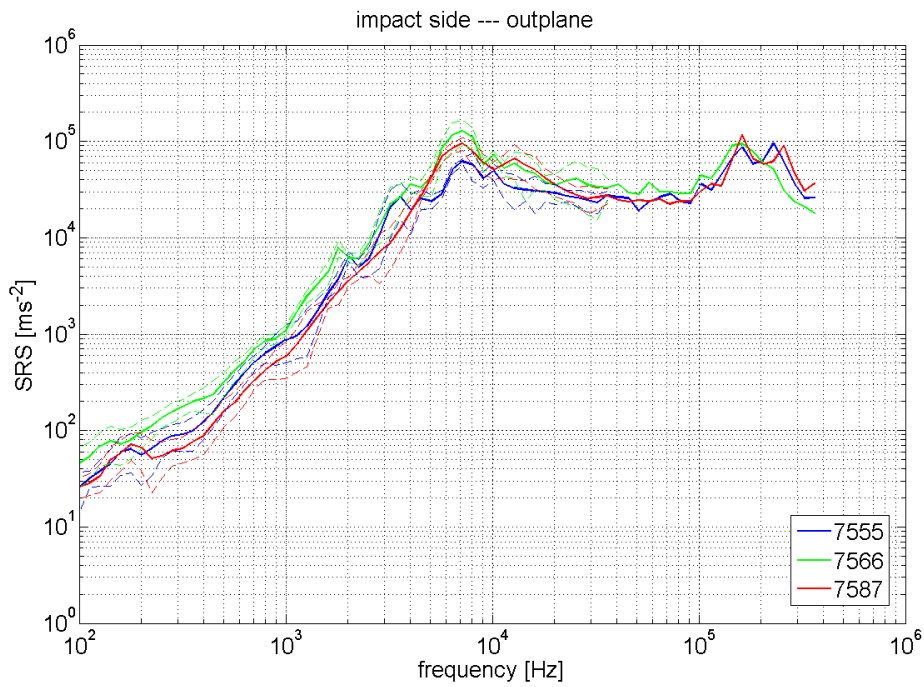
The examination of the above graphs suggests that the influence of target size on SRS is not significant (at least in our experimental range). Nevertheless, some systematic trend may be recognized in the high-frequency part of the spectrum (i.e. above  $\sim 7 \cdot 10^3$  Hz), with higher SRS obtained on experiments on the smallest target.

Anyway, such trend cannot be confirmed without deeper analysis on scaling effects.

Scaling effects with  $d_p=1.9$  mm

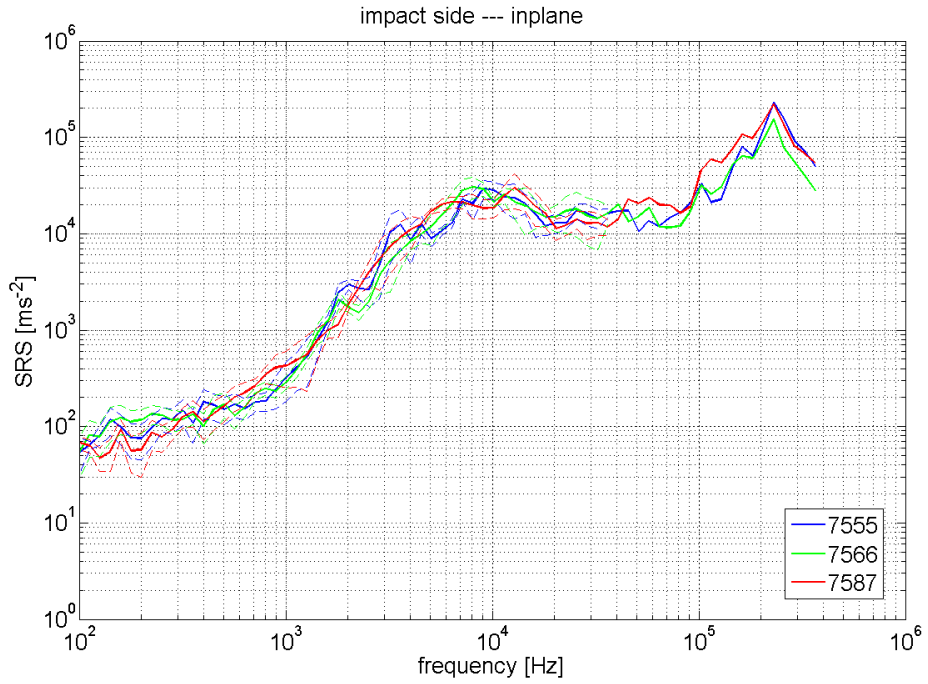
For  $d_p=1.9$ mm, results are reported from Fig. 6-21 to Fig. 6-25 for both front and rear side, for all the types of waves analysed.

Each plot presents the SRS obtained from each test, together with its own uncertainty band (dash-dot lines, estimated up to  $\sim 36$  kHz).

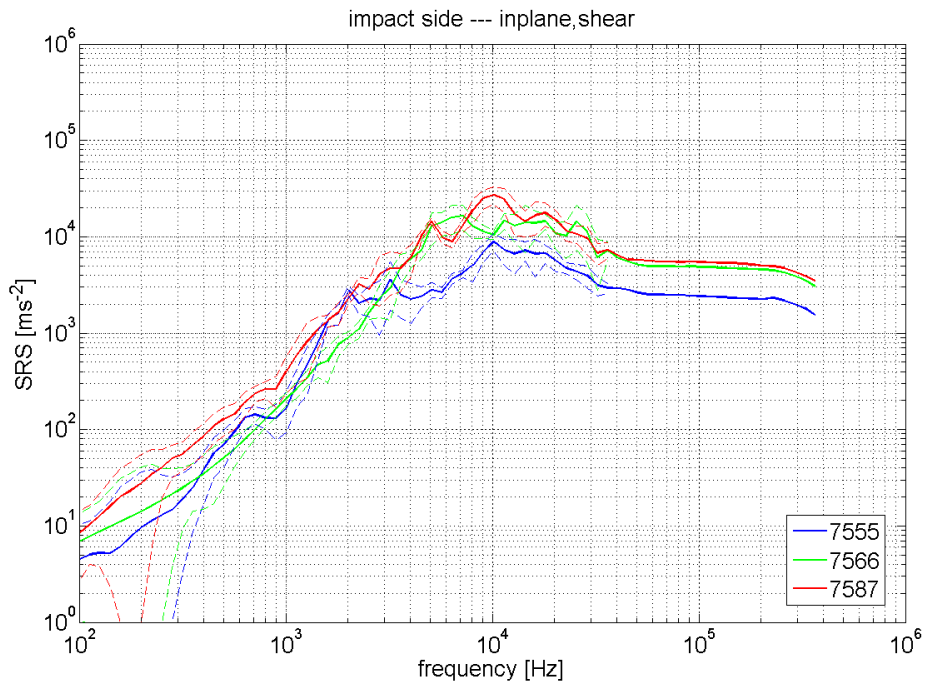


**Fig. 6-21. Scaling effects,  $d_p=1.9$ mm. Front side, out-plane.**

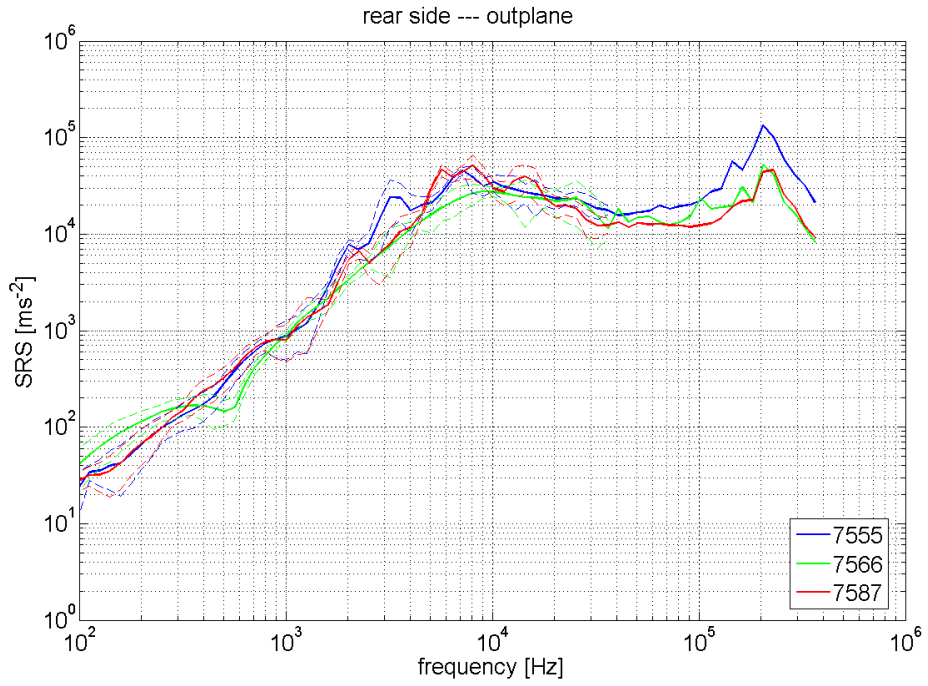




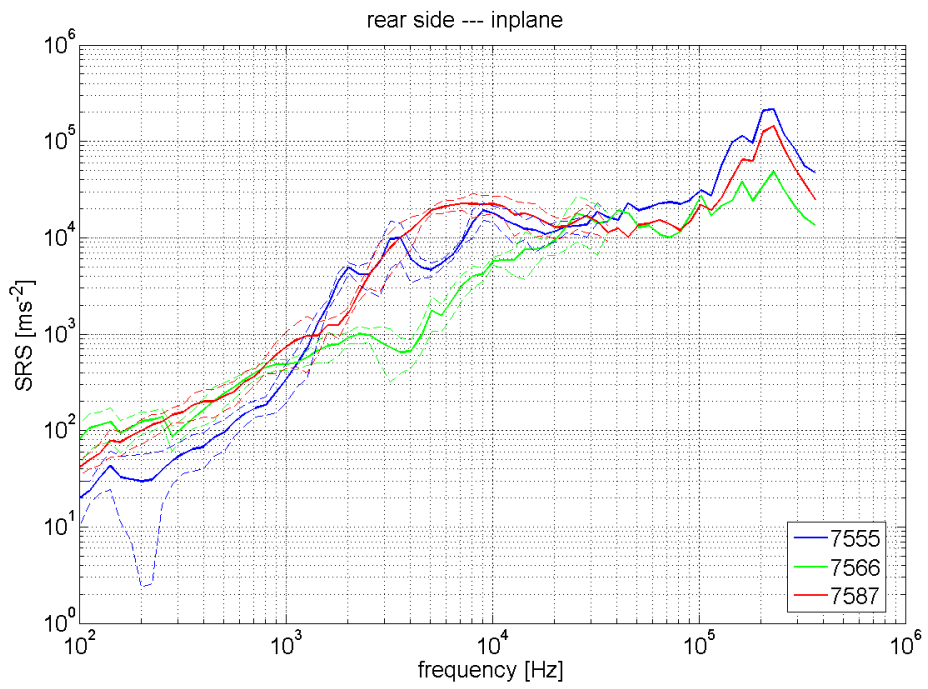
**Fig. 6-22. Scaling effects, dp=1.9mm. Front side, in-plane-longitudinal.**



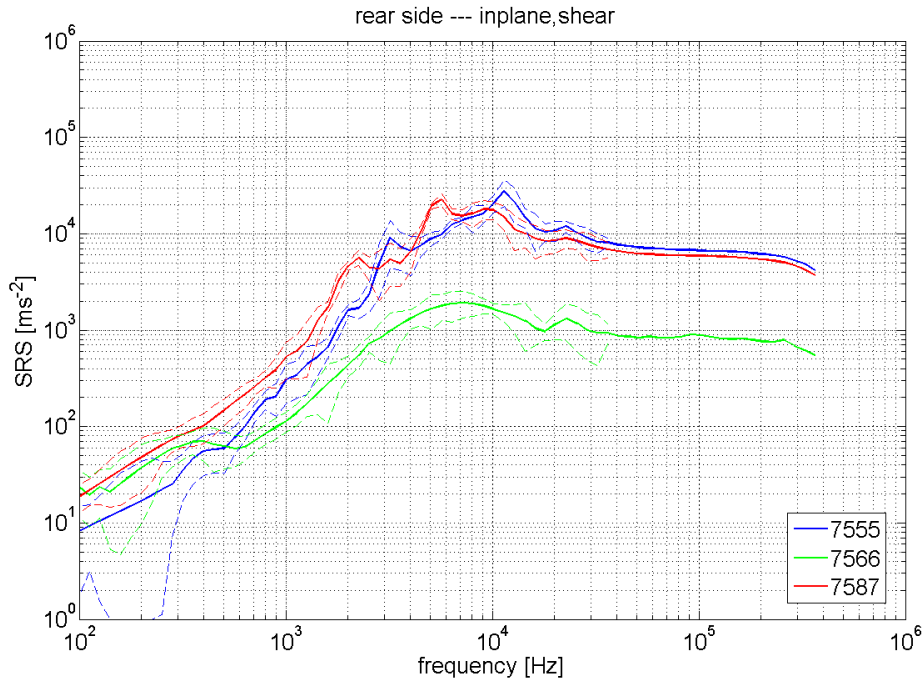
**Fig. 6-23. Scaling effects, dp=1.9mm. Front side, in-plane-shear.**



**Fig. 6-24. Scaling effects, dp=1.9mm. Rear side, out-plane.**



**Fig. 6-25. Scaling effects, dp=1.9mm. Rear side, in-plane-longitudinal.**



**Fig. 6-26. Scaling effects, dp=1.9mm. Rear side, in-plane-shear.**

The above plots confirm that the influence of target size on SRS is not significant (at least in our experimental range). The anomaly of test no. 7566 is due to sensor mounting detachment.

As for dp=1 mm tests, some systematic trend may be recognized in the high-frequency part of the spectrum (i.e. above few  $10^3$  Hz), with the highest SRS obtained on experiments on the smallest target. Anyway, such trend cannot be confirmed without deeper analysis on scaling effects.

#### 6.1.2.4 Load effects (TS227)

CISAS ID	ESA ID TS-	dp [mm]	vp [km/s]	Coarse damage	Comments
7595	227/2	1.5	5.2	NP	None
7596	227/3	1.5	5.1	BL>=	None

**Tab. 6-4. Summary of TS227**

The possibility of using different mountings for different sensors was taken into account regarding the resulting load effect on acceleration measurement, as it results from local alteration of targets dynamic properties.

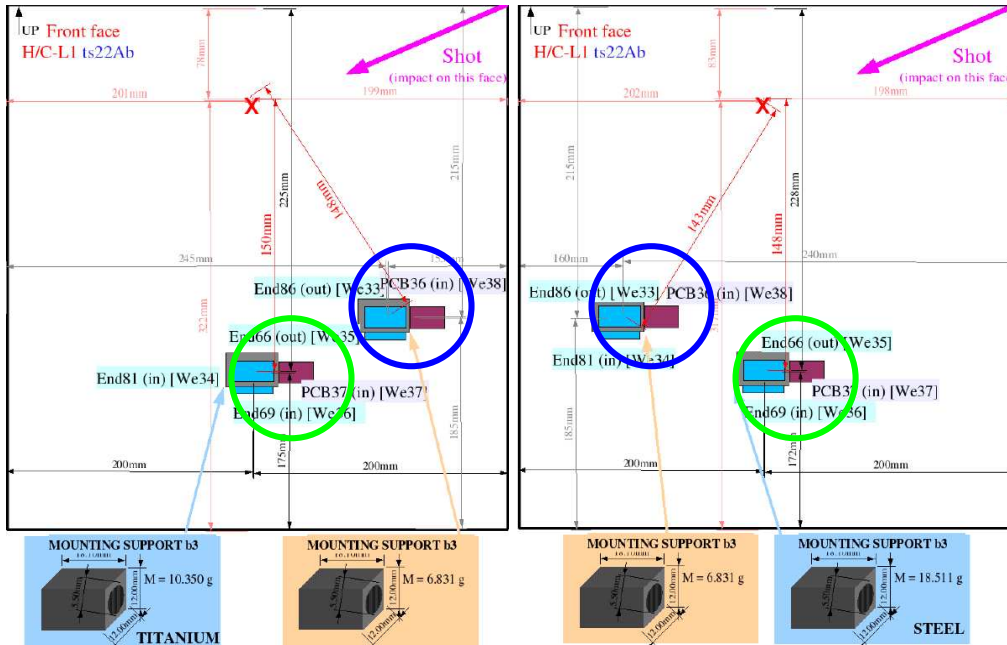
To assess this point, two tests were performed with on the configurations shown in Fig. 6-27. Impact conditions were nominally identical, i.e. dp=1.5mm launched at 5 km/s.

For shot no. 7595, the two mounting blocks were made of Al alloy (mass=6.8 grams, blue circle) and titanium alloy (mass=10.3 grams, green circle); for shot no. 7596, the two mounting blocks were made of Al alloy (mass=6.8 grams, blue circle) and steel (mass=18.5 grams, green circle).

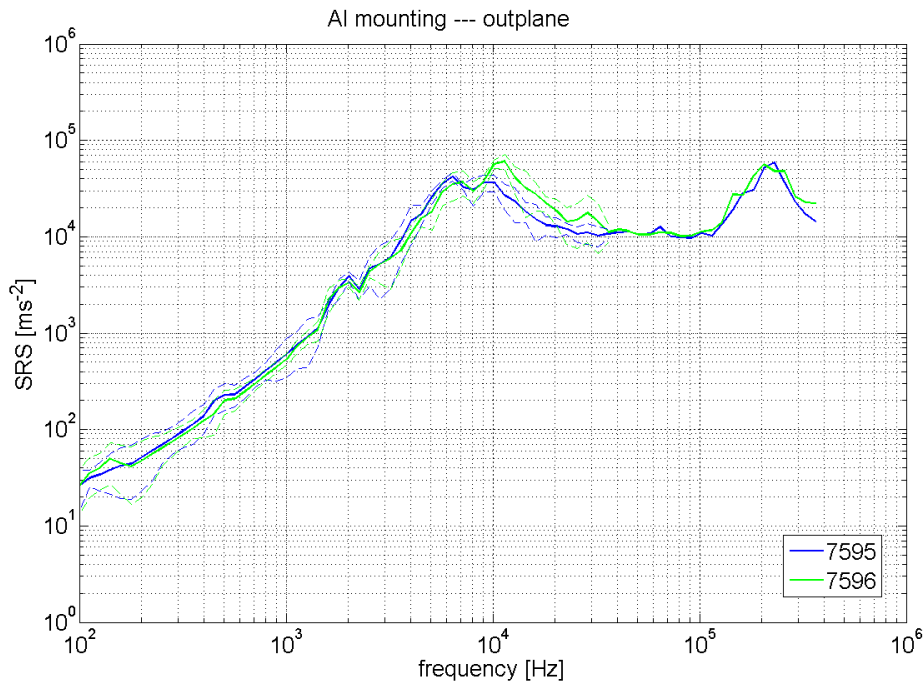
Two classes of comparisons were realised:

Between signals recorded by sensors mounted on homologous Al-alloy blocks (blue circles), to discover possible wave differences coming from different localized masses fixed away from the sensors location (see Fig. 6-28 and Fig. 6-29)

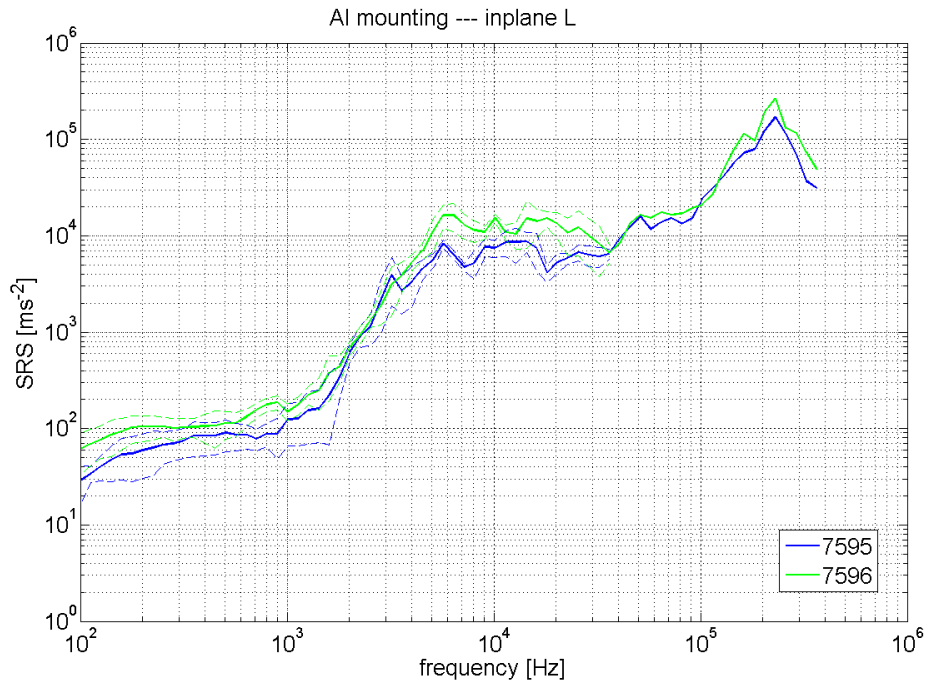
Between signals recorded by sensors mounted on different-mass blocks (green circles), to discover possible wave differences coming from different localized masses fixed collocated on the sensors location (see Fig. 6-30 and Fig. 6-31)



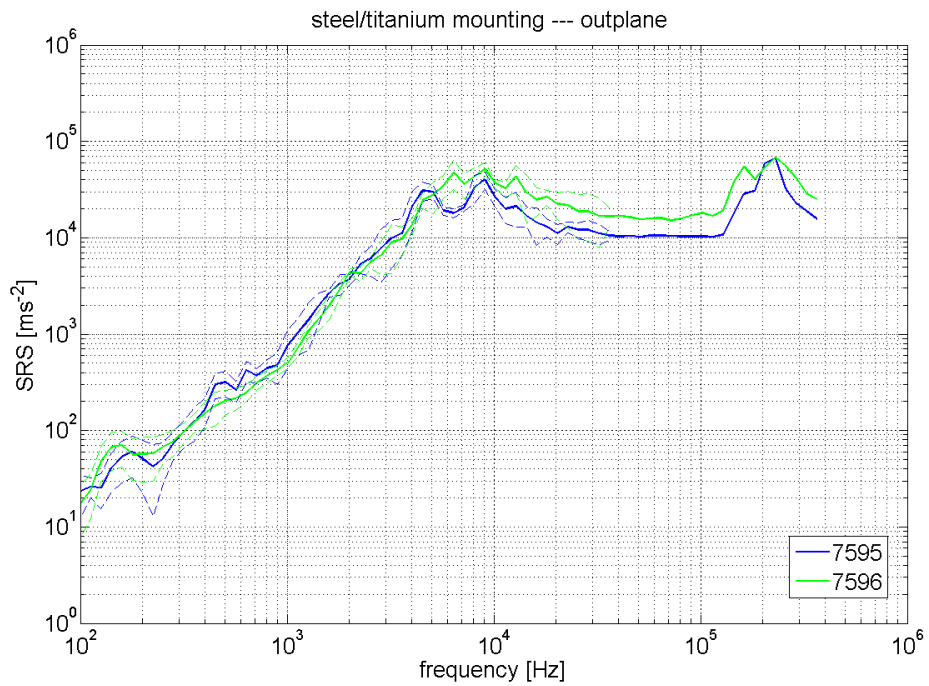
**Fig. 6-27. Targets configurations for TS227. Shot no. 7595 (right) and 7596 (left)**



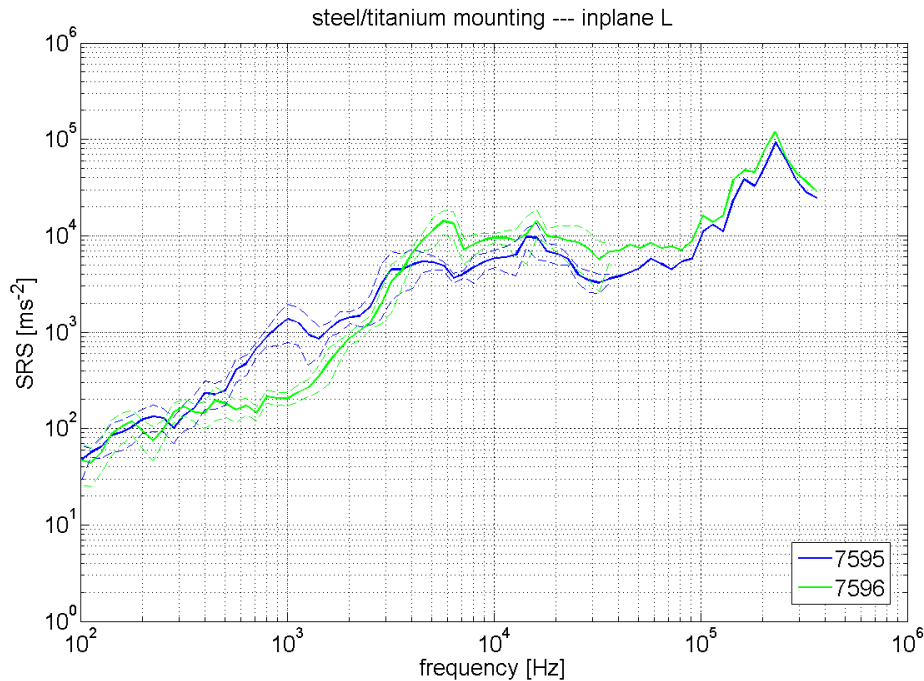
**Fig. 6-28. Load effects. Comparison between SRS from sensors mounted on blocks of same mass (blue circles in Fig. 6-27). Front size, out-plane**



**Fig. 6-29. Load effects. Comparison between SRS from sensors mounted on blocks of same mass (blue circles in Fig. 6-27). Front size, in-plane-longitudinal**



**Fig. 6-30. Load effects. Comparison between SRS from sensors mounted on blocks of same mass (green circles in Fig. 6-27). Front size, out-plane**



**Fig. 6-31. Load effects. Comparison between SRS from sensors mounted on blocks of same mass (green circles in Fig. 6-27). Front size, in-plane-longitudinal**

With the only exception visible in Fig. 6-31 (SRS discrepancies at frequencies around 1kHz, due to the bad SNR obtained at around 1 kHz for acquisition channel 36 during shot no. 7596; this information may be found on the detailed test report of the aforementioned test), it appears that load effects fall inside the uncertainty bands, considering the mass variation 6.8 - 18.5 grams for mounting blocks. This conclusion is obvious if we notice that the mass of mounting blocks were varied by around 1% of the target overall mass. Nevertheless, it must be kept in mind that the mass variation explored is representative of the maximum deviation of mass for the blocks used in the Study.

#### 6.1.2.5 Type of waves

CISAS ID	ESA ID TS-	dp [mm]	vp [km/s]	Coarse damage	Comments
7555	224/4	1.9	5.1	P	Test used also for TS224
7563	224/3	1.0	5.0	NP	Test used also for TS224

**Tab. 6-5. Test used for comparing the wave types**

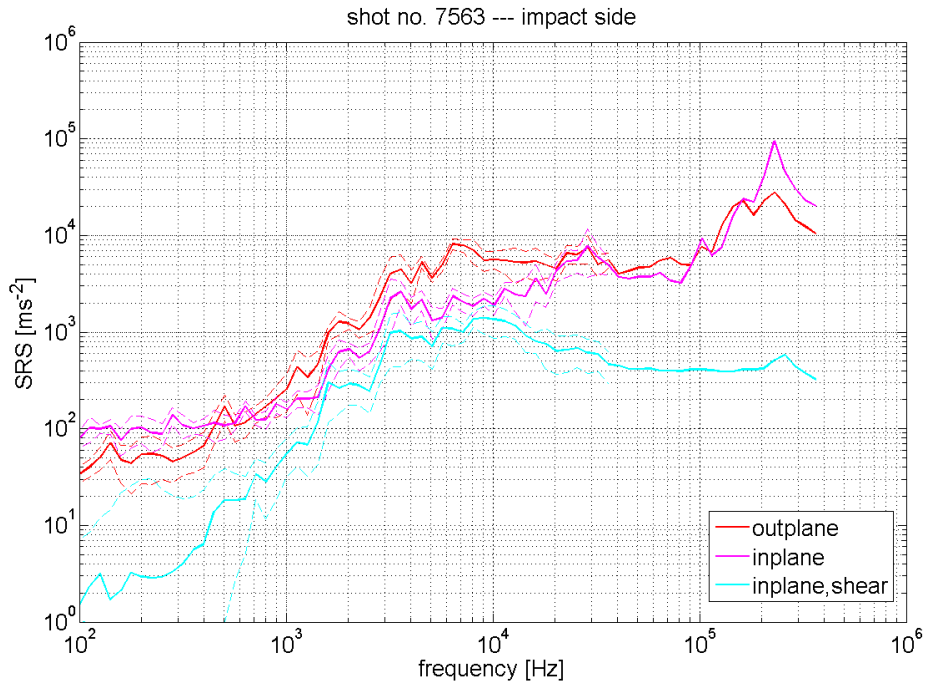
The two tests above were separately analyzed to acquire information on the different types of waves originating from a HVI. In particular, shot no. 7555 refers to an impact above BL and shot no. 7563 refers to an impact below BL.

For each of the two tests, the following comparisons were performed:

On front (impact) side, between out-plane, in-plane-longitudinal and in-plane-shear waves

On rear side, between out-plane, in-plane-longitudinal and in-plane-shear waves

Between out-plane waves recorded on the front and rear side of the target  
 (transmission through thickness)  
 Between in-plane-longitudinal waves recorded on the front and rear side of the target  
 (transmission through thickness)  
 Between in-plane-shear waves recorded on the front and rear side of the target  
 (transmission through thickness)  
 Type of waves below BL



**Fig. 6-32. Type of waves for dp=1mm (below BL). Impact side**



**Fig. 6-33. Type of waves for dp=1mm (below BL). Rear side**

A first comparison can be done looking at Fig. 6-32 and Fig. 6-33, which refer to the three wave directions on the front and rear target side, respectively.

For the front side (Fig. 6-32), it appears that:

Between  $10^2$  and  $\sim 4 \cdot 10^3$  Hz, the SRS of out-plane and in-plane-longitudinal waves are compatible, both rising from  $\sim 10^2$  to  $\sim 3 \cdot 10^3$   $\text{ms}^{-2}$ .

Between  $\sim 4 \cdot 10^3$  and  $\sim 2 \cdot 10^4$  Hz, the SRS of OP waves becomes higher than that of IP-L waves. They reach respectively  $\sim 8 \cdot 10^3$   $\text{ms}^{-2}$  and  $\sim 5 \cdot 10^3$   $\text{ms}^{-2}$ .

Between  $\sim 2 \cdot 10^4$  Hz and  $\sim 2 \cdot 10^5$  Hz, the SRS of OP and IP-L waves become again compatible, rising up to  $\sim 10^5$   $\text{ms}^{-2}$  at  $\sim 2 \cdot 10^5$  Hz

The SRS of in-plane-shear waves is lower than that of OP and IP-L at all frequency, ranging from  $< 10$   $\text{ms}^{-2}$  at  $10^2$  Hz to  $\sim 10^3$   $\text{ms}^{-2}$  at  $10^4$  Hz.

For the rear side (Fig. 6-32), it appears that:

Between  $10^2$  and  $\sim 4 \cdot 10^3$  Hz, the SRS of OP and IP-L waves are compatible, both rising from  $\sim 10^2$  to  $\sim 3 \cdot 10^3$   $\text{ms}^{-2}$ .

Between  $\sim 4 \cdot 10^3$  and  $\sim 2 \cdot 10^4$  Hz, the SRS of OP waves becomes higher than that of IP-L waves. They reach respectively  $\sim 8 \cdot 10^3$   $\text{ms}^{-2}$  and  $\sim 5 \cdot 10^3$   $\text{ms}^{-2}$ .

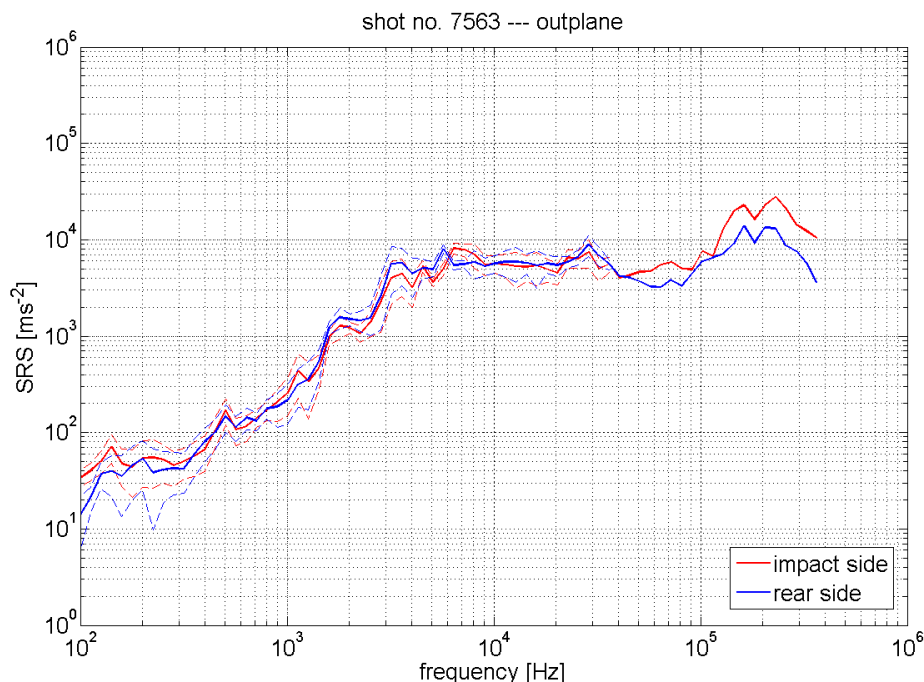
Between  $\sim 2 \cdot 10^4$  Hz and  $\sim 2 \cdot 10^5$  Hz, the SRS of OP and IP-L waves become again compatible, rising up to  $\sim 2 \cdot 10^5$   $\text{ms}^{-2}$  at  $\sim 2 \cdot 10^5$  Hz

Between  $10^2$  and  $\sim 2 \cdot 10^3$  Hz, the SRS of IP-S waves is lower than that of OP and IP-L, ranging from  $< 10$   $\text{ms}^{-2}$  at  $10^2$  Hz to  $\sim 3 \cdot 10^2$   $\text{ms}^{-2}$  at  $2 \cdot 10^3$  Hz.

Between  $2 \cdot 10^3$  Hz and  $10^4$  Hz, the SRS of IP-S becomes compatible to that of IP-L

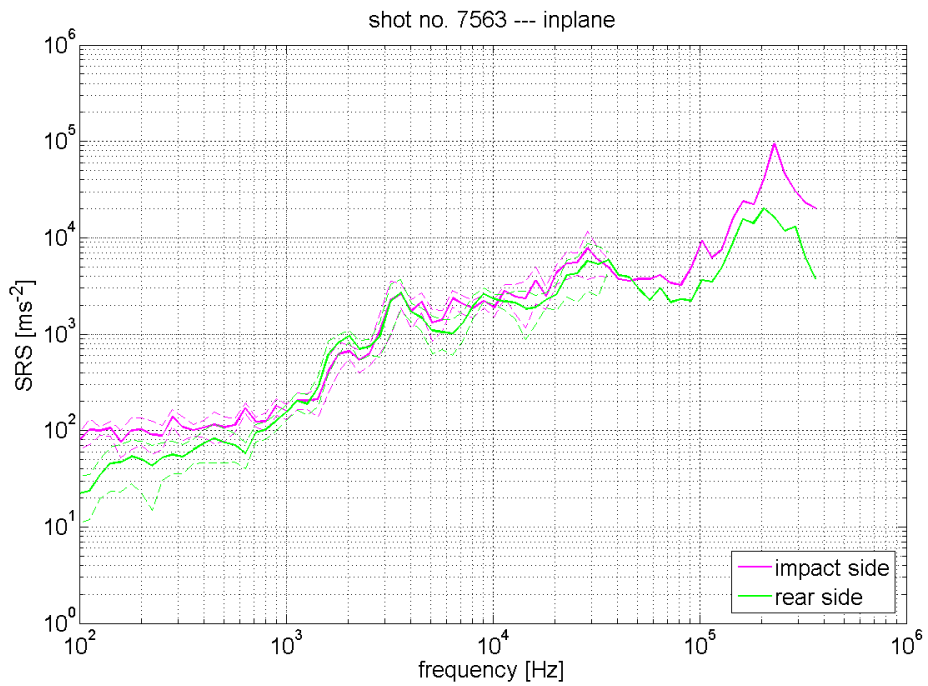
The following Fig. 6-34, Fig. 6-35 and Fig. 6-36 compares the SRS of the same type of wave (OP, IP-L and IP-S), between front and rear side. It may be observed that no significant difference results for each wave type through the target thickness.

Nevertheless, even though it is inside the uncertainty band, a trend may be observed for the IP-S: above  $10^3$  Hz, the SRS on rear side remains systematically above its front-side counterpart.

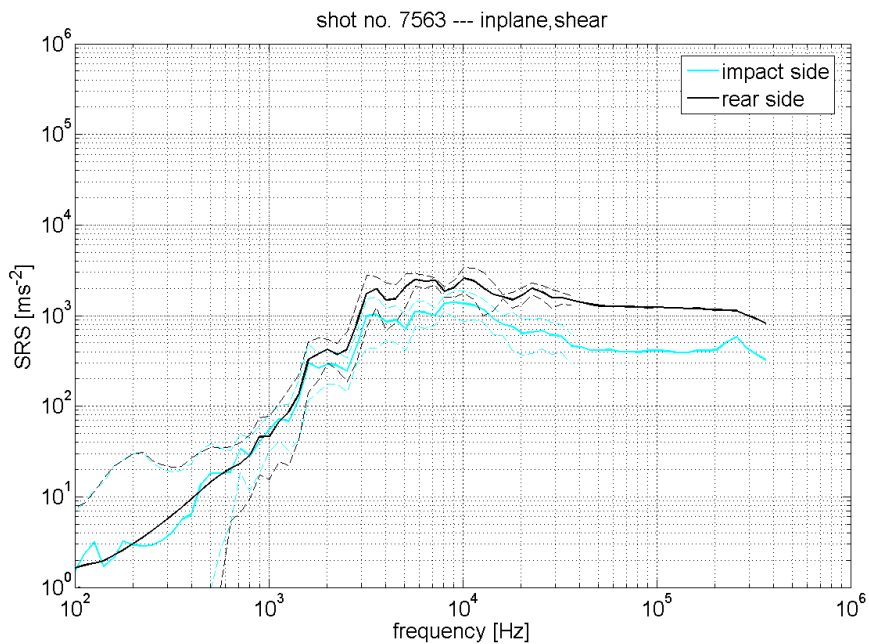




**Fig. 6-34. Out-plane waves for  $dp=1\text{mm}$  (below BL). Comparison between impact side and rear side**

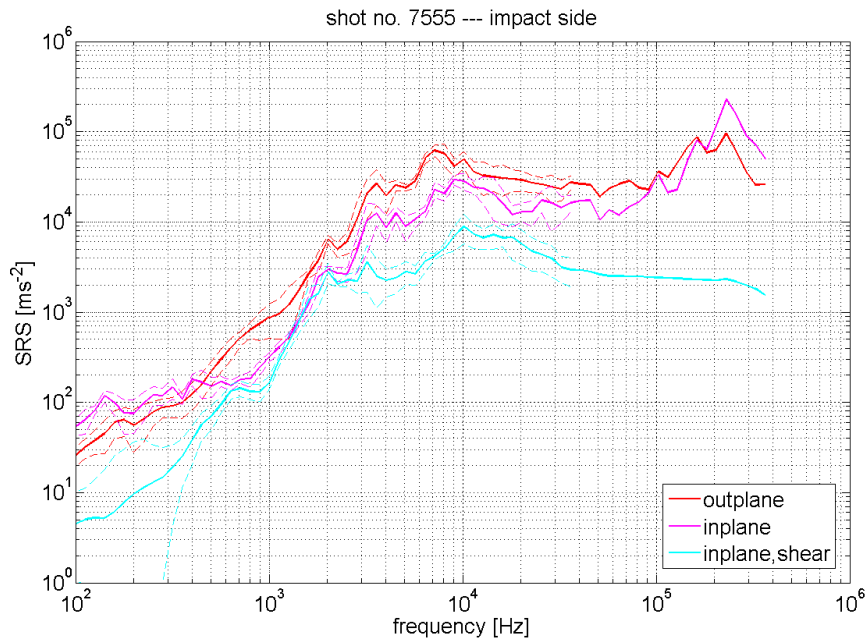


**Fig. 6-35. In-plane-longitudinal waves for  $dp=1\text{mm}$  (below BL). Comparison between impact side and rear side**

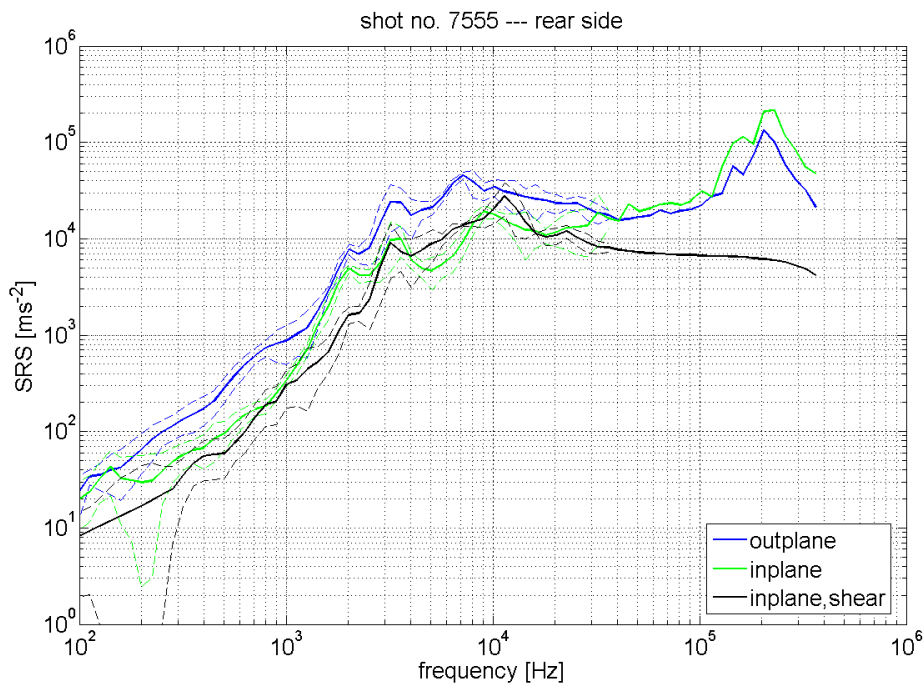


**Fig. 6-36. In In-plane-shear waves for  $dp=1\text{mm}$  (below BL). Comparison between impact side and rear side**

Type of waves above BL



**Fig. 6-37. Type of waves for dp=1.9mm (above BL). Impact side**



**Fig. 6-38. Type of waves for dp=1.9mm (above BL). Rear side**

A first comparison can be done looking at Fig. 6-37 and Fig. 6-38, which refer to the three wave directions on the front and rear target side, respectively.

For the front side (Fig. 6-37), it appears that:

Between  $10^2$  and  $\sim 4 \cdot 10^3$  Hz, the SRS of OP and IP-L waves are compatible, both rising from  $<10^2$  to  $\sim 2 \cdot 10^4$   $\text{ms}^{-2}$ . The only exception occurs around  $10^3$  Hz, where the IP-L SRS is lower than the OP SRS. This anomaly may be explained by noticing that the

original signal for IP-L is affected by a low SNR (see the complete test report for details)

Between  $\sim 4 \cdot 10^3$  Hz and  $\sim 10^4$  Hz, the SRS of OP waves becomes higher than that of IP-L waves. They reach respectively  $\sim 6 \cdot 10^4$   $\text{ms}^{-2}$  and  $\sim 3 \cdot 10^4$   $\text{ms}^{-2}$ .

Between  $\sim 10^4$  Hz and  $\sim 2 \cdot 10^5$  Hz, the SRS of OP and IP-L waves become again compatible, rising up to  $\sim 2 \cdot 10^5$   $\text{ms}^{-2}$  at  $\sim 2 \cdot 10^5$  Hz

Considering the anomaly of the IP-L signal at  $\sim 10^3$  Hz, the SRS of IP-S waves is lower than that of OP and IP-L at all frequency, ranging from  $< 10$   $\text{ms}^{-2}$  at  $10^2$  Hz to  $\sim 10^4$   $\text{ms}^{-2}$  at  $10^4$  Hz.

For the rear side (Fig. 6-38), it appears that:

Between  $10^2$  and  $\sim 4 \cdot 10^3$  Hz, the SRS of OP and IP-L waves are compatible, both rising from  $< 10^2$  to  $\sim 10^4$   $\text{ms}^{-2}$ . Again, an anomaly may be observed at  $\sim 10^3$  Hz, which may be explained as before

Between  $\sim 4 \cdot 10^3$  Hz and  $\sim 10^4$  Hz, the SRS of OP waves becomes higher than that of IP-L waves. They reach respectively  $\sim 4 \cdot 10^4$   $\text{ms}^{-2}$  and  $\sim 2 \cdot 10^4$   $\text{ms}^{-2}$ .

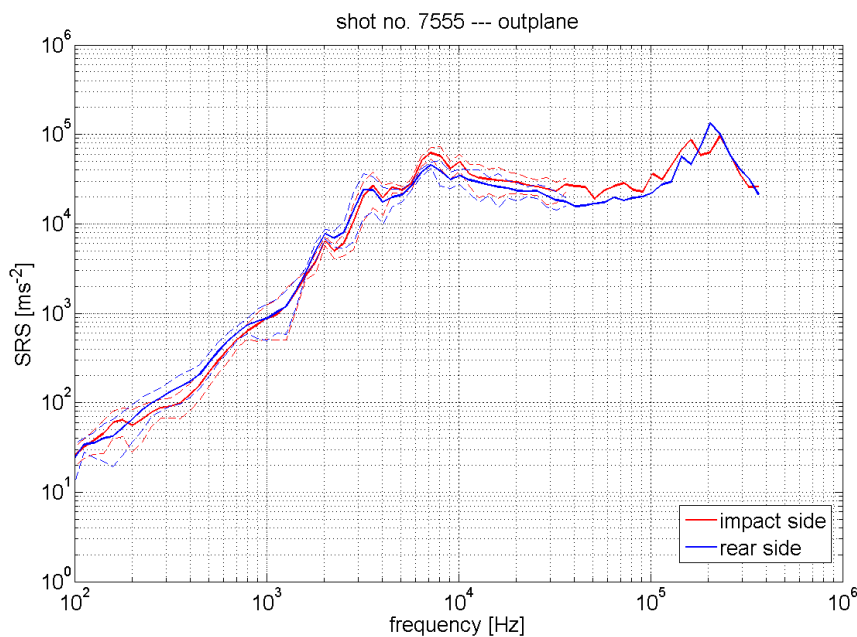
Between  $\sim 10^4$  and  $\sim 2 \cdot 10^5$  Hz, the SRS of OP and IP-L waves become again compatible, rising up to  $\sim 2 \cdot 10^5$   $\text{ms}^{-2}$  at  $\sim 2 \cdot 10^5$  Hz

Between 100 and 3000 Hz, the SRS of IP-S waves is lower than that of OP and IP-L, ranging from  $\sim 10$   $\text{ms}^{-2}$  at  $10^2$  Hz to  $\sim 10^4$   $\text{ms}^{-2}$  at  $3 \cdot 10^3$  Hz.

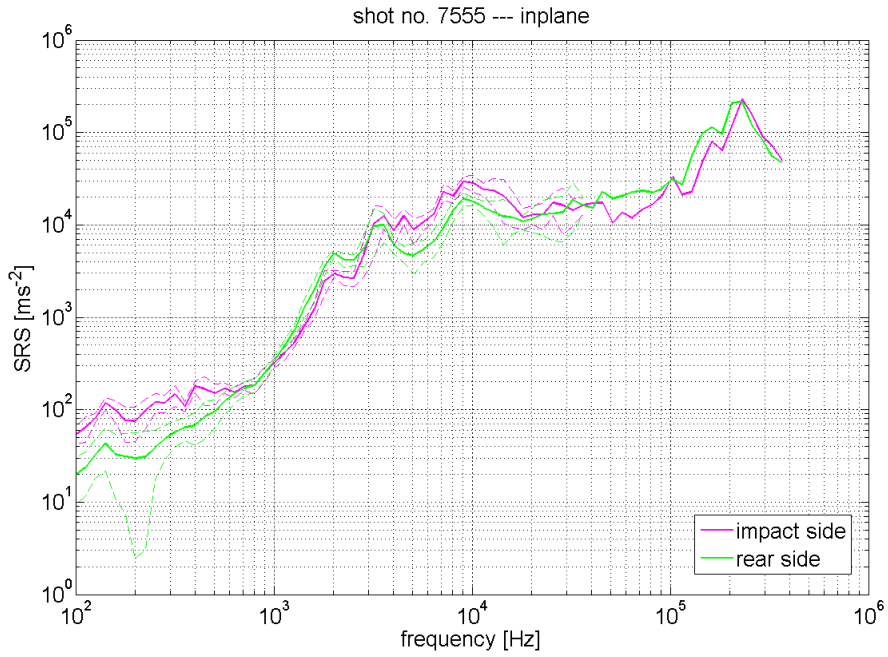
Between  $3 \cdot 10^3$  Hz and  $10^4$  Hz, the SRS of IP-S becomes compatible to that of IP-L

The following Fig. 6-39, Fig. 6-40 and Fig. 6-41 compares the SRS of the same type of wave (OP, IP-L and IP-S), between front and rear side. It may be observed that no significant difference results for OP and IP-L waves through the target thickness.

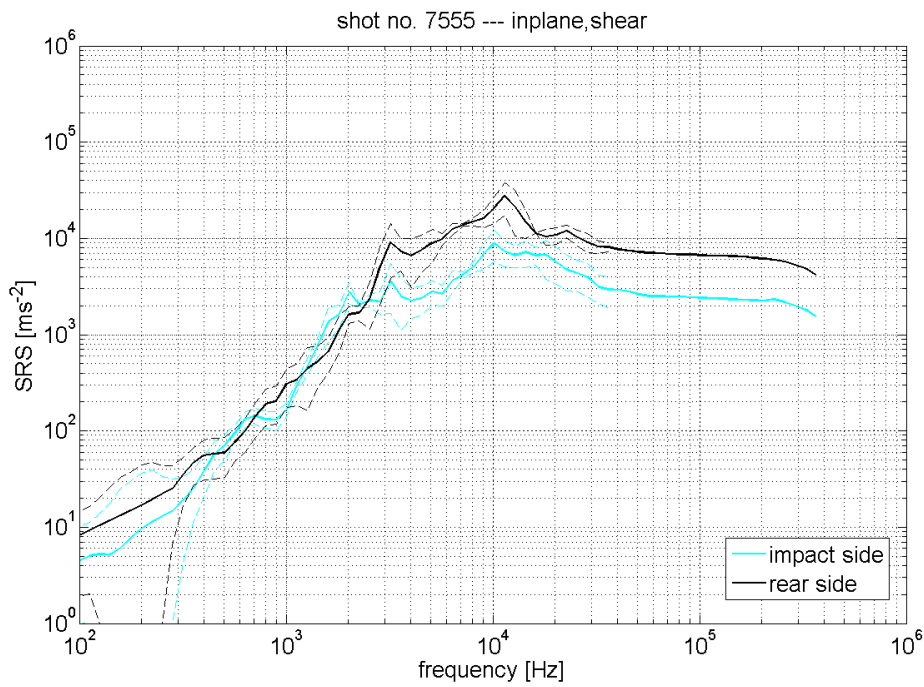
On the other hand, the same trend evidenced below BL may be observed for the IP-S: above  $2 \cdot 10^3$  Hz, the SRS on rear side remains systematically above its front-side counterpart. Since such effect becomes evident in tests above BL, it can be argued that it is related to the impact damage inside the HC core.



**Fig. 6-39. Out-plane waves for  $dp=1.9\text{mm}$  (above BL). Comparison between impact side and rear side**



**Fig. 6-40. In-plane-longitudinal waves for  $d_p=1.9\text{mm}$  (above BL). Comparison between impact side and rear side**



**Fig. 6-41. In-plane-shear waves for  $d_p=1.9\text{mm}$  (above BL). Comparison between impact side and rear side**

### 6.1.2.6 Effects of projectile mass (TS221 and TS223)

CISAS ID	ESA ID TS-	dp [mm]	vp [km/s]	Coarse damage	Comments
7555	224/4 221/11	1.9	4.9	P	Test used also for TS227
7564	221/1 224/1	1.0	4.9	NP	Test used also for TS224
7566	221/4 224/2	1.9	4.8	P	Test used also for TS224
7567	221/2	0.8	4.7	NP	None
7568	221/3	1.5	5.0	BL<=	None
7569	221/10	0.8	3.8	NP	None
7572	221/7	1.9	4.0	P	None
7573	221/6	1.5	3.8	BL<=	None
7574	221/8	2.3	4.4	P	None
7575	221/5	1.0	4.0	NP	Test used also for TS221
7576	221/9 223/1	2.3	5.1	P	Test used also for TS223

**Tab. 6-6. Summary of TS221 and 223**

The evaluation of the influence of projectile mass (momentum) on wave properties was done by launching 0.8, 1.0, 1.5, 1.9 and 2.3 mm projectiles at two different velocities, i.e. 4 and 5 km/s. Therefore, two different sets of results may be presented (paragraphs 6.1.2.6.1 and 6.1.2.6.2).

The mass of selected projectiles is reported in Tab. 6-7.

dp [mm]	mp [mg]	Mass (momentum) ratio
0.8	0.7	0.5
1	1.4	1.0
1.5	4.8	3.4
1.9	9.7	6.9
2.3	17.2	12.2

**Tab. 6-7. Projectiles mass and mass ratio (referred to dp=1mm)**

It is clear that each increasing step for dp roughly corresponds to a mass doubling (except for the step 1.0 mm  $\Rightarrow$  1.5 mm). Since the impact speed is nominally constant, this means that each increasing step for dp roughly corresponds to a momentum doubling.

Therefore, if we make the hypothesis that a linear momentum scaling exists for SRS, the curves should be equally spaced in the logarithmic plot. From the following figures, it appears that this is not true.

Hence, a linear momentum scaling does not hold for SRS.

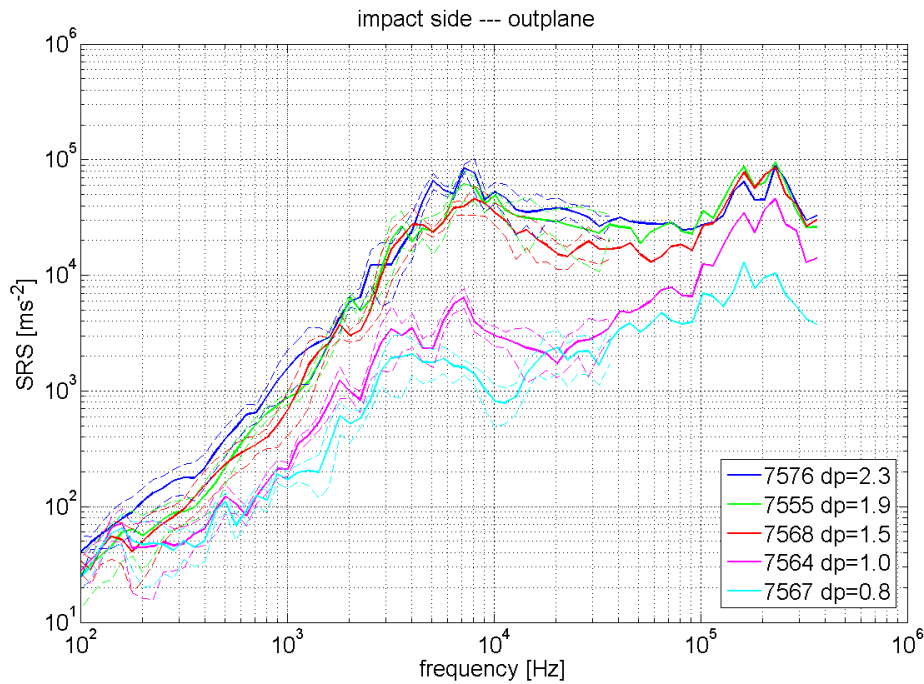
Rather, the SRS dependence from momentum appears to vary with frequency:

in the low-frequency range of the spectrum (below  $\sim 2 \cdot 10^3$  Hz), SRS are almost unchanged, indicating that small projectiles transfer momentum to targets in a more efficient way than large projectiles

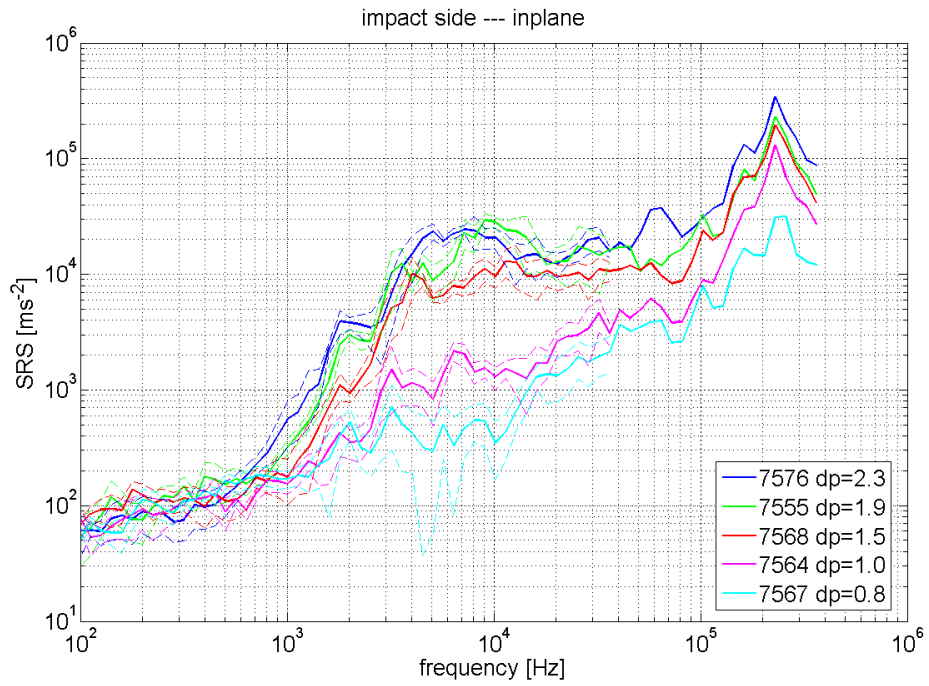
at frequency greater than  $\sim 2 \cdot 10^3$  Hz, SRS increase steeply from below to above BL, indicating that the momentum transferred to targets is nearly linearly dependent from the mass of impacting particle.

Previous observations emerge from plots of the SRS normalized by the projectile momentum (see for instance Fig. 6-48 and Fig. 6-49, referring to impact side IP-L and OP, 5 km/s tests).

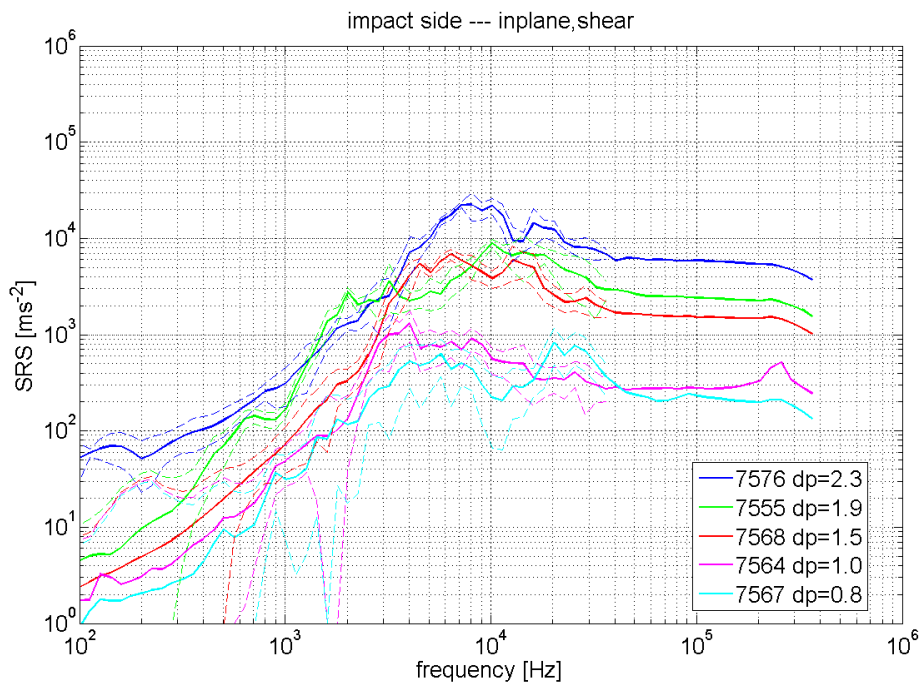
#### 6.1.2.6.1 Effect of projectile mass at 5 km/s



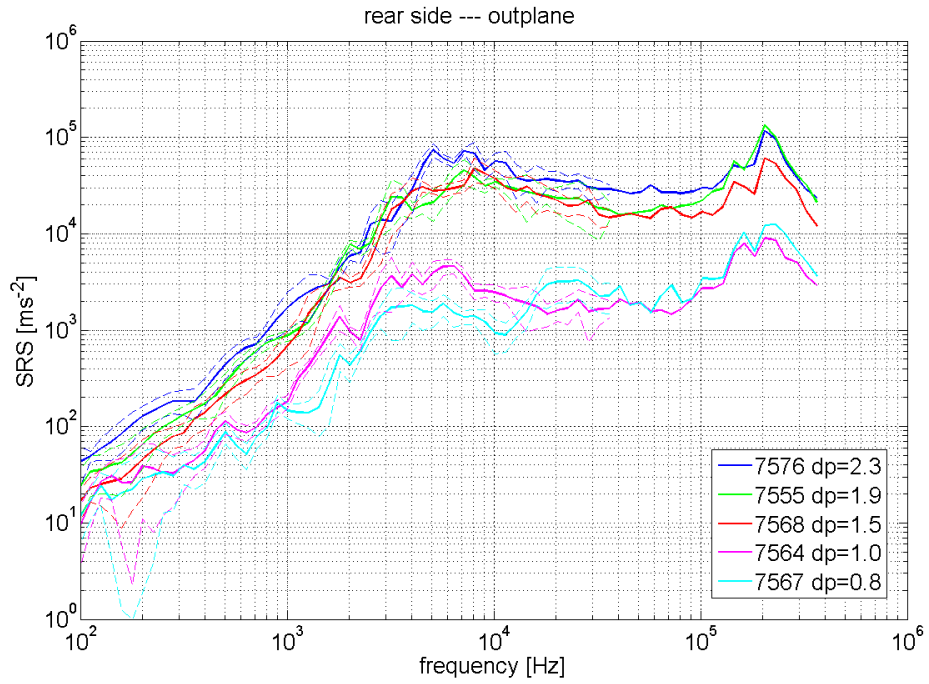
**Fig. 6-42. Effects of projectile mass at 5 km/s. Impact side, out-plane**



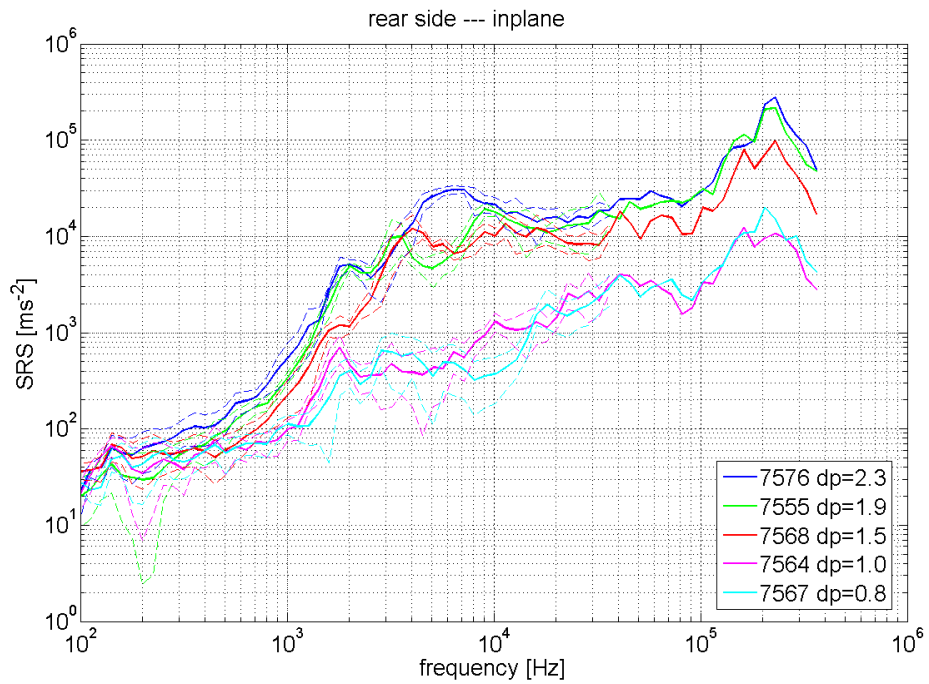
**Fig. 6-43. Effects of projectile mass at 5 km/s. Impact side, in-plane-longitudinal**



**Fig. 6-44. Effects of projectile mass at 5 km/s. Impact side, in-plane-shear**

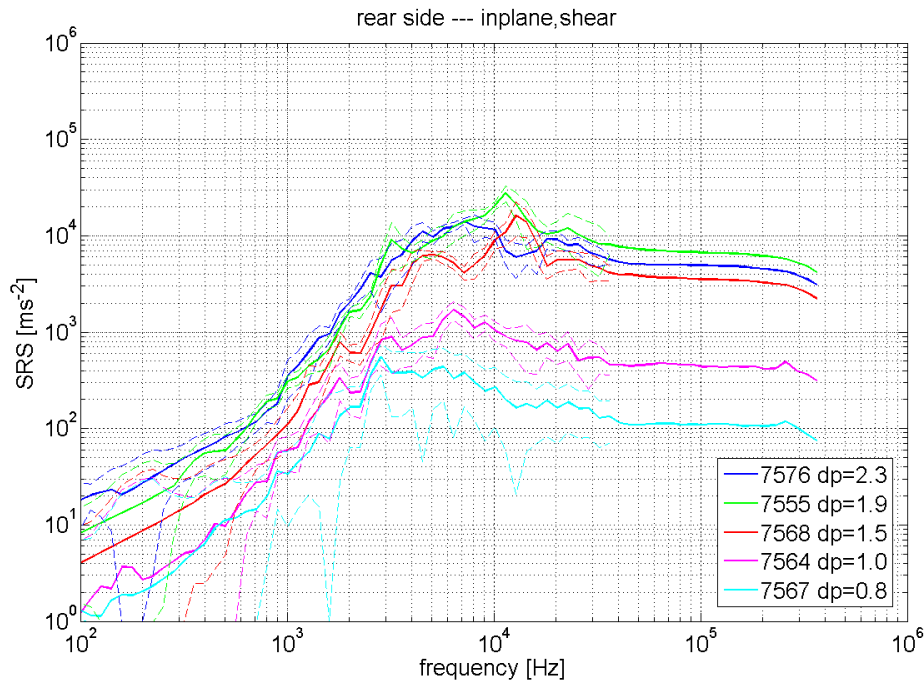


**Fig. 6-45. Effects of projectile mass at 5 km/s. Rear side, out-plane**



**Fig. 6-46. Effects of projectile mass at 5 km/s. Rear side, in-plane-longitudinal**





**Fig. 6-47. Effects of projectile mass at 5 km/s. Rear side, in-plane-shear**

For the front side (Fig. 6-42 to Fig. 6-44), it can be observed that the SRS of all types of wave increases with increasing dp. Nevertheless, some differences may be observed between OP, IP-L and IP-S:

#### OP waves

For tests above BL, the SRS are systematically higher than those for tests below BL, in the whole frequency range

the difference between SRS from P and NP experiments becomes significant above  $\sim 5 \cdot 10^2$  Hz.

For tests above BL, the SRS rise up to  $\sim 8 \cdot 10^4$   $\text{ms}^{-2}$  at  $\sim 7 \cdot 10^3$  Hz (dp=2.3 mm); for tests below BL, the SRS up to  $\sim 2 \cdot 10^3$   $\text{ms}^{-2}$  at  $\sim 7 \cdot 10^3$  Hz (dp=0.8 mm)

#### IP-L waves

For frequency below  $10^3$  Hz, the SRS from all tests are compatible, indicating that IP-L waves are not influenced by projectiles mass in this low frequency range

Above  $10^3$  Hz, the SRS from tests above BL are systematically higher than those for tests below BL

For tests above BL, the SRS rise up to  $\sim 3 \cdot 10^4$   $\text{ms}^{-2}$  at  $\sim 8 \cdot 10^3$  Hz (dp=2.3 mm); for tests below BL, the SRS up to  $\sim 5 \cdot 10^2$   $\text{ms}^{-2}$  at  $\sim 7 \cdot 10^3$  Hz (dp=0.8 mm)

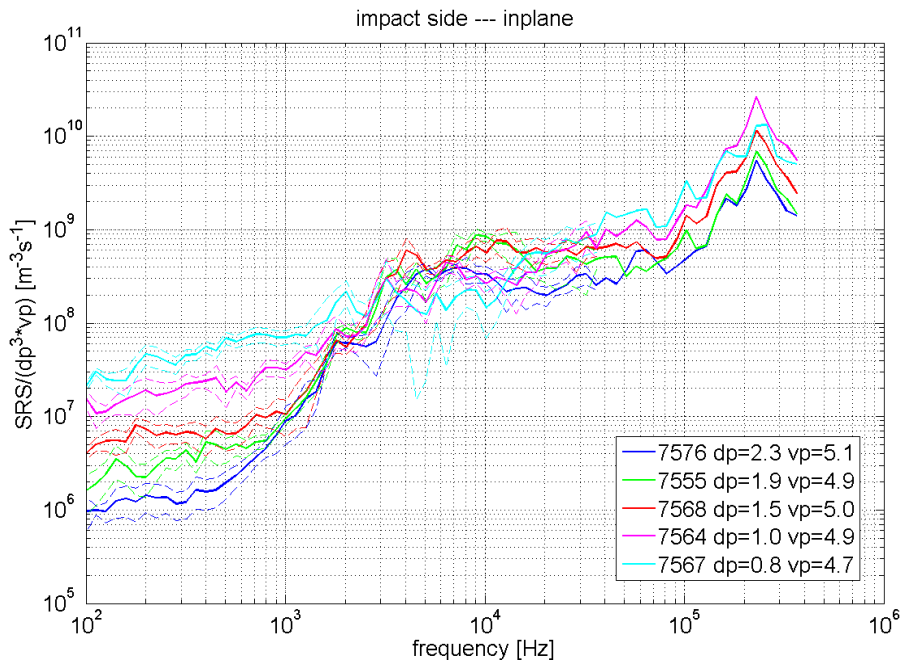
#### IP-S waves

For tests above BL, the SRS are systematically higher than those for tests below BL, in the whole frequency range

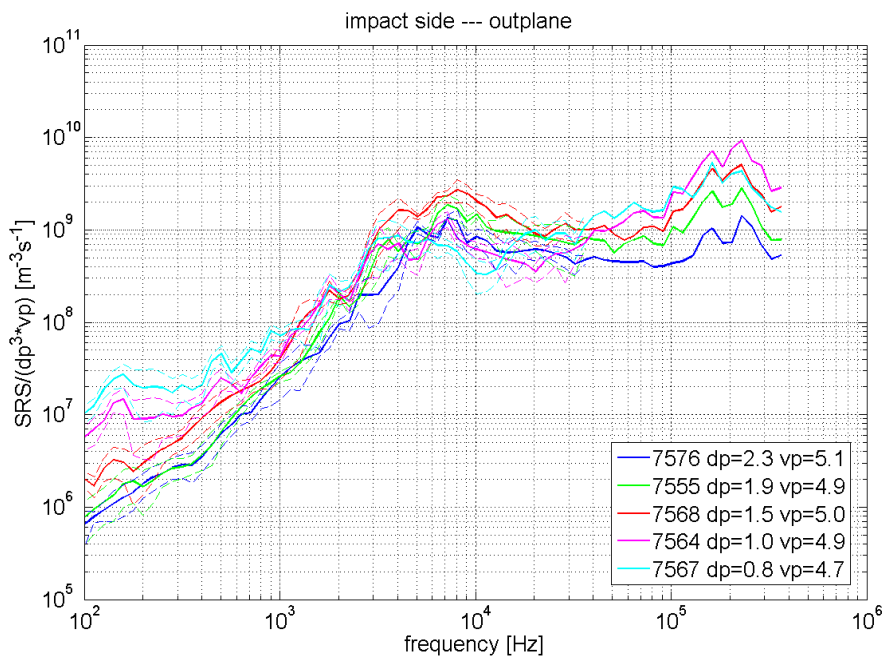
the difference between SRS from P and NP experiments becomes significant above  $\sim 10^3$  Hz.

For tests above BL, the SRS rise up to  $\sim 3 \cdot 10^4$   $\text{ms}^{-2}$  at  $\sim 7 \cdot 10^3$  Hz (dp=2.3 mm); for tests below BL, the SRS up to  $\sim 5 \cdot 10^2$   $\text{ms}^{-2}$  at  $\sim 7 \cdot 10^3$  Hz (dp=0.8 mm)

Similar observations can be made for the SP rear side, confirming that there is no significant difference between the two faces (Fig. 6-50 to Fig. 6-52).

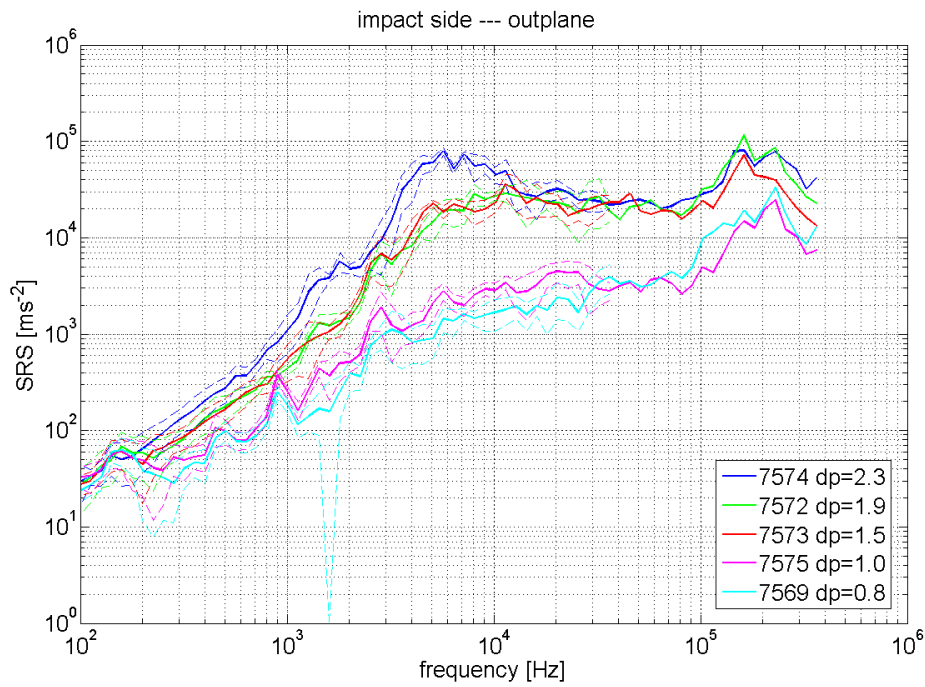


**Fig. 6-48. Effects of projectile mass at 5 km/s. Impact side, in-plane. SRS are normalized by the projectile momentum**

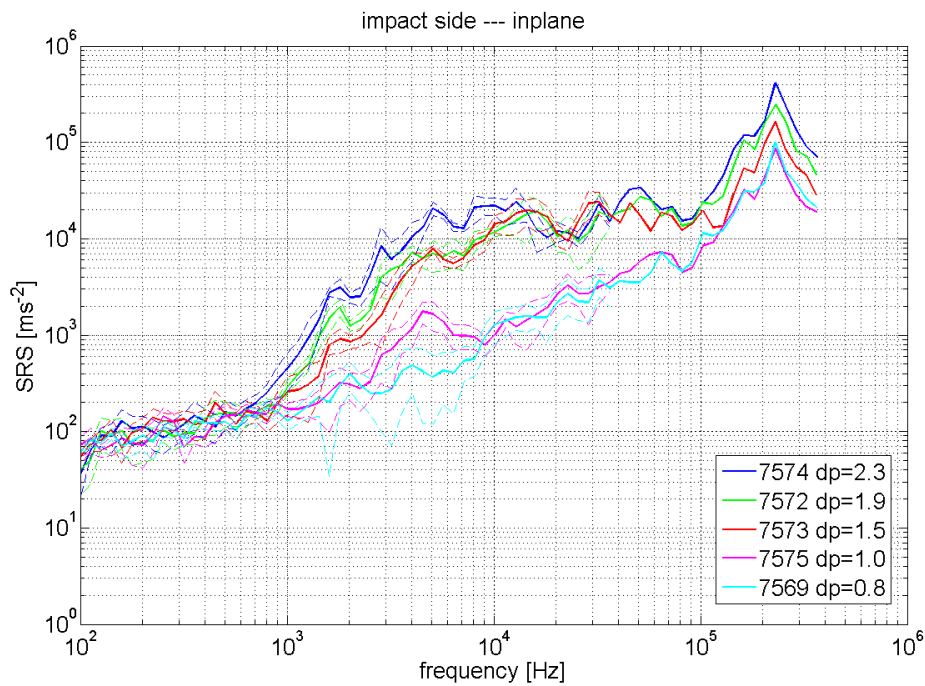


**Fig. 6-49. Effects of projectile mass at 5 km/s. Impact side, out-plane. SRS are normalized by the projectile momentum**

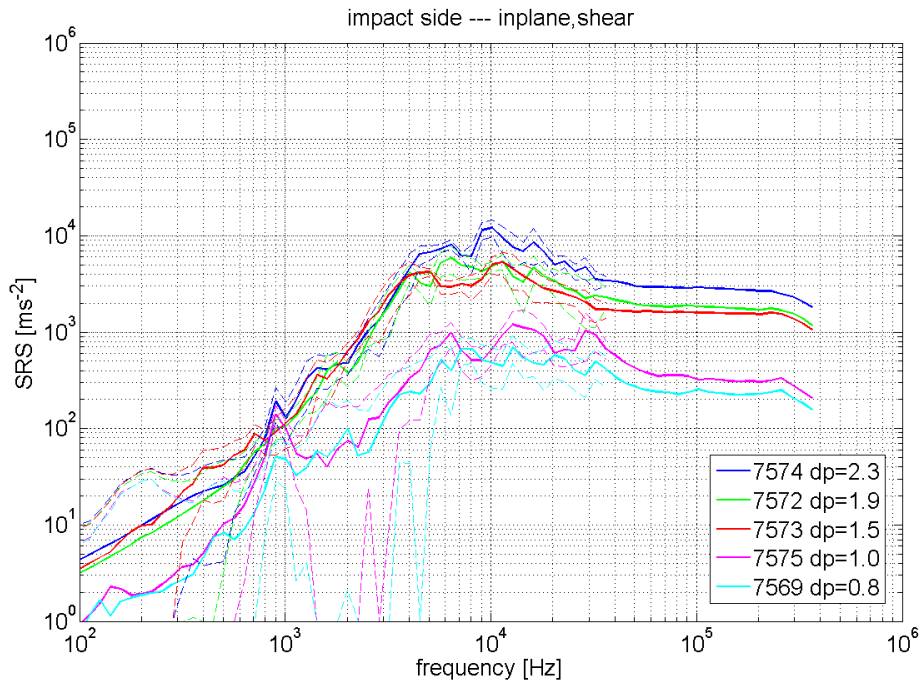
### 6.1.2.6.2 Effect of projectile mass at 4 km/s



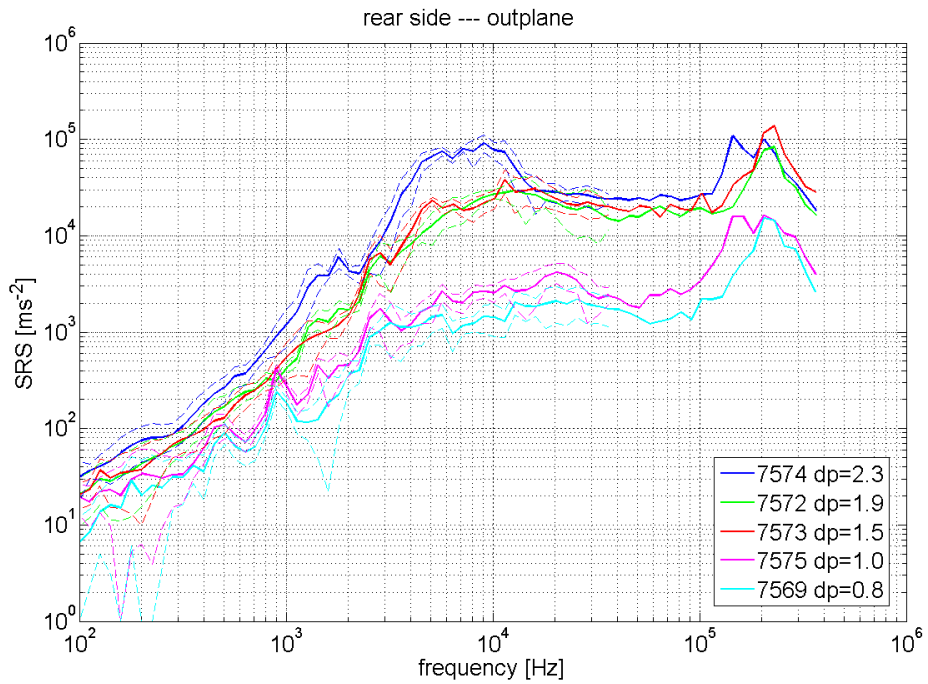
**Fig. 6-50. Effects of projectile mass at 4 km/s. Impact side, out-plane**



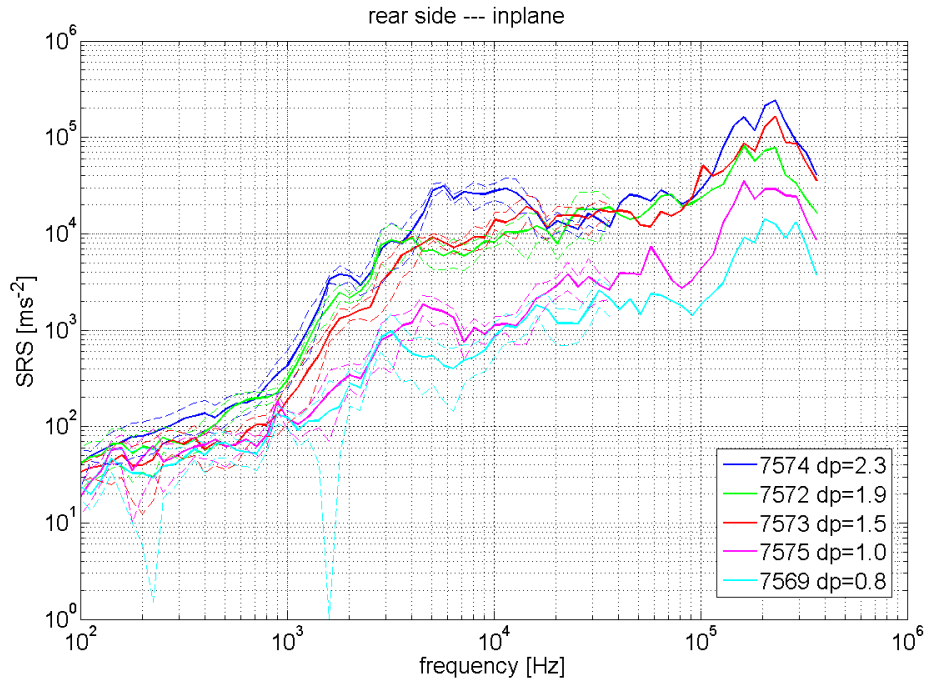
**Fig. 6-51. Effects of projectile mass at 4 km/s. Impact side, in-plane-longitudinal**



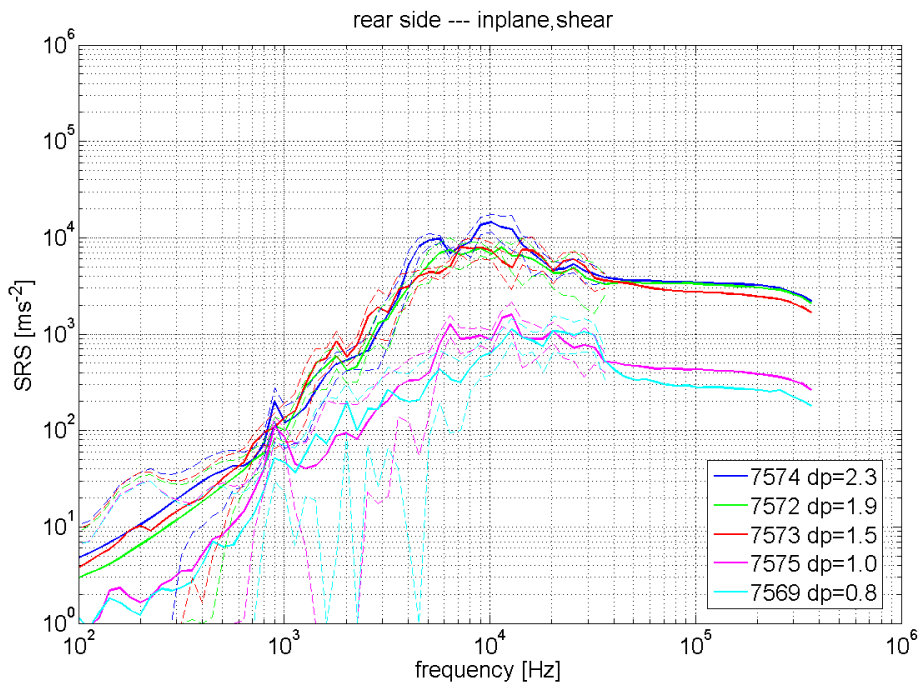
**Fig. 6-52. Effects of projectile mass at 4 km/s. Impact side, in-plane-shear**



**Fig. 6-53. Effects of projectile mass at 4 km/s. Rear side, out-plane**



**Fig. 6-54. Effects of projectile mass at 4 km/s. Rear side, in-plane-longitudinal**



**Fig. 6-55. Effects of projectile mass at 4 km/s. Rear side, in-plane-shear**

For the front side (Fig. 6-50 to Fig. 6-52), it can be observed that the SRS of all types of wave increases with increasing dp. Nevertheless, some differences may be observed between OP, IP-L and IP-S:

### OP waves

For tests above BL, the SRS are systematically higher than those for tests below BL, in the whole frequency range

The difference between SRS from P and NP experiments becomes significant above  $\sim 10^3$  Hz.

For tests above BL, the SRS rise up to  $\sim 8 \cdot 10^4 \text{ ms}^{-2}$  at  $\sim 7 \cdot 10^3$  Hz ( $dp=2.3$  mm); for tests below BL, the SRS up to  $\sim 2 \cdot 10^3 \text{ ms}^{-2}$  at  $\sim 10^4$  Hz ( $dp=0.8$  mm)

### IP-L waves

For frequency below  $10^3$  Hz, the SRS from all tests are compatible, indicating that IP-L waves are not influenced by projectiles mass in this low frequency range

Above  $10^3$  Hz, the SRS from tests above BL are systematically higher than those for tests below BL

For tests above BL, the SRS rise up to  $\sim 2 \cdot 10^4 \text{ ms}^{-2}$  at  $\sim 8 \cdot 10^3$  Hz ( $dp=2.3$  mm); for tests below BL, the SRS up to  $\sim 10^3 \text{ ms}^{-2}$  at  $\sim 10^4$  Hz ( $dp=0.8$  mm)

### IP-S waves

For tests above BL, the SRS are systematically higher than those for tests below BL, in the whole frequency range

The difference between SRS from P and NP experiments becomes significant above  $\sim 10^3$  Hz.

For tests above BL, the SRS rise up to  $\sim 10^4 \text{ ms}^{-2}$  at  $\sim 10^4$  Hz ( $dp=2.3$  mm); for tests below BL, the SRS up to  $\sim 5 \cdot 10^2 \text{ ms}^{-2}$  at  $\sim 10^4$  Hz ( $dp=0.8$  mm)

Similar observations can be made for the SP rear side, confirming that there is no significant difference from the two faces (Fig. 6-53 to Fig. 6-55).

## **6.1.2.7 Effects of impact velocity (TS221 and TS222)**

<b>CISAS ID</b>	<b>ESA ID TS-</b>	<b>dp [mm]</b>	<b>vp [km/s]</b>	<b>Coarse damage</b>	<b>Comments</b>
7563	222/1 224/3	1.0	5.0	NP	Test used also for TS224
7564	222/2 221/1 224/1	1.0	4.9	NP	Test used also for TS221 and TS224
7575	222/3 221/5	1.0	4.0	NP	Test used also for TS221
7577	222/4	1.0	3.2	NP	None
7581	222/5	1.0	3.6	NP	None
7590	222/6	1.0	3.0	NP	None

**Tab. 6-8. Summary of TS221 and 223**

The evaluation of the projectile speed on wave properties was done by comparing tests results obtained from launching 1.0 mm projectiles between 2.8 and 5 km/s.

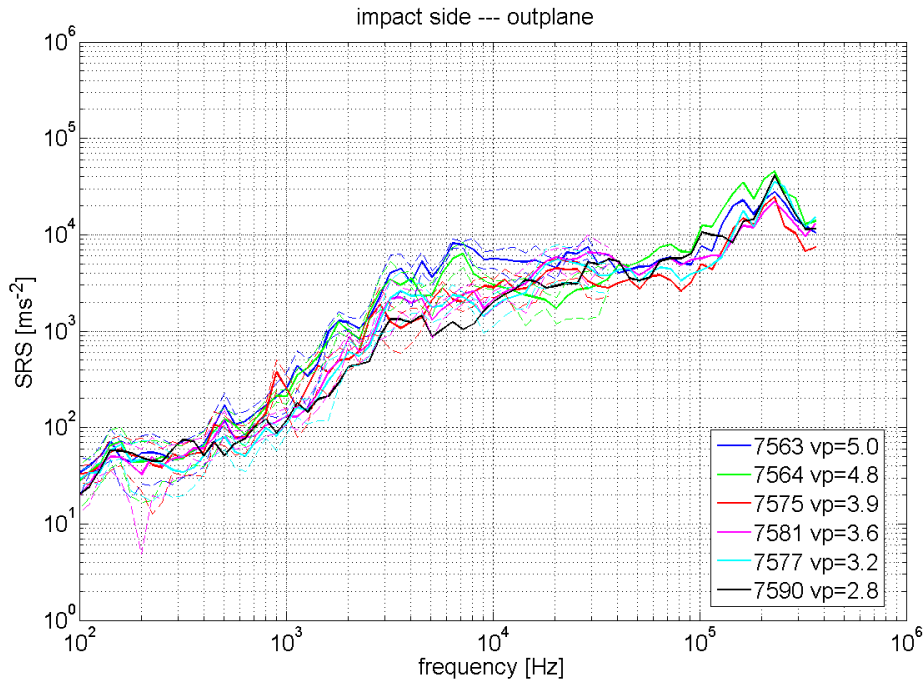
The resulting variation of projectiles velocity (momentum) is reported in Tab. 6-9.

CISAS ID	vp [km/s]	Velocity (momentum) ratio
7590	2.8	1.0
7577	3.2	1.1
7581	3.6	1.3
7575	3.9	1.4
7564	4.8	1.7
7563	5.0	1.8

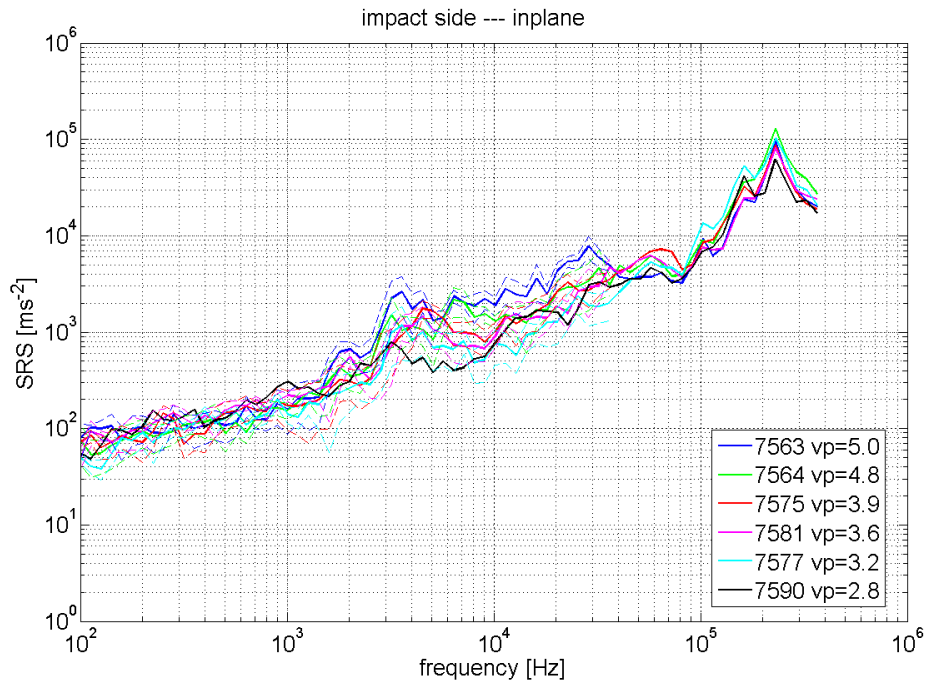
**Tab. 6-9. Projectiles mass and mass ratio (referred to vp=2.8 km/s)**

It is clear that the range of momentum spanned by varying the impact speed is considerably smaller than that spanned by varying the projectile diameter. This justifies the less significant differences between SRS plotted from Fig. 6-56 to Fig. 6-61.

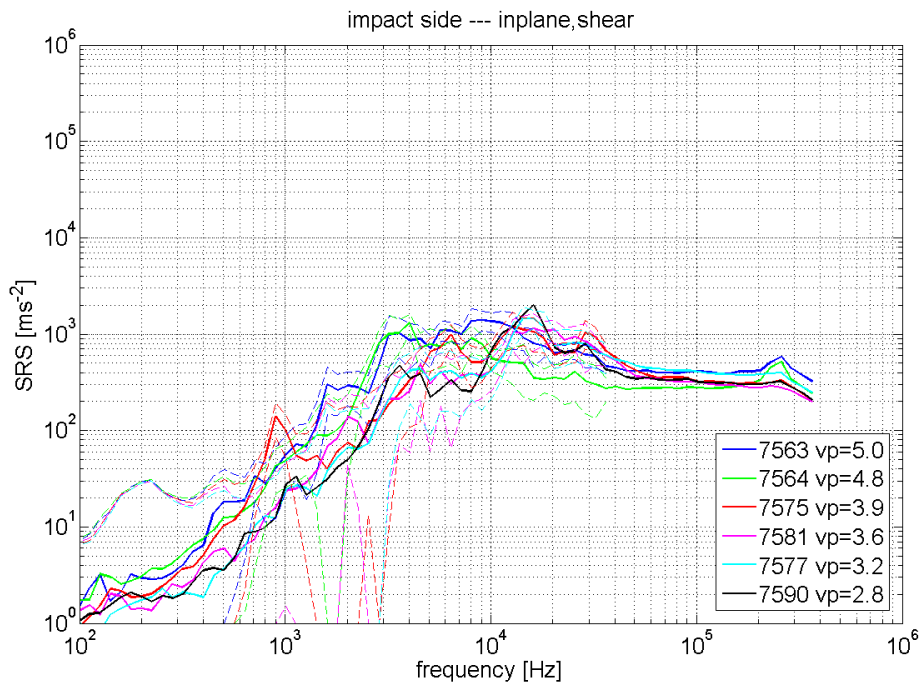
Nevertheless, a systematic increasing trend for SRS can be recognized for increasing impact speed for all types of wave. Such trend becomes evident in the frequency range from  $\sim 10^3$  to  $\sim 2\cdot 3\cdot 10^4$  Hz ( $10^4$  for IP-S).



**Fig. 6-56. Effects of projectile velocity from 2.8 to 5 km/s. Impact side, out-plane**

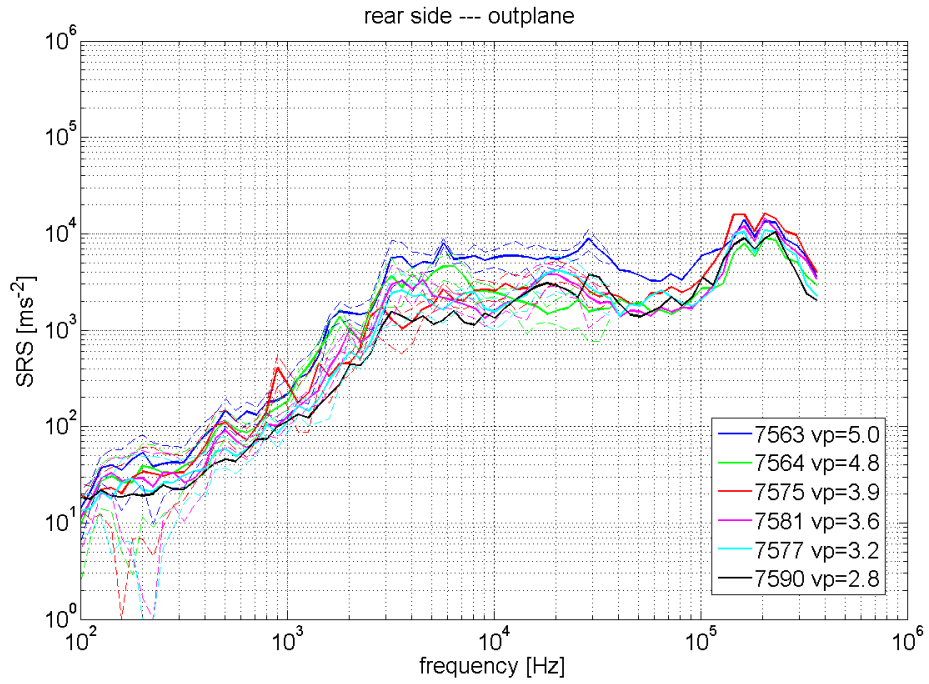


**Fig. 6-57. Effects of projectile velocity from 2.8 to 5 km/s. Impact side, in-plane-longitudinal**

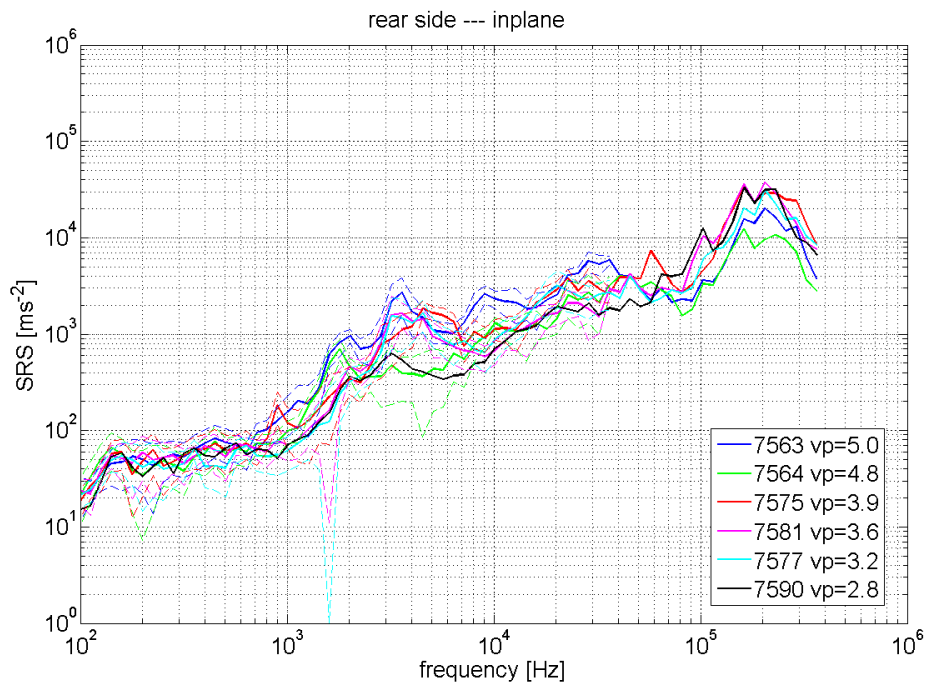


**Fig. 6-58. Effects of projectile velocity from 2.8 to 5 km/s. Impact side, in-plane-shear**

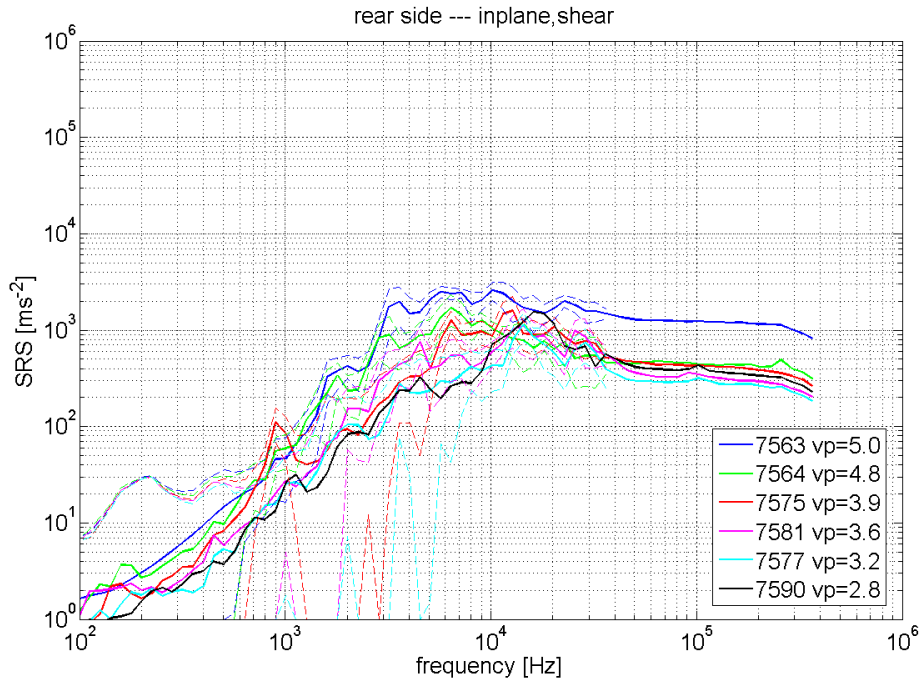




**Fig. 6-59. Effects of projectile velocity from 2.8 to 5 km/s. Rear side, out-plane**



**Fig. 6-60. Effects of projectile velocity from 2.8 to 5 km/s. Rear side, in-plane-longitudinal**



**Fig. 6-61. Effects of projectile velocity from 2.8 to 5 km/s. Rear side, in-plane-shear**

### 6.1.2.8 Oblique impacts (TS226)

CISAS ID	ESA ID TS-	dp [mm]	vp [km/s]	Coarse damage	Comments
7584	226/1	1.5	5.0	NP	Impact angle $\alpha=45^\circ$
7585	226/2	1.9	4.8	NP	Impact angle $\alpha=45^\circ$
7591	226/3	0.8	4.9	NP	Impact angle $\alpha=45^\circ$
7555	221/11 224/4	1.9	5.1	P	$\alpha=0^\circ$ , for comparison with 7585 Test used also for TS221 and TS224
7567	221/2	0.8	4.7	NP	$\alpha=0^\circ$ , for comparison with 7591 Test used also for TS221
7568	221/3	1.5	5.0	BL<=	$\alpha=0^\circ$ , for comparison with 7584 Test used also for TS221

**Tab. 6-10. Summary of TS226**

Three HVI experiments were realized with impact angle  $\alpha=45^\circ$ , by launching projectiles having  $dp=0.8, 1.5$  and  $1.9$  mm. The SRS computed for all wave types and for both front and rear SP side were then compared with three normal ( $\alpha=0^\circ$ ) tests performed at same nominal impact conditions.

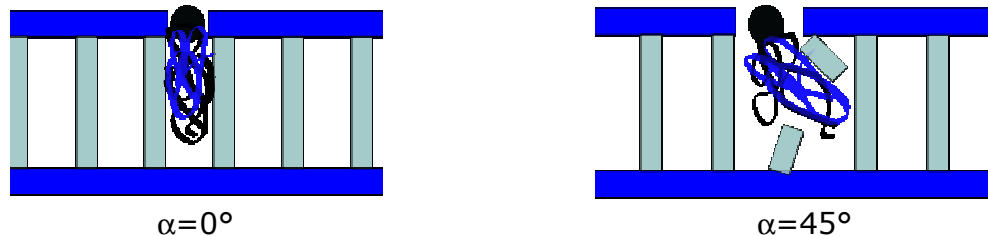
The effect of impact angle emerging from Fig. 6-63 to Fig. 6-80 is not univocal. Rather, it depends on  $dp$ :

For  $dp=0.8$  mm and for all types of wave, SRS resulting from the oblique HVI are higher than those of normal HVI, at frequency above  $\sim 4-5 \cdot 10^3$  Hz. In the low frequency range, impact obliquity does not affect SRS

For  $d_p=1.5$  mm and for all types of wave, SRS resulting from the oblique HVI are lower than those of normal HVI, at frequency above  $\sim 3-4 \cdot 10^3$  Hz. In the low frequency range, impact obliquity does not affect SRS

For  $d_p=1.9$  mm and for all types of wave, no difference can be observed between SRS resulting from oblique or normal HVI

This odd behaviour can be explained thinking at the internal damage of the HC core (see Fig. 6-62 for the case  $d_p=0.8$  mm):



**Fig. 6-62. HC core internal damage. Not to scale**

For  $d_p=0.8$  mm, the debris cloud diameter is close to the inner size of HC channels and hence no significant lateral expansion is allowed for the fragments when  $\alpha=0^\circ$  (channelling effect). On the other hand, for  $\alpha=45^\circ$  the inner damage of HC core increases significantly, resulting in higher SRS levels compared to those calculated from normal HVI

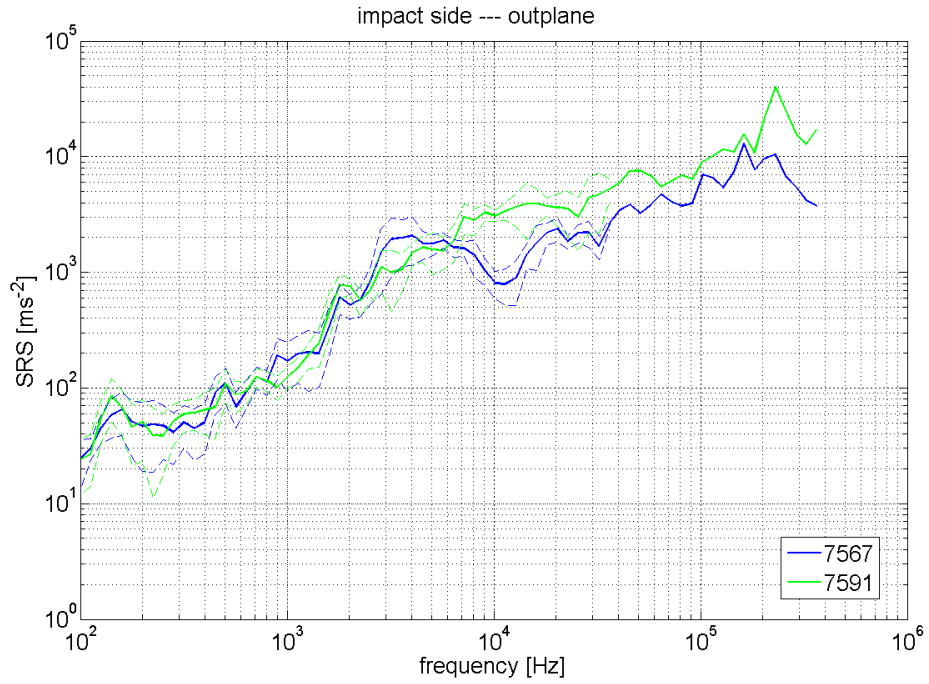
For  $d_p=1.9$  mm, the debris cloud diameter is large enough to produce a substantial damage to the HC core, even in case of  $\alpha=0^\circ$ . Therefore, differences between SRS obtained from normal and oblique impacts appears to be negligible

For  $d_p=1.5$  mm, oblique HVI are clearly NP with an internal HC damage that is less pronounced than that produced by normal HVI, that is close to BL (three bulges can be observed on the target rear side after test no.7568). Thanks to the closeness to BL, SRS from normal HVI is therefore higher than that from oblique HVI.

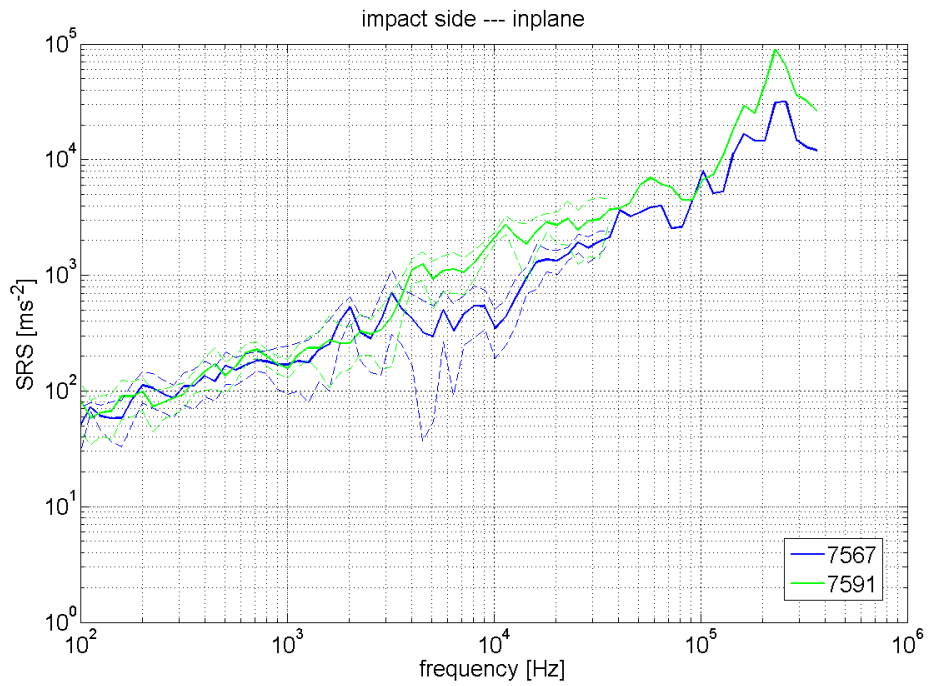
It may be concluded that oblique HVI can be more critical than correspondent normal HVI, depending on the extension of the HC core internal damage.

More specifically, oblique impacts produce higher SRS levels (at frequency above  $\sim 4 \cdot 10^3$  Hz) if the impacting debris is "small", i.e. if it produces a debris clouds having size comparable to that of the cross section of HC core channels.

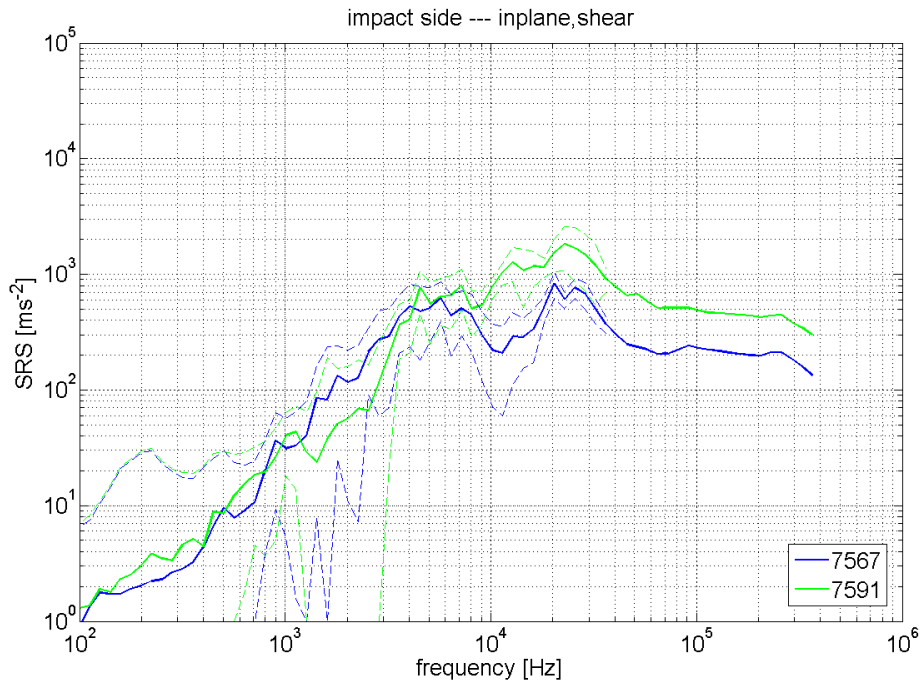
Oblique impacts with  $d_p=0.8$  mm



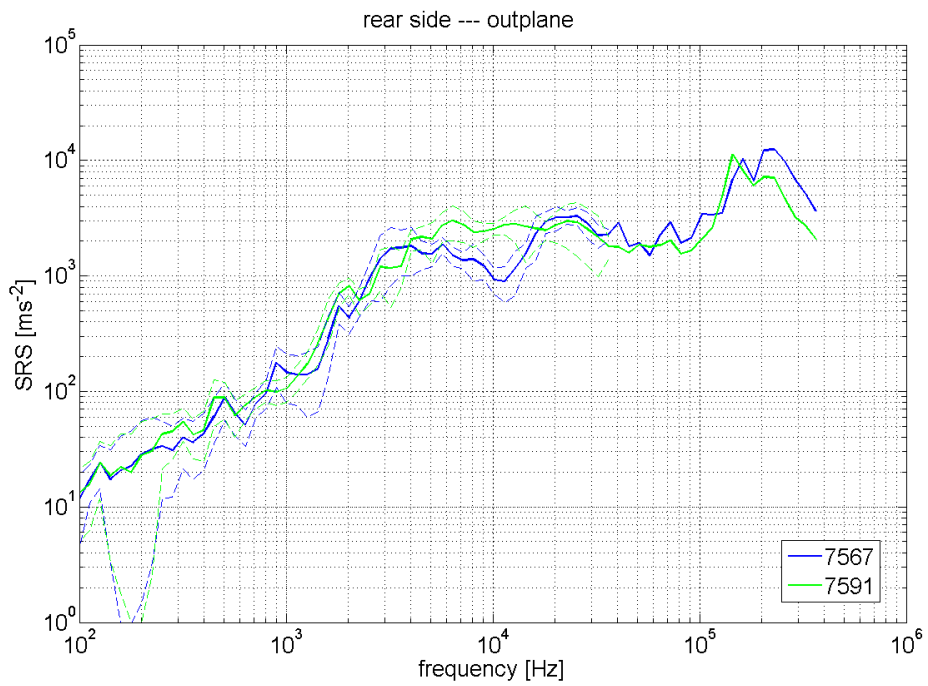
**Fig. 6-63. Effects of impact obliquity for  $dp=0.8$  mm. Front side, out-plane**



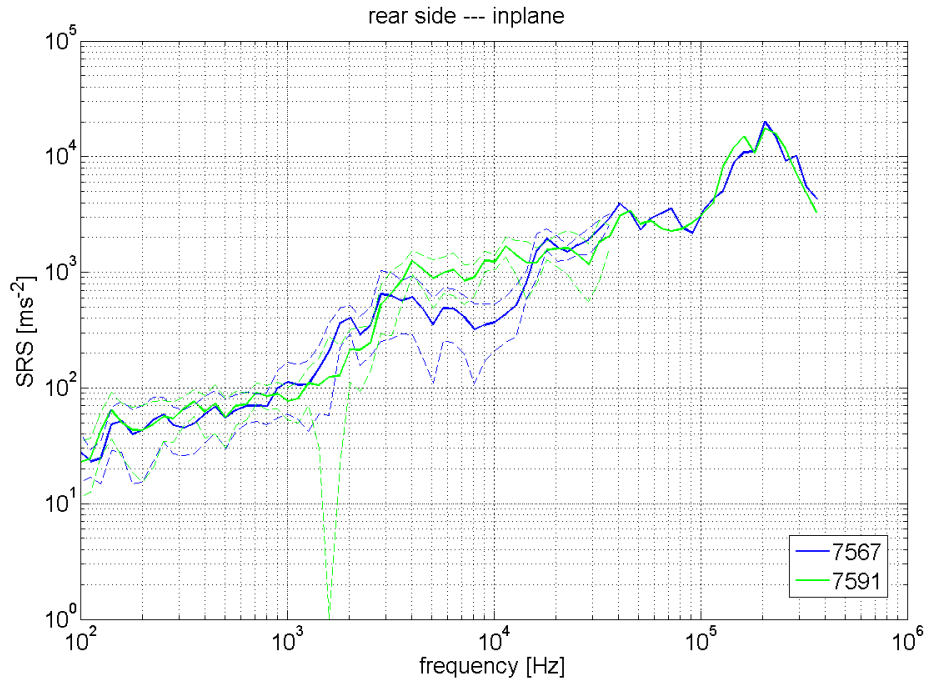
**Fig. 6-64. Effects of impact obliquity for  $dp=0.8$  mm. Front side, in-plane-longitudinal**



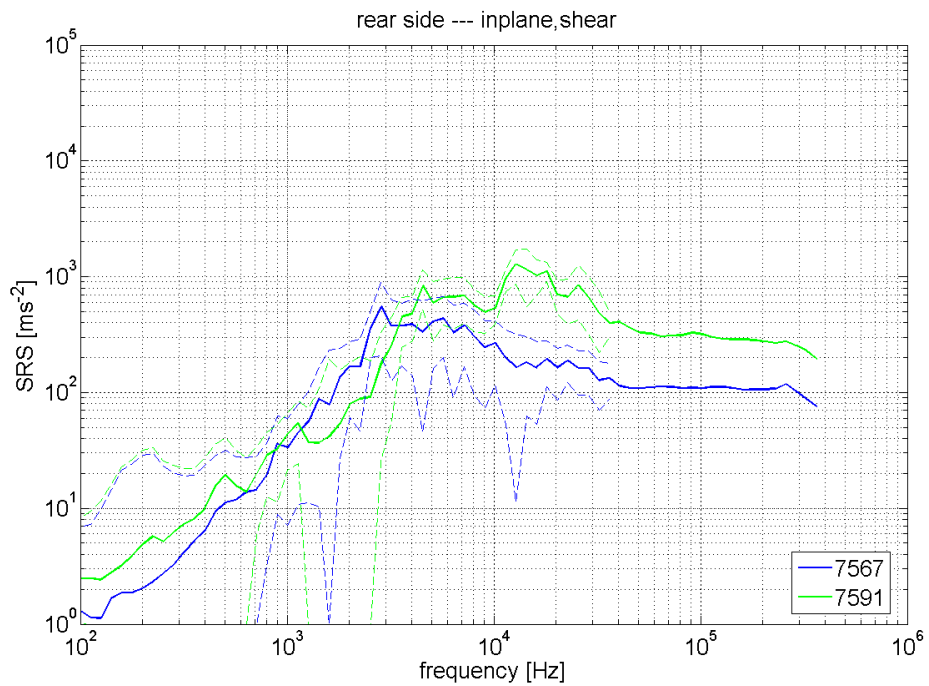
**Fig. 6-65. Effects of impact obliquity for  $d_p=0.8$  mm. Front side, in-plane-shear**



**Fig. 6-66. Effects of impact obliquity for  $d_p=0.8$  mm. Rear side, out-plane**

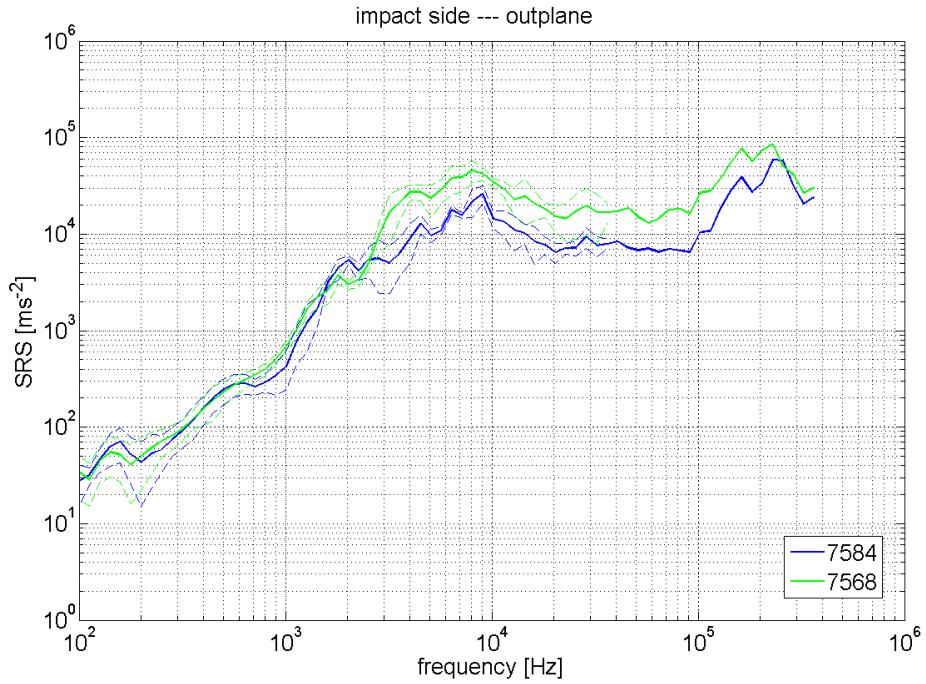


**Fig. 6-67. Effects of impact obliquity for  $d_p=0.8$  mm. Rear side, in-plane-longitudinal**

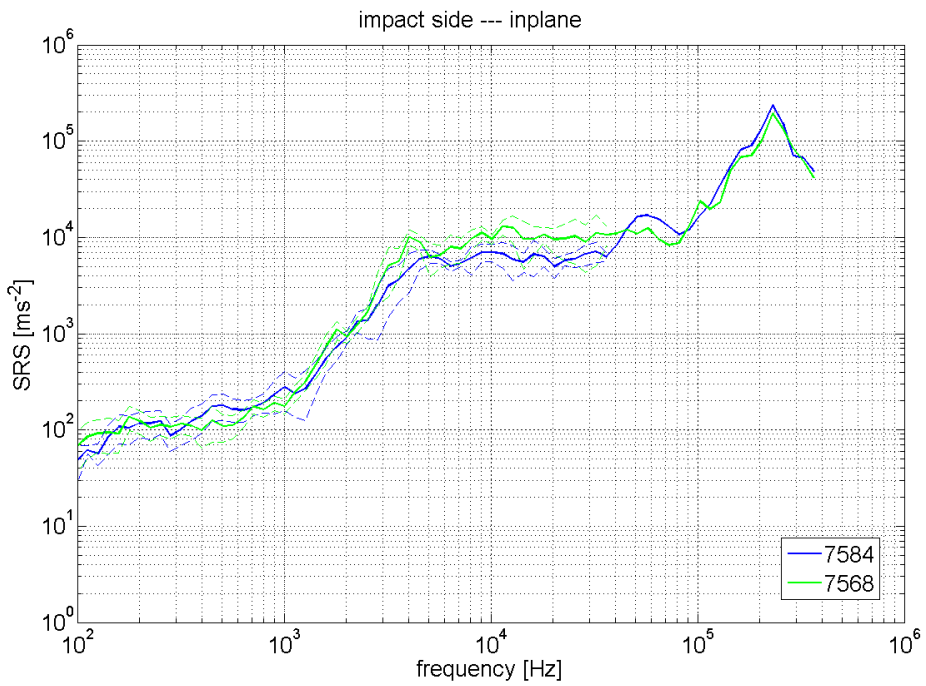


**Fig. 6-68. Effects of impact obliquity for  $d_p=0.8$  mm. Rear side, in-plane-shear**

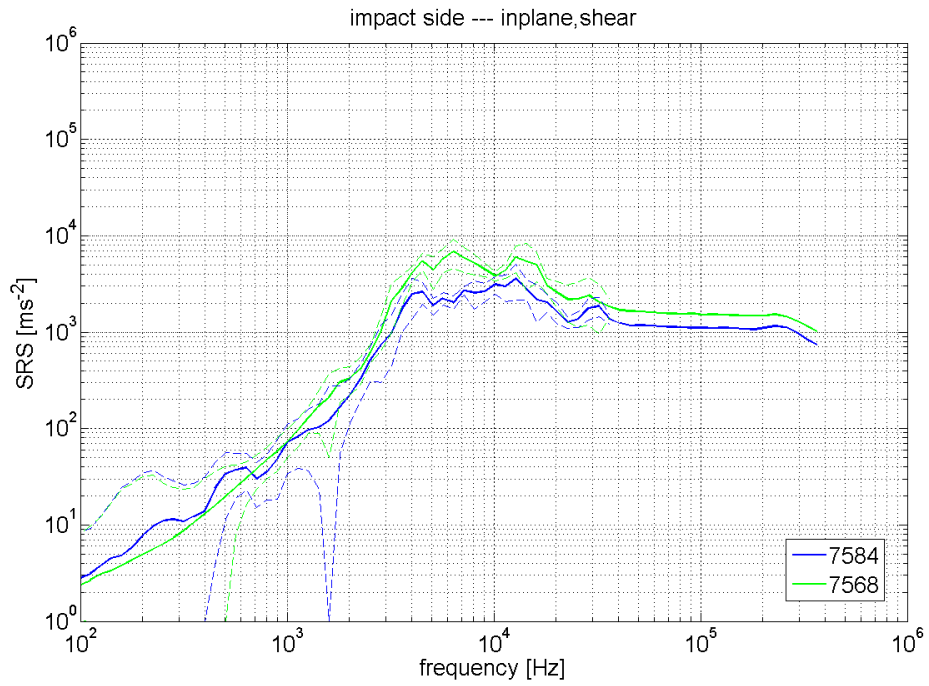
**Oblique impacts with  $d_p=1.5$  mm**



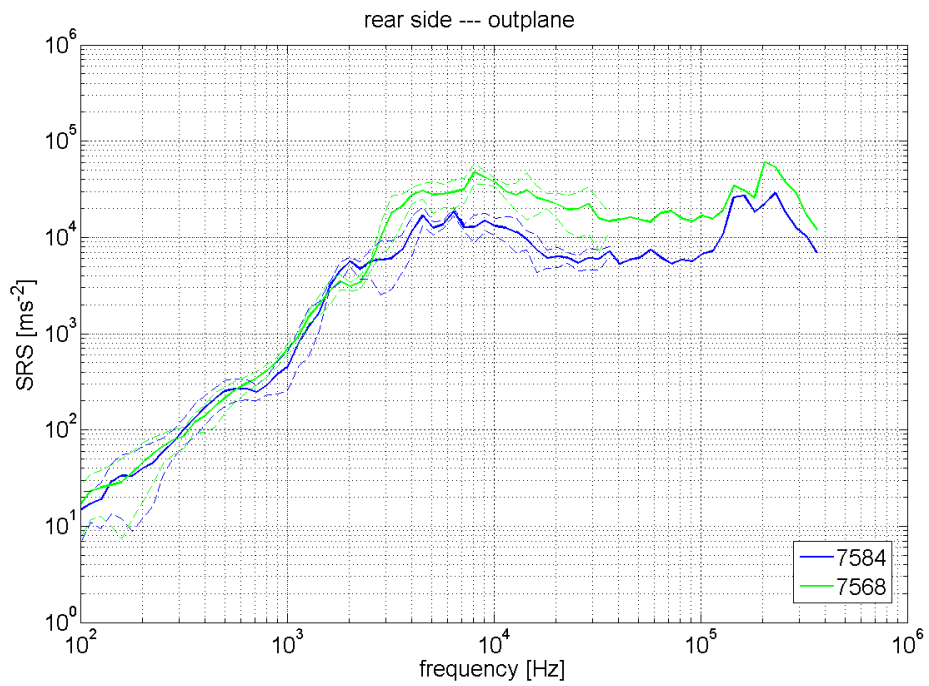
**Fig. 6-69. Effects of impact obliquity for  $d_p=1.5$  mm. Front side, out-plane**



**Fig. 6-70. Effects of impact obliquity for  $d_p=1.5$  mm. Front side, in-plane-longitudinal**

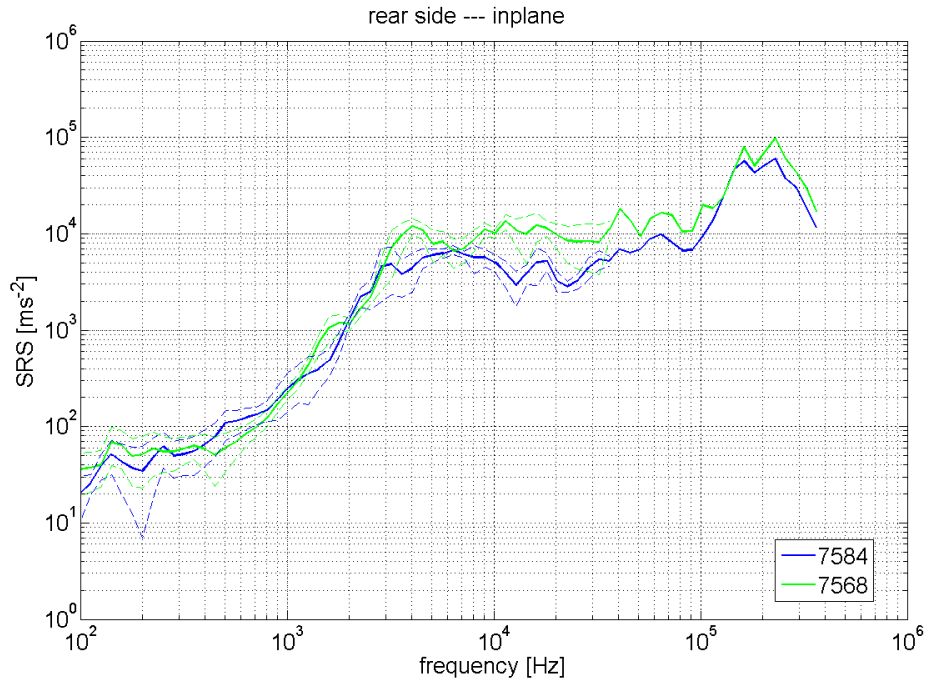


**Fig. 6-71. Effects of impact obliquity for  $d_p=1.5$  mm. Front side, in-plane-shear**

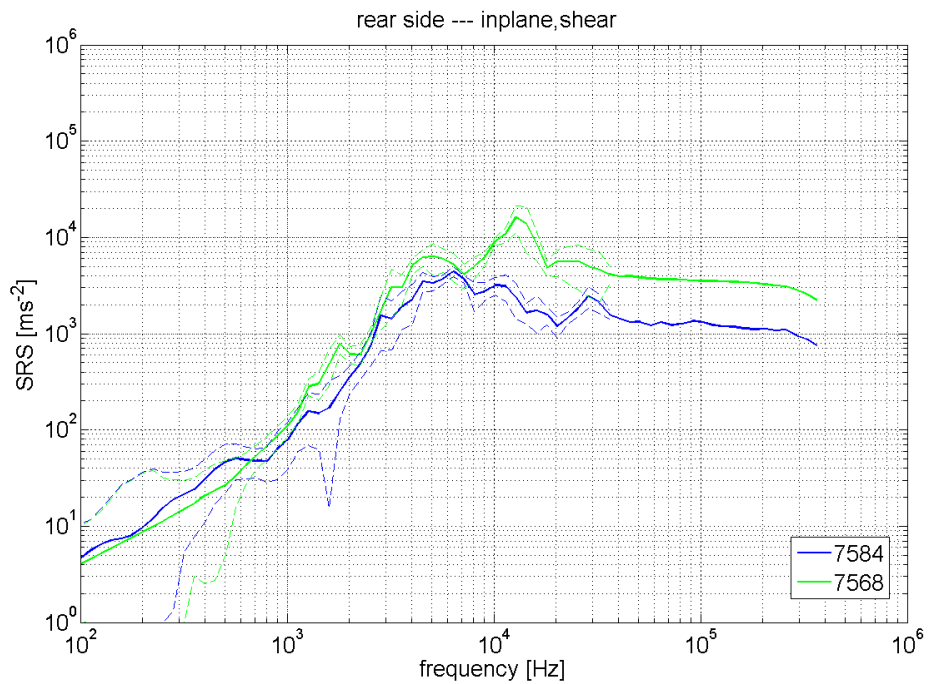


**Fig. 6-72. Effects of impact obliquity for  $d_p=1.5$  mm. Rear side, out-plane**



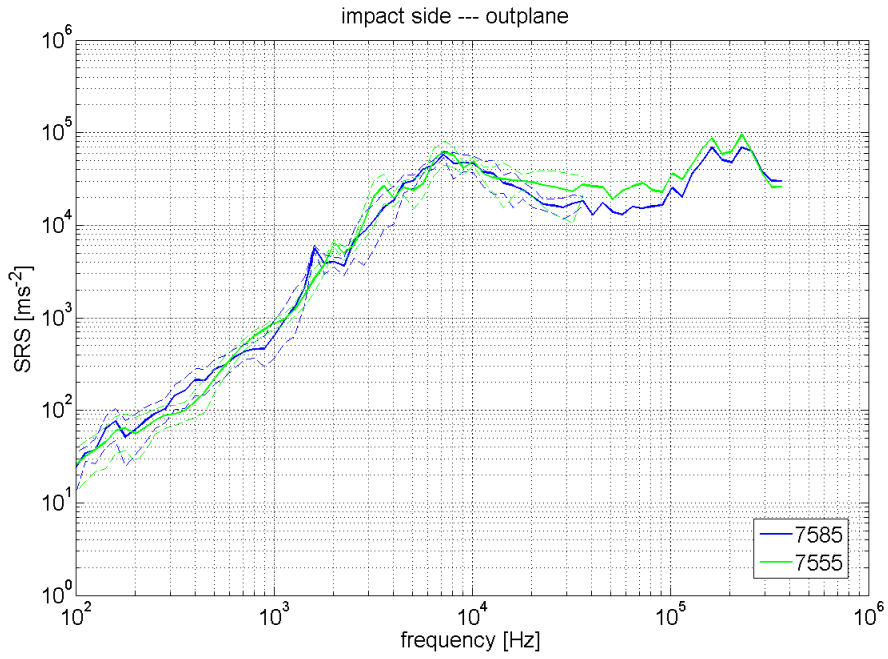


**Fig. 6-73. Effects of impact obliquity for  $d_p=1.5$  mm. Rear side, in-plane-longitudinal**

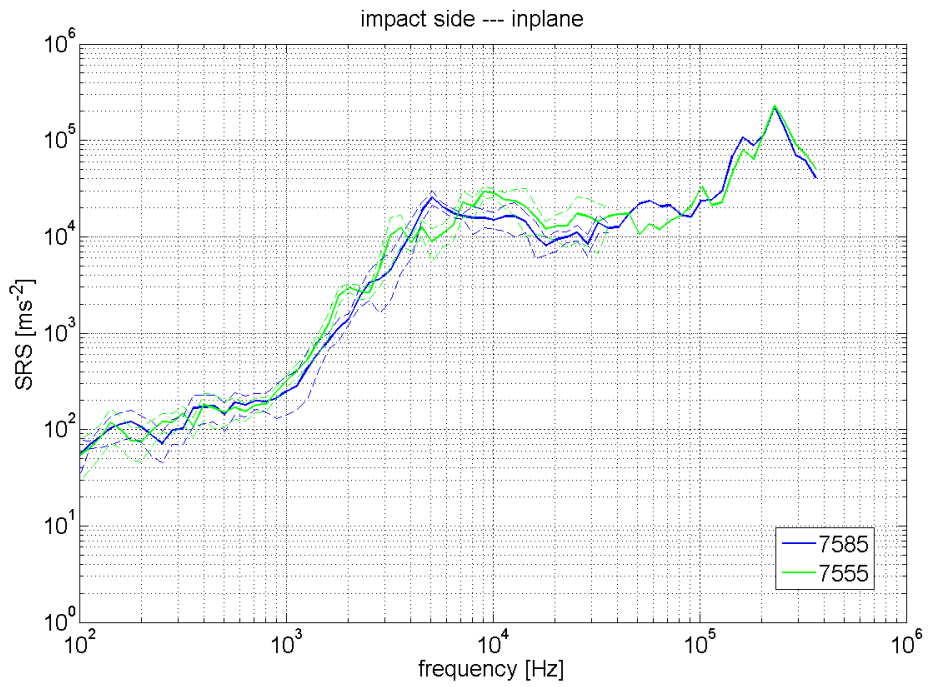


**Fig. 6-74. Effects of impact obliquity for  $d_p=1.5$  mm. Rear side, in-plane-shear**

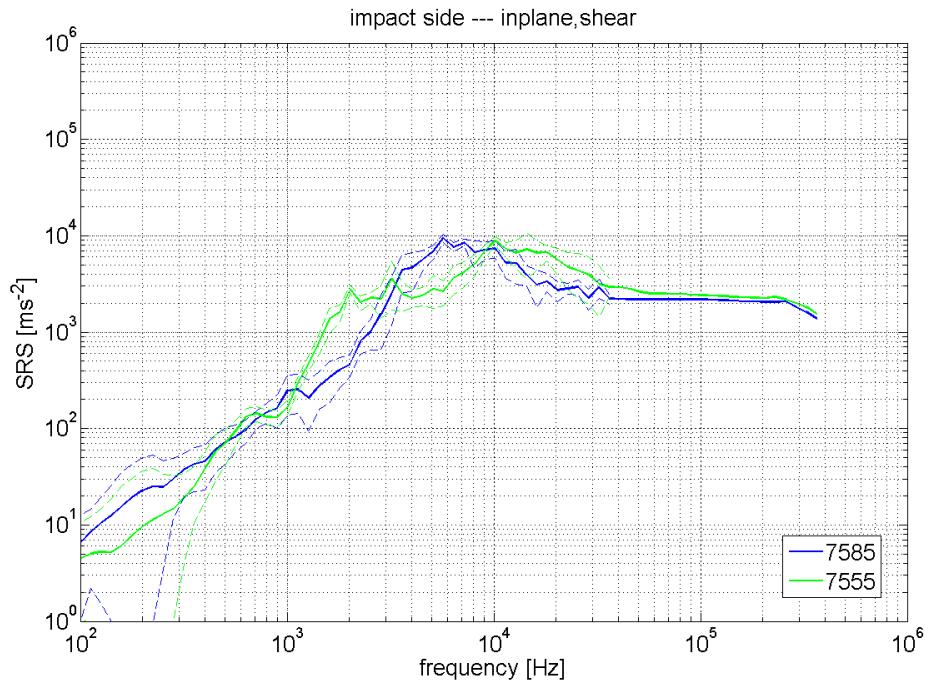
**Oblique impacts with  $d_p=1.9$  mm**



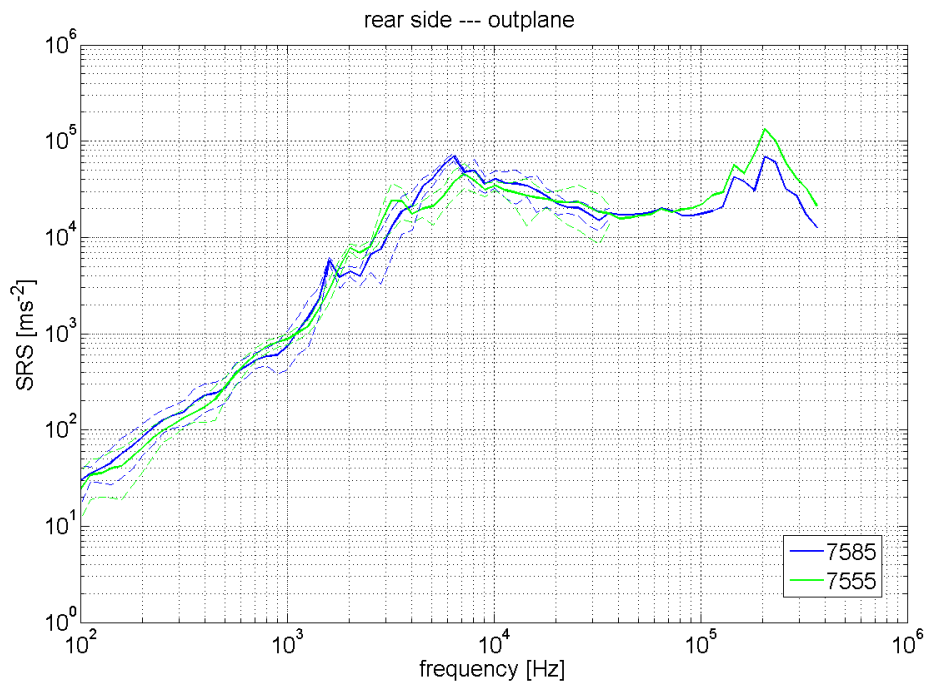
**Fig. 6-75. Effects of impact obliquity for  $d_p=1.9$  mm. Front side, out-plane**



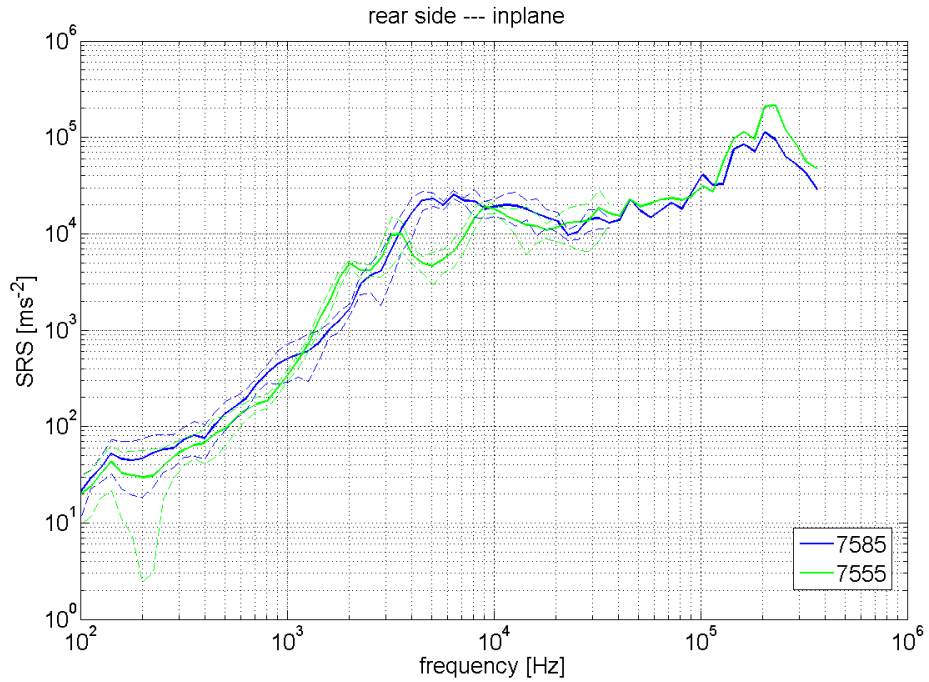
**Fig. 6-76. Effects of impact obliquity for  $d_p=1.9$  mm. Front side, in-plane-longitudinal**



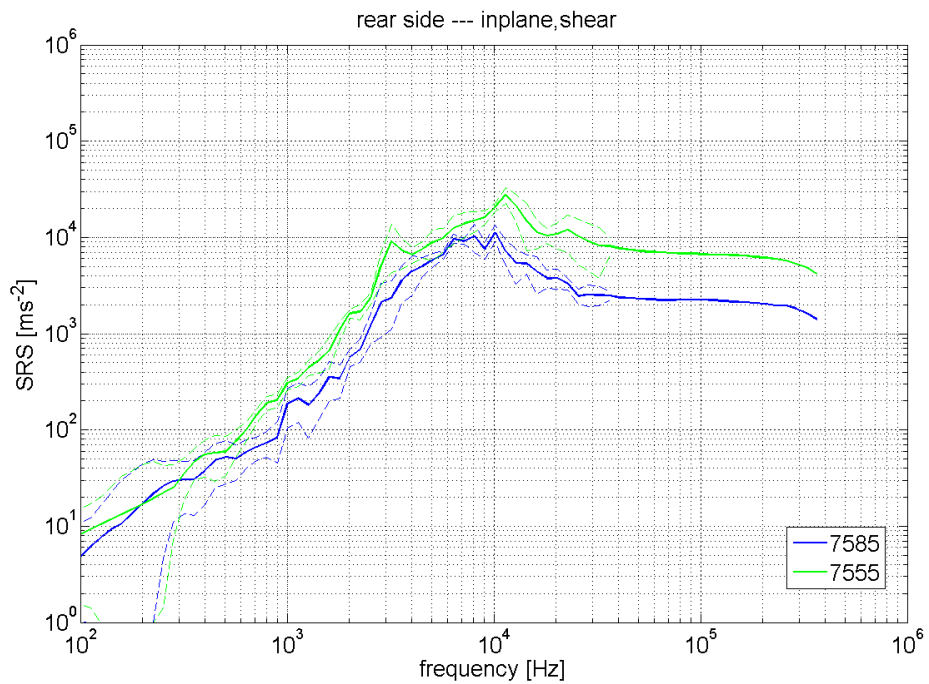
**Fig. 6-77. Effects of impact obliquity for  $d_p=1.9$  mm. Front side, in-plane-shear**



**Fig. 6-78. Effects of impact obliquity for  $d_p=1.9$  mm. Rear side, out-plane**



**Fig. 6-79. Effects of impact obliquity for dp=1.9 mm. Rear side, in-plane-longitudinal**



**Fig. 6-80. Effects of impact obliquity for dp=1.9 mm. Rear side, in-plane-shear**

### 6.1.2.9 Relevant results for AI HC SP

The main achievements of TS22 are hereafter summarised. Quantitative information on SRS values vs. impact conditions is provided in the above plots.

A HVI produces in both the front (impact) and rear side of the SP a vibration environment which can be described through the SRS of OP, IP-L and IP-S waves. For comparison purposes, three different frequency ranges are introduced: low-frequency (from  $10^2$  to  $\sim 3\text{-}4\cdot 10^3$  Hz), high-frequency (from  $\sim 3\text{-}4\cdot 10^3$  to  $\sim 10^4$  Hz) and very-high-frequency (from  $\sim 10^4$  to  $\sim 1\text{-}2\cdot 10^5$  Hz)

In general, it should be noticed that the most peculiar observations are done inside the so called "high-frequency range".

<b>Types of waves</b>	OP and IP-L SRS	OP and IP-L SRS have compatible magnitude in the low and very-high frequency ranges. In the high-frequency range, the magnitude of OP SRS is greater than that of IP-L. The SRS of IP-S are below OP and IP-L at all frequencies	
	Front/rear side	Regarding the SRS of OP and IP-L waves, no significant difference exists between front and rear side of the target in the whole frequency range. SRS of IP-S are higher on the rear side, in the high-frequency range.	
<b>Influence of projectile mass and velocity</b>	SRS scaling with projectile momentum	Below $\sim 2\cdot 10^3$ Hz SRS does not depend on momentum. Thus small projectiles transfer momentum to targets in a more efficient way than large projectiles. Above $\sim 2\cdot 10^3$ Hz, SRS scale linearly with projectile momentum	
		In the medium-high-frequency range (>2kHz)	SRS magnitude for P tests is substantially larger than that of NP tests
		Medium- Low frequency range (<4kHz)	Difference becomes less significant for OP and IP-S, and is negligible for IP waves.
		Front/rear side	Previous observations hold for both front and rear panel side.
<b>Impact obliquity</b>	Low and very-high frequency range	SRS obtained from oblique HVI ( $\alpha=45^\circ$ ) are compatible to those from normal HVI ( $\alpha=0^\circ$ )	
	High frequency range	Oblique impacts produce higher SRS levels if the impacting debris is "small", i.e. if it produces a debris clouds having size comparable to that of the cross section of HC core channels.	
<b>Existing damage</b>		Provided that any interference between internal HC core damages due to different HVI is avoided, SRS obtained from experiments on previously damaged targets are compatible to SRS calculated from completely new targets.	
<b>Scaling effects</b>	OP and IP-L	Inside our experimental range (from $200\times 200\text{ mm}^2$ to $430\times 450\text{ mm}^2$ ), no significant difference on SRS can be observed, for all types of wave and for both front and rear target side.	
	IP-S wave	IP-S wave has the largest SRS for the smallest target size. This happens in the high-frequency range of the spectrum.	

**Tab. 6-11. Relevant results for TS22**

## 6.2 Propagation of HVI-induced disturbances in complex targets

After having investigated the generation of transient disturbances close to impact points on aluminium honeycomb sandwich panels, the attention was focused on the propagation on vibrations on more complex structures, representative of real GOCE parts including structural joints.

The basic goal of this part of the study was to ascertain if shocks originating on the external shell of the spacecraft might arrive to sensitive components (e.g. sensors, electronic boxes, circuits, etc.) placed on the satellite's interior.

More precisely, several experiments were conducted on "complex targets" including joints, with the following main objectives:

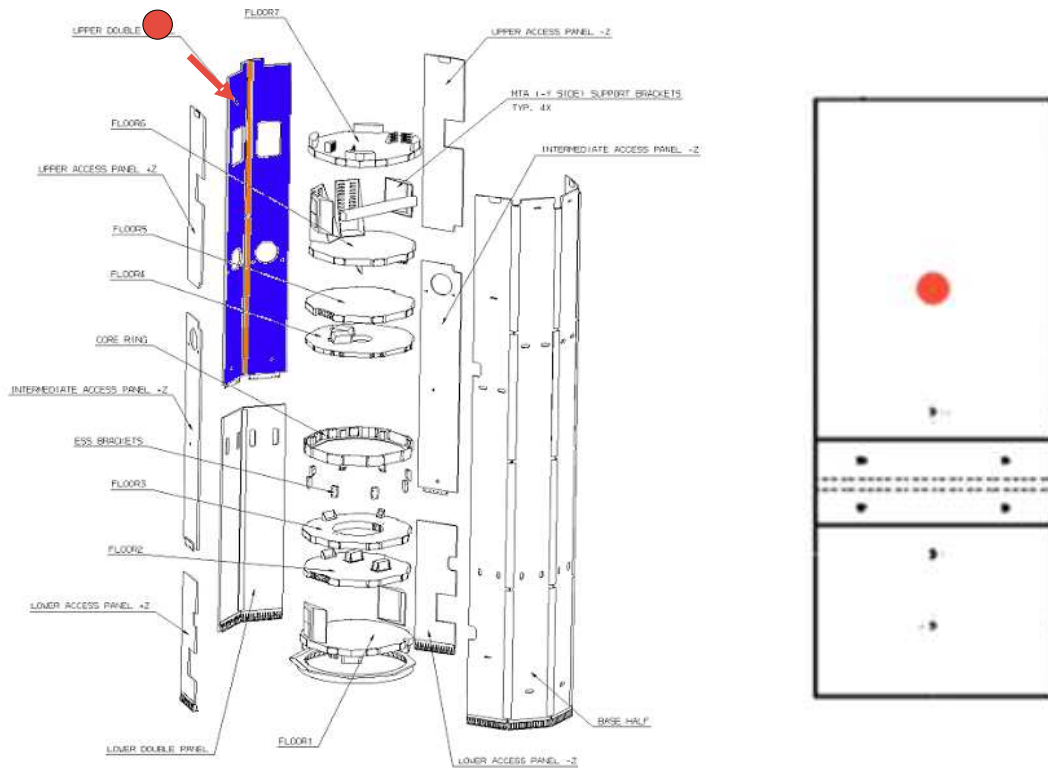
- To create an experimental database of the response to HVI of real spacecraft parts (describing realistic load paths from the exterior to internal components). Such database contains SRS from acceleration signals measured on different points along selected structural paths.
- To identify the basic features of wave propagation, attenuation and reflection through real spacecraft joints, from near- to far-field. This is done by computing a sort of "transfer function" referring to the ratio of Shock Response Spectra. If the SRS function on an impacted plate is known (or computed with simulations), the transfer function can be used to predict the vibration environment on a plate attached to it with joint, or transmitted along the plate length, without having to measure the SRS at that position

It's essential to stress that the HVI experiments conducted make it possible to analyse loading conditions (acceleration levels and frequency content) different from those normally reproducible with standard ground test facilities, thus providing the unique possibility of extending the knowledge on the transient and dynamic behaviour of spacecraft structural parts.

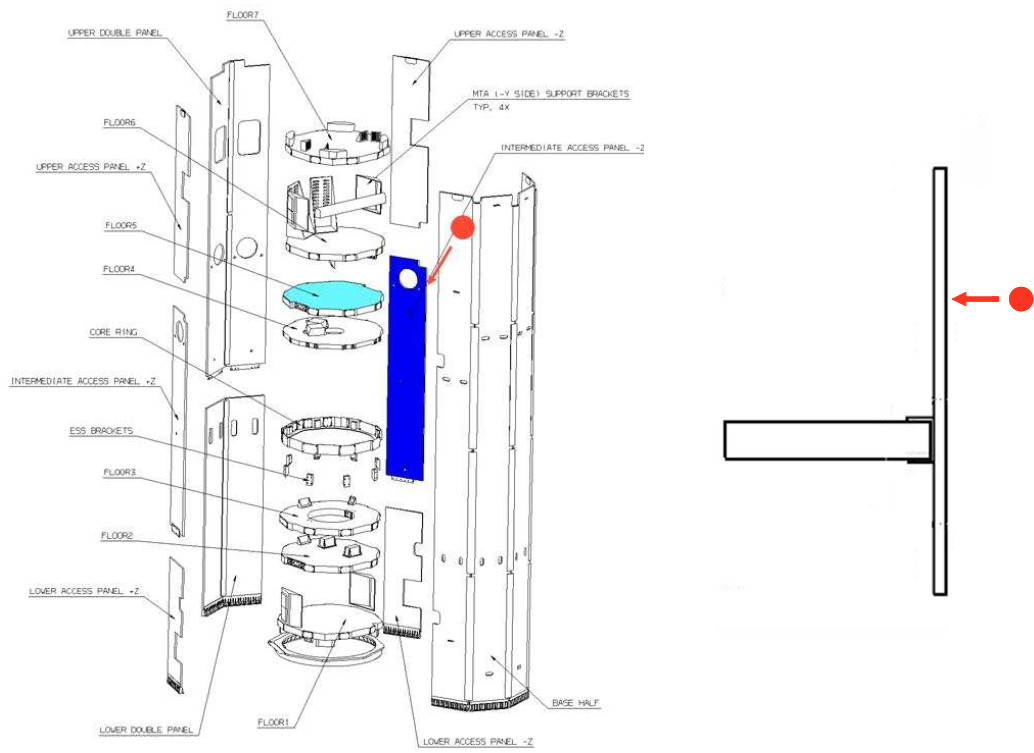
Moreover, collected data would be useful for tuning numerical models and tools necessary for extending the results on situations different from the experimental ones.

### 6.2.1 Method of analysis

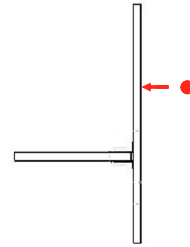
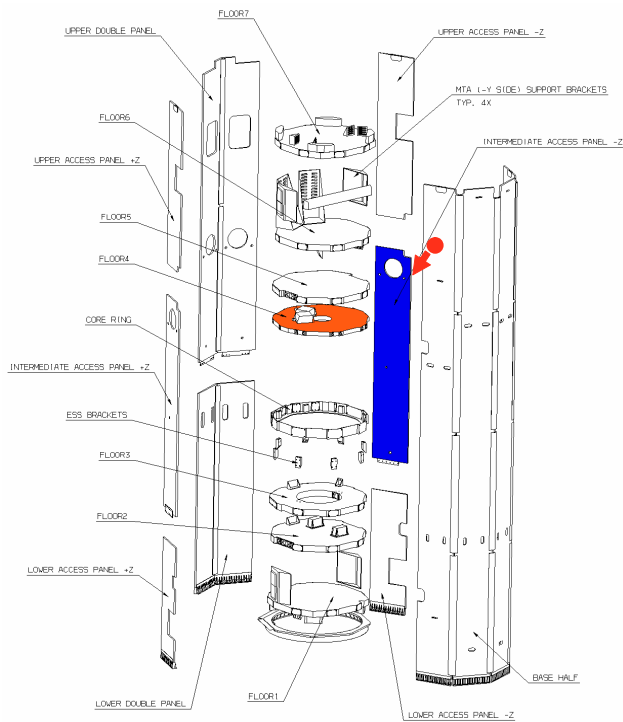
To realise the objectives discussed above, several impact experiments (with impact hammer and HVI) were carried out on targets representative of real parts of the GOCE satellite (from Fig. 6-81 to Fig. 6-84). It is clear that different target configurations were conceived to reproduce the most significant paths of propagation of disturbances from the external shell to internal components.



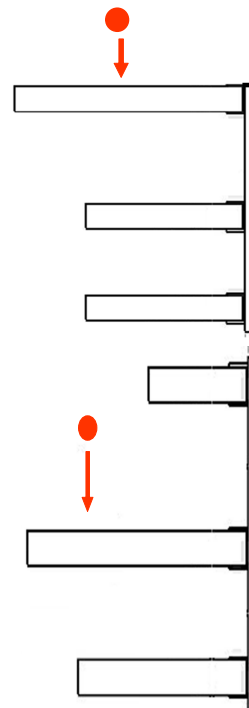
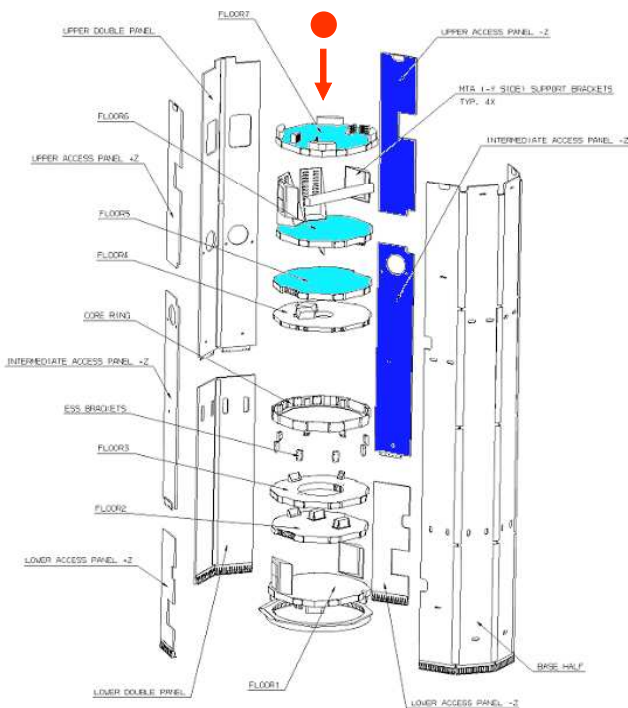
**Fig. 6-81 GOCE C target model**



**Fig. 6-82 GOCE D1 target model**



**Fig. 6-83 GOCE D2 target model**



**Fig. 6-84 GOCE E (up) GOCE G (down) target models**

In the following, the discussion will be limited to target E, with the objective of clarifying the method used in the framework of the study. The method of analysis is detailed the following points:

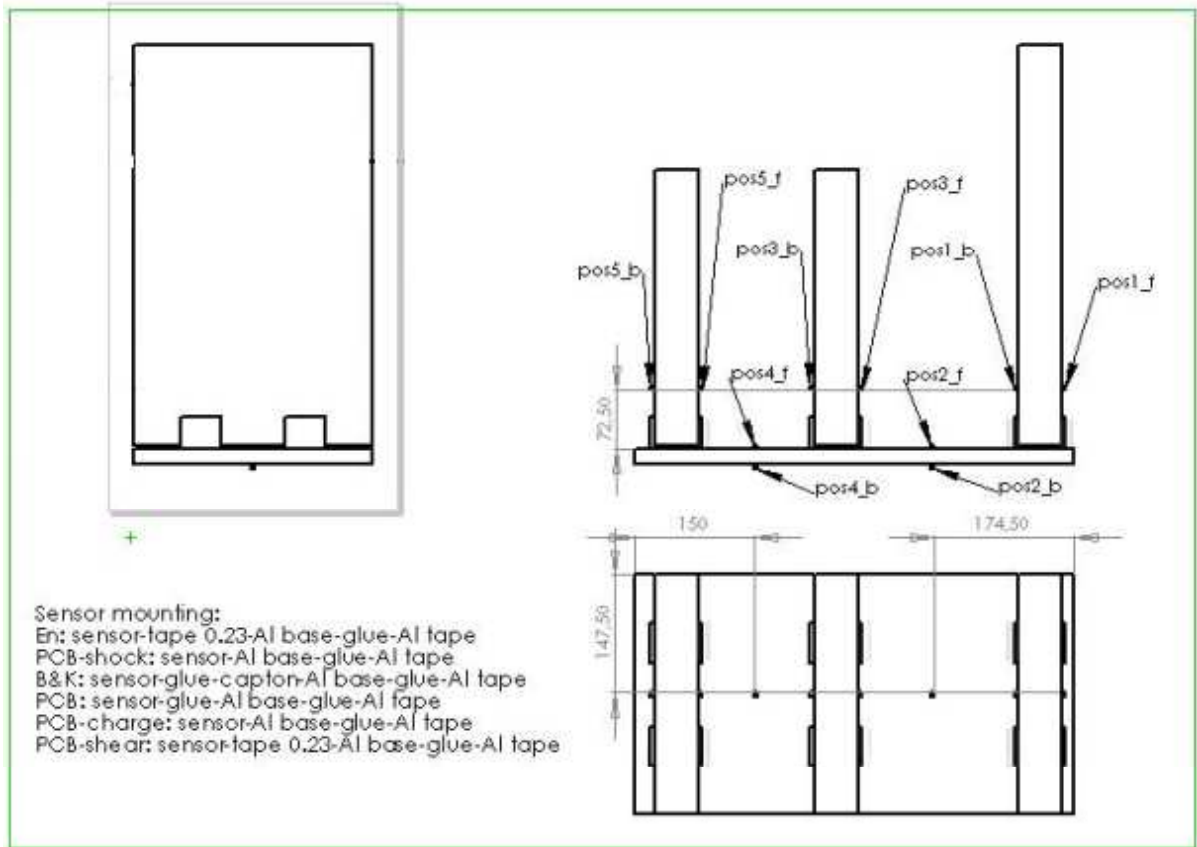


- Execution of impact experiments: impact test allowed to collect transient signals of acceleration using sensors on 3-axes assemblies for measuring both out-plane, in-plane longitudinal and in-plane-shear waves. Sensor assemblies were located along the most significant load paths through different panels and across joints. A wide range of experimental conditions (projectile mass and velocity; below, across and above the ballistic limit of the impacted panel)
- Computation of the SRS of each signal. For comparison purposes, even the uncertainty was assessed using the same approach already described for simple targets see paragraph 5.3.1. In particular, dedicated experiments were carried out for highlighting: (i) the impact facility background noise, (ii) the scattering of data and (iii) the load effect related to the accelerometers point masses located on the targets.
- Computation of the “transmission functions” between selected points along the load paths, in particular across junctions. The transmission functions are defined as the ratio between the SRS of acceleration signals measured on different points. These functions have been computed selecting six representative shots among those of paragraph 6.2.4

The three points above are detailed in the following paragraphs: paragraph 6.2.2 describes the targets configuration, the disposition of sensors and the experimental logic; 6.2.3 deals with the uncertainty on computed SRS and 6.2.4 reports the main results on the evaluation of the “transmission functions”.

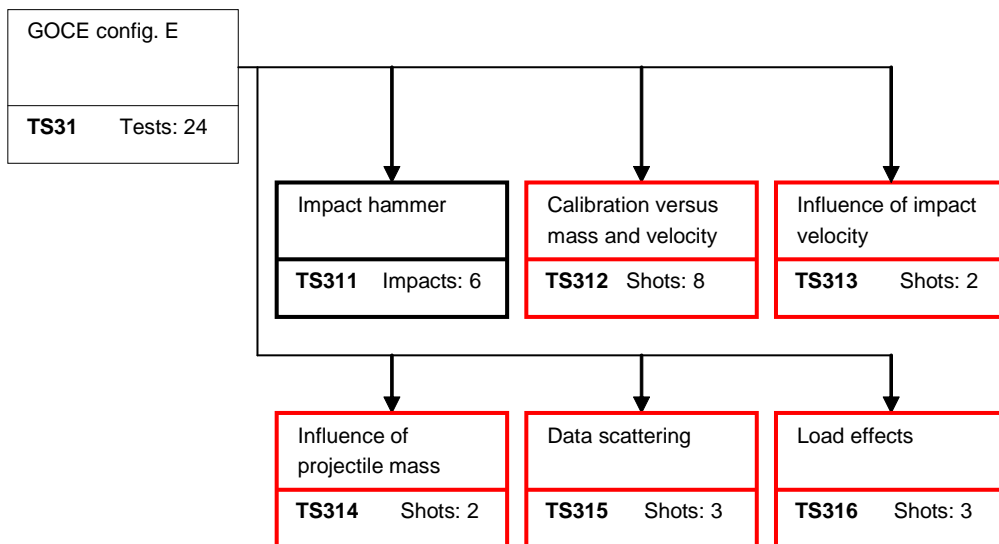
### **6.2.2 Target configuration and test logic**

In the following picture, the locations of accelerometers on target E are presented. On each location, three accelerometers are placed with the sensitive axis along X (in-plane-longitudinal), Y(out-plane) and Z (in-plane-shear) directions.



**Fig. 6-85 Accelerometer locations for Target E**

The experimental logic is presented in Fig. 6-86.



**Fig. 6-86 Target E tests**

The objective of each group of tests is briefly summarised hereafter:

- TS311 (hammer) tests: evaluation of component transfer functions in conditions of linear structural response. These test were necessary for the extrapolation activity (to complex assemblies and impact conditions not reproducible with the LGG) and are not herein presented
- TS312 tests: Preliminary investigation of the target response to hypervelocity impacts induced by different projectile sizes, impact velocity and type of damage
- TS313 tests: Additional experiments to evaluate the influence of impact velocity on HVI induced disturbance.
- TS214 tests: Additional experiments to evaluate the influence of projectile size on HVI induced disturbance
- TS315 tests: Evaluation of data scattering
- TS316 tests: Evaluation of the influence of load effects owing to accelerometer added masses on HVI induced disturbances.

### **6.2.3 Estimation of uncertainty**

The uncertainty of SRS, resulting from HVI on complex targets, has been computed as reported in paragraph 5.3.1. Each target configuration (E, G, D1, D2 and C) has been tested again following this procedure.

The main results are similar to those reported on paragraph 6.1.2.1. The only difference could be on the acoustic noise coupling due to the increased dimension of complex assemblies respect to simple targets. However, it appears that data scattering has complex dependence from frequency similar to that already assessed for the near field with its uncertainty band. It results that the noise due to the facility functioning is below 3 dB in the entire SRS frequency band (from 100 Hz to 30 kHz).

The following two paragraphs show the tests performed to estimate uncertainty due to data scattering and load effect (due to the sensors used to measure the disturbance field).

#### **6.2.3.1 Data scattering**

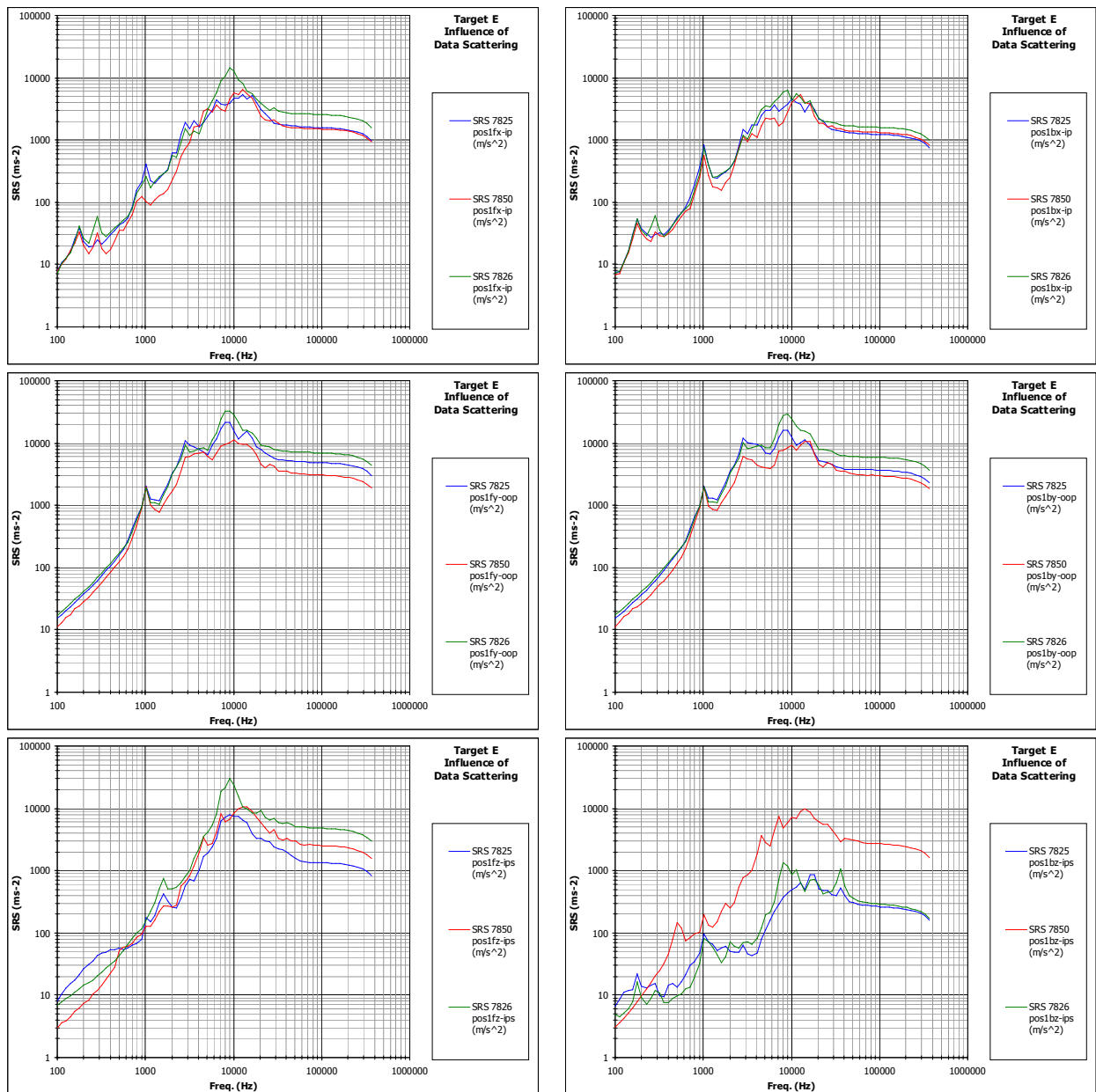
Three *non-perforating* HVI tests have been executed in order to evaluate data scattering. These types of shot have been selected due to their major not-repeatability respect to perforating ones.

The projectiles have a diameter of 1.5 mm and the impact velocity is around 5 km/s. Tab. 6-12 summarizes the main characteristics of each test. The seventh column of the table reports the hypervelocity impact location on the impacted sandwich panel (GOCE external panel – floor 7).

CISAS ID	ESA ID TS -	dp [mm]	vp [km/s]	Coarse Damage	Impact location
7825	315/1	1.5	5.3	BL<=	
7850	315/2	1.5	5.0	BL<=	
7826	315/3	1.5	5.1	BL<=	

**Tab. 6-12 Summary of TS315**

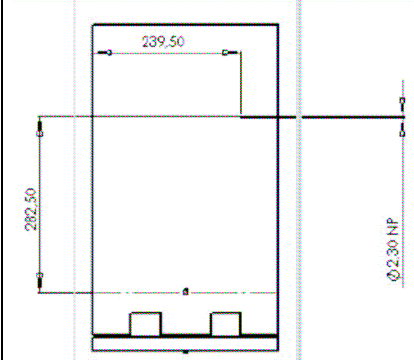
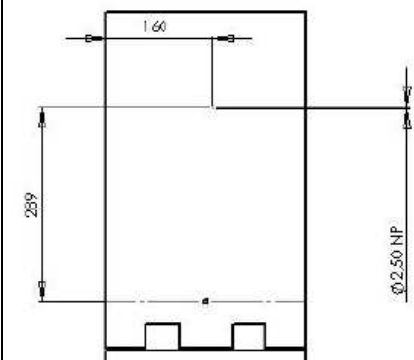
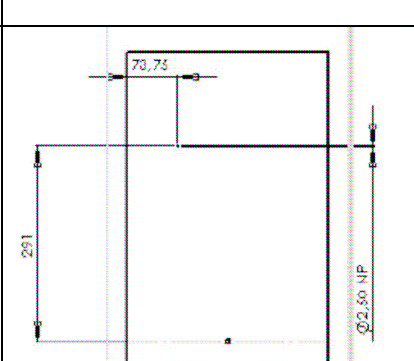
The out of plane and in plane SRS have been calculated on the all accelerometer location. Fig. 6-87 reports out-of-plane and in-plane SRS at position 1. The results coming from test 7818, 7843, 7848 and 7849, belonging to the groups labelled TS311, TS314 and TS315 have been used for the evaluation of the uncertainty due to noise, as already explained in case of simple target. The two types of uncertainty, due to data scattering and noise, have been finally combined together according to statistics rules, defining the uncertainty bands to be associated to each measured signal.



**Fig. 6-87 Data Scattering SRS "Pos1" Accelerometer Location)**

### 6.2.3.2 Load effects

Three shots with projectiles of 1.0 mm of diameter have been fired at about 5 km/s according to the test data reported in Tab. 6-13 to evaluate the load effects induced by accelerometer added mass.

CISAS ID	ESA ID TS -	dp [mm]	vp [km/s]	Coarse Damage	Impact location
7831	315/1	1.0	4.9	NP	
7844	315/2	1.0	5.2	NP	
7847	315/3	1.0	5.0	NP	

**Tab. 6-13 Summary of TS316**

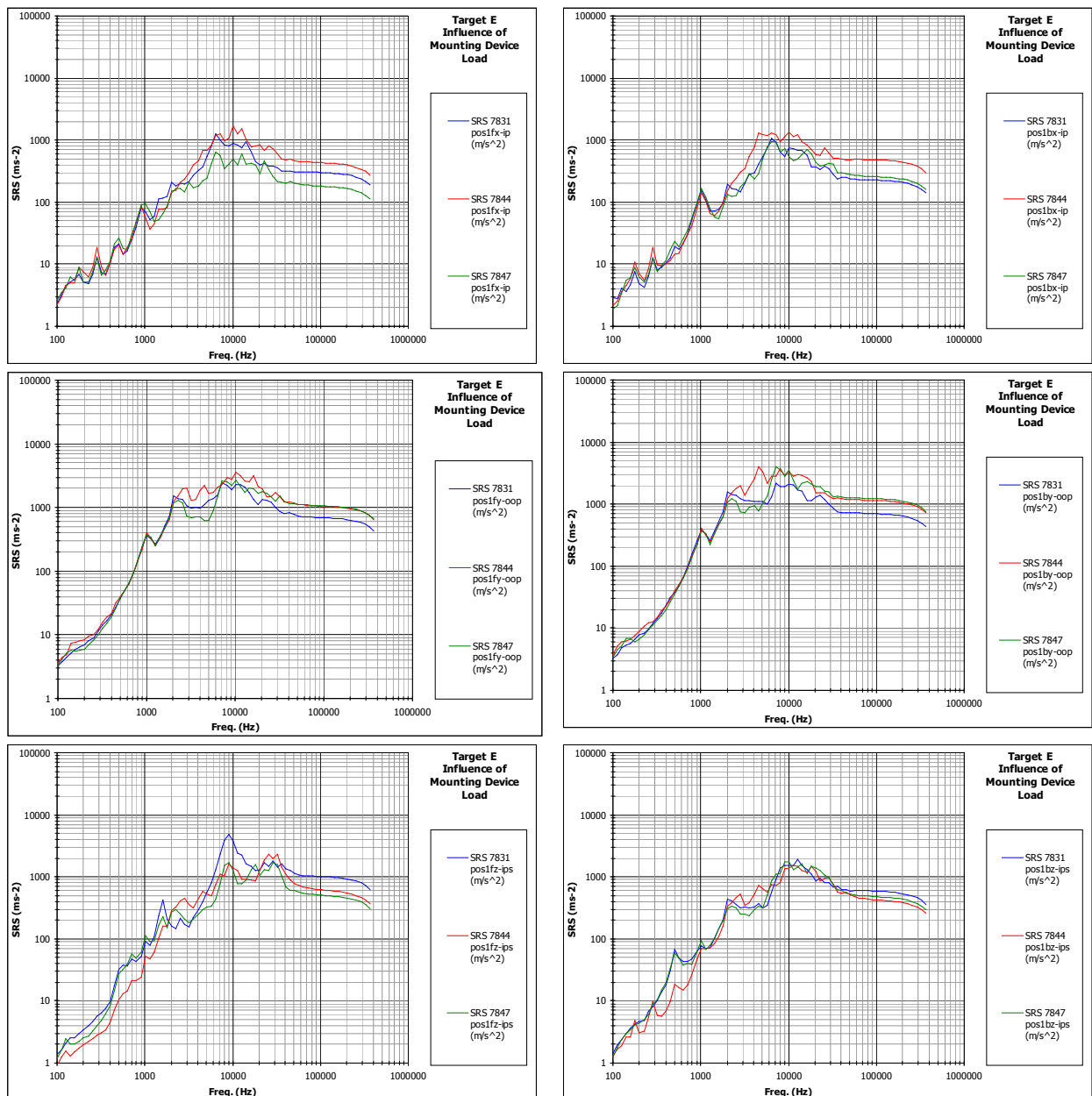
In the test 7844 the following masses were added at the five sensor locations:

- m1=6.638 (g)
- m2=1.397 (g)
- m3=1.397 (g)
- m4=1.397 (g)
- m5=3.255 (g)

In the test 7847 the following masses were added at the five sensor locations:

- m1=13.276 (g)
- m2=2.794 (g)
- m3=2.794 (g)
- m4=2.794 (g)
- m5=6.510 (g)

The out of plane and in plane disturbance SRS recorded on position 1 are reported on Fig. 6-88.



**Fig. 6-88 Influence of the Mounting Device Load SRS ("Pos1" Accelerometer Location)**

It result that uncertainty due to load effects was within 3 dB in the entire SRS frequency band and thus its value is negligible respect to the uncertainty associated with the SRS computation due to scatter. In fact, the uncertainty due to data scattering has a growing trend. Its maximum value increases from  $\sim 2$  dB to  $\sim 4$  dB above  $10^3$  Hz and is below 4 dB (respect to the measure) in the entire SRS frequency band (from 100 Hz to 30 kHz).

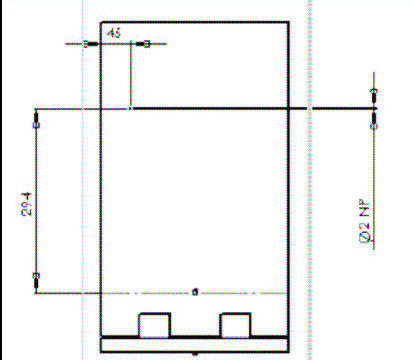
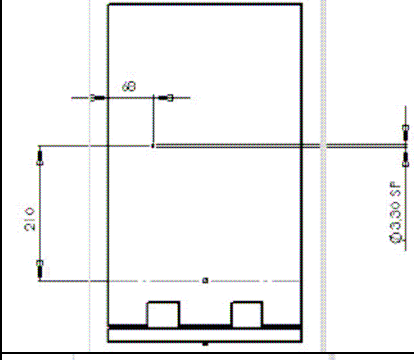
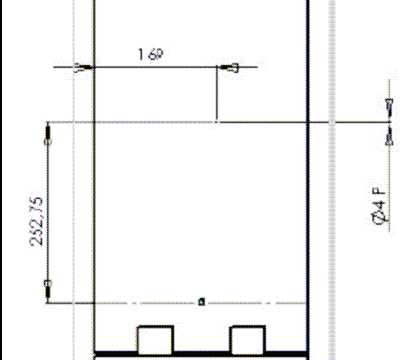
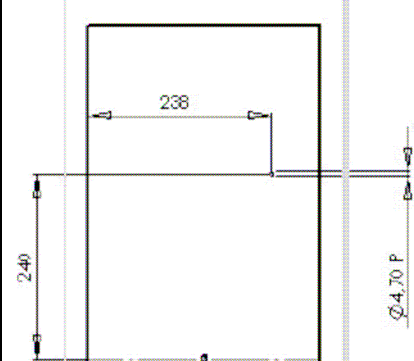
### 6.2.4 Transmission functions (calibration vs mass and velocity)

Eight HVI tests have been conducted for calibration, varying mass and velocity, with generation of damages with and without perforation. The results of these tests are to

be used together with the tests planned to evaluate the influence of impact velocity and projectile size on disturbances. This activity and the results are described in paragraph 6.2.5 and paragraph 6.2.6. The TS312 tests data are summarised in Tab. 6-14.

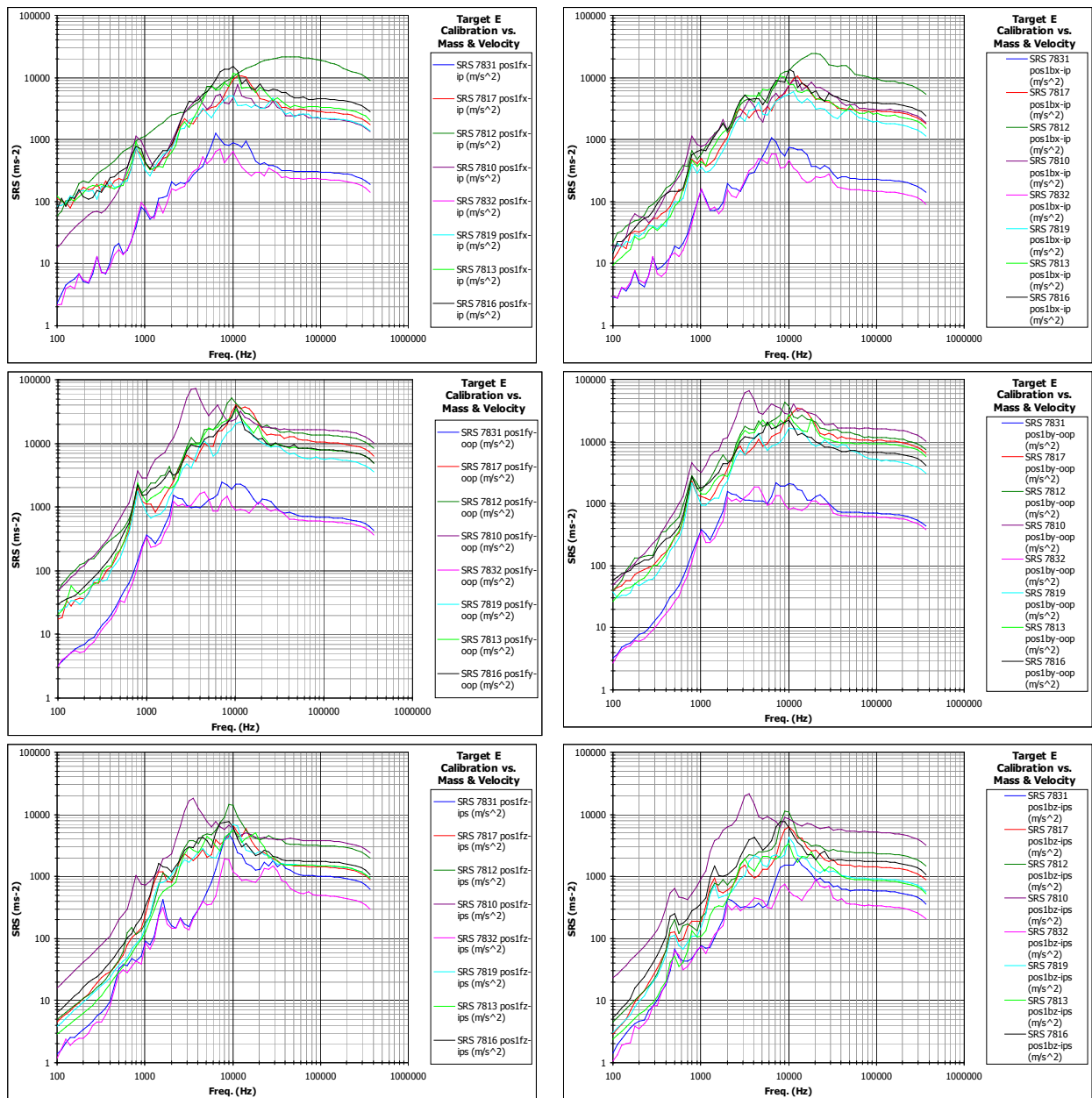
CISAS ID	ESA ID TS -	dp [mm]	vp [km/s]	Coarse Damage	Impact location
7831	312/1	1.0	4.9	NP	
7817	312/2	1.5	5.4	BL >=	
7812	312/3	1.9	5.2	P	
7810	312/4	2.3	5.1	BL >=	



7832	312/5	1.0	4.0	NP	
7819	312/6	1.5	4.1	BL > =	
7813	312/7	1.9	4.2	P	
7816	312/8	2.3	4.4	P	

**Tab. 6-14 Summary of TS312**

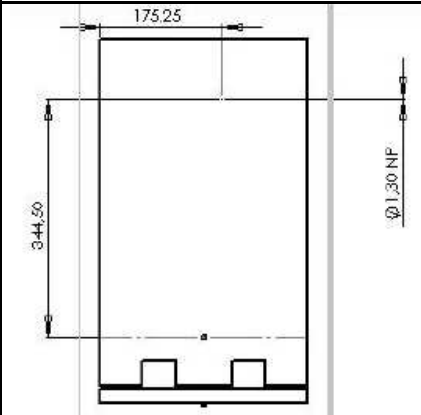
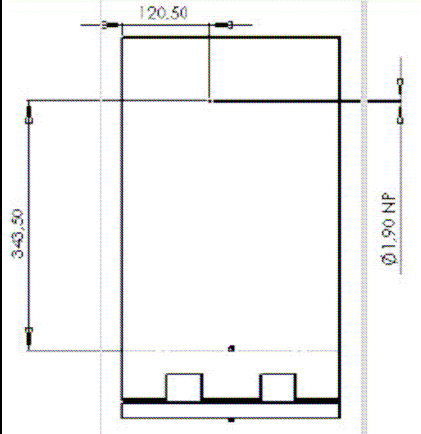
The out of plane and in plane SRS have been calculate on the all accelerometer location. Fig. 6-89 reports out-of-plane and in-plane SRS at position 1.



**Fig. 6-89 Calibration vs. Mass and Velocity SRS ("Pos1" Accelerometer Location)**

### 6.2.5 Influence of impact velocity (TS313)

Together with TS312 tests, two additional hypervelocity tests (see Tab. 6-15) have been conducted to evaluate the influence of the impact velocity on disturbance. Projectiles with the same mass and different velocity have been fired.

CISAS ID	ESA ID TS -	dp [mm]	vp [km/s]	Coarse Damage	Impact location
7828	313/1	1.0	2.6	NP	
7829	313/2	1.0	3.4	NP	

**Tab. 6-15 Summary of TS313**

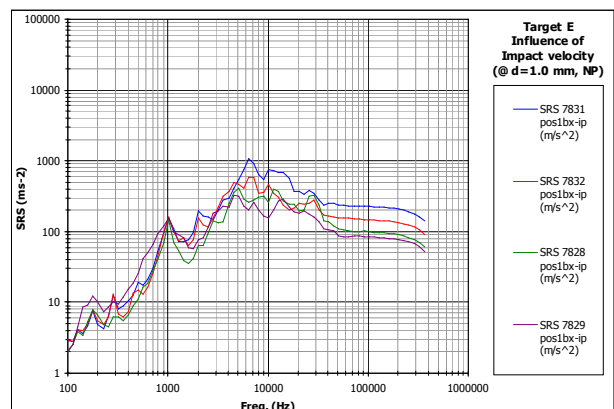
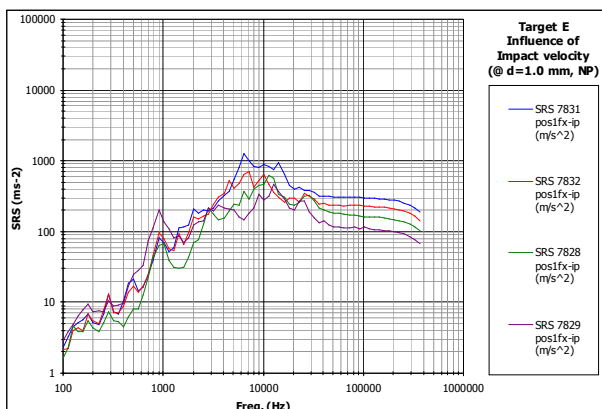
The influence of impact velocity has been evaluated analysing the following groups of tests:

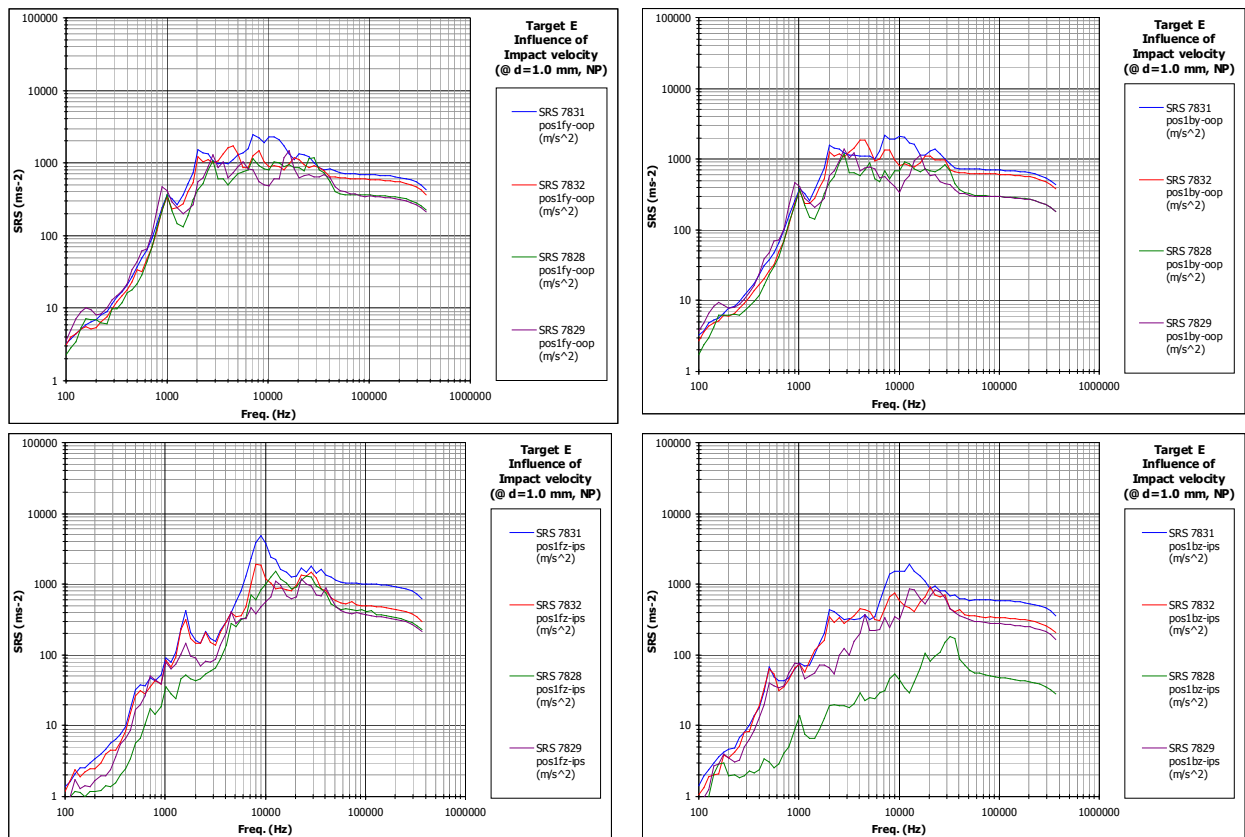
7831, 7832, 7828, 7829. (Projectile diameter: 1.0 mm; No Perforation)

7812, 7813. (Projectile diameter: 1.9 mm; Perforation)

7817, 7819. (Projectile diameter: 1.5 mm; Perforation close to Ballistic Limit)

SRS calculated, based on signals recorded on location 1 during, is presented in Fig. 6-90.





**Fig. 6-90 Influence of Impact Velocity SRS per  $d_p=1.0$  mm, NP ("Pos1" Accelerometer Location) test 7831**

### 6.2.6 Influence of projectile mass (TS314)

Together with TS312 tests, two additional hypervelocity tests (see Tab. 6-16) have been conducted to evaluate the influence of the impact mass on disturbance. Projectiles with the same velocity and different mass have been fired.

CISAS ID	ESA ID TS -	dp [mm]	vp [km/s]	Coarse Damage	Impact location
7838	314/1	0.8	5.1	NP	
7840	314/2	0.6	5.0	NP	

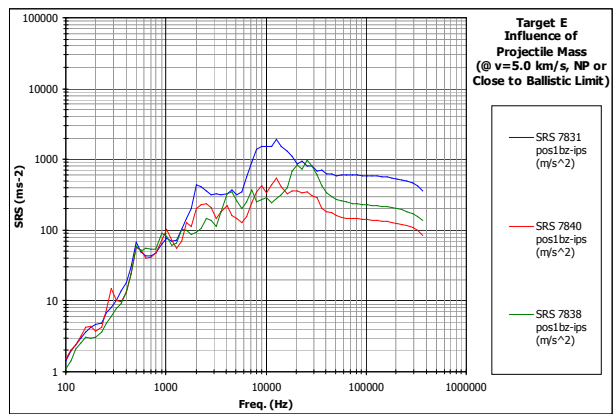
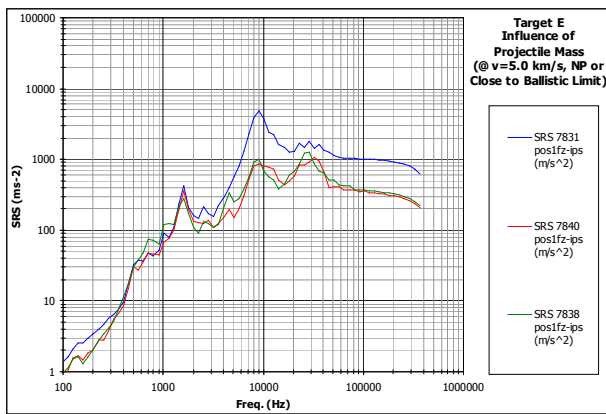
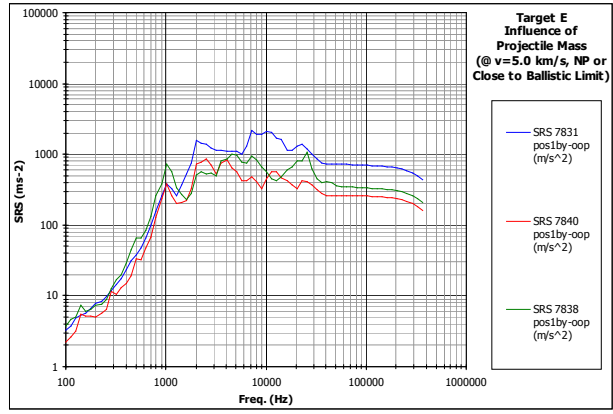
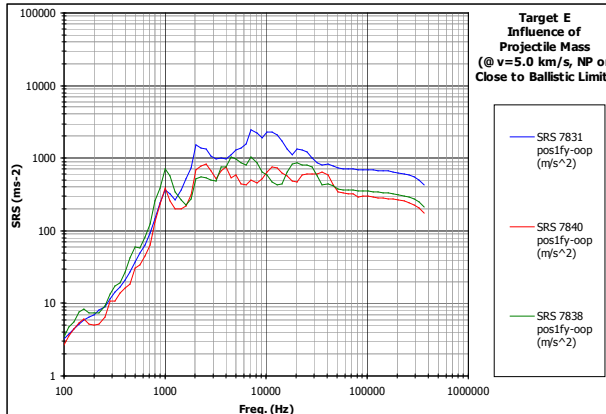
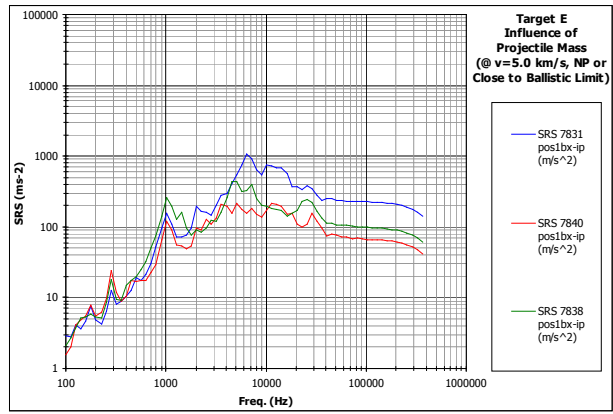
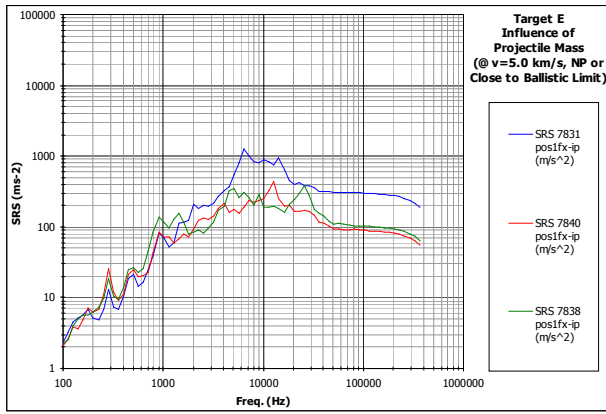
**Tab. 6-16. Summary of TS314**

The following two different groups of tests have been considered in the analysis of the influence of the projectile mass:

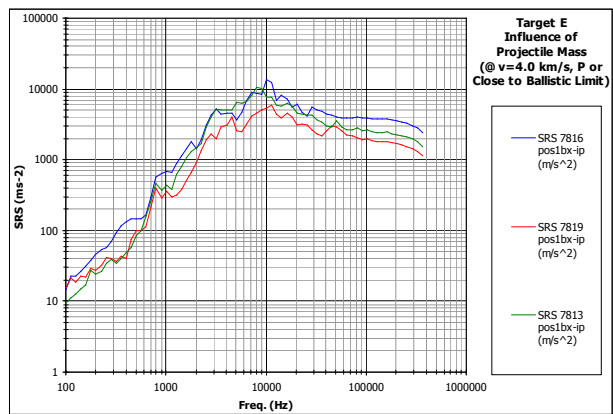
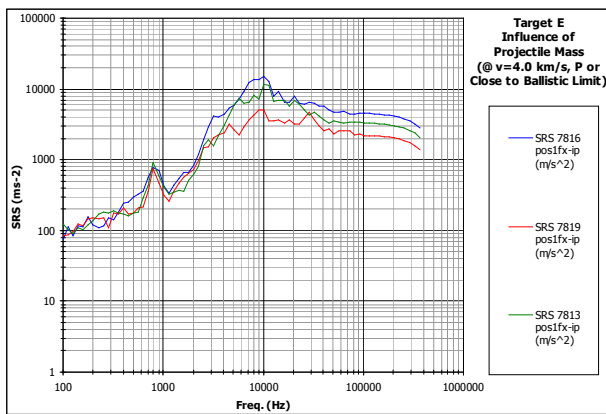
Tests characterised by a damage of No Perforation (or close to Ballistic Limit) and by an impacting velocity of 5.0 km/s.

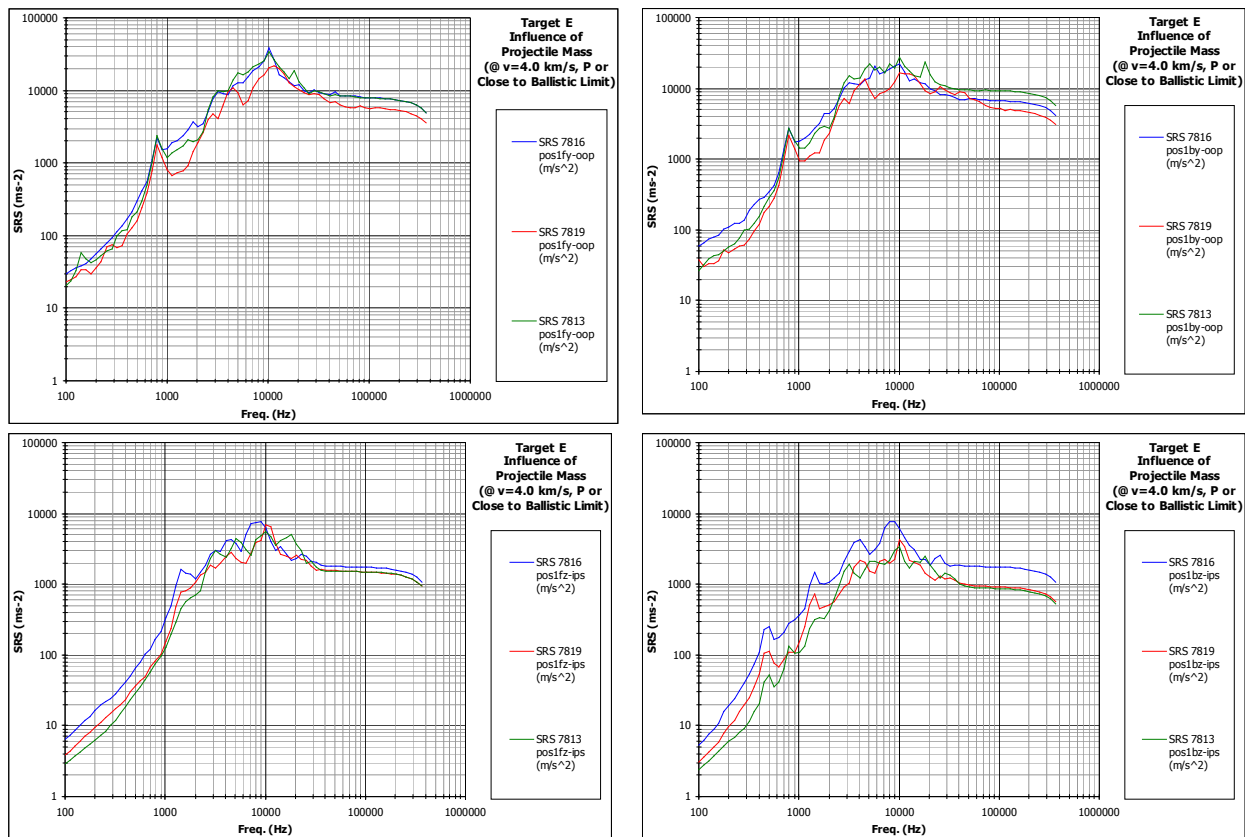
Tests characterised by a damage of Perforation (or close to Ballistic Limit) and by an impacting velocity of 4.0 km/s.

Analysis has been conducted on the all accelerometer locations. Fig. 6-91 presents the SRS calculated based on signal recorded on pos.1 on the 5km/s No penetrating HVI – test. Fig. 6-92 presents the SRS calculated based on signal recorded on pos.1 on the 4km/s Penetrating HVI–test.



**Fig. 6-91 Influence of Projectile Mass SRS per  $V_p=5$  km/s, NP or Close to Ballistic Limit ("Pos1" Accelerometer Location).**





**Fig. 6-92 Influence of Projectile Mass SRS per  $V_p=4$  km/s, P or Close to Ballistic Limit ("Pos1" Accelerometer Location)**

### 6.2.7 Summary of results

Analysis of tests TS312, TS313 and TS314 has conducted at the following considerations:

- Out of plane and in plane disturbance SRS related to the tests with perforation are between 10 to 20 dB higher with respect to the ones related to the tests without perforation (7831, 7832)
- For the tests close to the Ballistic Limit the disturbance SRS are within 5 dB. SRS generally translate linearly with momentum transferred by the projectile, however, this behaviour is most evident above 4000 -5000Hz especially for impact at high velocity (5km/s).
- The measured SRS in the in-plane directions are within 5dB lower than to the SRS measured in the out-of-plane direction.
- SRS dispersion with added mass was within 3dB, which is the SRS dispersion due to repeatability and background effects, thus no further source of uncertainty has been associated to load effect
- SRS dispersion due to data scattering was within 5dB

### 6.2.8 Joints and propagation attenuation functions due to HVI

The post-processing of the SRS functions coming from this GOCE Configuration E test campaign has been also devoted to the extraction of the experimental **transfer functions** of disturbances due to effects of:

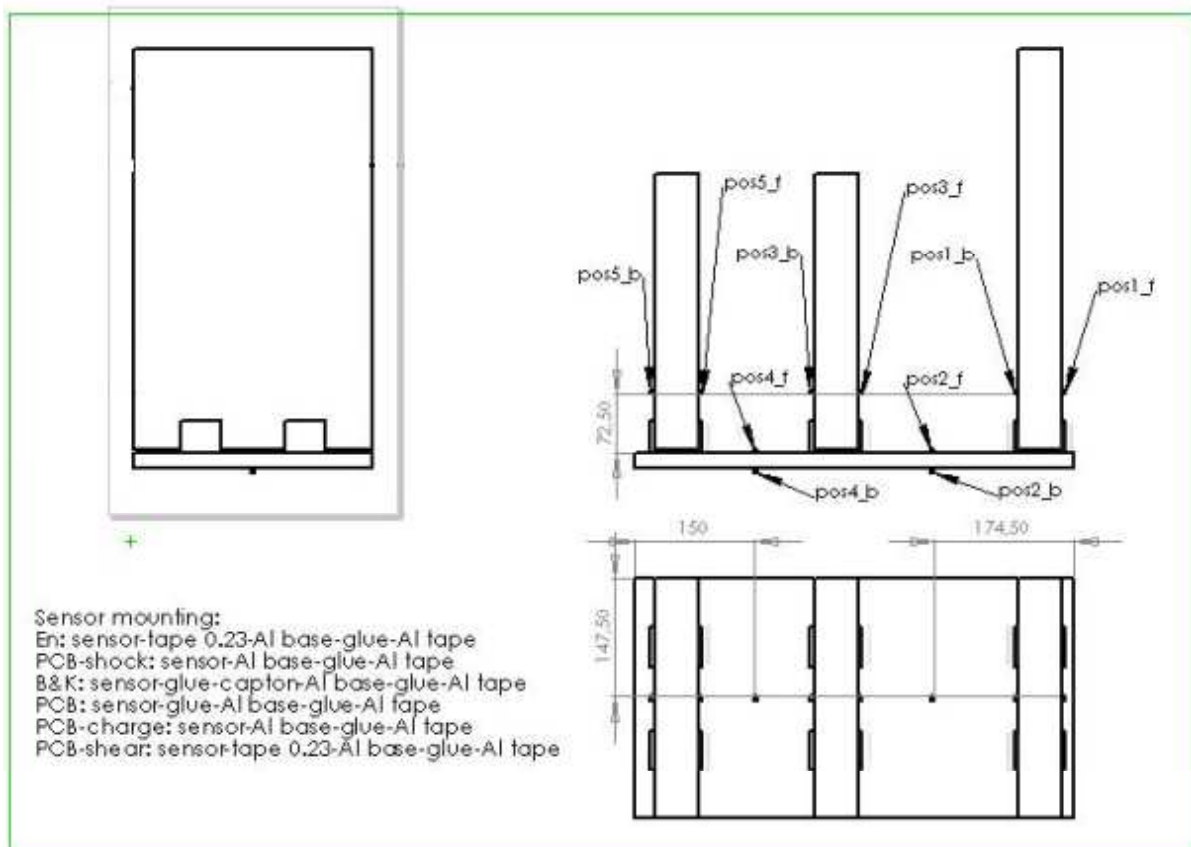
- Junctions

- Distance from hypervelocity impact point

As a first step it was derived, on each accelerometer location, the SRS function that envelope the six experimental SRS functions measured at each accelerometer location:

- The three SRS on the front face along the
  - X Axis (in plane direction)
  - Y Axis (out of plane direction)
  - Z Axis (in plane shear direction)
- The three SRS on the back face along the
  - X Axis (in plane direction)
  - Y Axis (out of plane direction)
  - Z Axis (in plane shear direction)

Fig. 6-93 shows the meaning of the index pos1, pos2, pos3 etc.



**Fig. 6-93 GOCE type E: position indexes**

Then, the results in terms of SRS ratio have been extracted as follow:

- Between the impacted panel (i.e. accelerometer location "pos1") and the connected panels (i.e. accelerometer locations "pos3" and "pos5") to evaluate the global effects of two and three junctions on disturbances in the aluminium vertical panels, located at different distances from the impact point



- Between the impacted panel (i.e. accelerometer location "pos1") and the connected panel (i.e. accelerometer locations "pos2" and "pos4"), to evaluate the influence of one and two junctions on disturbances in the CFRP sandwich panel at different distances from the impact point

In order to obtain the SRS transfer functions (calculated as ratio between different SRS as explained above) representative in different shot parameter conditions (i.e. at different projectile speed, mass and type of impact) the shots reported in Tab. 6-17 and in Tab. 6-18 have been selected.

Shot type	Shot ID	ESA code	Dp (mm)	Vp (km/s)	P/NP	Notes
Calibration Vs. mass & velocity	7819	TS-312/6	1.5	4.1	P	--
Data scattering	7850	TS-315/2	1.5	5.0	P	--
Calibration Vs. mass & velocity	7816	TS-312/8	2.3	4.3	P	--
Calibration Vs. mass & velocity	7810	TS-312/4	2.3	5.1	P	--

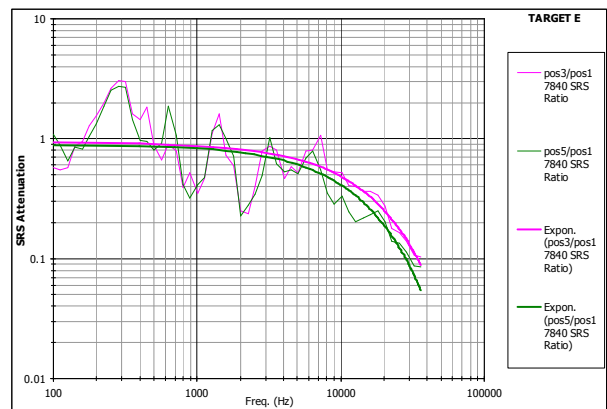
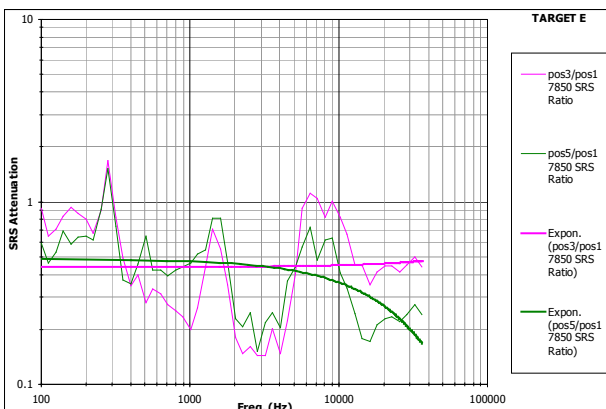
**Tab. 6-17 Penetrating selected shots**

Shot type	Shot ID	ESA code	Dp (mm)	Vp (km/s)	P/NP	Notes
Influence of projectile mass	7840	TS-314/2	0.6	5.0	NP	--
Influence of impact velocity	7829	TS-313/2	1.0	3.4	NP	--
Calibration Vs. mass & velocity	7831	TS-312/1	1.0	4.9	NP	--

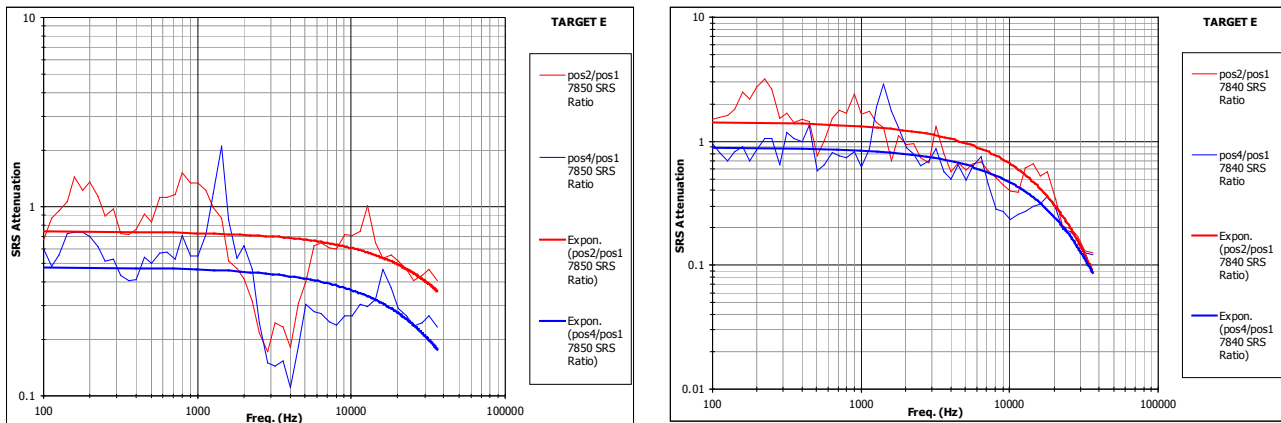
**Tab. 6-18 Non-Penetrating selected shots**

An example of the SRS attenuation functions named "pos3/pos1" and "pos5/pos1" are plotted in Fig. 6-94, while the SRS attenuation functions named "pos2/pos1" and "pos4/pos1" are plotted in Fig. 6-95.

In addition, the exponential trend-lines associated to the SRS attenuation functions are also plotted to represent, in a more useful form, the attenuation effects.



**Fig. 6-94 pos3/pos1 and pos5/pos1 attenuation functions for shot 7850 (P) on the left and 7840 (NP) on the right**



**Fig. 6-95 pos2/pos1 and pos4/pos1 attenuation functions for shot 7850 (P) on the left and 7840 (NP) on the right**

The following observations can be outlined from the analysis of the computed SRS attenuation functions.

Pos5/pos1 and pos3/pos1 attenuation functions:

No significant differences have been found for the two-junctions attenuation ("pos5/pos1" SRS ratio) with respect to the one-junction attenuation ("pos3/pos1" SRS ratio).

In the low frequency range, (i.e. from 100 Hz to about 3000 Hz) the exponential trend-lines associated to the SRS attenuation functions are constant over the frequency range.

In the high frequency range, (i.e. above 3000 Hz) the exponential trend-lines associated to the SRS attenuation functions are decreasing with the frequency.

The corresponding attenuation plateau values are:

From 0.5 to 0.2 for the shots with penetration

From 0.95 to 0.65 for the shots without penetration

Pos4/pos1 and pos2/pos1 attenuation functions

Reduction of about 30-40% has been found from the near location ("pos2/pos1" SRS ratio) to the far location ("pos4/pos1" SRS ratio).

In the low frequency range, (i.e. from 100 Hz to about 3000 Hz) the exponential trend-lines associated to the SRS attenuation functions are constant over the frequency range.

In the high frequency range, (i.e. above 3000 Hz) the exponential trend-lines associated to the SRS attenuation functions are decreasing with the frequency.

The corresponding attenuation plateau values are:

- Between 0.25 and 0.75 for the shots with penetration
- Between 0.65 and 1.5 for the shots without penetration

Considering joint behaviour the following observation can be made on the conversion between IP and OP waves (presented only for NP shots for brevity):

- The transmission of the OP wave on the shooter panel to an IP wave on the receiver panel induces an averaged attenuation effect of 80 % related to the NP shot test. By this transmission, the junction acts as an absorber due to different mechanical impedance between the panels and the junction itself, as expected.
- The transmission of the IP wave on the shooter panel to an OP wave on the receiver panel induce firstly an averaged amplification factor of 2 at 1 kHz related to the P shot test 1.9 and at 1 kHz related to the NP shot test. Secondly an averaged attenuation effect of 87.5% related to the NP shot testing. By this transmission the junction act as a resonant structure that induce an amplification and attenuation effect

The transmission between front skin to rear skin for not-perforating (NP) test:

- OP transmission: no relevant attenuation effect; but an amplification factor of 1.8 due to a system resonance at around 2.6 KHz
- IP direction: attenuation effect of 30 % due to the induced shear movement of the skins, as expect

### 6.2.9 Relevant results for TS31 (GOCE E target)

The main achievements of TS31 are summarised hereafter. Quantitative information is provided in the above plots.

<b>Impact hammer</b>	Low, medium and High frequency range	SRS quality data exploitable up to 4 KHz SRS magnitude < 1KHz comparable with the one got by shot test while for frequency > 1 KHz significantly lower than the one got by shot test The data are usable for the derivation of the: <ul style="list-style-type: none"> <li>• Junction effect</li> <li>• Amplification &amp; attenuation effect</li> <li>• Core effect</li> </ul>
	Front/rear side	Exploitable data for the IP and OP core effect derivation
<b>Junction effect</b>	Dynamics effect of the junction considering the transmission from OP ⇒ IP wave	The transmission of the OP wave on the shooter panel to an IP wave on the receiver panel <b>induce an averaged attenuation effect</b> of: <ul style="list-style-type: none"> <li>66.7 % related to the hammer test</li> <li>80 % related to the NP shot test</li> </ul> By this transmission, the junction acts as an absorber due to different mechanical impedance between the panels and the junction itself, as expected.
<b>Amplification &amp; attenuation effect</b>	Dynamics effect of the junction considering the transmission from IP ⇒ OP wave	The transmission of the IP wave on the shooter panel to an OP wave on the receiver panel induce firstly an averaged amplification factor of <ul style="list-style-type: none"> <li>1.35 at 1 KHz related to the hammer test</li> <li>2 at 1 kHz related to the P shot test</li> <li>1.9 at 1 kHz related to the NP shot test</li> </ul> secondly an averaged <b>attenuation effect of 40 %</b> and <b>87.5%</b> respectively related to the hammer and the NP shot testing. By this transmission the junction act as a resonant structure that induce an amplification and attenuation effect as expected..

<p><b>Core effect</b></p>	<p>Dynamics effect of the core considering the wave transmission from Front skin ⇒ rear skin</p>	<p>Related to the hammer testing:  <b>OP</b> transmission ⇒ no relevant attenuation effect; but an <b>amplification factor of 1.8</b> due to a system resonance at around 2.6 KHz  <b>IP</b> direction <b>attenuation effect of 20 %</b> due to the induced shear movement of the skins ,as expected.  Related to the NP shot testing:  <b>OP</b> transmission ⇒ no relevant attenuation effect; but an <b>amplification factor of 1.8</b> due to a system resonance at around 2.6 KHz  <b>IP</b> direction <b>attenuation effect of 30 %</b> due to the induced shear movement of the skins, as expect</p>
---------------------------	--	---

**Tab. 2-6-19. Relevant results for TS31**

**6.2.10 Relevant result for other test**

Experiments has been done on others GOCE configurations other than E. The results of such test are reported in the following three paragraphs for completeness.

- **TS32** GOCE target type G
- **TS33** GOCE target type D
- **TS34** GOCE target type C

**6.2.11 Relevant results for TS32**

The main achievements of TS32 are summarised hereafter. Quantitative information is provided in the above plots.

<p><b>Impact hammer</b></p>	<p>Low, medium and High frequency range</p>	<p>SRS quality data exploitable up to 4 KHz  SRS magnitude &lt; 1KHz comparable with the one got by shot test while for frequency &gt; 1 KHz significantly lower than the one got by shot test  The data are usable for derivation of:</p> <ul style="list-style-type: none"> <li>• Junction effect</li> <li>• Amplification &amp; attenuation effect</li> <li>• Core effect</li> </ul>
	<p>Front/rear side</p>	<p>Exploitable data for the IP and OP core effect derivation.</p>
<p><b>Junction effect</b></p>	<p>Dynamics effect of the junction considering the transmission from OP ⇒ IP wave</p>	<p>The transmission of the OP wave on the shooted panel to an IP wave on the receiver panel induce an averaged <b>attenuation effect of:</b>  <b>66.7 % related to the hammer test</b>  <b>64% related to the P shot test</b>  <b>77.4% related to the NP shot test</b>  By this transmission, the junction acts as an absorber due to different mechanical impedance between the panels and the junction itself, as expected.  This phenomenon is observed for both type of transitory excitation i.e. the Hammer and the shot ones.</p>

<b>Amplification &amp; attenuation effect</b>	Dynamics effect of the junction considering the transmission from IP $\Rightarrow$ OP wave	The transmission of the IP wave on the shooter panel to an OP wave on the receiver panel induce firstly an averaged amplification factor of <b>1.35</b> at 1 KHz related to the hammer test <b>2</b> at 1 kHz related to the penetrating (P) shot test <b>1.9</b> at 1 kHz related to the non penetrating (NP) shot test Secondly, an averaged <b>attenuation effect of 40 %</b> and <b>87.5%</b> respectively related to the hammer and the NP shot testing. By this transmission, the junction acts as a resonant structure that induces an amplification and attenuation effect as expected.
<b>Core effect</b>	Dynamics effect of the core considering the wave transmission from Front skin $\Rightarrow$ Rear skin	Related to the hammer testing: <b>OP</b> transmission $\Rightarrow$ no relevant attenuation effect; but an <b>amplification factor of 1.8</b> due to a system resonance at around 2.6 KHz <b>IP</b> direction <b>attenuation effect of 20 %</b> due to the induced shear movement of the skins, as expected. Related to the NP shot testing: <b>OP</b> transmission $\Rightarrow$ no relevant attenuation effect; but an <b>amplification factor of 1.8</b> due to a system resonance at around 2.6 KHz <b>IP</b> direction <b>attenuation effect of 30 %</b> due to the induced shear movement of the skins, as expected

**Tab. 2-6-20. Relevant results for TS32**

### 6.2.12 Relevant results for TS33

The main achievements of TS33 are summarised hereafter. Quantitative information is provided in the above plots.

<b>Impact hammer</b>	Low, medium and High frequency range	SRS quality data exploitable up to 4 KHz SRS magnitude < 1KHz comparable with the one got by shot test while for frequency > 1 KHz significantly lower than the one got by shot test The data are usable to for deriving: <ul style="list-style-type: none"> <li>• Junction effect</li> <li>• Amplification &amp; attenuation effect</li> <li>• Core effect</li> </ul>
	Front/rear side	Exploitable data for the IP and OP core effect derivation.

<b>Junction effect</b>	Dynamics effect of the junction considering the transmission of IP waves from the emitter to the receiver panel	The transmission of the IP wave to the receiver panel induce an averaged <b>attenuation effect o :</b> <b>38% on the IP direction related to the NP shot test</b> <b>38.5% on the IP direction related to the P shot test</b> By this transmission, the junction acts as an absorber due to different mechanical impedance between the panels and the junction itself, as expected. This phenomenon is observed for both type of transitory excitation i.e. the Hammer and the shot ones.
<b>Amplification &amp; attenuation effect</b>	Dynamics effect of the junction considering the transmission OP waves from the emitter to the receiver panel	The transmission of the OP wave to the receiver panel induce firstly an averaged amplification factor of <b>3.0</b> at 400 Hz related to the non penetrating (NP) shot test on OP direction Secondly, an averaged <b>attenuation effect of 40 %</b> related to the NP shot testing. By this transmission the junction act as a resonant structure that induce an amplification and attenuation effect as expected.
<b>Core effect</b>	Dynamics effect of the core considering the wave transmission from <i>Front skin</i> ⇒ <i>rear skin</i>	Related to the NP shot testing: <b>OP</b> transmission ⇒ an <b>attenuation effect of 43%</b> due to the different mechanical impedance between the panel face sheets and the HC core <b>IP</b> direction ⇒ <b>attenuation effect of 40 %</b> due to the induced shear movement between the panel face sheets and the HC core.

**Tab. 2-6-21. Relevant results for TS33**

### 6.2.13 Relevant results for TS34

The main achievements of TS34 are summarised hereafter. Quantitative information is provided in the above plots.

<b>Impact hammer</b>	Low, medium and High frequency range	SRS quality data exploitable up to 4 KHz SRS magnitude < 1KHz comparable with the one got by shot test while for frequency > 1 KHz significantly lower than the one got by shot test The data are usable for deriving the: <ul style="list-style-type: none"> <li>• Junction effect</li> <li>• Amplification &amp; attenuation effect</li> <li>• Core effect</li> </ul>
	Front/rear side	Exploitable data for the IP and OP core effect derivation.

<p><b>Junction effect</b></p>	<p>Dynamics effect of the junction considering the transmission from <i>OP</i> ⇒ <i>IP</i> wave</p>	<p>The transmission of the OP wave on the shooter panel to an IP wave on the receiver panel induce an averaged <b>attenuation effect of: 80% related to the non penetrating shot test</b>  By this transmission, the junction acts as an absorber due to different mechanical impedance between the panels and the junction itself, as expected.  This phenomenon is observed for both type of transitory excitation i.e. the Hammer and the shot ones.</p>
<p><b>Amplification &amp; attenuation effect</b></p>	<p>Dynamics effect of the junction considering the transmission from <i>IP</i> ⇒ <i>OP</i> wave</p>	<p>The transmission of the IP wave on the shooter panel to an OP wave on the receiver panel induce firstly an averaged amplification factor of <b>2.6</b> at 1kHz related to the NP shot test. Secondly, an averaged <b>attenuation effect of 40 %</b> related to the NP shot testing.  By this transmission the junction act as a resonant structure that induce an amplification and attenuation effect as expected</p>
<p><b>Core effect</b></p>	<p>Dynamics effect of the core considering the wave transmission from <i>Front skin</i> ⇒ <i>Rear skin</i></p>	<p>Related to the NP shot testing:  <b>OP</b> transmission ⇒ an <b>attenuation effect of 43%</b> due to the different mechanical impedance between the panel face sheets and the HC core  <b>IP</b> direction ⇒ <b>attenuation effect of 40 %</b> due to the induced shear movement between the panel face sheets and the HC core</p>

**Tab. 2-6-22. Relevant results for TS34**

### 6.3 Momentum transfer evaluation (TS4)

Whether the main objective of this work was to investigate the transient disturbances induced by HVI (micrometeoroids and space debris), it also provided a fundamental input to predict the vibration environment on a general spacecraft structure. In fact, the definition of transfer functions on complex assemblies (see paragraph 6.2.4) provides a tool for propagating the disturbance field on not-impacted plates employing simple and fast numerical codes (NASTRAN and FEA) only knowing the momentum transferred by the projectile to the target. The procedure is detailed in the following.

Three types of codes were used: a hydrocode (Autodyn2D by Century Dynamics Ltd.) to simulate the HVI dynamics, a finite element solver (Nastran by MSC) for structural transient dynamics calculations in the vicinity of the impact point (near-field) and a statistical energy solver (AutoSEA by ESI) for shock propagation along large structures including joints (mid- and far-field).

SPH was used to simulate the perforation dynamics thus providing the requested near-field input to Nastran, expressed by an **Equivalent-Force-Time-History** (EFTH). The EFTH is defined as the force-time-history that, if applied to the structure, generates, below 10 kHz, an SRS within 3dB respect to the experimental one, see Fig. 6-96 (the experimental impact site coincides with the point of application of the equivalent EFTH and acceleration are evaluated at the same location where accelerometers are placed in reality).

The EFTH has been calculated from the **Force Time History** obtained with SPH simulation (FTH), since this function has a frequency band much higher respect to that tolerated by finite elements calculations. The EFTH is computed from the FTH from the equivalence of the transferred momentum between the projectile and the impacted target. In other words, EFTH is different from the real one provided by HVI on the structure (which happens at time scales much shorter than those), it nevertheless has the capacity of transferring to the target the same amount of momentum (which is the force-impulse Ns).

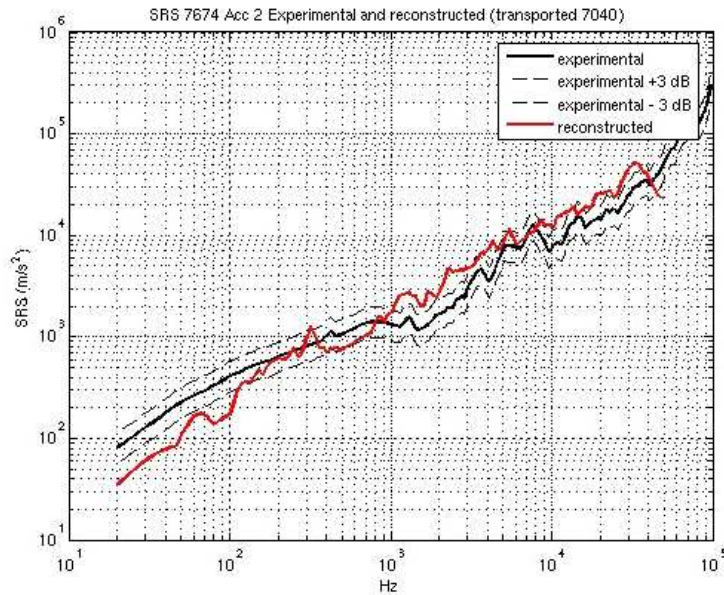
If such constraint is satisfied, SRS reconstruction was successfully performed for simple aluminium plates and for aluminium honeycomb sandwich panels, for both OP and IP waves within 3dB (see for instance Fig. 6-96, referring to a 5 km/s impact of a 2.3 mm sphere onto an simple aluminium plate).

The validation of the EFTH reconstruction method came out from the comparison of momentum computed by numerical codes (SPH and NASTRAN) and momentum experimentally measured (presented in this paragraph).

In summary, the EFTH can be applied to finite element model to allow data extrapolation to different structures or for different impact conditions.

Only the experimental procedure for momentum evaluation is presented in this thesis, the result of simulations and comparison between experiments and codes can be found in [28].





**Fig. 6-96 FEM reconstruction of experimental SRS through an equivalent force impulse. OP wave.**

The momentum transferred by HVI to a target has been measured using a ballistic pendulum. The result of the experimental tests has been used to assess the numerical simulations made with SPH.

The content of paragraph 6.3 is summarised in Tab. 6-23.

Main task	Description	Page
Test logic for TS4	Summary of the tests performed to evaluate momentum transferred to different targets	129
Measurement method	Description of the measurement principle	129
Experimental set-up	Hardware configuration	131
Calibration	Calibration to find out the relationship between hammer pulse input and transferred momentum, to be used for extrapolations from HVI	132
Uncertainty analysis	Evaluation of uncertainty to be applied for extrapolations on momentum transferred during HVI	135
Background noise	Extrapolation of the momentum imparted by propellant to the experimental arrangement	136
Simple Al plates (TS41)	Momentum transfer to simple Al plates: measurements after HVI	137
Al HC SP (TS42)	Momentum transfer to Al HC SP: measurements after HVI	137
CFRP HC SP (TS42)	Momentum transfer to CFRP HC SP: measurements after HVI	138
Relevant results about momentum transferred by HVI to targets	Summary of the main engineering results relevant to TS4	138

**Tab. 6-23 Summary of contents for paragraph 6.3**

### 6.3.1 Test logic for TS4

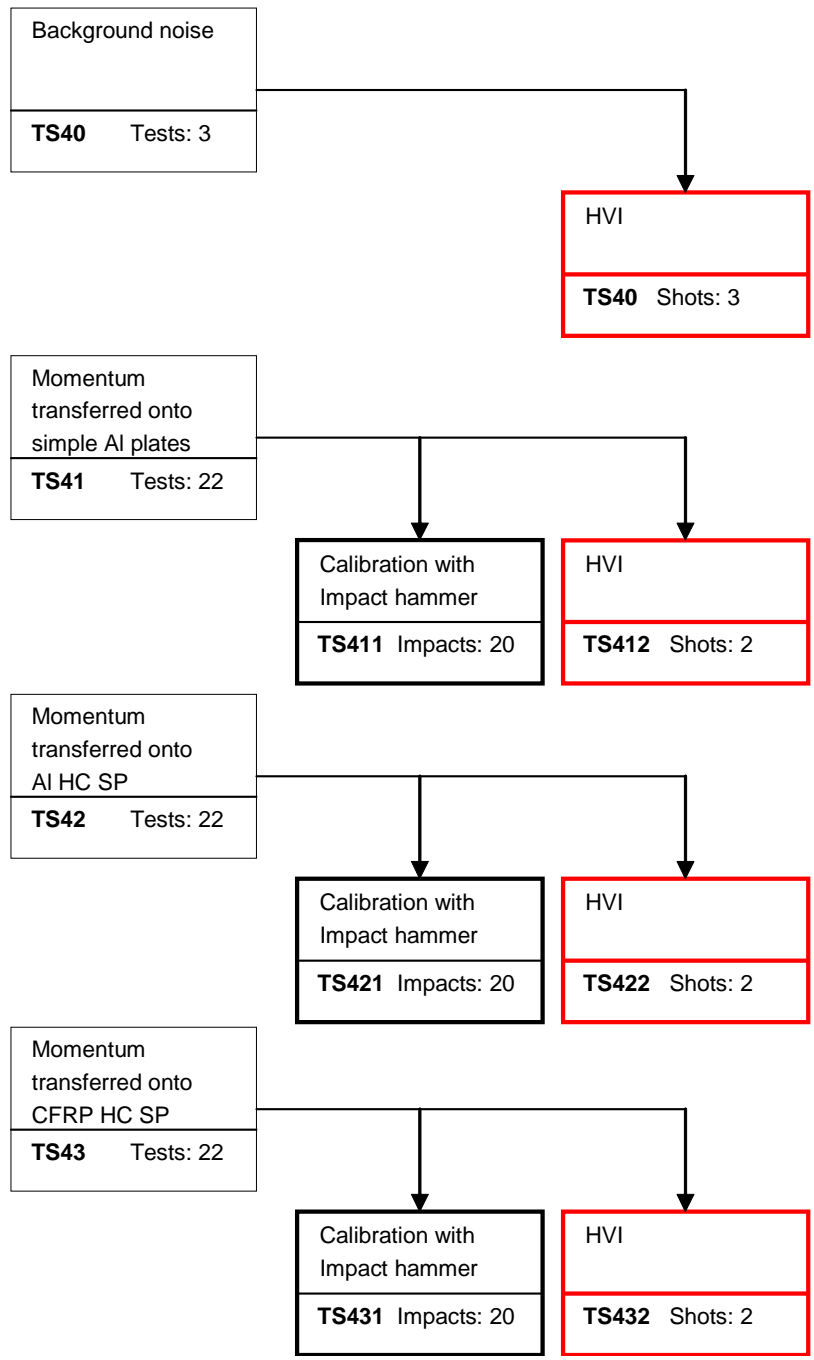
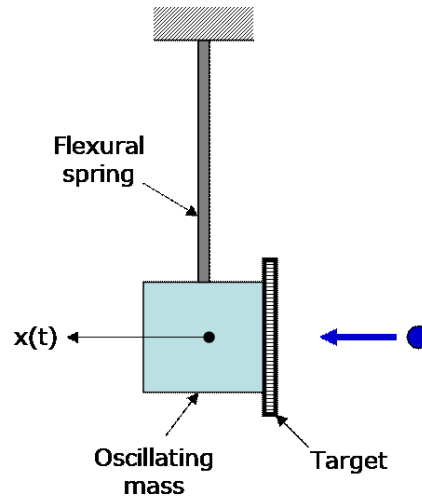


Fig. 6-97. Test logic for TS4.

### 6.3.2 Measurement method

The momentum transferred to targets is estimated through a ballistic pendulum, composed by a spring-suspended-oscillating-mass on which the target (simple Al plate, Al HC SP, CFRP HC SP) is mounted (Fig. 6-98).



**Fig. 6-98. Ballistic pendulum. Single degree of freedom schematic**

According to a simplified single degree of freedom model, the frequency response of the pendulum to an ideal force pulse of amplitude  $F_0$  is:

$$X(f) = \frac{F_0/k}{\left(\frac{i2\pi f}{\omega_n}\right)^2 + 2\zeta \frac{i2\pi f}{\omega_n} + 1} \quad \text{Eq. 6-1}$$

with the following meaning for symbols:

$m$	Pendulum mass	$f_n = \frac{\omega_n}{2\pi} = \frac{1}{2\pi}$	Natural frequency of the single degree of freedom system
$k$	Stiffness of the flexural spring	$\zeta = \frac{c}{2\sqrt{k \cdot m}}$	Damping ratio
$c$	Damping factor of the suspension		

It is clear from Eq. 6-1 that the amplitude of oscillations is proportional to the force pulse.

Another way of seeing the same problem it is to apply the energy conservation, between the initial state immediately after the impact, (assuming no target displacement. Due to the short duration of the impact the target has only an initial velocity) and the final position (on which velocity is zero and the all initial kinetic energy is converted in spring elastic energy):

$$\frac{1}{2} \cdot m \cdot v_{target}^2 = \frac{1}{2} \cdot k \cdot x_{max}^2 + E_d \quad \text{Eq. 6-2}$$

with the following meaning for symbols:

$v_{target}$ :	Initial speed of target centre of mass	$x_{max}$	Maximum target displacement
$E_d$	energy dissipated through atmospheric drag and spring hysteresis		

From equation Eq. 6-2 neglecting  $E_d$ , the initial target velocity becomes:

$$v = \sqrt{\frac{k}{m}} \cdot x_{max} = 2 \cdot \pi \cdot f_n \cdot x_{max} \quad \text{Eq. 6-3}$$

where  $f_n$  is the natural frequency of the suspended system.  
Thus finally we get:

$$q = m_{target} \cdot \omega_n \cdot x_{max} \quad \text{Eq. 6-4}$$

Where  $q$  is the total momentum transferred to the target computed in the direction of the single degree of freedom system.

Therefore, the momentum transferred to the target can be evaluated from the measurement to the maximum displacement after impact on the target itself.

### 6.3.3 Experimental set-up

Several considerations shall be done on the application of such a method to the real system:

The real arrangement should be as close as possible to a single degree of freedom system, allowing momentum gain only in the direction of interest. Spurious translational or rotational modes could interfere with the measurement procedure. Calibration procedures are highly recommended to account for actions that cannot be modelled easily, i.e. those producing energy dissipation terms.

Taking account previous statements, the following system has been set-up (Fig. 6-99). The oscillating mass is an Al alloy supporting frame (200x200x30 mm<sup>3</sup>, 3.2 kg) with a large central hole to avoid the debris cloud capture by the pendulum. In this way, the pendulum measures only the fraction of projectile momentum, which is transferred to the target, without accounting for that part belonging to the debris cloud.

The system is suspended in such a way that the first natural mode is the translation motion in the direction of the projectile flight and all the other modes occur at much higher frequencies.

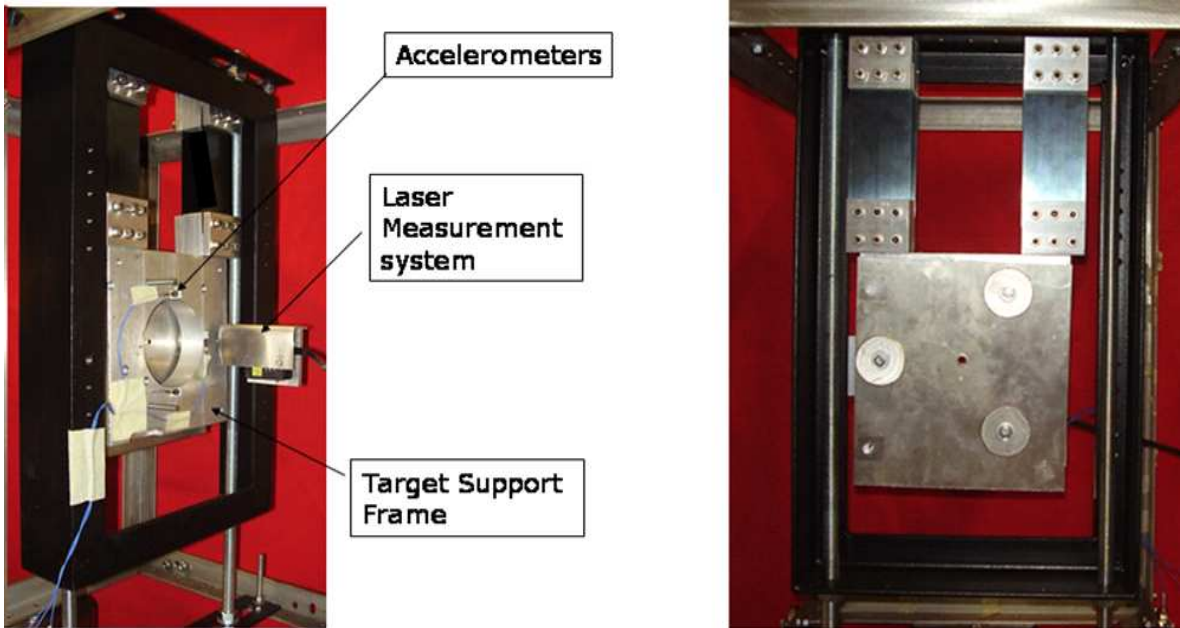


Fig. 6-99 Ballistic pendulum mechanical set-up

Displacement is measured by means of an optoelectronic distance sensor MEL M5/10:

Sensor	Range [mm]	Linearity (mm)	Resolution	Sampling frequency
MEL M5/10	10	±0.02	0.003	2.5 kHz

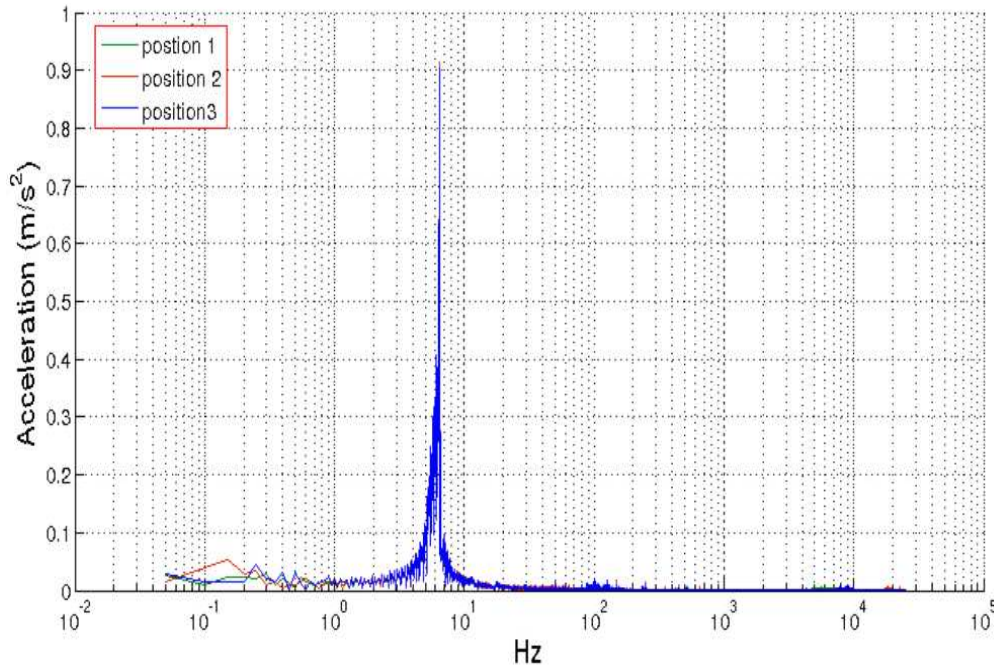
### 6.3.4 Calibration

The system has been calibrated:

- To verify the decoupling between pure transactional mode in the direction of the projectile and other natural modes
- To determine the correlation function between momentum transferred and target displacement (using hammer testing)
- To evaluate the uncertainty to be applied to momentum measurements

#### Natural frequencies

Natural frequencies of the system have been characterized using six accelerometers located onto the pendulum to analyse motion along six degrees of freedom. Below 10 kHz, signal FFT showed no natural mode other than the transactional one, at around 7 Hz (Fig. 6-100).



**Fig. 6-100. Modal response of the ballistic pendulum assembly**

Correlation function between pendulum displacement and hammer input

The correlation function has been characterized hitting the target with an instrumented hammer, which provides the force impulse applied to the target. The measured maximum displacement has been then correlated to the applied momentum through a regression fit.

The total momentum applied to the target  $q_{tot}$  is equal to the integral of the force applied by the hammer (i.e. impulse  $I_{hammer}$ ) minus the integral of the force applied by constraint-reaction-forces on the same time interval (i.e. impulse  $I_{elastic}$ ).

$$q_{tot} = I_{hammer} - I_{elastic}$$

$$I_{hammer} = \int_0^{\Delta t} F \cdot dt$$

$$I_{elastic} = \int_0^{\Delta t} k \cdot x \cdot dt$$

Eq. 6-5

$F$	The force applied by the hammer	$k$	Constraints equivalent stiffness
$\Delta t$	Time duration of the pulse applied by the hammer	$x$	Constrain displacement

It was found that the momentum  $I_{elastic}$  applied by elastic forces may be neglected in previous equation.

In fact, in the time being the hammer hits the target,  $I_{elastic}$  can be calculated considering the analytic response of a single degree of freedom system to a rectangular pulse load. If hypothesis of small displacements are applicable, the ratio of

hammer-impulse to elastic force impulse (in the same time step) can therefore be expressed as follows

$$I_{hammer} / I_{elastic} = (\omega_n \cdot T)^2 \quad \text{Eq. 6-6}$$

$$\omega_n = 2 \cdot \pi \cdot f_n$$

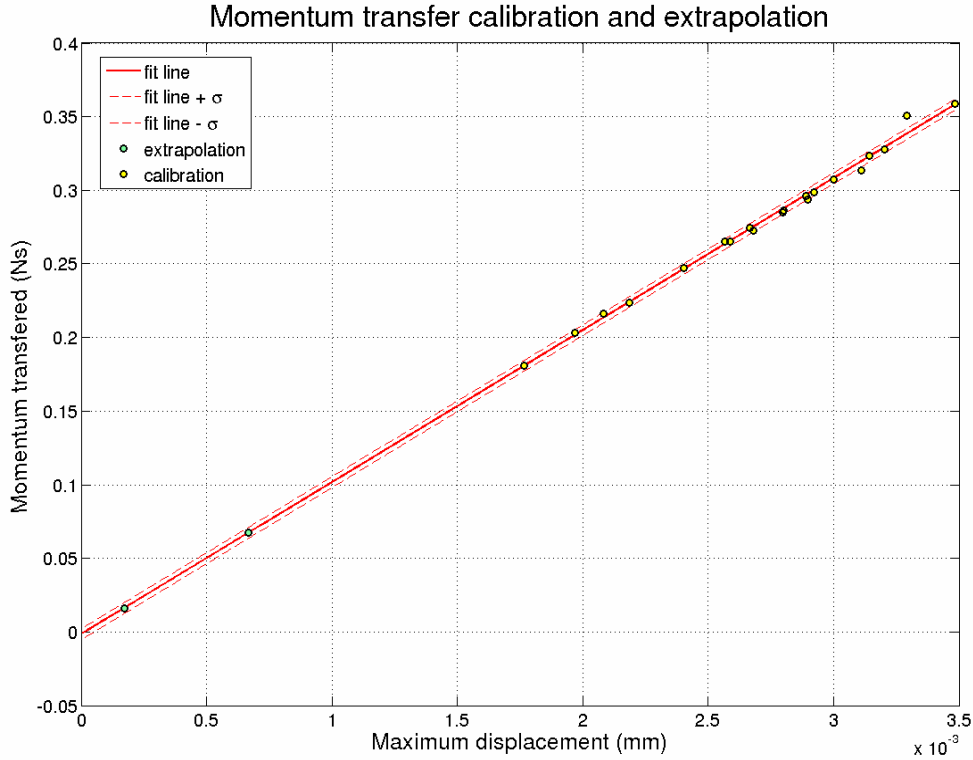
where  $f_n$  is the transactional natural frequency ( $\sim 7$  Hz in our case ) and  $T$  is the time duration of the impact (during calibration was always  $< 1$  ms). Hence, from Eq. 6-6 it comes up that the error related to the assumption  $q_{tot} = I_{hammer}$  is less than 0.2 %.

With the aforementioned assumption, several calibration tests were performed on each target configuration, and the mean-square-root-regression-method was applied to determine the correlation line between applied momentum and pendulum displacement (see for example Fig. 6-101). For each calibration function, standard deviation is finally determined through the following expression:

$$\sigma_{fit} = \sqrt{\frac{\sum_{i=1}^n (y_i - \bar{y}_i)^2}{n-1}} \quad \text{Eq. 6-7}$$

With the following meaning for symbols:

$y_i$	On each test is the momentum applied	$n$	Number of test
$\bar{y}_i$	Is the mean square root value correspondent to the i-test		



**Fig. 6-101 Example of ballistic pendulum calibration curve**

### 6.3.5 Uncertainty analysis

Uncertainty on momentum measurement is related to:

Uncertainty on the calibration procedure, represented by  $\sigma_{fit}$  (Eq. 6-7)  
Momentum transferred by propellant gas hitting the target.

Momentum transferred from propellant gas has been considered as a systematic impulse, thus it can be measured and subtracted from the estimation. Three tests have been performed to characterize this input. An average value and related standard deviation have been calculated ( $\sigma_{gas}$ )

At this point, the momentum transferred by the projectile on each configuration has been calculated, according to ENV 13005 [4], subtracting from the measured momentum the average momentum transferred from the gas, and applying an uncertainty band calculated as follows:

$$\sigma_T = \sqrt{\sigma_{fit}^2 + \frac{\sigma_{gas}^2}{n_{gas}}} \quad \text{Eq. 6-8}$$

where  $n_{gas}$  is the total number of tests to evaluate momentum transferred from gas (three).



In the following tables it is also presented the ratio between momentum transferred to the target and projectile momentum ( $r_{T/P} = q_T/q_P$ ) with its uncertainty calculated as suggested by ENV 13005 [4]:

$$\sigma_{t/p} = \sqrt{\left(\frac{1}{q_p}\right)^2 \cdot \sigma_T^2 + \left(\frac{q_T}{q_p^2}\right)^2 \cdot \sigma_p^2} \quad \text{Eq. 6-9}$$

$q_p$	momentum carried by the projectile	$q_T$	Momentum transferred to the target
$\sigma_p$	Standard deviation on projectile momentum	$\sigma_P$	Standard deviation on total momentum transfer

$\sigma_p$  is calculated propagating the uncertainty on projectile speed on the momentum equation neglecting uncertainty on mass:

$$\sigma_p = m_p \cdot \sigma_v$$

On which  $\sigma_v$  is the standard deviation on speed measurement.

### 6.3.6 Back ground environment (TS40)

In the coming paragraphs the following symbols are used:

$q_{tot}$	Total momentum transferred to the target from the projectile and gas
$\sigma_{tot}$	Standard deviation on total target momentum
$q_{gas}$	Average momentum transferred from propellant gas
$q_t$	Total momentum due to the projectile $q_t = q_{tot} - q_{gas}$
$\sigma_t$	Standard deviation on total momentum due to the projectile
$r_{T/P}$	$q_t/q_p \times 100$
$\sigma_{rt/p}$	Standard deviation on $r_{T/P} \times 100$

The propellant gas following the projectile transfers momentum to the target, thus it must be considered as a fundamental component of uncertainty on momentum measurements.

CISAS ID	ESA ID TS -	Target Type	dp [mm]	vp [km/s]	Coarse Damage	Comments
7910	40/1	Al HC SP 200x200x52.8	-	-	-	Sabot with no projectile inside: test for background noise assessment
7913	40/2	Al HC SP 200x200x52.8	-	-	-	Sabot with no projectile inside: test for background noise assessment
7933	40/3	Al HC SP 200x200x52.8	-	-	-	Sabot with no projectile inside: test for background noise assessment

Tab. 6-24. Summary of TS41

CISAS ID	vp [km/s]	Momentum transferred $q_T$ [Ns]	Uncertainty [Ns]
7910	-	9.68E-03	3.80E-003
7913	-	1.10E-02	3.80E-003
7933	-	1.05E-02	3.80E-003

**Tab. 6-25 Momentum transferred and its uncertainty**

From these tests, the average momentum transferred induced by gas on target is  $1.04E-2 \pm 4.65E-3$  Ns

Tests on Al HC SP (TS42)

CISAS ID	ESA ID TS -	Target Type	dp [mm]	vp [km/s]	Coarse Damage	Comments
7930	42/1	Al HC SP 200x200x5 2.8	1.9	5.2	P	None
7932	42/2	Al HC SP 200x200x5 2.8	1.0	4.9	NP	None

**Tab. 6-26. Summary of TS4-2**

CISAS ID	dp [mm]	vp [km/s]	$q_{tot}$ [Ns]	$\sigma_{q_{tot}}$ [Ns]	$q_T$ [Ns]	$\sigma_{q_T}$ [Ns]	$r_{T/P}$ [Ns]	$\sigma_{r_{T/P}}$ [Ns]
7930	1.9 P	5.2	6.73E-02	3.80E-003	5.69E-02	4.67E-03	111	9.1
7932	1.0 NP	4.9	1.63E-02	3.80E-003	5.85E-03	4.67E-03	79	63.1

**Tab. 6-27. Summary on momentum transferred on tests TS 42**

A test on aluminium honeycomb show that most of the momentum carried by the projectile is transferred to the target. This is expected, since the debris cloud is mostly trapped inside the panel, thus transferring most of its momentum to it. Differences on fraction of momentum carried by the projectile to the target are expected in decreasing from NP to P, due to the momentum carried by debris cloud in the perforating case. However, this trend is hidden on experimental data by the momentum transferred by the propellant gas. This increases uncertainty on measurement conducted in the NP case.

Tests on CFRP HC SP (TS43)

CISAS ID	ESA ID TS -	Target Type	dp [mm]	vp [km/s]	Coarse Damage	Comments
7935	43/1	CFRP HC SP 200x200x5 2.8	1.9	5.3	P	None
7936	43/2	CFRP HC SP 200x200x5 2.8	1.0	5.2	NP	None

Tab. 6-28. Summary of TS4-3

CISAS ID	dp [mm]	vp [km/s]	$q_{tot}$ [Ns]	$\sigma_{qtot}$ [Ns]	$q_T$ [Ns]	$\sigma_{qt}$ [Ns]	$r_{T/P}$ [Ns]	$\sigma_{rT/P}$ [Ns]
7935	1.9-P	5.3	8.65E-02	2.10E-03	7.61E-02	3.43E-03	148	6.7
7936	1.0-NP	5.2	2.72E-02	2.10E-03	1.68E-02	3.43E-03	230	47.0

Tab. 6-29. Summary on momentum transferred on tests TS 43

Tests on CFRP confirm trend emerged from experiments onto Al HC SP, showing also that a stronger rear ejecta is present increasing transferred momentum respect to Al HC SP. CFRP panels, due to the larger momentum transferred to the target by the projectile are less sensitive to the disturbance by propellant gas than Al HC

### 6.3.7 Relevant results for TS4

Results show a decrease of momentum transfer from no perforation-to-perforation region. However, special attention must be put on the role of uncertainty, which is mainly due to momentum transferred from gas propellant. Uncertainty greatly affects impact conditions on which total momentum transferred by the projectile is low compared to that transferred by propellant gas, some times hiding the expected trend.

<b>Al HC SP</b>	Momentum transferred	Ratio between projectile momentum and target momentum apparently increase from no- perforation (79%) to perforation (111%). However, NP values are much more affected by uncertainty and the real trend could be hidden
	Uncertainty	Uncertainty mainly due to propellant gas affects momentum measured in NP conditions by 60 %
<b>CFRP HC SP</b>	Momentum transferred	Ratio between projectile momentum and target momentum decreases from no-perforation (230%) to perforation (148%)
	Uncertainty	Uncertainty mainly due to propellant gas affects momentum measured in not perforation condition by 25 %

Tab. 6-1 Relevant results for TS4

## 6.4 Wavelet analysis

This chapter detail a detailed analysis about wave propagation inside plates and honeycomb panels. The HVI-induced disturbance field results from interference of waves generated at the impact point, which reflect at the target boundaries and superimpose to give the measured vibration. Until now, the disturbance was assessed using SRS; now the disturbance physic and behaviour is detailed using the same acceleration signal used for the analysis presented in the previous chapters. The measure of acceleration is post-processed using the Wavelet Transform, to extract from simple acceleration signal the main features of the wave field (generated by HVI) and to gain a better physical understanding of the resulting disturbance field.

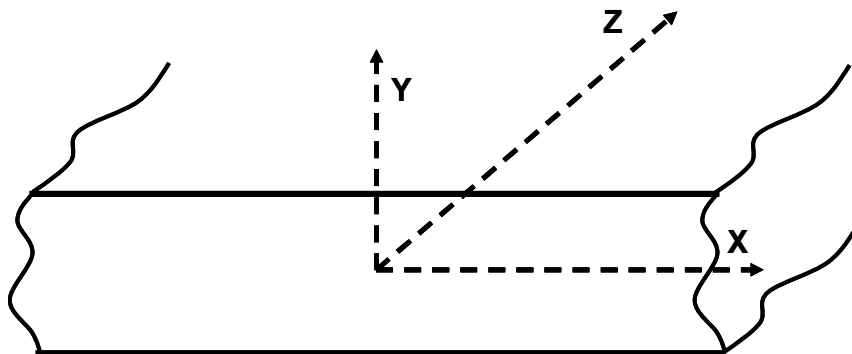
### 6.4.1 Mathematical model of elastic waves inside plates

Analytical solutions are presented hereafter for the propagation of elastic waves inside plates [7]. Starting from the 3D equations of waves, solutions are searched for to represent harmonic perturbations; this leads to an algebraic relation (frequency equation) whose roots describe different wave shapes: each of them is characterized by a particular frequency and speed of propagation.

This decomposition is useful since any complex disturbance can be obtained by an appropriate superimposition of such elementary harmonic wave constituents. In particular, elastic perturbations generated by an impact have a narrow width in time (because of the short duration of the phenomenon) and therefore they can be thought as the sum of waves spread in a large frequency band (wider bands result from shorter waves); this set of waves is called wave group.

The remainder of this paragraph presents the 3D equation of waves and the harmonic form for its solution [7]. After that, the solution of the frequency equation is discussed, to show the theoretical dependence, which exists between the shape of harmonic waves, their speed of propagation and frequency content.

The reference model is an unconstrained homogeneous flat aluminium plate [7]. The plate and reference axes are shown in Fig. 6-102.



**Fig. 6-102 Reference axis for the plate used in the mathematical model. The plate has infinite extent in the x and z directions**

Eq 1 is the 3-D (exact) wave equation for an elastic body:

$$(\lambda + \mu)\nabla\Delta + \mu\nabla^2 u = \rho \frac{\partial^2 u}{\partial t^2} \quad \text{Eq 1}$$

Where  $u = u(x, y, z, t)$  is the vector displacement,  $\lambda$  and  $\mu$  are the material Lamé constants and  $\Delta = \nabla u = \varepsilon_x + \varepsilon_y + \varepsilon_z$  is the dilatation of the material in the three axis direction.

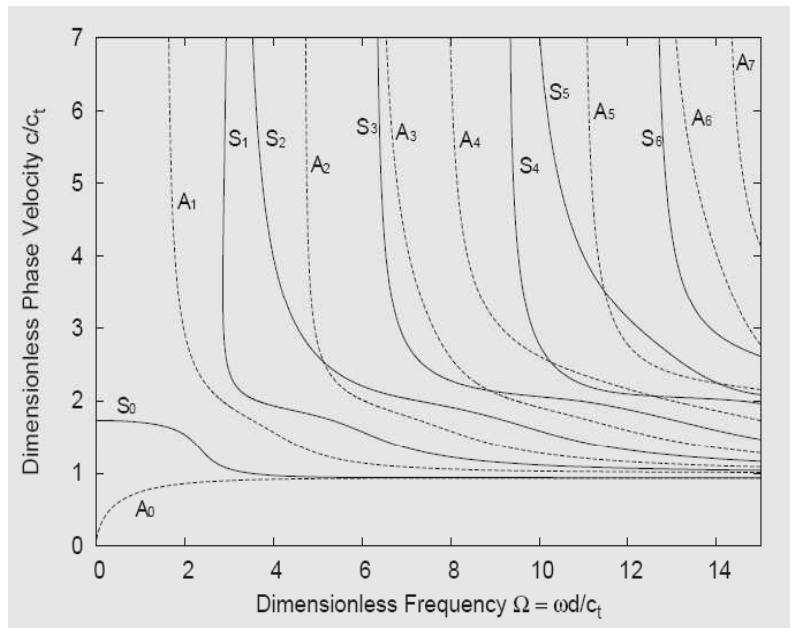
Eq 2 represents a 3D harmonic wave, which is the elementary constituent of real waves.

$$\begin{aligned} u_x(x, y, z, t) &= h(y)e^{i(\xi x - \omega t)} \\ u_y(x, y, z, t) &= i(y)e^{i(\xi x - \omega t)} \\ u_z(x, y, z, t) &= j(y)e^{i(\xi x - \omega t)} \end{aligned} \quad \text{Eq 2}$$

Where  $\omega$  is the radial frequency and  $\xi$  is the wavenumber (the ratio between  $\omega$  and  $\xi$  equals the wave phase speed  $\omega/\xi = c$ ).  $h(y)$ ,  $i(y)$  and  $j(y)$  are the amplitudes of the three displacements, which vary along the plate thickness.

The waves described by Eq 2 travel along the plate length (x direction) and change their amplitude along the plate's thickness (y direction). The values for  $\omega$ ,  $\xi$  and for the amplitude function are calculated through the substitution of Eq 2 into Eq 1 and adding the boundary conditions (the plate surfaces are traction free; see [7] for the complete development of the equations).

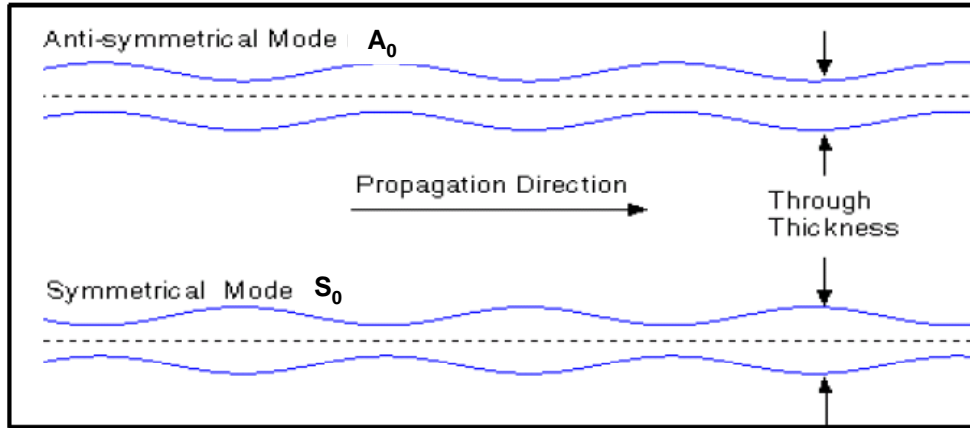
The wave solutions (Eq 2) are shown in Fig. 6-103.



**Fig. 6-103 Solutions of the wave equation for simple plates: dimensionless phase velocity as function of dimensionless frequency.**

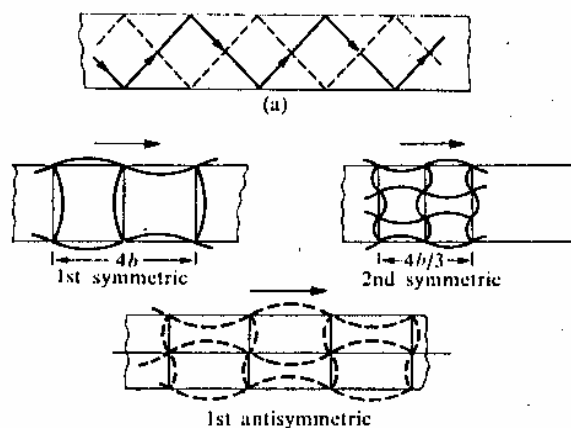
$\Omega$  is the dimensionless wavenumber,  $c$  is the dimensionless phase velocity and  $d$  is half of the plate thickness. Each curve represents a solution of Eq 2 and the corresponding allowed values  $\xi$  and  $\omega$ . For example, an  $S_0$  wave can propagate in an infinite plate only if its radial frequency  $\omega$  and wavenumber  $\xi$  belong to the  $S_0$  curve shown in Fig. 6-104 shows the resulting displacement modes, if the  $A_0$  and  $S_0$  solution are taken.

It is worth highlighting that the solutions (Eq 2) can be divided in two components: symmetric and anti-symmetric with respect to the plate mid plane. Symmetric (S) and antisymmetric (A) waves (also called Lamb or guided waves) can propagate with various displacements modes, represented with increasing indexes ( $A_0, A_1, A_2, S_0, S_1$ , higher index characterize a more complex displacement pattern).



**Fig. 6-104 Displacement pattern of  $A_0$  and  $S_0$  Lamb waves.**

Each wave displacement mode is the result of the interference of waves travelling inside the material and bouncing at the plate surfaces. These bouncing waves can be dilatational or transversal, and travel with their own velocity ( $c_t$  and  $c_d$ ). Such velocity depends only on the material properties (for aluminium  $c_d = 6100$  m/s and  $c_t = 3100$  m/s.). For instance, the interference of a wave bouncing with an inclination of  $45^\circ$  gives the displacement field shown in Fig. 6-105 (see [7] for additional references on dilatational and transverse waves). If the bouncing wave is transversal, the resulting displacement pattern will be antisymmetric (A); if the bouncing wave is distortional, the displacement pattern will be symmetric (S).

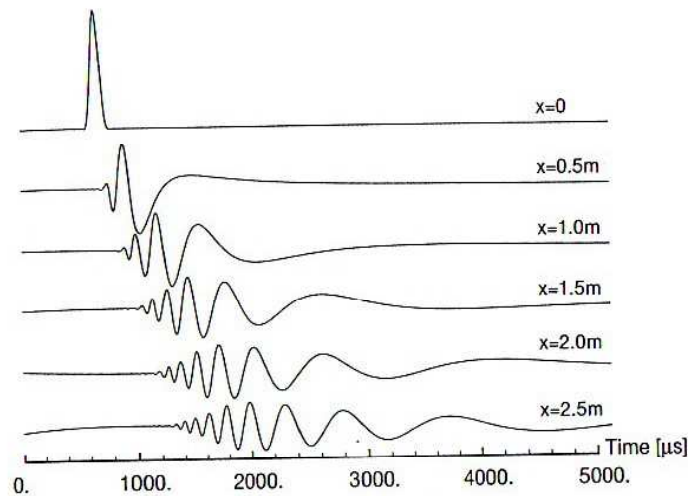


**Fig. 6-105 The interference of waves bouncing at  $45^\circ$  inside the plate generates a Lamb wave (upper image). The mid image shows the resulting  $S_0$  and  $S_1$  symmetric modes, the lower image shows the  $A_0$  mode.**

In summary, the wave that propagates along the surface of a flat and infinite plate is the result of interference of waves travelling inside the material and the displacement pattern depends on the type and velocity of such constituent waves.

There is a cut-off frequency for each Lamb wave, under which it cannot propagate. For plates with small thickness, only the first symmetric  $S_0$  and antisymmetric  $A_0$  Lamb waves are usually excited after a short time excitation (e.g. point impact). In the experimental results presented hereafter, there will be only two excited wave-modes.

A real disturbance (wave group) results from interference of many Lamb waves with different frequencies and in general Lamb waves experience dispersion. This means that their phase velocity depends on frequency. Therefore, a wave group can change its shape while propagating, since it may be composed by Lamb waves having different speed of propagation (again see [7] for additional references).



**Fig. 6-106 Example of a dispersive wave: it changes its shape while propagating. This occurs because the phase velocity of its constituents is different. In this case, constituents with high frequency travel faster than low frequency ones**

Referring to Fig. 6-103, it appears that for dimensionless frequency below 2, the first symmetric  $S_0$  Lamb wave is not dispersive, while the first antisymmetric  $A_0$  is highly dispersive. Therefore, a wave group made by  $S_0$  components will not change its shape while propagating, while a wave group made by  $A_0$  components will grow wider in space, since its elementary components travel with different velocity. Therefore, the resulting wave group is dispersive.

The velocity of the group (combination of elementary Lamb waves) is defined as:

$$c_g = c + k \frac{\partial c}{\partial k} \quad \left( k = \frac{2\pi}{\xi} \right) \quad \text{Eq 3}$$

and equals the phase velocity of its components only if the wave is not a dispersive one (in this case  $\frac{\partial c}{\partial k} = 0$  and the group wave speed is not a function of wavenumber or frequency).

#### 6.4.2 Validation of the WT method

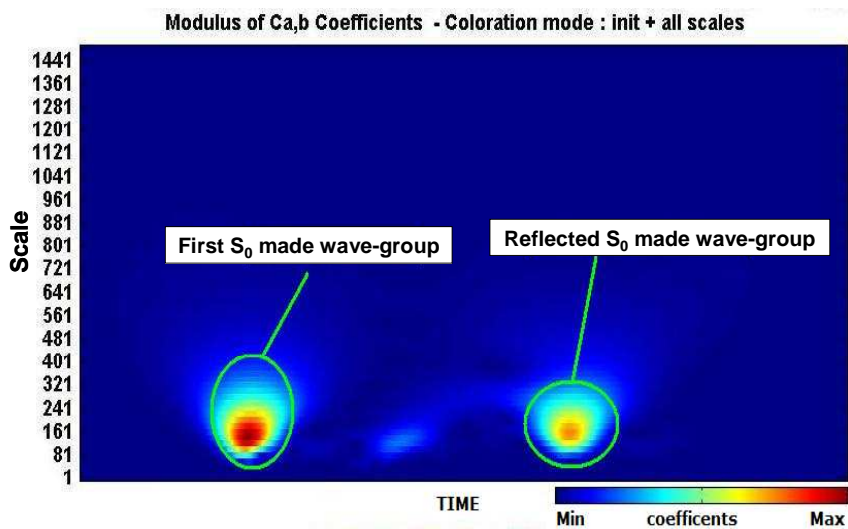
Before applying wavelet analysis to waves generated by HVI, this method was validated in two steps. First, by perturbations generated by HVI on aluminium plate

targets and simulated with a SPH code. Second, by acceleration signals generated by a low velocity impact on a real Al plate and sampled with accelerometers.. The objective was to identify by steps how the two wave modes ( $A_0$  and  $S_0$ ) appear in a WT spectrum using signals of increasing complexity.

Numerical signals

A HVI simulation was performed with Autodyn 2D, on a Al-6061-T6 aluminium plate having size 300x300x0.8 mm. Impact conditions referred to a 1 mm diameter Al-2084 sphere launched at 5 km/s. The total simulation time was 66  $\mu s$ . The software allows for a separate calculation of the out of plane (OP) and in plane (IP) accelerations, which were acquired by a virtual sensor located in the mid plane of the plate 150 mm away from the impact point.

Fig. 6-107 shows the resulting wavelet spectrum of IP waves. The plot presents in a colour scale the magnitude of the WT coefficients, as a function of the time (horizontal axis) and the "scale", which is the inverse of the wave frequency (vertical axis). At any given frequency, the maxima of the WT represent the arrival time of each frequency component of the wave group.



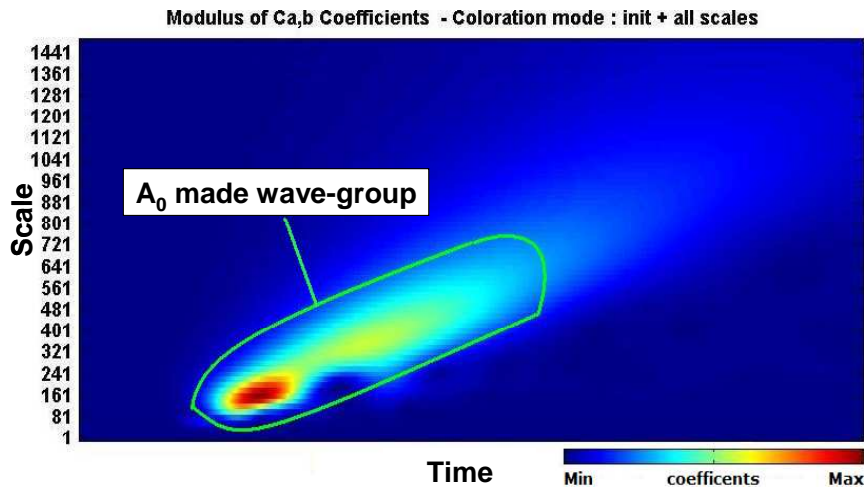
**Fig. 6-107 WT spectrum of the  $S_0$  made wave-group**

Two bright spots are evident looking at Fig. 6-107, which represent wave groups made by  $S_0$  Lamb waves. Since they appear in a WT spectrum like bright spots, the wave groups do not present a dispersive behavior. They have maintained an unchanged shape, because their frequency components (Lamb waves) travel with the same speed. The central frequency of the spots maxima (dark red in figure) is around 200 kHz. The maximum value of the left spot corresponds to the arrival of the first wave group at the virtual sensor, while that on the right represents the arrival time of the same wave, reflected from the plate boundaries. The group velocity of this wave is around 4.5 km/s. It has been computed simply from the ratio of the known distance between the sensor and the plate edge, and the time between the passage of the first and second spot in the WT spectrum. This velocity agrees very well with the theoretical value, in accordance with Fig. 6-103.

Similar considerations can be repeated for OP wave constituents (Fig. 6-108). In this case, only a stretched spot can be highlighted representing a wave in which high frequency components (low scale) arrive to the sensor in a shorter time with respect to low frequency ones (high scale). This means that high frequency constituents of OP



group waves travel faster than low frequency ones. Referring again to Fig. 6-103, this represents a wave group made by  $A_0$  Lamb waves, behaving like the one shown in Fig. 6-106. This wave group results from Lamb waves ( $A_0$ ), which travel with different velocity.



**Fig. 6-108 WT spectrum of the  $A_0$  made wave-group**

In this case, there is no evidence of the wave group made by  $S_0$  Lamb waves because the virtual sensor is located on the plate mid plane. The displacement of  $S_0$  Lamb waves is symmetric across the mid plane, so the resulting OP acceleration of this wave group is always zero (see Fig. 6-104).

### 6.4.3 Experimental signals: low velocity impacts on simple plates

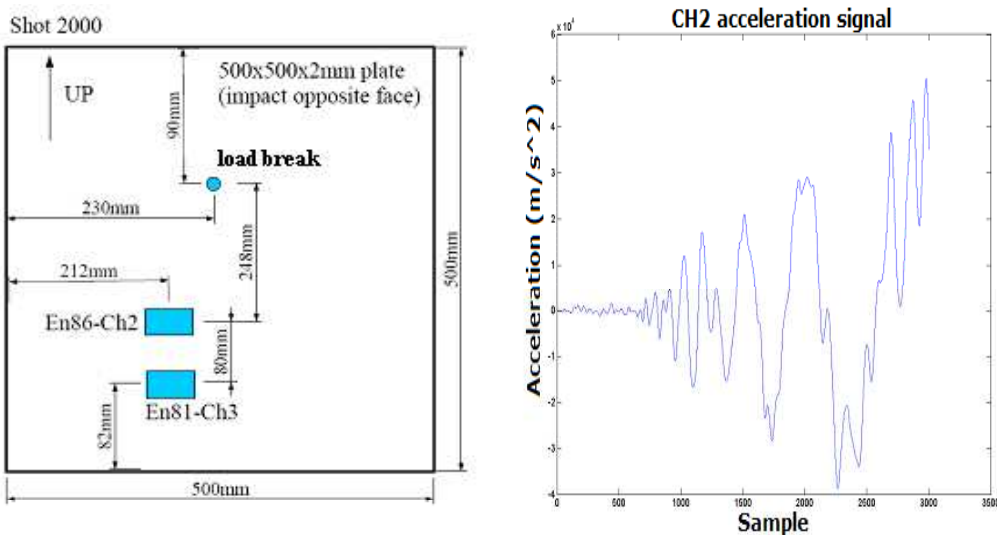
Impact tests were performed at both low velocity and hypervelocity. In particular, experiments were realized at the CISAS Impact Facility, using a Light Gas Gun, which is capable of accelerating 150 mg projectiles up to 5.8 km/s. Impact-induced accelerations were measured by Endevco 200k accelerometers (1.2 MHz resonance,  $2 \times 10^6$  m/s<sup>2</sup> max acceleration peak) connected to amplifiers having bandwidth up to 400 kHz. The sampling frequency was of 5 MHz with a sampling window of 0.1 s. Test samples were aluminium (Al 2024-T81) 500x500x2 mm plate, suspended by low stiffness springs inside the LGG vacuum chamber.

In the case of low-velocity impacts, a steel ball with diameter equal to 5 mm was launched in a single-stage mode on a hanged Al thin plate. Fig. 6-109 (left) shows the sensor position and the impact point: Tab. 6-30 summarizes the accelerometers set-up.

The aim of this test was to validate the wavelet method through the identification of wave modes using real signals. The sensors were directly fixed to the plate surface. In this case, only OP acceleration can be sampled (both the  $S_0$  and  $A_0$  made wave group have OP acceleration components).

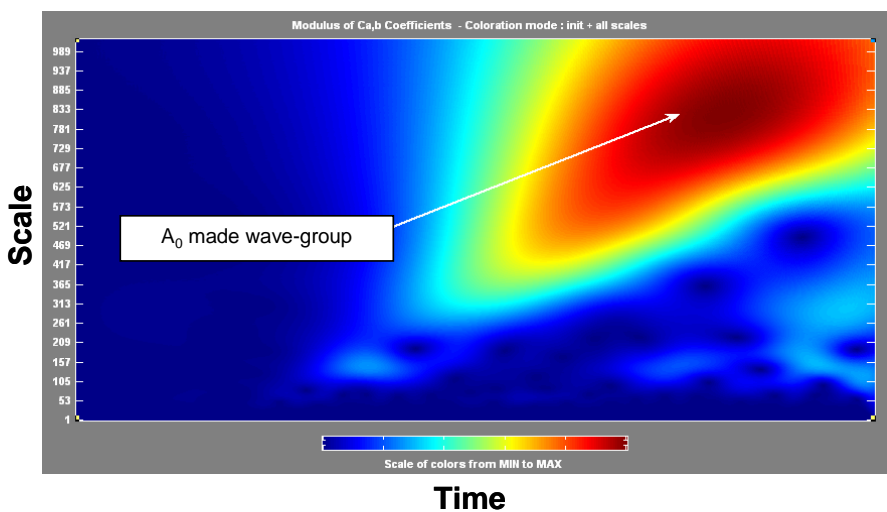
Sensor	Accelerometer range	Distance from the impact point	Channel	Plate fixing method
Endevco 200k	$2 \times 10^6$ (m/s <sup>2</sup> )	248 (mm)	Ch2	Acrylic glue
Endevco 200k	$2 \times 10^6$ (m/s <sup>2</sup> )	328 (mm)	Ch3	Acrylic glue

**Tab. 6-30 Summary of the accelerometers used in low-velocity impact on thin aluminium plate**



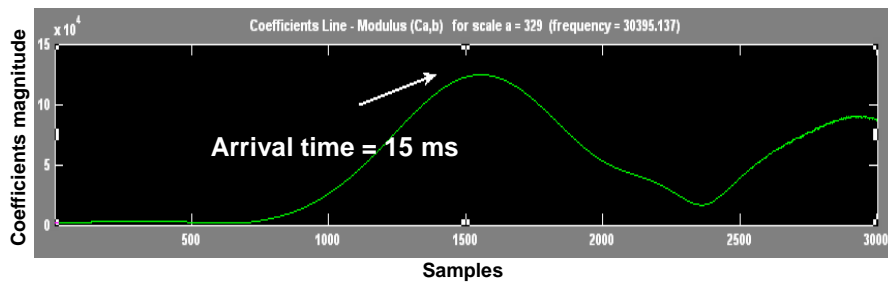
**Fig. 6-109 On the left is shown low velocity impact set-up, on the right, the earlier part of the Ch2 acceleration signal**

Fig. 6-110 shows the WT spectrum of the Ch2 signal. The x-axis reports the time shift, while the y-axis is the scale (inverse of the frequency).



**Fig. 6-110 WT spectrum of the Ch2 acceleration signal**

The high frequency part of the perturbation travels faster than the low frequency one; in fact, the red part of the spectrum (high value of the coefficients) appears first for low values of the scale (high frequency). This feature highlights that this wave group (dispersive) is made by  $A_0$  Lamb waves. The phase velocity of the wave group components follows the dispersion characteristics reported in Fig. 6-103. The arrival time of each wave constituent may be evaluated from horizontal sections of the plot of Fig. 6-110. Fig. 6-111 shows the time variation of the WT coefficients at 30 kHz frequency: the Lamb wave arrives at the sensor at time  $\cong 15$  ms.



**Fig. 6-111 Section of the WT spectrum at 30 kHz and scale 329**

We can repeat this evaluation for the other wave components (with different frequencies), thus obtaining the arrival time for each of them. Referring to the second sensor (Ch3), the dispersion feature can be computed in a similar way.

The phase speed of each component is derived using the following formula:

$$c_{ph}(f) = \frac{y_2 - y_1}{b_2(f) - b_1(f)} \quad \text{Eq 4}$$

$C_{ph}$  is the velocity of each Lamb wave,  $y_2 - y_1$  is the distance between the sensors and  $b(f)$  is arrival time of each wave: this is identified by the peak maxima for each constant-frequency line in the WT spectra.

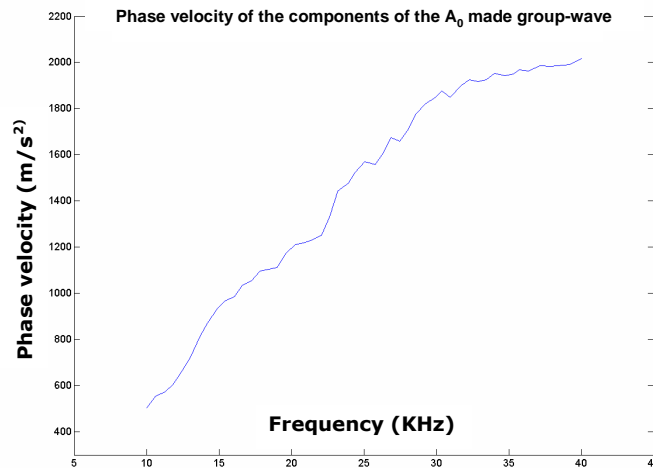
The following Tab. 6-31 summarizes the phase velocities computed for each frequency:

Frequency (kHz)	Scale	Phase velocity (m/s)
30	329	1900 ± 250
25	391	1500 ± 250
21	464	1200 ± 250
14	694	1000 ± 250

**Tab. 6-31 phase velocities of the  $A_0$  made wave group**

Fig. 6-112 shows the phase speed for the Lamb waves computed with the above method. The curve shown is fully compatible with the  $A_0$  Lamb waves at the same frequency range (see Fig. 6-103).

Moreover, since the low velocity impact is not perforating, the  $S_0$  made wave group has not been excited. In fact, no spots appear in the WT spectrum.



**Fig. 6-112 Dispersion feature for the components of the  $A_0$  mode wave-group**

#### 6.4.4 HVI on simple aluminium plates

In previous chapters, the WT method was explored through its application to numerical (SPH) and simplified experimental test cases. At this point, a qualitative analysis of the disturbance field produced by HVI on simple plates and honeycomb panels is presented, using the methods above mentioned.

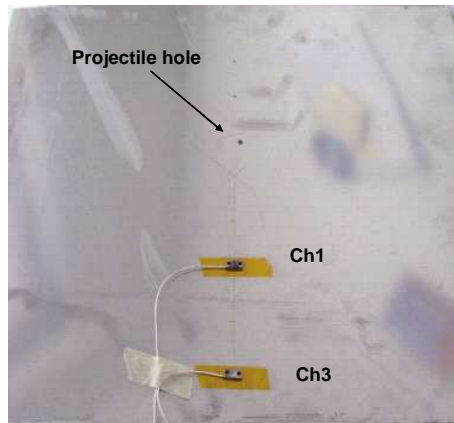
This chapter deals with HVI on simple aluminium plates, chapter 6.4.5 reports on HVI tests on honeycomb aluminium panels.

The target plate was hanged inside the LGG vacuum chamber. A 1.5 mm diameter projectile was launched at 4700 m/s.

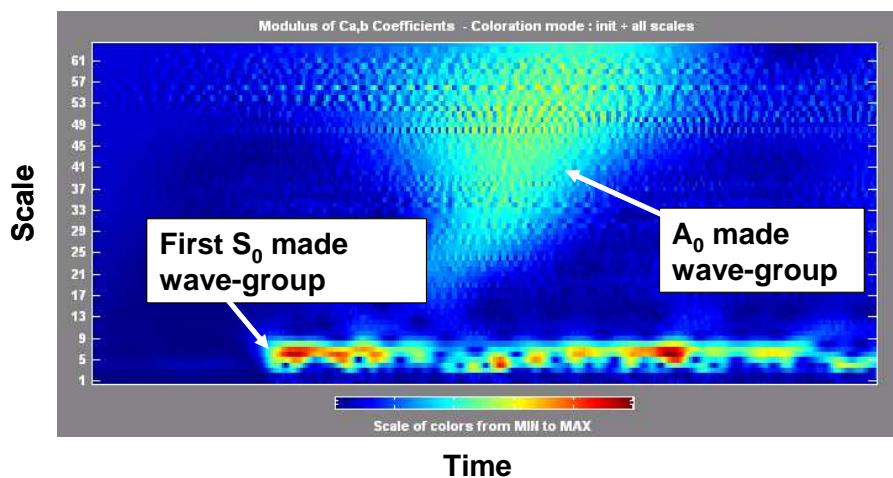
The target set-up is shown in Fig. 6-113. Hypervelocity impacts on thin plates generate signals with very high amplitude and frequency content. This requested to place sensors far away from the impact points. They were attached using adhesive tape instead of acrylic glue, to ease the accelerometers detachment after tests. The adhesive tape was experimentally validated and it does not interfere with the acceleration measurement.

Sensor	Accelerometer range	Distance from the impact point	Channel	Plate fixing method
Endevco 200k	$2 \times 10^6$ (m/s <sup>2</sup> )	140 (mm)	Ch1	Adhesive tape
Endevco 200k	$2 \times 10^6$ (m/s <sup>2</sup> )	240 (mm)	Ch3	Adhesive tape

**Tab. 6-32 Summary of the accelerometers used in hypervelocity impact on thin aluminium plate**

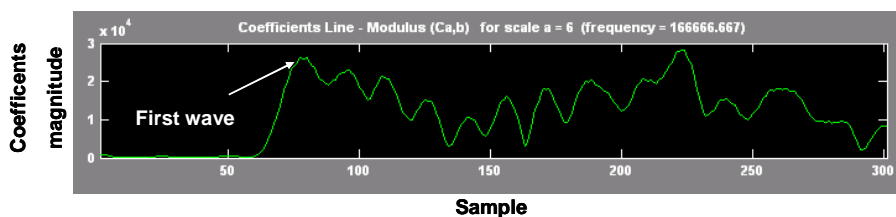


**Fig. 6-113 Target set-up with accelerometers**



**Fig. 6-114 The WT spectrum of the signal as recorded by Ch1**

The lower scale peaks of the WT coefficients (as shown in Fig. 6-115) correspond to a frequency of 166 kHz. Since there is no dispersion, each peak represents the arrival time of a  $S_0$  made wave group.



**Fig. 6-115 WT spectrum of Ch1 at constant scale value, corresponding to 166 kHz**

Fig. 6-115 shows the constant scale plot (scale 6 in Fig. 6-114). Computing the time shift between the first peak (at 166 kHz) of Ch1 WT spectrum and the first peak at the same frequency of the Ch3 WT spectrum, the wave group speed results  $5380 \pm 250$  m/s. In fact, for a not dispersive wave the phase speed coincides with the group speed. This is in good accordance with the group wave speed predicted analytically for the same perturbation propagating in a 2 mm thickness plate and having a frequency of 166 kHz. The peaks following the first one represent reflections of the wave at the plate boundaries.

Comparing the group speed to that of the first case presented (SPH simulation); this wave group seems to travel faster. This is due to the lower frequency of its components. The central frequency of the wave group in the SPH simulation was 200 kHz and it experiences dispersion, because it is made by high frequency Lamb waves. Instead, the group wave generated by the HVI has a lower central frequency of 166 kHz and thus experiences less dispersion. For this reason, the group velocity of this wave is higher (remember the velocity/frequency relation of Eq 3).

The wide spot at scale between 24 and 64 (corresponding to 41 kHz and 16 kHz respectively) represent an  $A_0$  mode wave group. In fact, it shows strong dispersion behaviour, as seen for the low velocity impact (Fig. 6-106). The ratio between the Ch1 and Ch3 distance and the time shift between the arrival time of their first peak in the WT spectrum (at 20 kHz), gives a wave phase speed of  $1100 \pm 250$  m/s. This computation can be made for various frequency values (like in the low velocity test), and the results are again in good accordance with the analytical solution shown in Fig. 6-103.

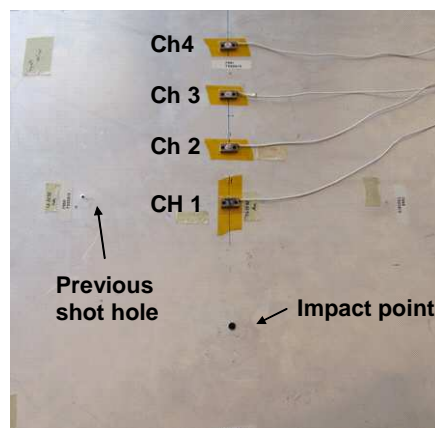
#### 6.4.5 HVI on honeycomb aluminium panels

HVI tests were performed on all-aluminium honeycombs sandwich panels, having size 400x400x52.7 mm and skin thickness equal to 1 mm. Projectiles were 2.3 mm diameter aluminium spheres launched at 5 km/s. Such impact conditions resulted in the target complete perforation.

Impact-induced accelerations were measured by four Endevco 200k accelerometers connected to amplifiers having bandwidth up to 400 kHz. The sampling frequency was 5 MHz with a sampling window of 0.1 s.

In the following, the description of the results of the most representative experiment is presented.

Fig. 6-116 shows the test target and the accelerometers set-up. The Endevco sensors were connected directly on the impacted honeycomb skin, with adhesive tape. Tab. 6-33 shows the accelerometers used on this test.

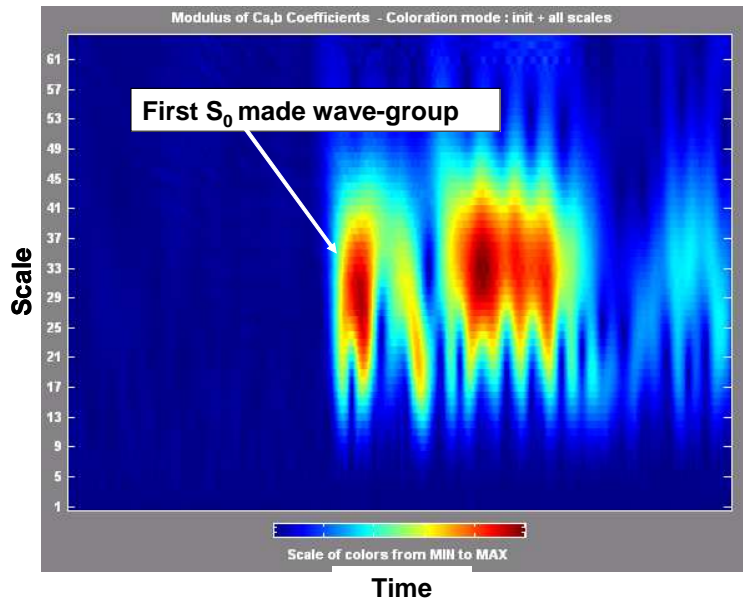


**Fig. 6-116 Honeycomb test target: four accelerometers were attached on the panel aluminium skin (on the left is visible a small hole, resulting from a past impact)**

Sensor	Accelerometer range	Distance from the impact point	Channel	Plate fixing method
Endevco 200k	$2 \times 10^6$ (m/s <sup>2</sup> )	100 (mm)	Ch1	Adhesive tape
Endevco 200k	$2 \times 10^6$ (m/s <sup>2</sup> )	150 (mm)	Ch2	Adhesive tape
Endevco 200k	$2 \times 10^6$ (m/s <sup>2</sup> )	200 (mm)	Ch3	Adhesive tape
Endevco 200k	$2 \times 10^6$ (m/s <sup>2</sup> )	250 (mm)	Ch4	Adhesive tape

**Tab. 6-33 Summary of the accelerometers used for hypervelocity impact on honeycomb panels**

The WT spectrum computed on the acceleration signal recorded by sensor number 1 (Ch1) is shown in Fig. 6-117.



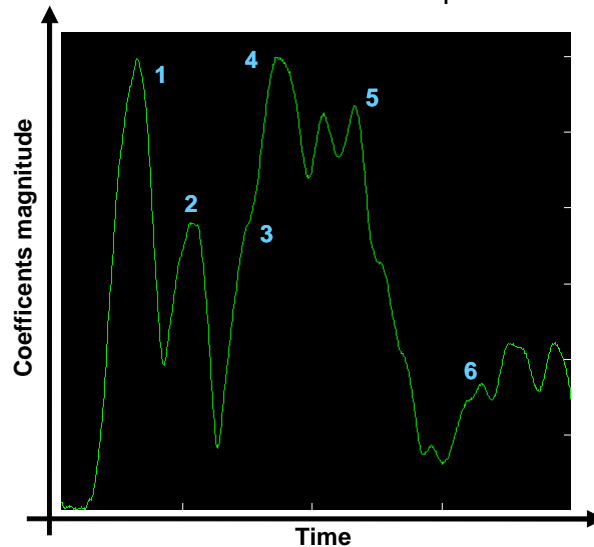
**Fig. 6-117 Wavelet spectrum of the acceleration signal recorded by sensor number 1 (scale = 30 corresponding to 160 kHz frequency)**

The first peak in the WT spectrum represents the arrival of the first wave group. The group central frequency is 160 kHz, the same in all spectra. Since there is no evidence of dispersion, this wave group is made only by  $S_0$  waves. Its group velocity can be computed comparing the arrival times at each sensor couple. The three computed velocities are shown in Tab. 6-34.

Sensor 1-2	Sensor 2-3	Sensor 3-4
$5102 \pm 250$ m/s	$5400 \pm 250$ m/s	$5208 \pm 250$ m/s

**Tab. 6-34 Speed of propagation of the first wave group, computed through the comparison of waves arrival times between each sensor couple**

Looking at the four WT spectra there is no evidence of a wave group made by  $A_0$  Lamb waves. This is probably due to the high flexural stiffness of the honeycomb plate. Instead, in all spectra there are many other peaks after the first one. Fig. 6-118 shows the coefficient line at 160 kHz of the wavelet spectrum for sensor 1.



**Fig. 6-118 Section of the WT spectrum of Fig. 6-117, corresponding to 160 kHz frequency (scale = 30)**

In the following text, the velocity measurements uncertainty is always  $\pm 250$  m/s.

The second peak is smaller and wider with respect to the first. It coincides with a wave travelling at 5200 m/s and reflected back by the second accelerometer. The third peak corresponds to a wave reflected from a pre-existing hole in the plate (a past HVI impact). Its propagating velocity of 5200 m/s demonstrates this.

Peak number 4 coincides with the wave propagated on the back honeycomb plate, and transmitted to the sensor through the lamina of the honeycomb core connecting the two Al skins. The projectile was supposed to travel through the honeycomb thickness with its impact velocity of 4950 m/s, while the wave transmitted by the core's lamina was supposed to be an  $A_0$  mode wave travelling at 1600 m/s. This last velocity value is confirmed by peak number 7, which coincides exactly with the arrival time of the same wave, bouncing between the front and the back Al plates.

Peak number 5 represents the arrival time of the wave reflected by the lateral edges of the plate (travelling at 5200 m/s) and the arrival time of the wave reflected by the impact hole (travelling at 5200 m/s).

Peak number 6 corresponds to the wave reflected from the most distant edge, located behind sensor number 4 and travelling at 5130 m/s.

This analysis was made for the other three spectra with the same results. Every wave reflected or scattered coincides to a feature in the WT spectra: a peak or an inflection point. The wave behaviour becomes rapidly complex after some reflections, and it is very hard to identify them all. However, this has demonstrated the WT can successfully identify waves propagating in honeycomb panels after HVI.



# 7 Shock wave propagation into minor bodies of the Solar System

## 7.1 Introduction

The most part of the minor bodies of the Solar System observed and/or visited by spacecrafts show evidences for a very low bulk density and a significant porosity [e.g. Britt et al. 2002, Fujiwara et al. 2006]. The porosity must dampen the shock wave propagation in the interior of the asteroids affecting the behaviour during cratering and collisional disruption.

In this chapter, HVI simulations are examined on scale models of asteroids, i.e. spheres made of porous concrete, in order to investigate the shock wave propagation within the target by means of wavelet transform analysis.

The aim is to analyse the waves generated by an HVI on such targets and infer quantitative information about the impacted target and impact dynamics. These data can be used to:

- Validate the physical models and constitutive equations of materials' behaviour (equations of state, EOS), physical models of materials and porosity, critical issues in the model consistency)
- Provide parameters to assess a comparison between HVI experiments on scale models and Smooth Particle Hydrocode (SPH) simulations.

The main characteristics of wave disturbance field (velocity, frequency, reflections, and interference) have been characterised by analysing time history signals of acceleration as monitored at different points within the targets. Each parameter gives the following information:

- Velocity: the material characteristic (molecular structure, elastic strength and density, that depends on the porosity)
- Frequency: the frequency of the waves depend on the time of contact between the projectile and the sphere: if the frequency of the waves correspond to experiments, the dynamic of the impact and fragmentation has been correctly modelled
- Reflection: interface between the target and the surrounding medium. Moreover, the first wave could change the material characteristic. As example, the compression of the porous cells due to the passage of the first wave could lead to the reduction of the overall material porosity; thus the magnitude of the reflected waves may depends on the first wave and on the initial porosity

### 7.1.1 Constitutive models

SPH codes employ many different models to simulate the impact, fragmentation and wave history in materials. The main issue is the determination of the constants used to be used within the mathematical description of materials:

- Conservation equations (momentum, energy and mass) for the elastic solid in which the stress tensor has a no-diagonal part, the so called deviatoric stress tensor
- Plasticity, introduced by modifying the stress above the elastic limit (i.e. using Von Mises yielding relation)
- Fracture model (i.e. the one based on nucleation of incipient flaws whose number density is given by the Weibull distribution [Jager and Cook, 1969]):

the extent to which fracture affects the local properties of matter is described by the scalar state variable called "damage"

- Equation of state (EOS): a relation like the well-known  $pV = RT$  for ideal gases, but for solids under high energy and high velocity deformation regimes (pressure of several GPa)

### 7.1.2 Target material: Concrete

The scale model of asteroids has been built with porous concrete. Why concrete? Because its properties have shown to be similar to those of the chondrites (asteroids' meteorite analogs), more than typical terrestrial basalts [Flynn et al. 1999].

### 7.1.3 Porosity

Porosity is an important physical characteristic of the minor bodies, affecting their behaviour during cratering and greatly lengthening the collisional lifetimes of porous asteroids. Porous targets are likely to have average sound velocity lower than those of nonporous targets composed of same material. In fact, compaction of initially porous materials can produce rapid attenuation of the shock, thus affecting energy propagation during collisions.

The effect of porosity on shock propagation through meteorite can be assessed by comparing the wave velocities in meteorites with those in compact objects, like terrestrial surface materials. Alexeyeva (1960) measured longitudinal wave velocities ranging from 2050 to 4200 m/s in eight ordinary chondrite falls, other authors found different velocities from different materials (Flynn, Bjurbole, Saratov et al.). These seismic wave velocities are smaller than those observed in terrestrial igneous rocks (typically between 5400 and 5600 m/s).

## 7.2 Signal analysis strategy

Simulations have been made on porous concrete spheres (25 mm radius) as target, impacted by an aluminium projectile with velocity of 5000 m/s using Smooth Particle Hydrocode approach.

The procedure followed is:

1. To make SPH simulations of HVI on planetary scale models.
2. To analyse the acceleration signal sampled at points on the surface and inside the target. Using Wavelet Transform (WT), the velocity and frequency of the propagating waves are quantified, together with their type and reflections
3. To repeat simulations with added masses that simulate the accelerometer used to measure the waves field. The sensor has been attached on the target's surface, to assess the possibility of the load effect on the sampled signal
4. To determine a suitable sensor (accelerometer) with a dynamical range able to withstand the shock environment and to measure the waves. Besides the accelerometer, other measurement techniques (i.e. laser sensors) can be applied for characterize this high frequency/intensity disturbance field
5. To perform experimental impact tests on scale models in conditions similar as much as possible to the ones simulated
6. To analyse signals recorded during experiments (acceleration, displacement etc.) and retrieve the wave field characteristics
7. To compare the wave parameters computed from simulations and from experiments. This activity will help in modifying and assessing the constitutive models used to run simulations.

Simulations have been performed using a SPH code (ANSYS – Autodyn 2D), the characteristics of material and of the constitutive models used are summarised in the following table.

Equation of state (including porosity)	P-Alpha
Solid EOS	Polynomial
Compaction curve	Standard
Strength	RHT* concrete
Tensile failure	Hydro (Pmin)
Failure	RHT* concrete

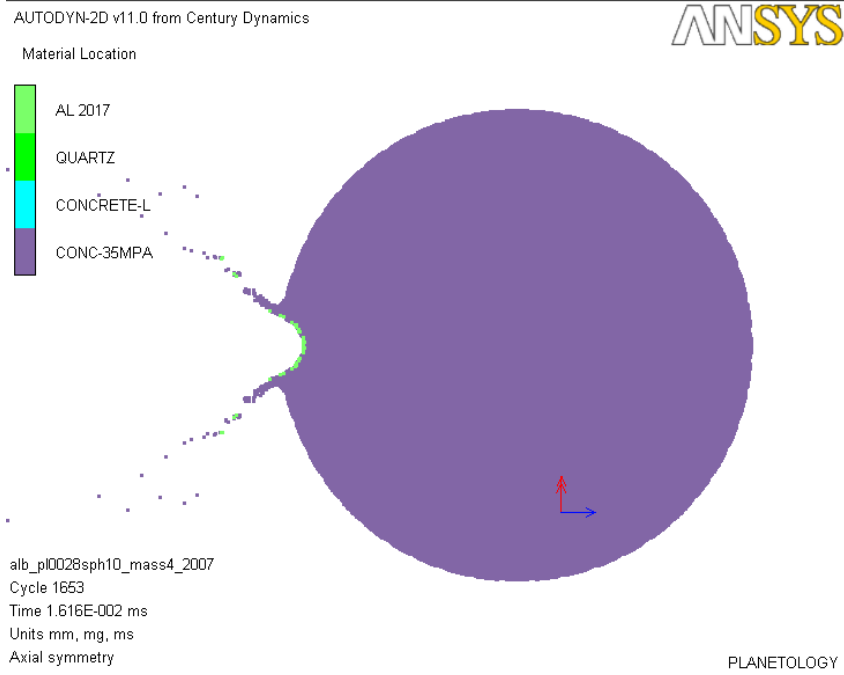
*\*Modular strength model derive experimentally by Riedel, Hiemaier and Thoma of the Ernst Max Institute (EMI) included in the Autodyn library.*

### 7.3 Waves in spheres made of porous concrete

Two simulations have been run with porous concrete; the impacted sphere has a radius of 25 mm and is made of 35-MPa concrete; the projectile is a 1-mm sphere of aluminium and impacted the sphere at 5000 m/s:

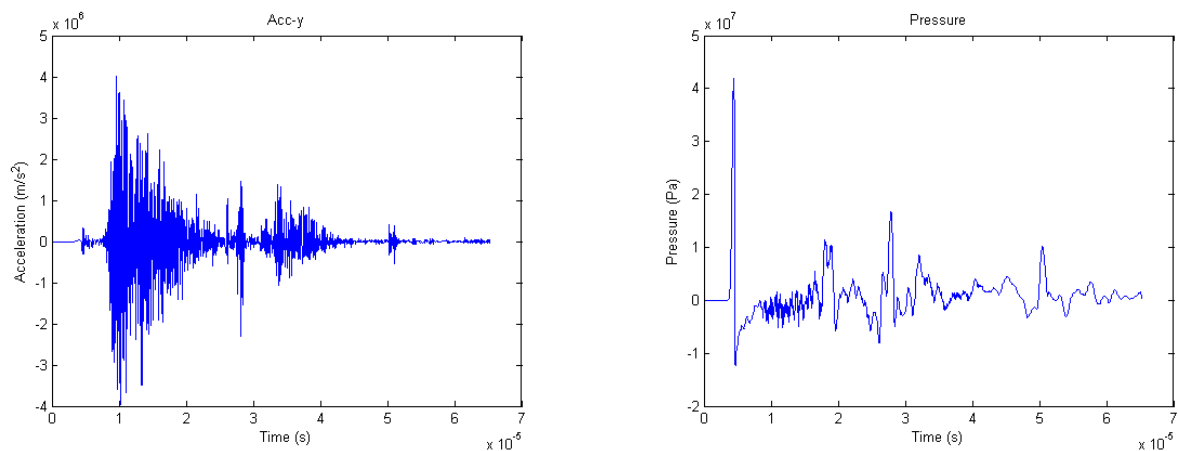
- Impact on standard target without added mass: the aim is to understand and quantify the wave propagation inside the concrete sphere
- Impact on standard target with added mass: the aim is to compare the waves morphology respect to the simulation without mass in order to estimate possible load effect by the accelerometer

Displacement, acceleration and pressure time histories have been measured on target points: displacement and acceleration are provided both in the x direction (impact axis) and y direction (perpendicular to the impact axis). Fig. 7-1 shows the target positions within the target relevant to the second simulation: the target points are the same of simulation one, plus three new points that have been added under the concentrated mass simulating the sensor.



**Fig. 7-1 SPH Simulation set-up: the projectile remnants can be seen on the crater (green points)**

Fig. 7-2 shows a typical acceleration and pressure signal in the y direction



**Fig. 7-2 SPH simulation out-put: on the left Y-acceleration signal, on the right pressure signal both in direction Y perpendicular to impact axis, are recorded at the target point 5.**

Acceleration and pressure data have been analysed using the CWT (complex wavelet transform). Data about arrival time of the waves have been retrieved using the modulus of the transform spectrum. The analysing mother wavelet is the Complex Morlet, that is able (thanks to its narrow time or frequency Gaussian-spectrum) to analyse wave propagation signals [16]. The procedure is the same used in paragraph 6.4 for identifying wave propagation velocity and frequency. The selected resolution for the mother wavelet used in this study is the standard value for the complex Morlet (1-1 using MatLab notation) and is the best compromise between time resolution and frequency resolution.

### 7.3.1 Wave speed and frequency

The first step is to measure the wave velocity. It results from the peaks of the WT modulus at a given frequency (or scale). We know the impact moment, the arrival time of the first wave (a sonic P-wave) and the distance it has covered.

The velocity has been retrieved from both x and y accelerations since the P-wave defroms the matter in both directions.

The sonic wave speed (for a longitudinal/compression P-wave) resulting from the elastic wave propagation theory is:

$$c = \sqrt{\frac{E}{\rho}}$$

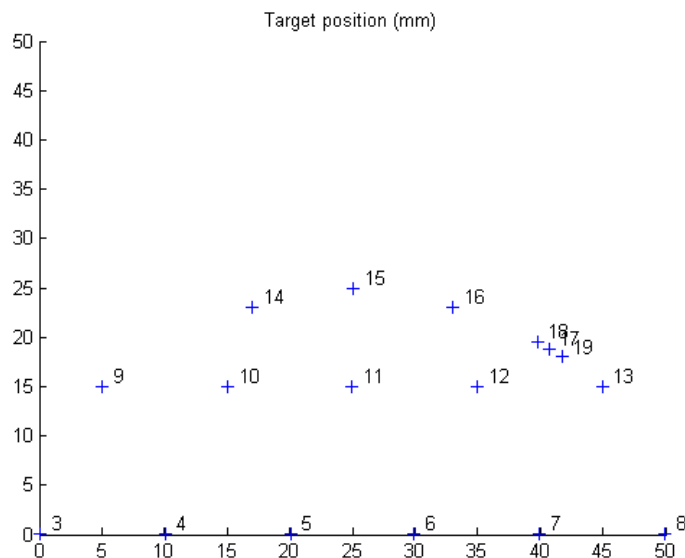
For porous concrete  $E = 40 \text{ GPa}$ ,  $\rho = 2300 \text{ kg/m}^3$ :  $c = 4170 \text{ m/s}$ .

The uncertainty in the evaluation of the velocity depends only on the identification of the maximum in the WT spectrum (peaks): the error has been estimated as twenty times the time step ( $dt=20*\text{time\_step}$ ) and is due to irregularities on the peak lines (due to the simulation time step and mother wavelet amplitude). The uncertainty on velocity computation results:

$$dv = \frac{x}{t^2} dt$$

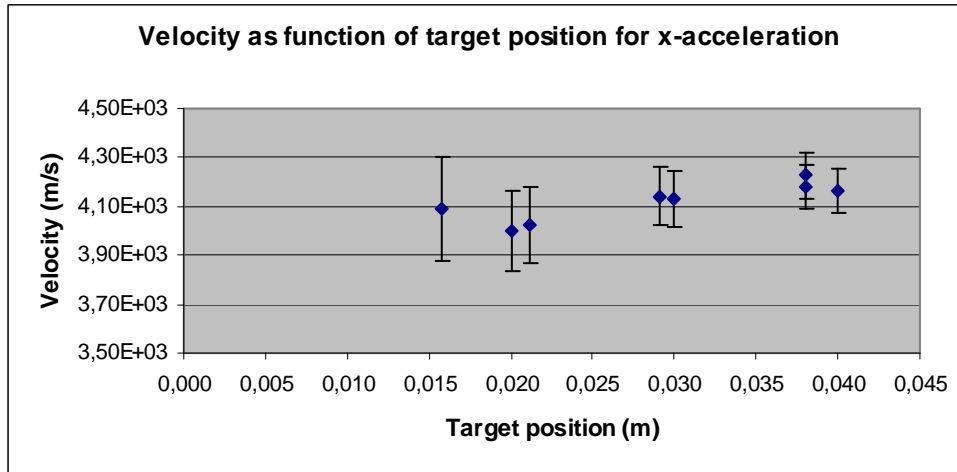
A compressed mother wavelet will reduce the uncertainty; but doing this the frequency resolution gets worse (see [16]).

The geometrical positions of the target points are shown in Fig. 6-3.



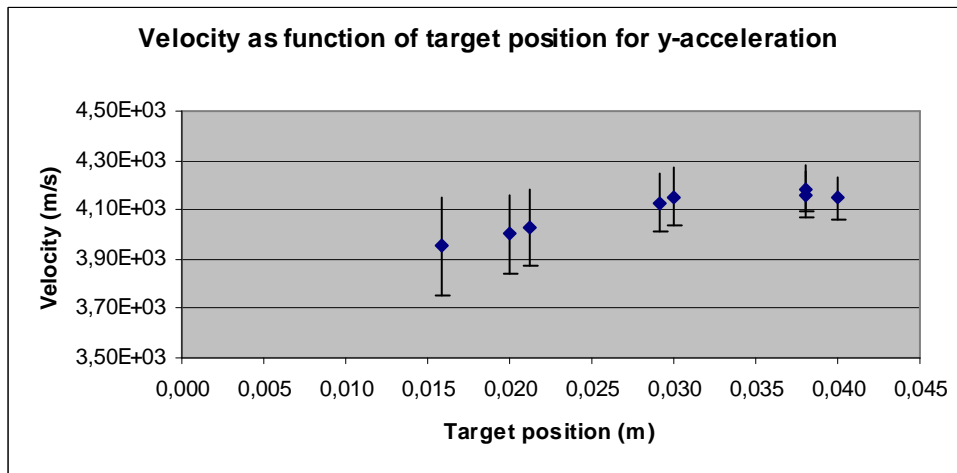
**Fig. 7-3 Target positions in the concrete sphere (for sake of simplicity only a quarter of the sphere is reported). Targets 3, 9, 14, 15, 16, 13 and 8 are on the sphere surface. Targets 17, 18 and 19 are placed under the added mass (second simulation)**

The velocity computed from x-acceleration signals at the different target locations, is reported in Fig. 6-4. The velocity of the first wave is in the range between 4000-4200 km/s and coherent with the speed of sound within the target material.



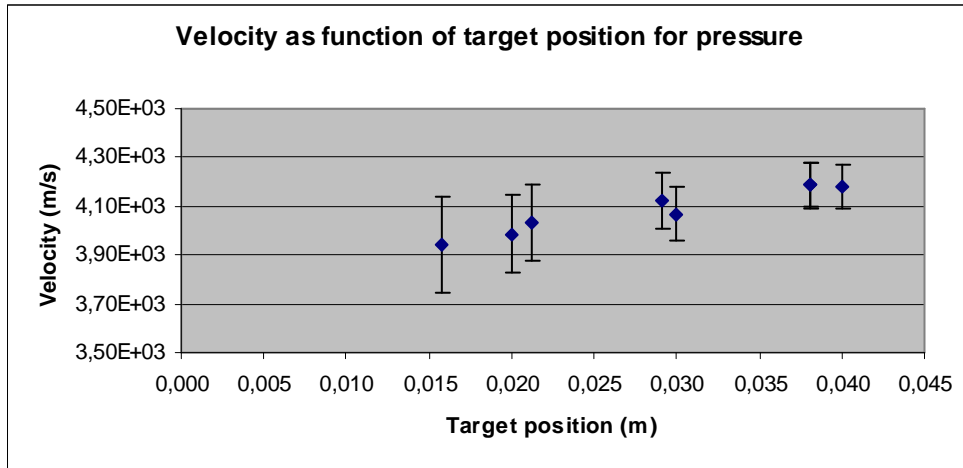
**Fig. 7-4 Velocity of the first wave at the different target locations (x-acceleration signal)**

Similarly in Fig 6-6, the velocity computed from the y-acceleration signal is shown.



**Fig. 7-5 Velocity of the first wave at the different target locations (y-acceleration signal)**

The same calculation can be made for pressure signals; in Fig. 7-6 the computed velocity at the different target locations is reported.



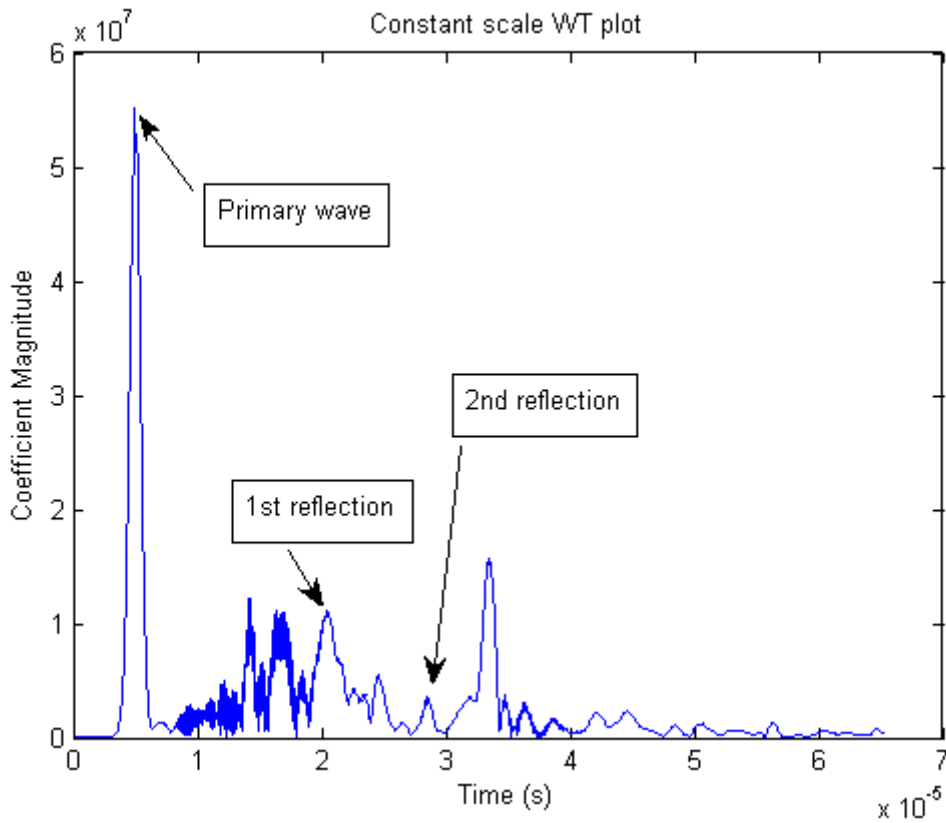
**Fig. 7-6 Velocity of the first wave at the different target locations (pressure)**

The centre frequency of the primary P-wave is computed as the peak in the WT spectrum at a fixed time (the arrival time for the wave). The frequency for the “acceleration wave” is 1.6 MHz, while the centre-frequency for the “pressure wave” is 610 kHz. The centre frequency is defined as the average/mean of the upper and lower frequencies of the wave components whose magnitude is above 50% of the peak magnitude (computed in the WT spectrum).

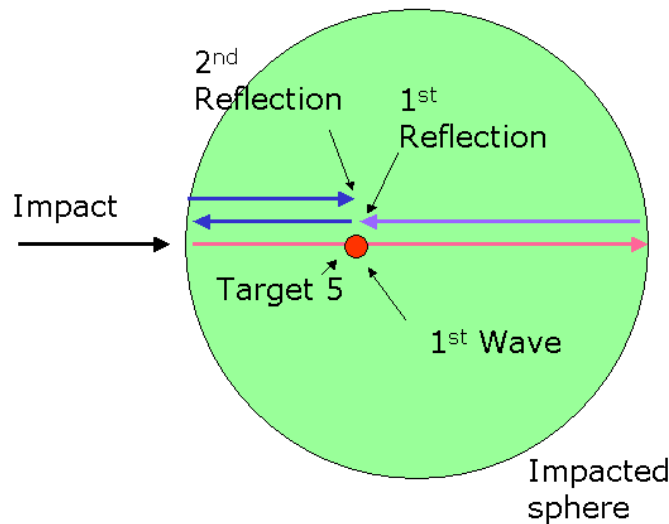
### 7.3.2 Wave reflection

The most important outcome of wavelets is the capability to identify the reflections. When a wave reflects from the medium boundary, it does not change its frequency or velocity, so in a WT spectrum it will appear similar to the first wave. In the constant scale plot of the wavelet spectrum, each peak in the WT represents a wave reflection (paragraph 6.4).

Fig. 7-7 shows the WT of x-acceleration wave on target point #5 (at constant scale). The wave reflections are represented by the peaks. The reflections identified are due to the P-Wave travelling along the sphere axis and reflecting from the opposite side of the impact point. Fig. 7-8 explains the reflection dynamics. Only the peaks corresponding to the wave propagating along the axis of the sphere are shown.



**Fig. 7-7 Constant scale plot of WT: wave reflection at target point #5, x-acceleration signal**



**Fig. 7-8 Wave reflection dynamic at target point #5**

Regarding the peaks identified in Fig. 7-7: target point #5 is placed at 20 mm from the impact point; the sphere diameter is 50 mm. The peaks shown in Fig. 7-7 represent the arrival time of three waves. They have been identified computing the



speed of propagation for the first wave, and measuring the time delay between the subsequent passages of the wave with that velocity at target point #5. There is a peak in the WT for each wave passage.

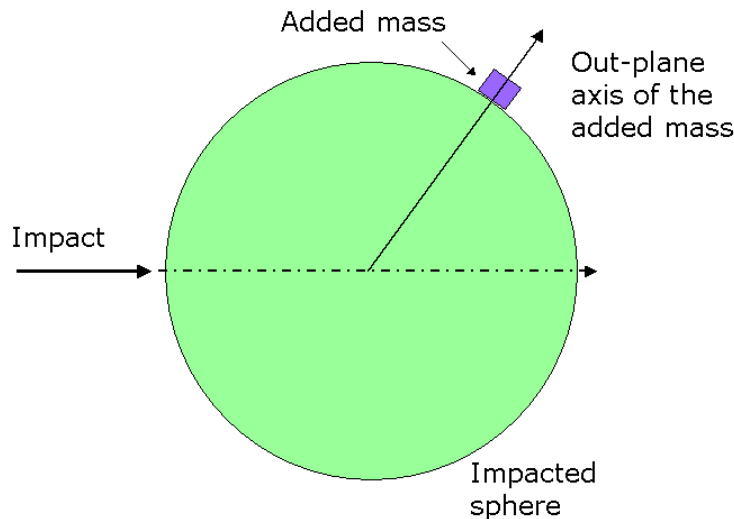
There are other peaks, but they belong to waves reflecting from the sphere upper and lower boundaries. In particular, a secondary wave is propagated after the passage of the first wave at the sphere upper end (see Fig. 7-9).

**Fig. 7-9 Second wave generated at the sphere surface**

This example shows how waves appear in the constant scale plot of the WT.

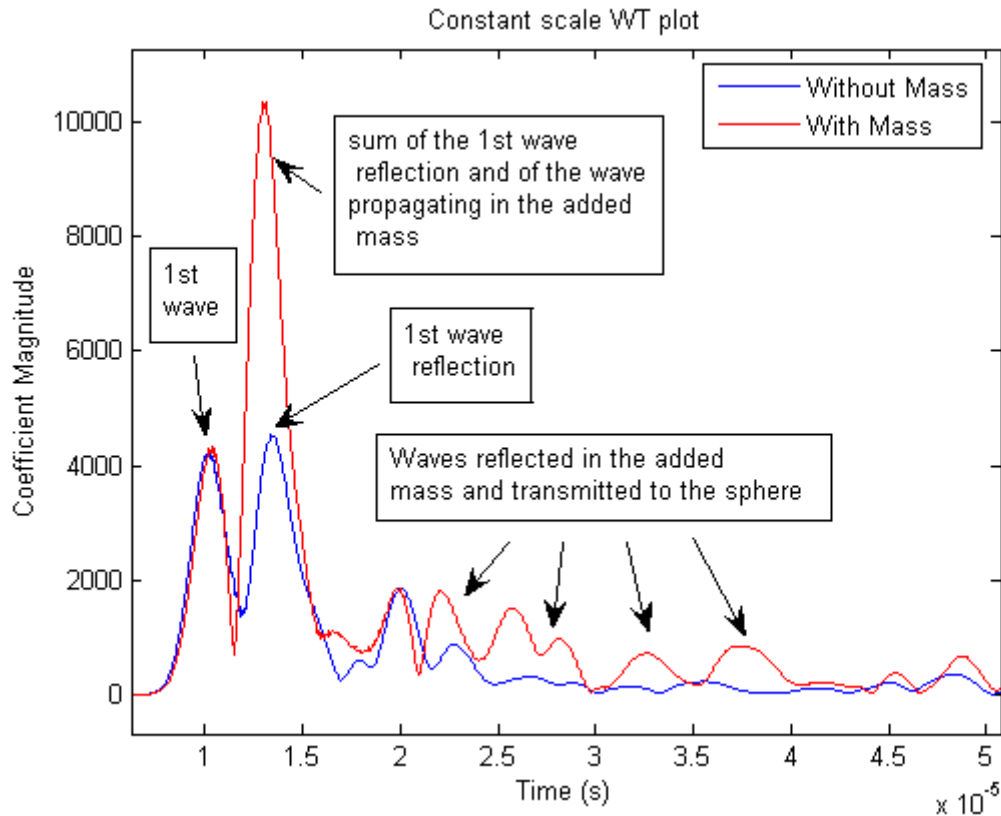
### 7.3.3 Load effect

The aim of simulation with the added mass simulating the sensor, visible in Fig. 7-1, is to provide a first estimate of its load effect and to assess the vibration environment that the accelerometer shall sustain and measure during HVI experiments. The target (sphere made of concrete), the impact conditions and the projectile are the same of the previous simulations. As said in the introduction, the parameters we want to identify are: the wave velocity, the reflection behaviour and their frequency and magnitude. Fig. 7-10 shows the simulation set-up.



**Fig. 7-10 Screen sfera con massa e asse out-plane su target 17**

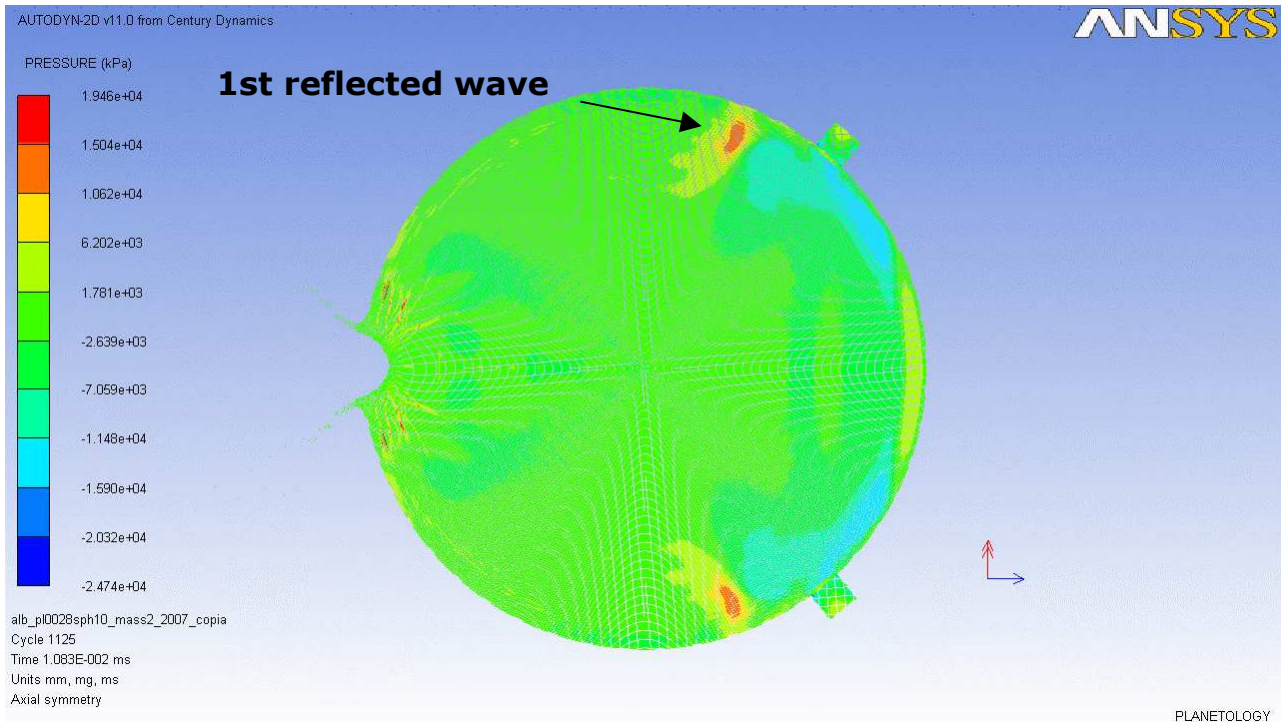
The added mass effect should be to change the reflection behaviour and thus change the way waves are reflected near its position. This issue has been investigated comparing waves reflection with and without added mass in target point #17 (see Fig. 7-3). Fig. 7-11 shows the coefficients of the modulus of the WT.



**Fig. 7-11 Scale plots of the acceleration signal (out-plane) with and without mass at target #17. The coefficient magnitude has to be multiplied by  $1e3$**

There are several differences between the peaks, so we can infer there is a load effect:

- The arrival time and magnitude of the first wave is the same. Obviously, the mass is "invisible" to the first wave since it has not yet impacted the mass
- The second wave (blue line) has a higher magnitude respect to the first wave, because of the porosity compaction due to the first compression wave passage. This wave (it is a reflection) is generated at the sphere upper boundary (see Fig. 7-12)
- With the added mass, the second peak is much higher. This is due to the constructive interference of the first reflected wave (the second peak in the blue line, Fig. 7-12) and of the wave that is transmitted in the mass (when the first wave pass-by) and reflects inside and is transmitted back in the sphere
- There are other peaks that represent other waves transmitted by the mass to the sphere



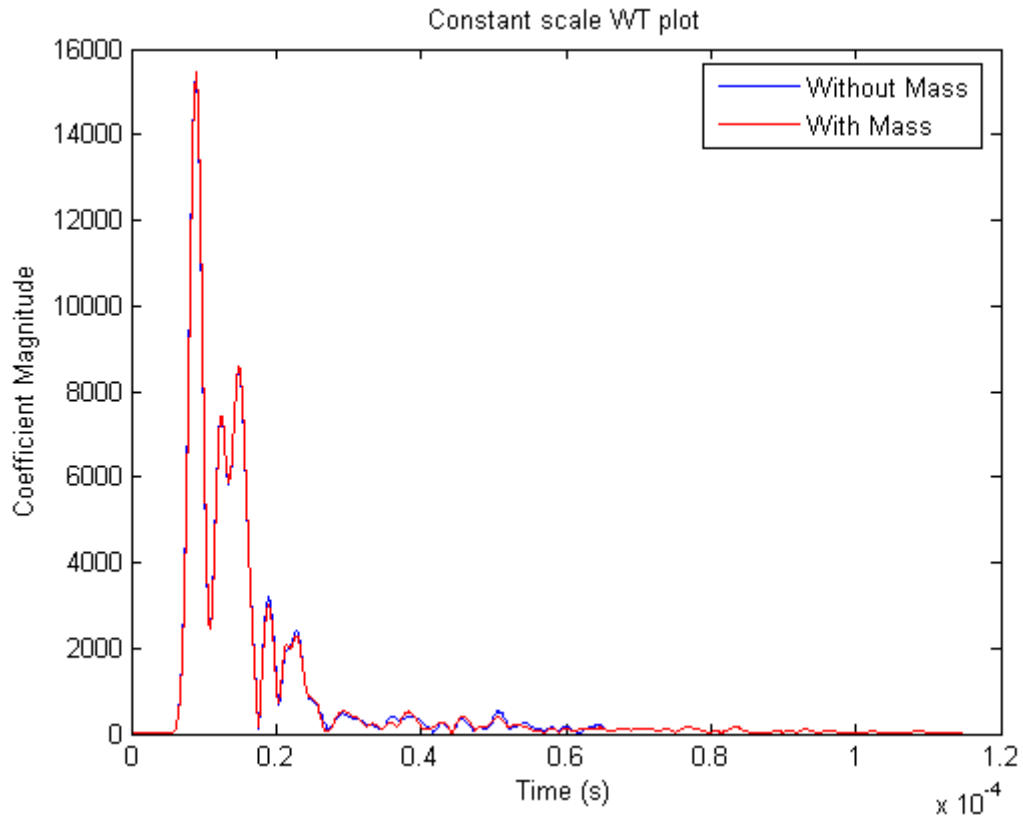
**Fig. 7-12 Fig 1 Reflection of the first wave, due to the boundary of the sphere. This wave propagates only near the surface since its depth is around two times the height of the added mass**

The result is that the first wave obviously suffers no load effect. The reflections instead are heavily modified by waves transmitted (both in time shift and in magnitude) in and out from the added mass. There is a generation of new waves with the added mass and the change of the mass will change the load effect.

Regarding the signal acquisition, the frequency of these waves lie between 500 kHz and 1.2 MHz. This means that the hypothetical measurement chain shall have high performance. Endevco shock accelerometers have a resonance frequency of 1.2 MHz and a linearity under 3 dB until before 200 kHz, thus they can measure this type of signal. The real issue is the signal-amplifier (of the voltage output exits from Endevco accelerometer), which can be linear up-to 700 kHz. Its response after this limit shall be measured in modulus and phase and non-linearity assessed. Doing this, the acceleration can be reconstructed even if it exits the standard dynamic-response-field of the sensor and amplifier.

The acceleration peak is around  $5e06 \text{ m/s}^2$ . The accelerometer maximum range is  $\pm 2e6 \text{ m/s}^2$ , thus the sphere dimension shall be increased, to lower the wave intensity at the sensor location.

The added mass does not modify the wave behaviour far from the mass location. Looking at the target #12, the differences between the signal with and without mass are negligible (see Fig. 7-13). The result is that the waves generated by transmission and reflections inside the added mass are damped in less than 5 mm and thus do not interfere with the global wave propagation in the concrete sphere.



**Fig. 7-13 Scale plots of the acceleration signal (out-plane) with and without mass at target #12. The coefficient magnitude has to be multiplied by 1e3**

## 8 Conclusions

### 8.1 Preparatory tests

The maximum acceleration expected peaks have been assessed through the preliminary tests performed on simple (near field environment) and complex targets (mid and far field).

#### Near-field

Acceleration levels for sensors mounted near the impact point have been measured, for both Al thin plates and Al HC. The aim of the experiments was to analyze the vibration intensity, to correctly set-up the measurement chain.

Endevco sensors result to be suitable for the task:

- The acceleration levels are under the  $2e6 \text{ ms}^{-2}$  limits of the Endevco sensors, but too high for a safe use of accelerometer with a lower dynamic range (like B&K).
- The impact generates waves with too high frequency for Endevco amplifiers (if sensors are attached to their mounting blocks with glue). For this reason a double layer tape have been used as connecting interface between sensor base and their mounting prism.

#### Mid- and far-field

Acceleration levels for sensors mounted on complex targets have been measured. The aim of the experiments was to analyse the vibration intensity on jointed components, to correctly set-up the measurement chain for target types "E", "C" and "D".

- Joints attenuate most of the high frequency/acceleration content in the case of type "E" and "D". For these configurations, the measure of HVI induced accelerations on not-impacted plates does not require Endevco.
- Joints do not attenuate the high frequency/acceleration content in the case of type "C", especially in plane accelerations. However, the resulting acceleration field can be acquired with low resonance sensors like B&K. In fact, the acceleration intensity after joints (positions 3 and 4) is well inside the dynamic range of B&K sensors ( $2e5 \text{ ms}^{-2}$ ), in fact their resonance does not overload the amplifiers (i.e. first case presented on paragraph 5.1.2).

### 8.2 HVI on satellite structures

This part of thesis document reported the main results of an experimental activity carried out to study the generation and propagation of transient disturbances induced by hypervelocity impacts (HVI) on spacecraft structures.

The selected approach is based on the construction of a unique experimental database, containing the accelerations measured on different locations of targets, dependently from impact conditions.

Aluminium spheres ranging from 0.6 to 2.3 mm were used as projectiles, and the impact speed was varied between 2 and 5 km/s. Two classes of target structures were considered:

- Simplified targets, that include simple aluminium panels and aluminium honeycomb sandwich panels. Experiments realised on these set-ups aimed at discovering the most important features of impact-induced vibrations on the near-field environment, i.e. at distance  $< \sim 300$  mm from the impact point where the HVI footprint is not yet altered by propagation and joints
- Complex targets, representing real GOCE structural configurations including joints. Experiments on these set-ups aimed at characterizing the behaviour of real spacecraft assemblies from the near-field to the far-field, in working conditions that are not normally considered with standard structural testing because of the high frequency content produced by HVI

In summary, experimental results provide a unique set of data about transient response of satellite structures, which was not available to date because of the level and frequency limitations of experimental techniques normally used in the structural field. In other words, HVI testing provides a new mean for loading structures up to working conditions not yet explored.

The most relevant experimental methods and results are summarized in the following.

Each experimental signal was subjected to validation according to international standards for transient shock analysis, performing checks for signal saturation and clipping, spikes occurrence, zero-shift, SNR value, SRS and velocity validation.

Then, it is necessary to remind that the impact chamber of a LGG is not a vibration-free environment and signals acquired from accelerometers are affected by interferences associated to the gun operations. It was therefore necessary to collect information on the facility background noise, to reduce it and correctly account for it when correlating signals to HVI phenomenon.

It was found that the background noise belongs primarily to the injection of propellant inside the impact chamber and can produce acceleration peaks as high as  $300 \text{ ms}^{-2}$ , for both in-plane and out-plane waves.

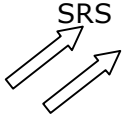
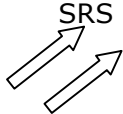
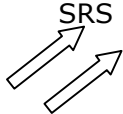
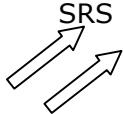
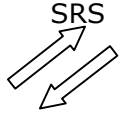

On the other hand, the background noise on complex targets is much related to the target configuration and accommodation inside the impact chamber. It was therefore evaluated for each relevant set-up.

### **8.2.1 Simple targets (near-field environment)**

#### Simple aluminium plates

Targets were made of Al 2024-T81, having thickness equal to 1 and 2 mm. The standard size of each panel was 500x500 mm.

The following observations were made on the dependence of out-plane and in-plane waves from impact conditions.

Mass effect		Velocity effect		Scaling effect	Thickness effect
NP	P	NP	P	NP/P	NP/P OP/IP
 SRS Mass	 SRS Mass Only for $f > 5\text{kHz}$	 SRS Velocity OP: $f > 3\text{kHz}$ IP: $f > 4\text{kHz}$	 SRS Velocity OP: $f < 2\text{kHz}$ IP: inverse trend	 SRS Target Size	 SRS Thickness

### Aluminium honeycomb sandwich panels

Targets were Al2024-T81 1mm 3.1 3/16 5056 10P, panel height 52.8 mm. The standard size of each panel was 400x400 mm. They are representative of GOCE floors 1, 2, 5, 6 and 7.

A HVI produces in both the front (impact) and rear side of the sandwich panel a vibration environment, which can be described through the SRS of OP, IP-L and IP-S waves. For comparison purposes, three different frequency ranges are introduced: low-frequency (from 102 to  $\sim 3\text{-}4 \cdot 10^3$  Hz), high-frequency (from  $\sim 3\text{-}4 \cdot 10^3$  to  $\sim 10^4$  Hz) and very-high-frequency (from  $\sim 10^4$  to  $\sim 1\text{-}2 \cdot 10^5$  Hz). In general, it should be noticed that the most peculiar observations are done inside the so-called "high-frequency range".

Considering the aforementioned classification for the wave types, it was found that OP and IP-L SRS have compatible magnitude in the low and very-high frequency ranges. In the high-frequency range, the magnitude of OP SRS is greater than that of IP-L. The SRS of IP-S are below OP and IP-L at all frequencies.

Regarding the SRS of OP and IP-L waves, no significant difference exists between front and rear side of the target in the whole frequency range. Nevertheless, in the high-frequency range SRS of IP-S are higher on the rear side.

The influence of projectile mass and velocity on SRS appeared to vary with frequency: in the high-frequency range SRS magnitude for P tests is substantially larger than that of NP tests, in the medium-low frequency range difference becomes less significant for OP and IP-S, and is negligible for IP waves. These observations hold for both impact and rear side of the panel.

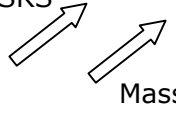
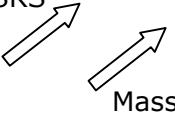

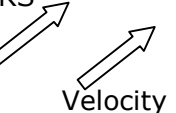


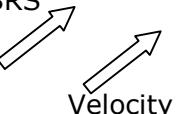
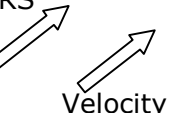
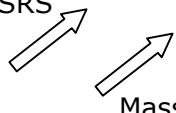

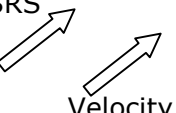
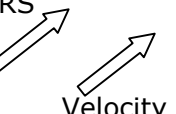
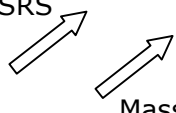
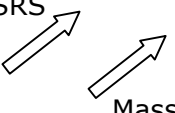
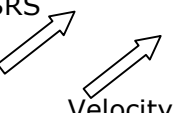
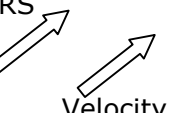

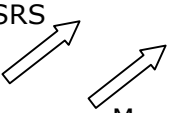
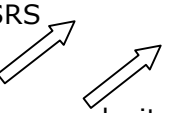
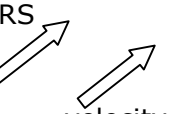
In the low and very-high frequency range, SRS are not affected by impact obliquity. In the high frequency range, oblique impacts produce higher SRS levels if the impacting debris is "small", i.e. if it produces a debris clouds having size comparable to that of the cross section of HC core channels.

Provided that any interference between internal HC core damages due to different HVI is avoided, SRS obtained from experiments on targets with existing damage are compatible to SRS calculated from completely new targets.

### **8.2.2 Complex targets (mid- and far-field environment)**

SRS behaviour vs. impact conditions

As general conclusion, it was found that SRS increase when projectile mass and/or impact speed increases, for all complex targets and for both NP and P experiments:

Target Type	Mass effect		Velocity effect	
	NP	P	NP	P
GOCE E	SRS  Mass	SRS  Mass	SRS  Velocity	SRS  Velocity
GOCE G	SRS  Mass	SRS  Mass	SRS  Velocity	SRS  Velocity
GOCE C	SRS  Mass	SRS  Mass	SRS  Velocity	SRS  Velocity
GOCE D1	SRS  Mass vp= 4 km/s vp= 5 km/s	SRS  Mass vp= 4 km/s vp= 5 km/s	SRS  Velocity As trend	SRS  Velocity * dp=1.9mm * As trend for dp=2.3mm
GOCE D2	SRS  Mass vp= 4 km/s vp= 5 km/s	SRS  Mass vp= 4 km/s vp= 5 km/s	SRS  velocity As trend	SRS  velocity * dp=1.9mm * As trend for dp=2.3mm

SRS transmission through joints and propagation

It was found from the experiments target geometrical configurations and joint disposition considerably affect the transmission of disturbances along structures.

For GOCE E, G, D1 and D2 junctions connect plates not disposed on a single plane and therefore cause a “transformation” of OP in IP waves and vice-versa. This effect does not occur for GOCE C targets, on which both OP and IP waves are transmitted from the emitter to the receiver plate without changing direction. Taking into account this preliminary consideration, the following observations were carried out:

- The joint effect is present for the transmission OP to IP, due to different mechanical impedances between plates and junctions. In this case junctions act as a mechanical filter, reducing SRS levels up to 80% (GOCE E, G, D1 and D2)
- The amplification and subsequent attenuation appear when the transmission of the wave is IP to OP; in this condition junctions act as a mechanical “bracket” inducing an amplification zone at junction resonant frequency followed by an attenuation zone (GOCE E, G, D1 and D2). The amplification of IP waves may rise up to a factor of 3, while subsequent attenuation is around 40%.
- For IP to IP transmission, a junction effect is evident (GOCE C). It may produce a SRS attenuation up to 80%



- In case of OP to OP transmission, joints act as resonant frequency, with an amplification zone and a subsequent attenuation zone (GOCE C). The amplification may rise up to a factor of 2.5, while subsequent attenuation is around 40%.

Even a HC core effect was highlighted, for both OP and IP transmission on the same panel. Attenuation was observed only for IP SRS, due to the shear movement between the skins and the core: this effect is evident for CFRP HC panels (targets C, D1 and D2) and slightly appreciable for Al HC SP.

OP waves are almost unchanged from front to rear side, with the exception of a local amplification correspondent to a system resonance, which is probably related to a combined HC core-junction effect.

### 8.3 Momentum transferred to targets by HVI

The evaluation of the momentum transferred to targets by HVI was performed using a special ballistic pendulum on which targets were mounted during impact experiments. The pendulum was designed to have a dynamic behaviour very close to a single degree of freedom oscillating mass. In this way, the momentum transferred to target was estimated through the measurement of the maximum displacement caused to the pendulum by the HVI.

For each target configuration (simple Al plate, Al HC SP, CFRP HC SP), the arrangement was calibrated to obtain a set of correlation curves useful for extrapolating the required momentum information from the measurement of the pendulum displacement.

Measurements are affected from uncertainty related to the momentum transferred to targets by the propellant gas injected into the impact chamber, which could be large in case of small momentum transferred to the target.

Main results are hereafter summarized:

- For simple Al plates, the ratio between momentum transferred to targets and projectile momentum is 3% for P tests and 330% for NP. It is necessary to underline that measurement uncertainty can be as high as 200% for this class of targets
- For Al HC SP, the ratio between momentum transferred to targets and projectile momentum is 111% for P tests and 79% for NP. In this case, measurement uncertainty is larger for NP experiments, rising up to 60%
- For CFRP HC SP, the ratio between momentum transferred to targets and projectile momentum is 148% for P tests and 230% for NP. In this case, measurement uncertainty is larger for NP experiments, rising up to 25%

Even though the measurement uncertainty is large, previous numerical results may be justified by thinking at the momentum contribution of the front and rear ejecta in P and NP tests respectively:

- For P experiments, a large amount of momentum is carried away by the front part of the debris cloud, especially on Al plates. This explains the small part of projectile momentum absorbed by the target. On the other hand, sandwich panels have the ability of capturing a large part of the debris cloud, thus taking from the projectile a larger amount of momentum
- For NP experiments, the existence of rear ejecta results in the transmission to targets of a momentum amount higher than that carried by the projectile itself.

The measures of momentum transferred to Al plates and Al HC SP were compared to FEA and SPH numerical results, highlighting a good agreement between the three techniques [28].

## 8.4 Wavelet analysis on satellite components

Wavelet Transform (WT) was applied to study the transient waves propagating in plates and honeycomb sandwich panels due to impacts at hypervelocity.

Two types of waves groups have been experimentally observed on simple plate target. The first group is made by symmetric ( $S_0$ ) Lamb waves, while the second by antisymmetric ( $A_0$ ) (symmetry and antisymmetric respect to the plate's mid plane). Wavelet analysis was able to identify both the frequency content and the propagation velocity. In case of the non-perforating impact, antisymmetric group waves are predominant (see low velocity test).

On honeycomb-panel-skins, the symmetric waves are dominant. Antisymmetric waves have not been identified, probably due to the high stiffness of the plate (which determines flexural  $A_0$  Lamb waves with very low amplitude). Moreover, on honeycomb panel, reflections on edges and discontinuity have been captured.

The use of the Wavelet Transform for the analysis of acceleration data demonstrated the possibility of identifying perturbations propagating after an impact. Special applications are the detection of the wave's constituents and the separation of the original wave from its reflections. This makes it possible to generalize experimental results obtained on laboratory-scaled targets on which edge effects may play an important role.

## 8.5 Shock wave propagation into minor bodies of the Solar System

This preliminary work on waves propagation on porous targets demonstrated that the WT is able to identify and characterise waves propagating and reflecting on a scale mock-up of a planetary minor body, as so as for satellite aluminium H/C panels.

The velocity of waves (both acceleration and pressure) corresponds to the sonic velocity in the material (concrete) with an uncertainty of  $\pm 5\%$  and is due to the Morlet wavelet time resolution.

Reflections have been identified matching the waves speed velocity (with the same uncertainty band of  $\pm 5\%$ ).

A second simulation has been run to assess the load effect of an added mass on the wave propagation behaviour (the added mass simulates an accelerometer or its mounting block). The SPH simulation and the results of the wavelet signal analysis seems to indicate that the mass does change the way waves reflect and superimpose due to waves transmission and reflection inside the added mass: there is a strong interference effect and generation of new waves.

Besides, the measurement of these high frequency and amplitude acceleration signals is difficult, but feasible with the proper instrumentation.

These results are preliminary and limited to one specific case, but demonstrate that WT analysis and the combination of numerical and experimental simulations could be very efficient for investigating the shock wave propagation within planetary bodies. There is of particular interest for investigating impact process and collisional evolution

of the solid bodies of the Solar System, but also to evaluate and mitigate possible hazards for asteroid impact with the Earth.

## 9 References

- [1] Piersol, A.G., "Pyroshock Recommendations in Proposed MIL-HDBK on Guidelines for Dynamic Data Acquisition and Analysis", Journal of the IES, Sept./Oct. 1992
- [2] Handbook for Dynamic Data Acquisition and Analysis, Institute of Environmental Sciences and Technology
- [3] NASA Technical Standard Pyroshock test criteria, NASA-STD-7003, 1999
- [4] ENV 13005:1999, "Guide to the expression of uncertainty in measurement"
- [5] Jeong, H., Jang, Y., "Wavelet analysis of plate wave propagation in composite laminates", Composite Structures, vol. 49, 2000, pp. 443-450
- [6] Doyle, J.F., "Wave propagation in structures", Mechanical Engineering Series, 1997, pp. 27-41
- [7] Graff, K.F., "Wave motion in elastic solids", Calderon Press – Oxford 1975, p. 457
- [8] MatLab user manual
- [9] SDH Team, "Test plan", ALS-SDH-TNO-002, TN2 of the ESA Contract 17854/03/NL/CH "Spacecraft Disturbances from HVI", 23/05/2005
- [10] Graff Karl F., Wave Propagation in Elastic Solids, Calderon Press, Oxford 1975
- [11] Meo M., Zumpano G. Impact identification on a sandwich plate from wave propagation responses. Composite structures 71 (2005) 302-306
- [12] Wang L., Yuan F.G. Group velocity and characteristic wave curves of Lamb waves in composites: Modeling and experiments. Composites Science and Technology 67 (2007) 1370-1380
- [13] Newland D.E. Ridge and Phase Identification in the Frequency Analysis of Transient Signals by Harmonic Wavelets. Journal of Vibration and Acoustics vol. 121 (April 1999)
- [14] Park H.C., Kim D.S. Evaluation of the dispersive phase and group velocities using harmonic wavelet Transform NDT&E International 34 (2001) 457-467
- [15] Cattani C. The wavelet-based technique in dispersive wave propagation. International Applied Mechanics, Vol. 39, No. 4, 2003
- [16] Newland D. E. Harmonic wavelets in vibrations and acoustics. Phil. Trans. R. Soc. Lond. A(1999) 357, 2607-2625
- [17] CNES activity report at the 19th IADC meeting DLR March 22-23, 2001 cologne-Porz, Germany.
- [18] Pavarin D., Francesconi A., Debei S., Caporal G., Preliminary design of a test bed to evaluate the requirements of an accelerometric instrumentation to study the effects of hypervelocity impacts on space shield, Mechanical Measurements Conference, 17-19 Sept. 2002, Abano Terme, Italy.
- [19] C. Giacomuzzo, F. Ferri, A. Bettella: Hypervelocity experiments of impact cratering and catastrophic distruption of minor bodies of the Solar System, COSAPAR 2006.
- [20] Prosser W. H., Application of Advanced, Wavefrom Based AE Techniques for testing Composite Material, Proceeding of the SPIE Conference on Nondestructive Evaluation Technique for Aging Infrastructure and

- manufacturing: Material and Composites, December 2-5, 1996, Scottsdale, Arizona.
- [21] Prosser W.H., Gorman Michael R. and Humes Donald H.,. Acoustic emission signal in thin plates produced by impact damage, Journal of acoustic emission vol 17(1-2) (June 1999), pp 29-36.
- [22] Faraud M., Meteoroids and Debris Environment Analysis for Disturbance Assessment on the Gradiometer GO-TN-AI-0092, Issue 01, 30 July 2002.
- [23] Faraud M., Disturbances induced by MMOD impacts GO-TN-AI-0099, Issue 01, 20 May 2003
- [24] Pavarin D., Lambert M., Francesconi A., Destefanis R., Bettella A., Debei S., De Cecco M., Faraud M., Giacomuzzo C., Marucchi-Chierro P.C., Parzianello G., Saggin B. and Angrilli F. Analysis of GOCE's disturbances induced by hypervelocity impact" 4th European, Conference on Space Debris Darmstadt 2005 .
- [25] Pavarin D., Francesconi A , Destefanis R., Lambert M.,.Bettella A., Debei S., De Cecco M., Faraud M., Giacomuzzo C., Marucchi-Chierro P.C., Parzianello G., Saggin B. and Angrilli. Acceleration Fields Induced By Hypervelocity Impacts On Spacecraft Structures. International Journal of Impact Engineering. Vol. 33, Pp. 580-591 Issn: 0734-743x.
- [26] Francesconi A., Pavarin D., Bettella A., Giacomuzzo C., Faraud M, Destefanis R., Lambert M. and Angrilli F. Generation of transient vibrations on aluminum honeycomb sandwich panels subjected to hypervelocity impact Hypervelocity Impact Symposium 23-27 september 2007, Williamsbug (Virginia USA), to be published on the International Journal of Impact Engineering Issn: 0734-743x.
- [27] Bettella A., Francesconi A., Pavarin D., Giacomuzzo C. and Angrilli F. Application of wavelet Transform to analyze acceleration signals generated by HVI on thin aluminum plates and all-aluminum honeycomb sandwich panels, Hypervelocity Impact Symposium 23-27 september 2007, Williamsbug (Virginia USA), to be published on the International Journal of Impact Engineering Issn: 0734-743x..
- [28] Giacomuzzo C., Pavarin D., Francesconi A., Lambert M., Angrilli F. "SPH evaluation of out-plane peak force transmitted during a hypervelocity impact", Hypervelocity Impact Symposium 23-27 september 2007, Williamsbug (Virginia USA), to be published on the International Journal of Impact Engineering Issn: 0734-743x..
- [29] NASA "DYNAMIC ENVIRONMENTAL CRITERIA" NASA-HDBK-7005 MARCH 13, 2001
- [30] S-50/95-TD-HTS, ESTEC CONTRACT 11540/95/NL/JG, ESABASE/DEBRIS Release 2, Technical Description, August 1998
- [31] Rubin, S., "Concepts in Shock Data Analysis", Ch. 23, Shock and Vibration Handbook, 4th ed., (Ed: C. M. Harris), McGraw-Hill, NY, 1996.
- [32] Trubert, M., and Salama, M. A., Generalized Modal Shock Spectra Method for Spacecraft Loads Analysis, AIAA J., Vol. 18, No 8, pp. 988-994, Aug. 1980.
- [33] NASA/JSC Orbital debris models, Nicholas Johnson and Eric Christiansen, Proceeding of the Second European Conference on space debris, ESOC, Darmstadt, Germany, March 1997

- [34] Britt, D., Yeomans, D., Housen, K., et al. Asteroid density, porosity, and structure, in: Bottke Jr., W.F., Cellino, A., Paolicchi, P., Binzel, R.P. (Eds.), *Asteroids III*. University of Arizona Press, Tucson, pp. 485– 500, 2002.
- [35] Fujiwara A. et al The Rubble-Pile Asteroid Itokawa as observed by Hayabusa *Science* 312, 1330-1333, 2006
- [36] Flynn, G.J., Moore, L.B., Klock, W. Density and porosity of stone meteorites: implications for the density, porosity, cratering, and collisional disruption of asteroids. *Icarus* 142, 97–105, 1999.

## 10 List of abbreviations and acronyms

Al	Aluminium
ASAS	Acceleration Signals Acquisition Software
BL	Ballistic Limit A qualitative information of the damage with respect to BL is given as follows NP Clearly not penetrating BL≤ Not Penetrating, just below BL BL≥ Penetrating, just above BL P Clearly penetrating
CFRP	Carbon Fiber Reinforced Plastic
CWT	Continuous Wavelet Transform
DAS	Data Acquisition System
dB	Decibel. A signal $s$ may be expressed in dB using the formula on the right, where $s_0$ is an arbitrary reference value for $s$ . $s [dB] = 20 \log_{10} \frac{s}{s_0}$
DLF	SEA Damping Loss Factor
dp	Projectile diameter (mm)
EOS	Equation Of State
FEA	Finite Element Analysis
FFT	Fast Fourier Transform
FRF	Frequency Response Function (i.e. transfer function)
HC	Honey Comb
HT	Hammer Test
HVI	Hyper Velocity Impact
IP	In-plane IP-L: IP-longitudinal IP-S: IP-shear
LGG	Light-Gas Gun
MMOD	Micro Meteoroid and Orbital Debris
mp	Projectile mass
MW	Mother Wavelet
NP	Not Penetrating shot, i.e. below BL (see also BL)
OP	Out-plane
P	Penetrating shot, i.e. above BL (see also BL)
RMS	Root Mean Square
SEA	Statistical Energy Analysis
SNR	Signal to Noise Ratio
SP	Sandwich Panel
SRS	Shock Response Spectrum SRS <sup>+</sup> and SRS <sup>-</sup> are the positive and negative SRS, respectively
STFT	Short Time Fourier Transform
TS	Test Series
U	Uncertainty
vp	Projectile impact velocity
WT	Wavelet Transform
σ	Standard Deviation
PR	Piezoresistive
PE	Piezoelectric
ICP	Piezoelectric sensor with integrated charge-voltage converter
TR	Transfer Function